Photoelectron circular dichroism (PECD) of monoterpenes using laser and synchrotron radiation

Hassan Ganjitabar

Thesis submitted to the University of Nottingham for the degree of
Doctor of Philosophy

August 2020

“You are not a drop in the ocean; you are the entire ocean, in a drop.”

Mowlana, Jalal ad-Din

Acknowledgement

There are no proper words to convey my deep gratitude and respect for my thesis and research advisor, **Prof. Ivan Powis**, who accepted me as his PhD student. This work would not have been possible without his guidance and involvement, his support and encouragement on a daily basis from the start of the project till date. For all these, I sincerely thank him from the bottom of my heart and will be truly indebted to him throughout my lifetime.

I would like to express my very great appreciation to my co-supervisor **Prof. Katharine Read** who was always supportive and available especially when I was facing any problem on the way of my research.

I cannot forget the valuable discussions and conversations we had with **Dhirendra Portab Sing**, my friend and colleague. He was a nice friend of mine during the so many travels we had in the past four years in the framework of the ASPIRE network.

I also would like to thank the personnel of the DESIRS beamline of SOLEIL Synchrotron, particularly, **Prof. Laurent Nahon** and **Dr. Gustavo Garcia** for all of the supports I received from them during our collaboration. They played a huge role in performing the experiments and acquiring the majority of the data used in this thesis. I will always remember such nice persons with warm thoughts and memories.

I gratefully acknowledge the funding received towards my PhD from the European Union’s Horizon 2020 research and innovation programme, ASPIRE, under the **Marie Sklodowska–Curie Grant Agreement No. 674960**.

I owe thanks to a very special person, my wife, **Kimia**, for her continued and unfailing love, support and understanding during my PhD degree that made the completion of the thesis possible. She has been my best friend and great companion who loved, supported, encouraged, and helped me to complete this period in the most positive way.

Last, but not least, I deeply acknowledge the people who mean a lot to me, my parents, **Bourzoo Ganjitabar** and **Fouziyeh Ebrahimi**, for having faith in me and supporting me to achieve what I desired. I salute you all for the selfless love, care, pain and sacrifice you did to shape my life.

Abstract

The asymmetry in the photoelectron angular distribution (PAD) with respect to the propagation direction of light, known as Photoelectron Circular Dichroism (PECD), is a very important property of the chiral molecules, which can be exploited for analytical purposes. PECD can be used as a probe to several static (chemical substitution, conformation, dimerization, and clustering) and dynamic (vibrational motions, intermediate and cationic electronic states as well as photoelectron kinetic energy) phenomena as it is sensitive to all of them. In this project, the focus was on the dynamic ones; the dependency of PECD on vibrational motions and decouple that from the other dynamic effects like photoelectron kinetic energy is investigated. The other major part of the project was to introduce a new method to simultaneously measure the chemical composition (cc) and enantiomer excess (ee) in gas phase mixtures. The idea with the cc analysis was that the photoelectron spectrum of a mixture must be a linear combination of the photoelectron spectra of its compounds. Similarly, the PECD spectrum of the mixture can be presented as a linear combination of the weighted PECD spectra of the compounds.

The cc and ee of two essential oils, black pepper oil and Mexican lime oil, are studied as the benchmark. These two oils are mainly composed of volatile samples, a monoterpene family including α-pinene, β-pinene, limonene, 3-carene, sabinene and γ-terpinene, all of which are chiral except the last one. For cc analysis, we measured the high-resolution photoelectron spectra of the oils and their compounds at the DESIRS beamline of the SOLEIL synchrotron using Slow Photoelectron Spectroscopy (SPES) technique. We also measured the Velocity Map Imaging (VMI)-PES and VMI-PECD of the oils and their compounds at two fixed photon energies, $h\nu$=9.0 eV and $h\nu$=9.5 eV, from which the VMI-PES results were used to obtain the cc in a similar way to the SPES technique. The cc obtained using VMI-PES were in an excellent agreement with those obtained using the SPES technique, which itself verified the validity of our method. The VMI-PECD spectra weighted by the corresponding VMI-PES then were used to get the ee of each compound.

In addition, several synchrotron-based, single-photon experiments were carried out to investigate the sensitivity of PECD to the vibrational dynamics as well as to the kinetic energy of the photoelectrons. Our results show that PECD is intensively modulated by the vibrational structures. In addition, we argue that the PECD is more sensitive to the vibrational structures, particularly, in a VMI setup where the PES resolution goes worse by increasing the photoelectron kinetic energy. For example, we compared the VMI-PES and VMI-PECD

recorded at two photon energies, hν=9.0 eV and hν=10.5 eV. In contrast to VMI-PES, VMI-PECD spectra recorded at both photon energies showed roughly the same vibrational resolution. Furthermore, by recording the PECD of two of the monoterpenes, α-pinene, and 3-carene at different fixed photon energies ranging from near threshold up to 19.0 eV, we could successfully decouple the vibrational and photoelectron kinetic energy effects for the first time. The results of our Frank Condon (FC) simulation were leading us in this direction as they were crucial in the assignment of the vibrational structures.

Furthermore, a pump-probe laser experiment was carried out on α-pinene to investigate the dependency of PECD on vibrational and electronic quantum states at the intermediate level. Using a femtosecond laser system in the Artemis beamline of Central Laser Facility (CLF), we recorded the PECD of the molecule at three different wavelengths (λ=396.52 nm, λ=371.02 nm, and λ=200.66 nm). In this case, the interpretation of our experimental results was possible thanks to a combination of Time-Dependent Density Functional Theory (TD-DFT) and FC calculation we performed. Our experimental results showed that in addition to the first odd beta parameter b_1, there are higher asymmetry parameters like b_3 and b_5 contributing to the total PECD. We also could decouple the vibrational effects from the intermediate electronic states and photoelectron kinetic energy effects by comparing the PECD spectra recorded at different wavelengths.

Contents

1. Introduction 1

  1.1. Chirality 1

    1.1.1. Chirality in nature 1

    1.1.2. Chirality in Physical Chemistry 3

  1.2. Circular Dichroism (CD) 4

    1.2.1. Photoabsorption Circular Dichroism (PCD) 5

    1.2.2. Photoelectron Circular Dichroism (PECD) 5

  1.3. Current State of the Art in PECD Research 6

    1.3.1. Single Photon Ionization: a historical review 6

    1.3.2. Laser Based MP-PECD 30

    1.3.3. Conclusion 44

2. Experimental and Theoretical Methods 45

  2.1. Velocity Map Imaging (VMI) 45

  2.2. Time of flight mass spectroscopy (ToFMS) 51

    2.2.1. Basic ToFMS 51

    2.2.2. Wiley & McLaren ToFMS 53

  2.3. Photoelectron photoion coincidence spectroscopy (PEPICO) 55

  2.4. PES, PECD, and SPES 56

  2.5. CMS-Xα Method 60

  2.6. FC and OVGF calculations 61

3. Near threshold PEPICO and SPES of monoterpenes 63

  3.1. Results 65

    3.1.1. α -pinene 65

    3.1.2. 3-carene 73

    3.1.3. Limonene 80

    3.1.4. β-pinene 88

    3.1.5. sabinene 95

  3.2. Conclusion 101

4. Chemical Composition and Enantiomer Excess Analysis Using Photoelectron Spectroscopy 103

  4.1. Introduction 103

  4.2. Theoretical Approach 105

    4.2.1. SPES and VMI-PES fitting: cc analysis 105

    4.2.2. PECD fitting: ee analysis 109

4.3. Experiments 111
4.4. Black Pepper Oil 114
4.5. Mexican Lime Oil 121
5. Vibronic modulation of PECD in monoterpenes 129
5.1. Introduction 129
5.2. Results 131
5.2.1. α-pinene 131
5.2.2. 3-carene 134
5.2.3. Limonene 136
5.2.4. β-pinene 139
5.2.5. Sabinene 141
5.3. Conclusion 145
6. Decoupling the effect of vibrations and photoelectron kinetic energy on PECD 146
6.1. Results 147
6.1.1. 3-carene 147
6.1.2. α-pinene 156
6.2. Conclusion 165
7. Resonance Enhanced Multiphoton Ionization- (REMPI-) PECD of $\boldsymbol{\alpha}$-pinene 166
7.1. Laser system and experimental setup 167
7.2. Three-photon ionization PECD at 396.52 nm 170
7.3. Three-photon ionization PECD at 371.02 nm 179
7.4. Two-photon ionization PECD at 200.66 nm 184
7.5. Conclusion 187
8. Conclusion 189
9. Bibliography 192
10. Appendices 201
10.1. Appendix A: VMI calibration 201
10.1.1. Xenon calibration at 396.52 nm 204
10.1.2. CS2 calibration at 200.66 nm 211

List of Figures

Fig. 1: Flowers in nature showing chirality. 2
Fig. 2: Chirality in the spin of galaxies (A) and the shell of snails (B). 3
Fig. 3: Photoelectron anisotropy parameters $b2$, solid curves, and $b1$, dashed curves 8
Fig. 4: Schematic of the experimental setup for the PECD measurement in Ref. [34]. 9
Fig. 5: PES and PECD measurement in Ref. [34]. 10
Fig. 6: Circular dichroism in the photoelectron angular distribution of outermost orbital 11
Fig. 7: Valence (HOMO) (left) and core (O 1s) (right) photoelectron angular distribution parameters 13
Fig. 8: chemical structure of S-methyloxirane (I), trans-2S,3S-dimethyloxirane (II), ... 14
Fig. 9: PECD signal of the HOMO and HOMO-1 orbitals of S-MOX (black triangles) and R-TFMOX (red dots) 15
Fig. 10: (1R, 2R)-1,2-dibromo-1,2-dichloro-1,2-difluoroethane (I) and (S)-methyloxirane (II). 16
Fig. 11: Cross section σ, asymmetry parameter β and PECD parameter D of two valence orbitals, ... 16
Fig. 12: Cross section σ, asymmetry parameter β and PECD parameter D 17
Fig. 13: Dichroic parameter D of 14a orbital of different conformers of (S)-methyloxirane. 18
Fig. 14: Dichroic parameter for orbitals 11a-16a of methyl oxirane 19
Fig. 15: Theoretical/experimental comparison of endoborneol PECD measurements. 20
Fig. 16: (a) ToF mass spectrum of (1R)-(+)-camphor, (b) total photoelectron image 21
Fig. 17: Experimental dimer and monomer TPES. 22
Fig. 18: (top) usual anisotropy parameter, β, and (bottom) PECD parameter, $b1$, of (1R)-(+)-camphor 23
Fig. 19: a: Mass selected PES of first n-mers of S-glycidol (top panel) and 25
Fig. 20: PES and PECD of S-glycidol monomer and dimer in two clustering condition 26
Fig. 21: Dependency of anisotropy parameter, β, and PECD parameter, D 27
Fig. 22: Right: TPES of S-methyloxirane plotted together with FC simulation 28
Fig. 23: PECD of limonene over the X-band (an overlap of the HOMO and HOMO-1) 29
Fig. 24: First row: VMI images recorded for (R)-(+)-camphor using linear (left), LCP (middle) and RCP (right). 30
Fig. 25: (a) Schematic of intermediate states getting pumped in (2+1) REMPI of camphor 32
Fig. 26: Top row: the PECD images of (R)-(+)-camphor at different intensities 33
Fig. 27: REMPI-PECD of limonene enantiomers measured at three laser wavelengths 420 nm 35
Fig. 28: REMPI-PECD of fenchone for different intermediate states: 3s (red), $3p_1$ (blue) and $3p_2$ 36
Fig. 29: Linear relation of the PECD and ee 37
Fig. 30: Mass-selected PECD asymmetry parameter, G, measured in the PEPICO scheme 38
Fig. 31: Schematic of the TR-PECD measurement (a) and photoelectron image recorded 39
Fig. 32: Dependency of bi coefficients on the delay time between the pump and probe 40
Fig. 33: PECD row images for R- and S-cmphor (top row), R- and S-fenchone 42
Fig. 34: Intersection of a cylindrical beam line and a cylindrical molecular beam 45
Fig. 35: (a) Electric potential lines calculated around the electrodes 47
Fig. 36: (a) The points that three groups of electrons, initially making angles $0/180°$, $45/135°$ and 90 °, ... 47

Fig. 37: schematic view of a typical Newton sphere (a) and its projection on a 2-D detector (b) 48
Fig. 38: A Newton sphere with two shells (a) and its projection to a 2-D detector (b) 49
Fig. 39: Onion model of Newton sphere (a), 2-D projection of different shells 49
Fig. 40: Photoelectron image of $CO2$ molecules aligned with a free-electron laser 51
Fig. 41: Schematic view of a basic ToFMS... 52
Fig. 42: A basic ToFMS (a) versus a Wiley & McLaren ToFMS (b) 54
Fig. 43: A typical PEPICO experiment. Photoelectrons are detected by a VMI technique 56
Fig. 44: A typical PES matrix composed by adding all the one dimension PES arrays 58
Fig. 45: TPES and SPES of limonene 59
Fig. 46: Partitioning the molecular and out space into spherical regions in CMS-Xα method 61
Fig. 47: Chemical structure of the monoterpenes under the study 65
Fig. 48: Geometrical structure of α-pinene (a) and HOMO orbital of the molecule. 66
Fig. 49: The high resolution SPES of α-pinene with no mass tagged, the black curve. 67
Fig. 50: Mass-selected photoion efficiency curve of α-pinene. 68
Fig. 51: The PES matrix of α-pinene without mass selection (a), tagged with m/z 136 69
Fig. 52: Mass-selected SPES of the parent and fragments in the α-pinene scan. 70
Fig. 53: SPES spectrum of the parent over the X-band (green curve) 72
Fig. 54: Normal modes 1st (a) and 56th (b) of α-pinene cation. 73
Fig. 55: Geometrical structure of 3-carene (a) and HOMO orbital of the molecule. 73
Fig. 56: The high resolution SPES of 3-carene with no mass tagged, the black curve. 74
Fig. 57: mass-selected photoion efficiency curve of 3-carene. 75
Fig. 58: The PES matrix of 3-carene without mass selection 75
Fig. 59: mass-selected SPES of the parent and fragments present in the 3-carene scan. 76
Fig. 60: SPES spectrum of 3-carene (m/z 136) over the first peak in the X-band 78
Fig. 61: SPES spectrum of 3-carene (m/z 136) over the X-band 79
Fig. 62: Normal vibrational modes v1 (a), v2 (b), v3 (c), v56 (d), v60 (e) and v65 (f) 80
Fig. 63: Geometrical structure of the limonene (a), HOMO (b), and HOMO-1(c) orbitals. 81
Fig. 64: The high resolution SPES of limonene with no mass tagged, the black curve. 81
Fig. 65: Mass-selected photoion efficiency curve of limonene. 82
Fig. 66: The PES matrix of limonene without mass selection 83
Fig. 67: Mass-selected SPES of the parent and fragments present in the limonene scan. 84
Fig. 68: SPES spectrum of limonene (m/z 136) over the first peak in the X-band 86
Fig. 69: SPES spectrum of limonene (m/z 136) over the X-band 87
Fig. 70: Normal vibrational modes v1 (a), v2 (b), v3 (c), v18 (d), v50 (e) and v59 (f) 87
Fig. 71: Geometrical structure of β-pinene in its neutral (a) and cationic (b) ground state. (c) 89
Fig. 72: The high resolution SPES of β-pinene with no mass tagged, the black curve. 89
Fig. 73: Mass-selected photoion efficiency curve of β-pinene. 90
Fig. 74: The PES matrix of β-pinene without mass selection 91

Fig. 75: Mass-selected SPES of the parent and fragments present in the β-pinene scan. 92
Fig. 76: SPES spectrum of β-pinene (m/z 136) over the X-band.. 94
Fig. 77: Normal vibrational modes v2 (a), v5 (b), v6 (c), v10 (d), v24 (e) and v56 (f) of the β-pinene 94
Fig. 78: Geometrical structure of sabinene in its neutral (a) and cationic (b) ground state. (c)........................... 95
Fig. 79: The high resolution SPES of sabinene with no mass tagged, the black curve... 96
Fig. 80: Mass-selected photoion efficiency curve of sabinene. 97
Fig. 81: The PES matrix of sabinene without mass selection 98
Fig. 82: mass-selected SPES of the parent and fragments present in the sabinene scan.................................... 98
Fig. 83: Correction of the sabinene SPES with respect to the β-pinene impurity. 99
Fig. 84: The corrected SPES spectrum of sabinene (m/z 136) over the X-band 101
Fig. 85: Simplified schematic of interaction volume and its cross section to the radiation beam. 106
Fig. 86: VMI-PES of b-pinene recorded in March 2016, black, and June 2019, green. 113
Fig. 87: Black pepper oil SPES fitting. Top: the fit, red, on top of the experimental SPES of the oil, black. 115
Fig. 88: Black pepper oil VMI-PES fitting at hν=9.5 eV. 116
Fig. 89: Black pepper oil VMI-PES fitting at hν=9.0 eV. 116
Fig. 90: Black pepper oil VMI-PECD fitting at hν=9.5 eV... 118
Fig. 91: Black pepper oil VMI-PECD fitting at hν=9.0 eV... 119
Fig. 92: Mexican lime oil SPES fitting. 121
Fig. 93: Mexican lime oil VMI-PES fitting at hν=9.5 eV... 122
Fig. 94: Mexican lime oil VMI-PES fitting at hν=9.0 eV... 122
Fig. 95: Mexican lime oil VMI-PECD fitting at hν=9.0 eV. 125
Fig. 96: ToF spectrum of α-pinene at photon energies 9.0 eV, 9.5 eV, 10.5 eV and 12.0 eV. 132
Fig. 97: PES and PECD of (+)-(1R,5R)-α-pinene 133
Fig. 98: ToF spectrum of α-pinene at photon energies 9.0 eV, 9.5 eV, 10.5 eV and 12.0 eV. 135
Fig. 99: PES and PECD of (+)-(1S,6R)-3-carene.. 136
Fig. 100: ToF spectrum of limonene at photon energies 9.0 eV and 9.5 eV.. 137
Fig. 101: PES and PECD of (+)-(4R)-limonene at photon energies 9.0 eV (a), 9.5 eV (b). 138
Fig. 102: ToF spectrum of α-pinene at photon energies 9.0 eV, 9.5 eV, 10.5 eV and 12.0 eV. 139
Fig. 103: PES and PECD of (-)-(1S,5S)-β-pinene 140
Fig. 104: ToF spectrum of sabinene at photon energies 9.0 eV and 9.5 eV. 142
Fig. 105: PES and PECD of extract (-)-(1S,5S)-sabinene at photon energies 9.0 eV (a), 9.5 eV (b). 142
Fig. 106: The correction of sabinene PES for β -pinene impurity at photon energy 9.5 eV. 143
Fig. 107: The corrected PES and PECD of sabinene at photon energy 9.5 eV. 144
Fig. 108: PECD of α-pinene at photon energies 9.0 eV, red curve, and 9.5 eV, black curve.............................. 146
Fig. 109: PES of 3-carene at different photon energies.. 148
Fig. 110: FC simulation of 3-carene done at harmonic level using basis set aug-cc-pVDZ. 149
Fig. 111: Experimental PECD results of 3-carene for photon energies equal to and lower than 9.5 eV. 150
Fig. 112: PES and PECD of 3-carene recorded at different lower photon energies vs eKE, the axis on the top. 151

Fig. 113: PES and PECD of 3-carene recorded at different lower photon energies vs eKE, the axis on the top. 152

Fig. 114: PES and PECD of 3-carene recorded at hν=8.85 eV and hν=9.0 eV vs eKE, the axis on the top. 153

Fig. 115: PES (a) and PECD (b) of medium resolution data set (hν=10.5, 11.0,12.0 eV) of 3-carene. 154

Fig. 116: PES (a) and PECD (b) of low resolution data set (hν=13.0, 15.0,19.0 eV) of 3-carene. 154

Fig. 117: PECD of 3-carene as a function of electron kinetic energy 155

Fig. 118: PES of α-pinene at different photon energies. 157

Fig. 119: Experimental PECD results of α-pinene at photon energies equal to and lower than 9.5 eV. 158

Fig. 120: PES and PECD of α-pinene recorded at different lower photon energies vs eKE, the axis on the top. 159

Fig. 121: PES and PECD of a-pinene recorded 160

Fig. 122: PES and PECD of a-pinene recorded at two photon energies, ... 161

Fig. 123: PES and PECD of medium resolution data set (hν=10.5, 11.0, 12.0 eV) of α-pinene.......................... 162

Fig. 124: PES and PECD of low resolution data set (hν=13.0, 15.0, 19.0 eV) of α-pinene. 163

Fig. 125: PECD of α-pinene as a function of electron kinetic energy.. 164

Fig. 126: Schematic of the beamline... 167

Fig. 127: Spectra of the laser just before going into the ionization chamber for three wavelengths 168

Fig. 128: Two polarimetry at 396.52 nm.. 169

Fig. 129: VMI images recorded for 3-photon ionization of α-pinene at 396.52 nm.. 170

Fig. 130: PES spectrum obtained via pBASEX analysis for 3-photon ionization of α-pinene at 396.52 nm 171

Fig. 131: Differential image, left, and its Abel inverse transformation 172

Fig. 132: Differential image (a), and its symmetric (c) and antisymmetric (b) compound 173

Fig. 133: PES and PECD of S-α-pinene using 3-photon ionization at 396.52 nm 174

Fig. 134: TD-DFT calculation for α-pinene done with aug-cc-pVDZ basis set. 175

Fig. 135: TD-DFT calculation for α-pinene done using CAMb3LYP aug-cc-pVDZ basis set 176

Fig. 136: Schematic of two different ionisation channels available at 396.52 nm. 177

Fig. 137: Different odd beta parameters contributing to the PECD of S-α-pinene 178

Fig. 138: PES spectrum for 3-photon ionization of α-pinene at 371.02 nm 179

Fig. 139: Antisymmetrised differential image, left, and its Abel inverse transformation, ... 180

Fig. 140: PES and PECD of S-α-pinene using 3-photon ionization at 371.02 nm. 180

Fig. 141: Comparison between the PES and PECD of S-α-pinene using 3-photon ionization 181

Fig. 142: TD-DFT calculation for α-pinene done using CAMb3LYP aug-VDZ basis set 182

Fig. 143: Schematic of the two different ionisation channels available at 371.02 nm. 183

Fig. 144: Different odd beta parameters contributing in PECD of S-α-pinene 184

Fig. 145: PES of S-α-pinene at 200.66 nm with a laser power of 0.18 mW 185

Fig. 146: Antisymmetrised differential image, left, and its Abel inverse transformation 186

Fig. 147: PES and PECD -of S-α-pinene in 2-photon ionization at 200.66 nm 187

Fig. 148: fitting a line to the Xe calibration measurements.. 204

Fig. 149: different radii for PES spectrum peak of Xe calibration measurements 205

Fig. 150: fitting a line to data points $(R2, 1Vrep)$ obtained in Xe calibration at 396.52 nm............................ 206

Fig. 151: VMI images for Xe calibration measurements done at $\eta = 0.71$, but with different $Vrep$, ... 207

Fig. 152: VMI images for Xe calibration recorded at $Vrep = 400\ V$ 209

Fig. 153: (a) fitting $eKE = kR2$ to data points (eKE, R) for pulse energy of 20 μJ 210

Fig. 154: VMI image, left, and the PES spectrum, right, for CS2 calibration 211

List of Tables

Table 1: Asymmetry parameters and PECD of (+)-R-limonene measured in 1+1' (199 nm+402 nm) REMPIs 41

Table 2: The calculated frequencies of the vibrational normal modes of the neutral and cation of α-pinene.... 71

Table 3: The calculated frequency of vibrational normal modes of the neutral and cation of 3-carene 77

Table 4: The frequency of normal vibrational modes of the neutral and cation of limonene 85

Table 5: The frequency of normal vibrational modes of the neutral and cation of β-pinene 92

Table 6: The frequency of normal vibrational modes of the neutral and cation of sabinene 100

Table 7: Relation of the photon flux with the cache setting with the photon flux... 108

Table 8: list of al SPES and VMI measurements done for the EOs and their compounds; 111

Table 9: Pepper oil composition obtained through the SPES and VMI-PES fitting 117

Table 10: The ee of the pepper oil's compounds obtained through the VMI-PECD fitting 120

Table 11: Mexican lime oil composition obtained through the SPES and VMI-PES fitting. 124

Table 12: Mexican lime oil composition taken from Ref. [109] and references therein. 124

Table 13: The ee of the Mexican lime oil's compounds obtained through VMI-PECD fitting at hν=9.0 eV 127

Table 14: Calibration factor obtained in Xe calibration at 396.52 nm with a laser power of 20 mW 206

Table 15: Different values of η (extractor voltage) with the same repeller voltages 208

1. Introduction

1.1. Chirality

Chirality is a property of asymmetry that is very important in several branches of science including chemistry, biology, and physics. Any structure which is distinguishable from its mirror image is called 'chiral'. The word 'achiral' is used for those objects which are exactly the same as their mirror images. For example, a sphere is an achiral object while one of your hands is a chiral object. A chiral object and its mirror image are usually called 'enantiomorphs'. If we are dealing with molecules, it is more convenient to use the word 'enantiomers' instead of enantiomorphs.

The word 'chiral' originates from the Greek, χειρ (kheir), 'hand', a familiar chiral object and was coined by Lord Kelvin in 1894 [1]. In Oxford English Dictionaries, chiral is defined as 'Asymmetric in such a way that the structure and its mirror image are not superimposable' [2]. www.dictionary.com defines chirality (in the context of science) as 'the characteristic of a structure (usually a molecule) that makes it impossible to superimpose it on its mirror image.' [3].

1.1.1. Chirality in nature

Humans have always found lots of objects in nature fascinating from an aesthetic point of view. Snails, for example, have beautiful shells in which chirality is obvious; some individuals have shells that spiral in a right-handed direction, others have left-handed shells. In plants, the honeysuckle winds around its support in a left-handed helix while the bindweed prefers winding from right to left; and even in bacteria some of their colonies spiral from right to left yet as the temperature increases they reverse the spiral direction to left-handed turns [4]. In addition, by using huge telescopes we can recently observe the chiral behaviour of galaxies [5].

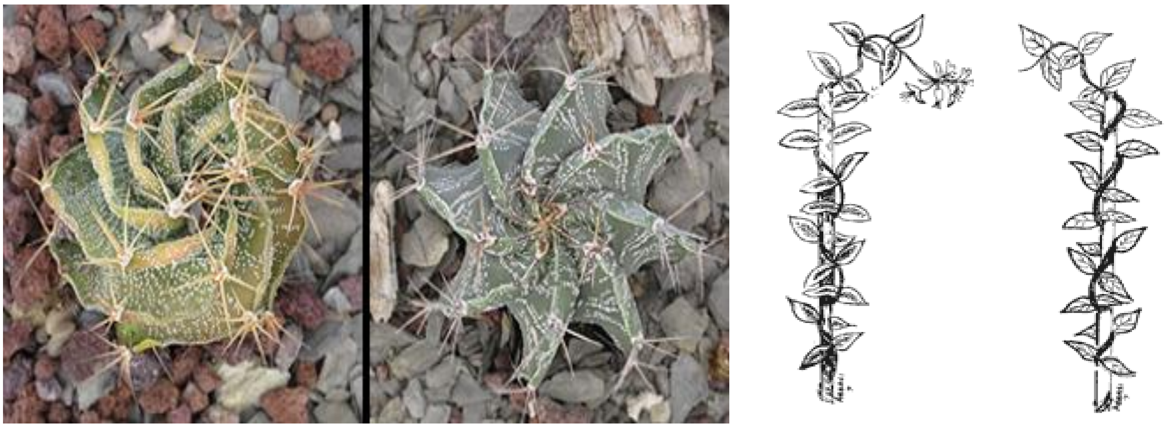

Fig. 1: Flowers in nature showing chirality.

Most important of all, amino acids as the human body building blocks, sugars and DNAs are chiral. This case makes the importance of chirality and the need for research on it clearer. It was Louis Pasteur who for the first time discovered the chirality occurring in organic molecules in 1848 [6]. When he was examining a certain salt of tartaric acid, he found that there are two different kinds of crystals there. Today, we know all sugars are right handed and all amino acids are left-handed but still there is not a clear reason for such a phenomenon. The two enantiomers of an amino acid, usually indicated as L- and D- (for Levo and Dextro, and there is a different nomenclature which calls them R and S), have all the same physical and chemical properties, and, importantly, they have then the same energy and stability, and therefore the same probability of occurrence. When the chemist synthesizes one of these compounds in the lab by normal synthetic means, he will obtain always a “racemic mixture”, namely a 50:50 mixture of the two [7]. However, this is not the situation in nature and it is one of the open questions in evolutionary science [8, 9]; why there is not an equal amount of L- and D- amino acids around us?

From the symmetry point of view, chirality is one of the consequences of breaking of mirror-image symmetry. In a variety of modern sciences, this symmetry breaking has attracted the attention of many scientists ranging from electroweak interactions in particle physics [10-12] to dimorphic chiral structures of microscopic planktonic foraminifera [13, 14] to population dynamics in snails [9, 15]. We will discuss the concept of chirality more and more in various contexts below.

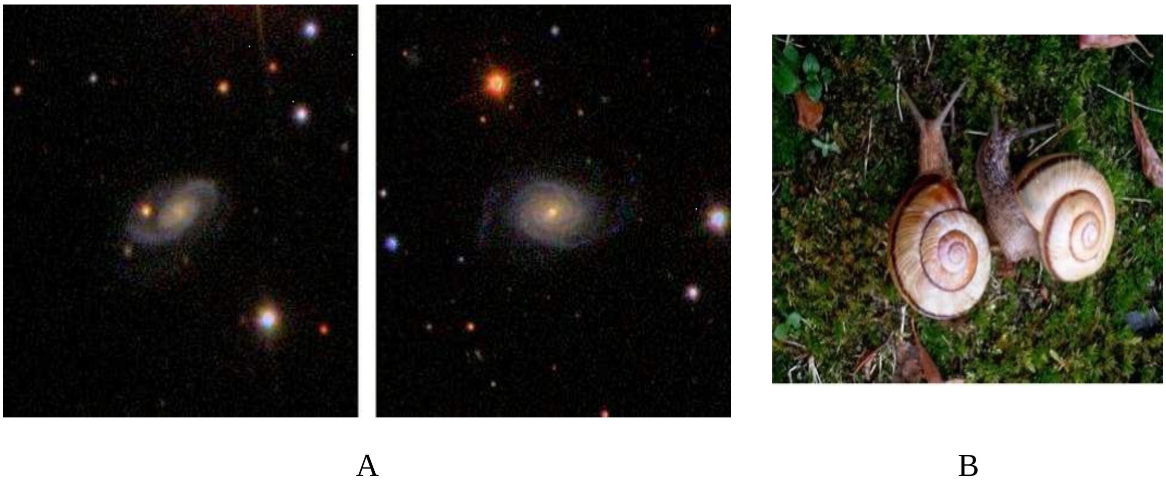

Fig. 2: Chirality in the spin of galaxies (A) and the shell of snails (B).

1.1.2. Chirality in Physical Chemistry

The attention of chemists has been directed to the chirality of different chemicals from 1848 when Louis Pasteur for the first time discovered that the solution of two types of crystals (same in construction but different in shape) changes the polarization of linearly polarized light to right- or left-handed polarization, depending on the shape of the crystals in the solution [6]. Later, Lord Kelvin used the word chirality for such behaviour and defined it in this way: 'I call any geometric figure, or group of points, chiral, and say it has chirality, if its image in a plane mirror, ideally realized, cannot be brought to coincide with itself'[16]. By this definition, Pasteur considered an object but chemists are interested to use it more about the molecules.

Many molecules like proteins, DNA, amino acids, sugars and many natural products such as steroids, hormones, and pheromones possess chirality [7]. Actually, the list of molecules having different biological activities for right- and left-handed forms is extensive [17] and many works have been written about chirality in molecules [18], separation of enantiomers [19] and optical effects of chiral molecules [20]. Recently, more physical chemists are applying advanced methods in experimental and theoretical chemistry and physics to study the problem of chirality in detail. Many issues like dynamics, interaction and reactivity of chiral molecules with light have been studied. One of the most useful methods to study the chiral molecules is spectroscopy by which physical chemists are looking at molecular structure, dynamics and vibrational states of the chiral matter. There are different types of spectroscopy to study the chirality. Optical Rotatory Dispersion (ORD) is a chiroptical measurement in which the rotation of linearly polarized light by a chiral media is studied. Circular Dichroism (CD) spectroscopy and Photoelectron Circular Dichroism (PECD) spectroscopy are two other important kinds of electronic spectroscopy used to study the chiral molecules. When CD is conducted in infrared region of the spectrum, the vibrational states are exited and Vibrational CD (VCD) is achieved. Physical chemists are also employing some experimental techniques like photoelectron photoion coincidence spectroscopy (PEPICO) [21], methods such as non-linear optics [22] and *ab_initio* calculation [23] and relatively new light sources like synchrotron radiation to study the chirality of molecules [24]. We will explain these techniques with more details in the subsequent sections.

The theory behind any of the aforementioned methods and techniques has deep roots in physics. Optics, electrodynamics, quantum mechanics, scattering theory, etc. are some branches of physics involved in many of the existing experimental and numerical methods. Being familiar with Stocks parameters and different possible polarization of light is essential to proper a beamline with the customized polarization in any given experiment. Understanding the mechanisms of light-matter interaction in the framework of quantum mechanics is crucial as well. Doing any experimental and numerical study is possible only by knowing the quantized energy levels of molecules obtained from quantum mechanics. Scattering theory is important because any kind of interaction between light and molecules, photoionization for example, can be seen as a scattering event. Therefore, studying the chirality of molecules is always done in the field of physical chemistry and related science fields.

1.2. Circular Dichroism (CD)

Circular dichroism refers to the differential response of chiral molecules (enantiomers) to circularly polarized light. As mentioned before, studies on the interaction of light with chiral media originated from Louis Pasteur’s works on solutions of chiral crystals. He noticed that the solutions of differently shaped crystals turn the polarization vector of linearly polarized light differently. In general, any medium like these solutions, which respond to light differently, are considered as optically active mediums. What Pasteur did was to use the same beamline passing through two different solutions of left- and right-handed crystals. Instead of what Pasteur did, one can use two different beamlines of different polarizations (circularly right/left polarized) and pass them through the same solution which only contains one type of those crystals. Today, the deviation that the circularly right/left polarized light, after going through a media, obtains with respect to its main path is measured as a function of the wavelength; this is called Optical Rotatory Dispersion (ORD) and is one of the earliest kind of circular dichroism. The amount of ORD is on the order 10^{-6} but, as it depends on the pathlength, for sufficiently long pathlengths, significant results can be obtained.

Recently, circular dichroism usually refers to another kind of differential interactions between chiral molecules and light. Below, two main kinds of circular dichroism are explained.

1.2.1. Photoabsorption Circular Dichroism (PCD)

What we may consider being conventional circular dichroism arises from the different photoabsorption of left- and right-circularly polarized light by target molecules of a specific handedness [18, 25, 26]. The chirally induced asymmetry can be expressed as a Kuhn g-factor [27] defined as:

$$g = \frac{(I_{lcp} - I_{rcp})}{I} \qquad \text{(Eq. 1)}$$

where $I_{lcp/rcp}$ is the signal obtained with right/left circularly polarized light and I is the mean or unpolarised signal.

However, if we wanted to probe the chirality of molecules by measuring photoabsorption circular dichroism (PCD) of randomly oriented samples, the signals are rather small, making it a difficult task. Indeed, the reason why these signals are so small (1 part in 10^5) is that PCD arises only from interaction between electric dipoles with magnetic dipoles [25]. For this reason, in more modern works on the measurement of optical activity of chiral matter, people are applying techniques in which the interaction between only electric dipoles are important.

1.2.2. Photoelectron Circular Dichroism (PECD)

An alternative to PCD is to study the photoelectrons ejected from chiral molecules when these molecules are irradiated by circularly polarized light. This method is called photoelectron circular dichroism (PECD). PECD is more powerful than PCD because it arises from interaction in the electric-dipole matrix elements alone [28, 29]. Photoelectron angular distribution in a single photon ionization of isotropically distributed gas-phase chiral molecules is given by [25]:

$$I^{\{p\}}(\theta) = 1 + b_1^{\{p\}} P_1(\cos\theta) + b_2^{\{p\}} P_2(\cos\theta) \qquad \text{(Eq. 2)}$$

Where p indicates the polarization of light ($p = 0$ for linear polarization and $p = +1/-1$ for left/right circular polarization), P_1 and P_2 are the first and the second Legendre polynomials and $b_1^{\{p\}}$ and $b_2^{\{p\}}$ are coefficients depending on the reaction dynamics and the polarization of the light as well. There are some relationships due to symmetry considerations [25]:

$$b_1^{\{0\}} = 0, b_1^{\{-1\}} = -b_1^{\{+1\}}, b_2^{\{0\}} = -\frac{1}{2} b_2^{\{\pm 1\}} \qquad \text{(Eq. 3)}$$

Using this relation, one can verify that for chiral molecules:

$$I_{lcp} - I_{rcp} = 2b_1^{\{+1\}} \cos\theta \qquad \text{(Eq. 4)}$$

By fitting the differential Photoelectron Angular Distribution (PAD) obtained above, $I_{lcp} - I_{rcp}$, to a $2\cos\theta$ curve we can compute the $b_1^{\{+1\}}$ which determines the chirality of molecules. In the following, we consider the quantity $2b_1^{\{+1\}}$ as PECD.

Similarly, one can obtain a general expression for differential PAD in multiphoton ionization, which is:

$$I_{lcp} - I_{rcp} = \sum_{i=1}^{n} 2\, b_{2i-1}^{\{+1\}}\, P_{2i-1}(\cos\theta) \qquad \text{(Eq. 5)}$$

For instance, in three-photon ionization coefficients $b_1^{\{+1\}}, b_3^{\{+1\}}\ and\ b_5^{\{+1\}}$ determine the value of PECD. A procedure to obtain what we consider as the PECD in multiphoton ionization is given in [30] defining the multiphoton PECD (MP-PECD) as

$$\mathrm{MP-PECD} = 2b_1^{+1} - \frac{1}{2} b_3^{+1} + \frac{1}{4} b_5^{+1} + \cdots \qquad \text{(Eq. 6)}$$

In order to obtain the quantity $I_{lcp} - I_{rcp}$ in the laboratory, we can arrange two different setups, the first of which is using the same polarization of light and changing the target molecules from left-handed to right-handed enantiomers and the second is to use a certain enantiomer and change the polarization of light from left-CPL to right-CPL.

1.3. Current State of the Art in PECD Research

1.3.1. Single Photon Ionization: a historical review

The starting point of PECD research goes back to a theoretical work by Ritchie in 1976 [31] where he argued that the PAD in single-photon ionization of randomly oriented chiral molecules, when a right/left circularly polarized photon is absorbed, can be presented as

$$I(\theta) = A \pm B cos(\theta) + C cos^2(\theta) \qquad \text{(Eq. 7)}$$

in which θ is the angle between the photoelectron momentum and the photon direction. Before his work, the middle term in the right-hand side of (Eq. 7), $\pm Bcos(\theta)$, was supposed to be zero for randomly oriented molecules. Later on with some more theoretical works on this subject and justifications to the experimental observations, (Eq. 7) was rewritten as below

$$I^{\{p\}}(\theta) = 1 + b_1^{\{p\}} P_1(\cos\theta) + b_2^{\{p\}} P_2(\cos\theta) \qquad \text{(Eq. 8)}$$

where $P_n(\cos\theta)$ are the Legendre polynomials and p is referring to the polarization of light, p=±1 for right/left circular polarization and p=0 for linear polarization. The next step in the field of PECD research was a computational work by Powis in 2000 [32]. In this work, Powis applied numerical calculations to demonstrate the circular dichroism in angular distribution (CDAD) created by photoionization of a given enantiomer, even when the target molecules are randomly oriented. Actually, Powis derived (Eq. 8) for the first time in this work by applying a nonrelativistic, frozen core, dielectric approximation to the scattering of photoelectrons from the chiral molecular potential as below:

$$\frac{d\sigma(\omega)}{d\Omega} = \frac{\alpha k a_0^2}{\pi\omega} \left|\langle \psi_{f,k}^- | \hat{\boldsymbol{e}}.\nabla | \psi_i \rangle\right|^2 \qquad \text{(Eq. 9)}$$

He used the CMS-$X\alpha$ method to calculate the radial part of the electronic wavefunction and expanded the angular part of the wavefunction for each atom up to angular momentum l_{max} which is chosen based on the size of each atom. However, the main drawback of the method was neglecting the vibrations, as CMS-$X\alpha$ assumes a frozen core approximation. At that time, there was no experimental evidence of how important the vibrational motions of the molecular core can be. Also, the molecules under study in Powis's work were structural isomers of $C_3H_6O_2$, two conformers of glyceraldehyde as well as lactic acid, for which there was not any experimental record at the time to compare the computational results. Nonetheless, his achievement was showing a significant b_1 parameter which was comparable to the other asymmetry parameter b_2, as it was predicted by Ritchie a while ago. So, Powis by referring to synchrotron radiation, which was partially available at that time, suggested PECD experiments in order to observe the first experimental evidence of the PECD effect. Indeed, he proposed the idea of enantiomer identification of optical isomers by PECD measurements in which circularly polarized light is exploited. Additionally, he speculated that the conformations of a given optical isomer can be distinguished by energy and angle-resolved photoelectron spectroscopy.

The other point he made in his work was that the PECD parameter would be smaller for photoelectrons which carry higher kinetic energies. His argument was that the more energetic the photoelectrons, the less they experience the effect of the chiral potential. The results he presented for lactic acid is shown in Fig. 3. In this figure both b_2 and b_1 are plotted with together to firstly compare their relative magnitude (which was a proof of principle that b_1 can be as large as b_2) and secondly show how b_1, for all the individual orbitals, is tending to zero for high energetic photoelectrons.

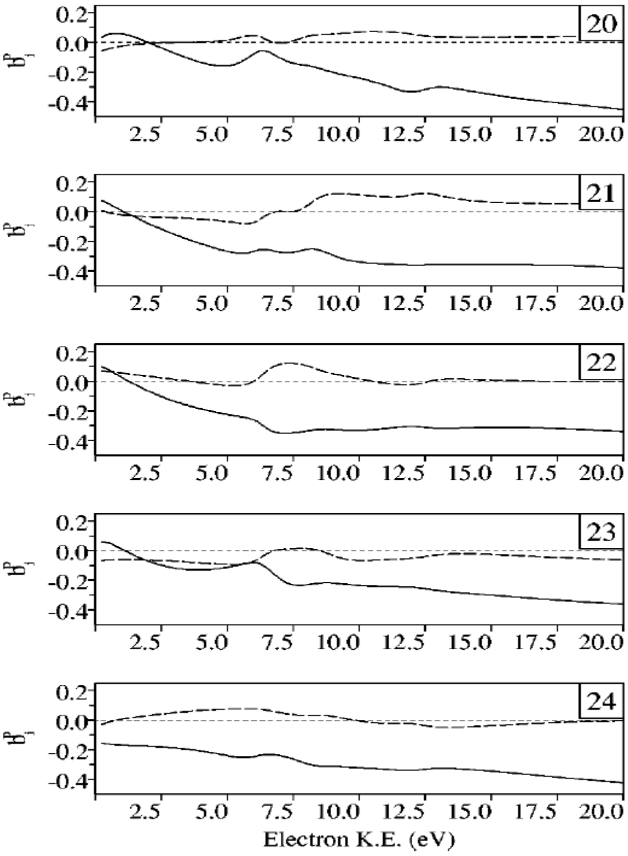

Fig. 3: Photoelectron anisotropy parameters b_2, solid curves, and b_1, dashed curves, for photoionization of the outermost valence orbitals of D-lactic acid with LCP light. The individual orbitals are identified in the top right corner of the relevant plot. Figure taken from Ref. [33].

The results he presented for lactic acid are shown in Fig. 3. In this figure both b_2 and b_1 are plotted together to firstly compare their relative magnitude (which was a proof of principle that b_1 can be as large as b_2) and secondly show how b_1, for all the individual orbitals, is tending to zero for high energetic photoelectrons.

In another computational work [32], Powis studied three conformers of the amino acid L-alanine (CH_3CHNH_2COOH). The conclusion of this work was briefly that the PECD signal depends on the orbital from which the photoelectrons are being ejected. The PECD signal for the three outermost orbitals (HOMO, HOMO-1, and HOMO-2) was not reported to be significant, i.e. just below a few percent. But on going deeper, and reaching the skeletal σ-bonding orbitals, HOMO-4 and HOMO-5, the asymmetry parameter could be as large as 40%. Powis interpreted this as the electrons ejected from outer orbitals are rather far from the centre of the chirality and consequently are not so sensitive to the chiral potential. In contrast, the electrons of skeletal σ-bonding orbitals feel the chiral potential more.

Finally, in 2001, the first experimental PECD measurement using VUV single-photon ionization in BESSY synchrotron was done by Böwering et al. [34]. The way through which Powis defined the PECD parameter is summarized above, when we derived (Eq. 4). In this case, the enantiomeric shape of the target is kept the same but the polarization of light is reversed. However, it can be said that the PECD effect can be seen by keeping the polarization of the light unchanged and instead changing the target molecules from one enantiomeric shape to another. The authors of Ref. [34] argued that there is a third option in which both the enantiomer and the polarization of the light can be kept the same, and a pair of detectors located in the forward/backward directions (or any two angles opposite to each other, preferably in magic-angle θ=55 and $\theta = 180 + 55$ where the second Legendre polynomial is going to be zero and there is no dependency to b_2 parameter) are used to simultaneously record the photoelectron spectrum. The schematic of this is shown in Fig. 4.

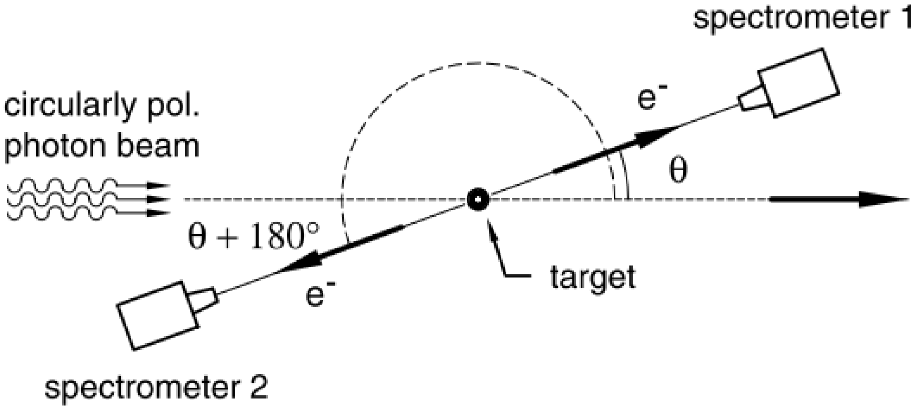

Fig. 4: Schematic of the experimental setup for the PECD measurement in Ref. [34]. The figure is taken from Ref. [34].

The definition of the PECD based on photoelectrons detected in two opposite emission directions is

$$PECD(\theta) = \frac{I(\theta) - I(\theta + 180)}{I(\theta) + I(\theta + 180)} \qquad \text{(Eq. 10)}$$

The molecule under study in this work was (1R)-(+) bromocamphor. Böwering et al. measured the PECD asymmetry parameter for this molecule using LCP and RCP and showed that the asymmetry parameter shows a nice mirroring behaviour for LCP/RCP, as expected. Fig. 5 shows the results of this work on the photoelectron spectrum and PECD measurement of (1R)-(+) bromocamphor.

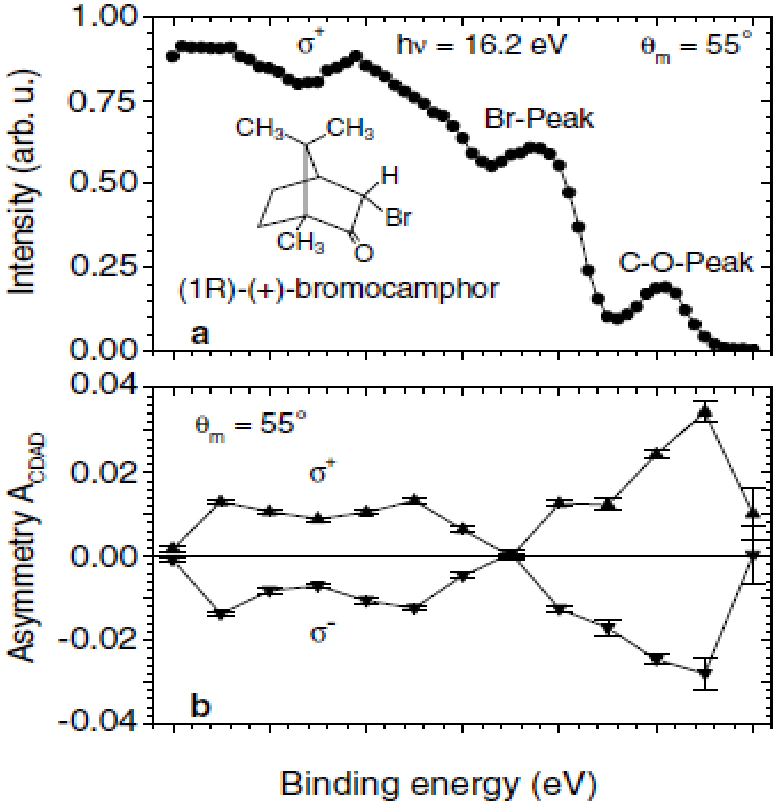

Fig. 5: PES and PECD measurement in Ref. [34]. a: photoelectron spectrum, b: PECD parameter for LCP/RCP at the magic angle. The figure is taken from Ref. [34].

It is worthwhile to make a distinction between PECD and CDAD here as it may be potentially confusing. By CDAD people mean any kind of asymmetry in the photoelectron angular distribution which sometimes maybe not be due to the chirality. We can, for example, align the molecules before ionisation and see some asymmetry in the PAD along to the direction of the alignment. In contrast, by PECD we mean any forward-backward asymmetry in the PAD which is originating from the chiral geometry of the molecules.

The next experiment in this direction was done at the SupperACO synchrotron, LURE France, by Garcia et al. [35]. They studied both enantiomers of camphor and for the first time measured the PECD by detecting a full angular distribution of a selected valence orbital. The advantage of their work was the 4π photoelectron and photoion collection, instead of photoelectron measurements at a fixed angle.

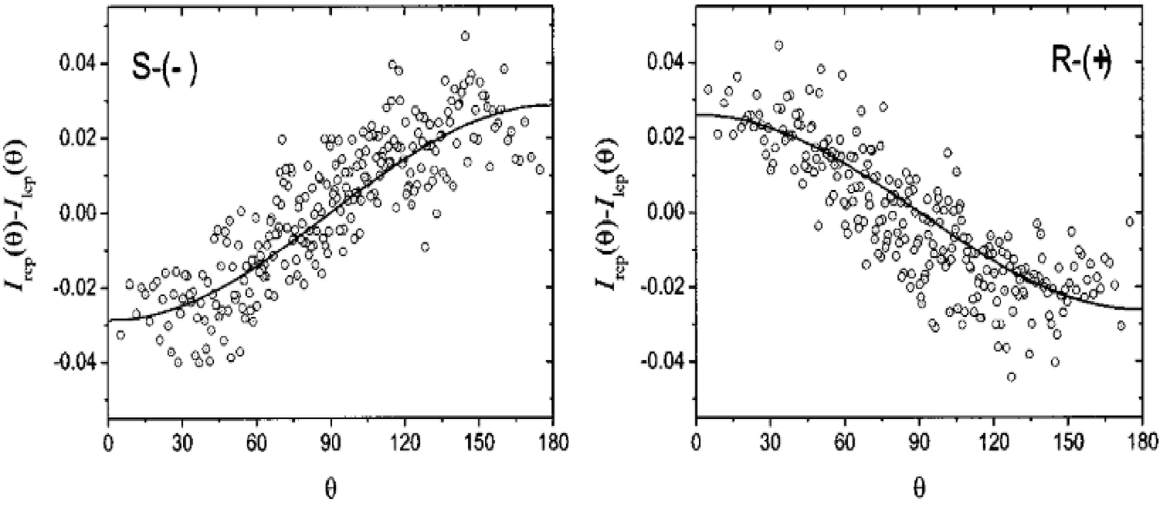

Fig. 6: Circular dichroism in the photoelectron angular distribution of outermost orbital of both S- and R-enantiomers of camphor. The best fit of $I_{rcp} - I_{lcp}$ to A cosθ gives the asymmetry parameter as A=-0.027 and A=+0.026 for S-(-) and R-(+) enantiomers, respectively. The figure is taken from Ref. [35].

Fig. 6 shows the results presented in Ref. [35], which can be considered as a successful confirmation of the Rithchie prediction about the circular dichroism in PAD of randomly oriented molecules when they are ionized by circularly polarized light. The PECD effect they observed was nearly 3% for the outermost carbonyl oxygen lone pair electrons, which is much larger than the conventional CD. They argued that for the deeper orbitals the asymmetry would be more significant because of the same argument Powis made in Ref. [32]. The authors also showed that the asymmetry parameter is changing sign by changing the synchrotron radiation polarization.

However, the limitation of their work was that their analysis was based on a 2D image which itself was the projection of the 3D PAD of the photoelectrons. Gustavo et al., in the same work, suggested the few bunch mode of the synchrotron radian as a suitable source of light which makes it possible to measure the time of flight of the electrons. Combining the time of flight of the electrons with two position coordinates of the electrons recorded in position-sensitive detectors will lead to a full 3D distribution of the photoelectrons. So then, the PECD parameter can be obtained directly from the full 3D PAD.

Later on, people studied PECD as a probe to static molecular structures as well as to molecular dynamics. Examples of the former include chemical substitution, conformational effects and dimerization and clustering while for the latter we can refer to vibrations and relaxation dynamics. In the following section, we will briefly review the main works studying the potentiality of PECD as a probe to the abovementioned properties of molecules.

1.3.1.1. Chemical Substitution

After proving that the PECD effect really exists experimentally, researchers put more effort to discover its potential applications. Some of these applications, as mentioned above, were initially speculated by Powis including the potentiality of PECD to be used as a probe of the chemical structure. In this section, the capability of PECD as a probe of the chemical substitution is considered. In 2004, Stener et al. published a computational work [36] on four chiral derivatives of oxirane, which can be considered as the first work on the sensitivity of PECD to chemical substitution. In this work, the authors calculated the total cross-section, the PECD parameter and the usual anisotropy parameter (noted by $\sigma, D\ and\ \beta$, respectively, in their work) for S-methyloxirane, trans-2S,3S-dimethyloxirane, S-fluoroxirane, trans-2S,3S-difluoroxirane in both valence and core-shell ionization.

The results for the HOMO and $O\ 1s$ orbitals are shown in Fig. 7. The first point immediately obvious from these result is that for both HOMO and O 1s orbitals, it can be seen that while the total cross-section and the usual anisotropy parameter ($\sigma\ and\ \beta$) are roughly the same for all the derivatives, the PECD parameter, D, depends on the substitution. The magnitude of the PECD observed for these species varies between a few percent to 25% around the threshold area.

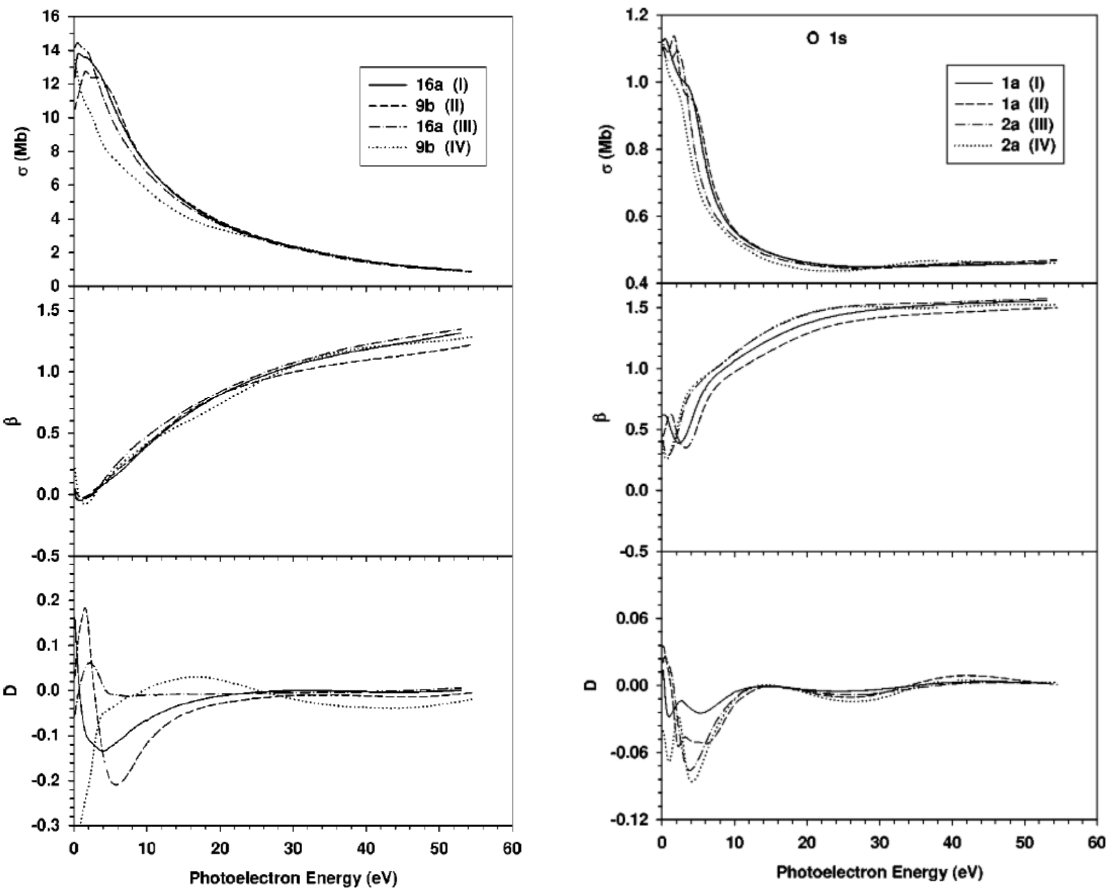

Fig. 7: Valence (HOMO) (left) and core (O 1s) (right) photoelectron angular distribution parameters for four oxirane derivatives (see the text). The figure is taken from Ref. [36].

There are two more important points in the results presented in Fig. 7 the first of which is the decay of the dichroism parameter above electron kinetic energies of 20 eV. This can be interpreted as the highly energetic photoelectrons feeling the chiral potential less, confirming what Powis had found before (see above). The other point can be realized by looking at the geometry of oxirane derivatives in Fig. 8. In all species, the HOMO orbital is a lone pair of oxygen, dominantly constituted by the O 2p atomic orbital, orthogonal to the oxirane ring which itself is not *chiral*. So, it can be said that the PECD signal is not arising from the shape of the initial orbital from which the photoelectrons are being ejected, but rather should be attributed to the effective molecular potential acting on the photoelectrons. This statement can be supported by looking at the PECD signal predicted for core orbitals, which in all cases are O 1s orbitals. These orbitals are even more symmetric than the HOMO orbitals, but still there is some non-zero PECD calculated for them.

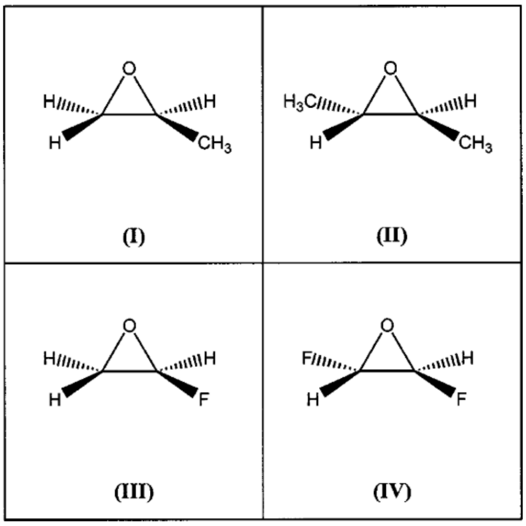

Fig. 8: chemical structure of S-methyloxirane (I), trans-2S,3S-dimethyloxirane (II), S-fluoroxirane(III), trans-2S,3S-difluoroxirane (IV). Image taken from Ref. [36].

Here, we can refer to an experimental/theoretical work in this direction done by Garcia et al. [37], which can be considered as an experimental demonstration of how PECD depends on substitution, as the molecules under study in their work are again some derivatives of oxirane. Gustavo et al. studied S-Methyl-oxirane (S-MOX) and R-trifluoromethyl-oxirane (R-TFMOX) which differ from each other by a replacement of the methyl group with a trifluromethyl group. The HOMO and HOMO-1 orbitals for both of these molecules are the same, so the PECD comparison between them, say for the HOMO orbital, reveals any dependency of PECD on chemical substitution. In Ref. [37], the authors have discussed the fragmentation pathways for the two molecules as well as showing that the HOMO orbital for both of them is quite stable while ionization from the HOMO-1 will cause a huge amount of fragmentation. Fig. 9 shows their results for PECD measurements of two outermost orbitals for S-MOX and R-TFMOX. There is a good agreement between the PECD signals for the higher electron kinetic energies. Actually, at higher photoelectron kinetic energies, not only the PECD for the two molecules are matching with each other experimentally but also they are in a good agreement with the calculated PECD obtained from CMS-Xα method. However, for kinetic energies below 3 eV, the PECD measurements for S-MOX and R-TFMOX are diverging. This can be seen more particularly in the case of the HOMO orbital where the PECD signal is showing totally different behaviour with an opposite sign for the two molecules.

The other point that Garcia et al. demonstrated in their experiment was the dependency of the PECD on the initial orbital from which the photoelectrons are ionized. This can be understood by comparing the PECD data for the HOMO and HOMO-1 orbitals of any individual molecule. For example, in the case of the S-MOX, the b_1 parameter at lower photoelectron kinetic energies has the opposite sign with an absolute difference of approximately 0.2.

Here, we just mentioned examples of some research on oxirane structural isomers to show the effects of the chemical group substitution on PECD; however more experimental/theoretical works in this direction can be found. The other interesting molecules are camphor and fenchone which have been studied frequently, but we are not going to mention them here; the reader is referred to references [35, 38-41] and a review paper by S. Turchini [42] for more details.

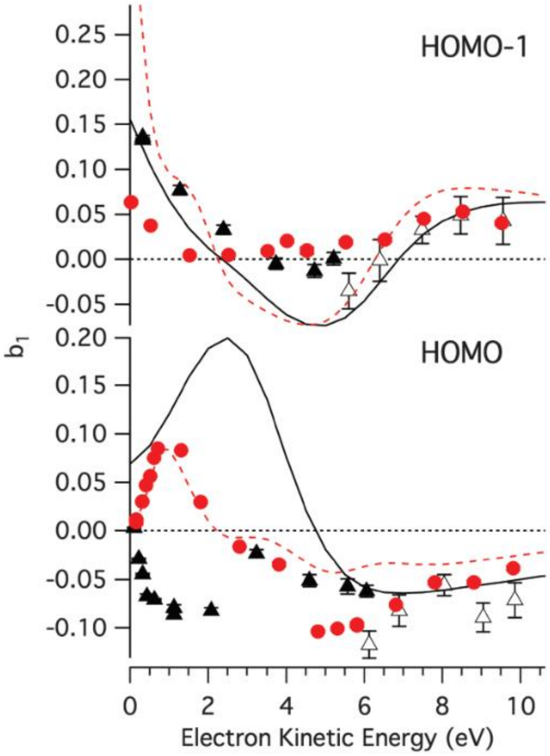

Fig. 9: PECD signal of the HOMO and HOMO-1 orbitals of S-MOX (black triangles) and R-TFMOX (red dots). The results of The CMS-Xa calculations, black solid and red dashed lines for the S-MOX and R-TFMOX, are shown as well. The figure is taken from Ref. [37].

1.3.1.2. Conformers

The first work on the conformational effects on PECD returns to a couple of theoretical papers by Powis in 2000 [32, 33] discussed above, where he studied the conformers of D-glyceraldehyde and L-alanine. In this paper, he for the first time it was suggested that the sensitivity of PECD can be used as an analytical tool to distinguish different conformers from each other. In 2004 another theoretical work [43] investigating the conformational effect in molecules (1R, 2R)-1,2-dibromo-1,2-dichloro-1,2-difluoroethane and (S)-methyloxirane, shown in Fig. 10, was carried out.

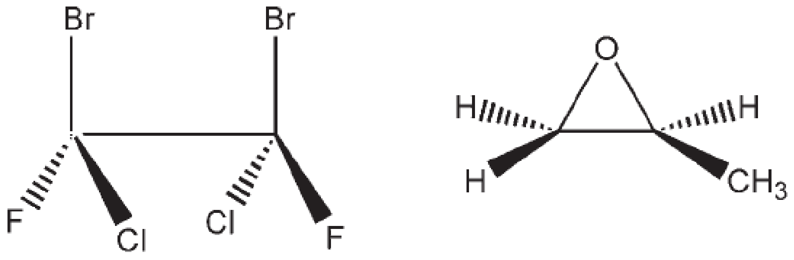

I **II**

Fig. 10: (1R, 2R)-1,2-dibromo-1,2-dichloro-1,2-difluoroethane (I) and (S)-methyloxirane (II). The image is taken from Ref. [43].

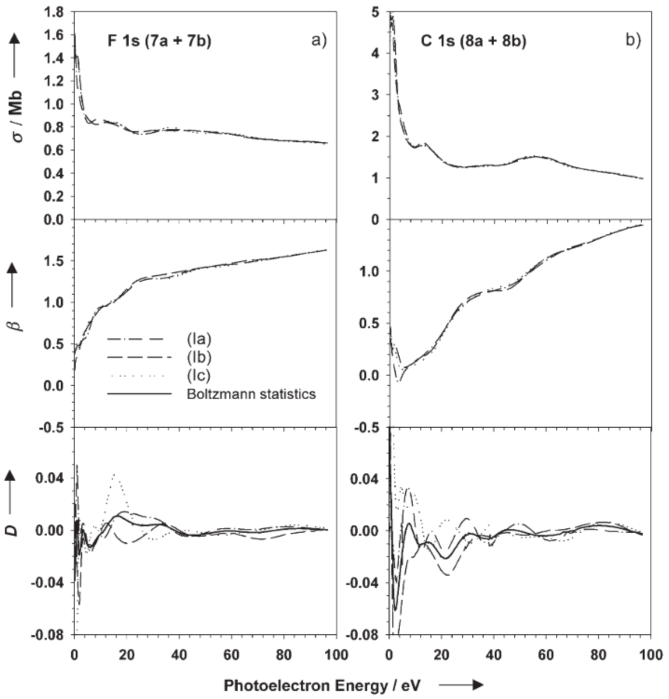

Fig. 11: Cross section σ, asymmetry parameter β and PECD parameter D of two valence orbitals, F 1s in the right and C 1s in the left, of (1R, 2R)-1,2-dibromo-1,2-dichloro-1,2-difluoroethane. Figure taken from Ref. [43].

The authors in this work were interested in the effect of rotation of chemical bonds, rotation around C-C bound in (1R, 2R)-1,2-dibromo-1,2-dichloro-1,2-difluoroethane and rotation of

$-\mathrm{CH_3}$ group in (S)-methyloxirane. In the former, there are three stable conformers (Ia, Ib, and Ic) of such kind available at room temperature (with respect to the barriers in potential energy surface) while for the latter any rotation of 15° was taken into account. Their results for two core orbitals (F 1s and C 1s), as well as one valence orbital (a lone pair of Fluorine), are presented in Fig. 11 and Fig. 12, respectively. In the figure, the averaged PECD values obtained based on Boltzmann statistics are also plotted.

In Fig. 11, it is clear that the σ and β parameters of the core orbitals are nearly the same for all three conformers while the PECD parameter (denoted by D) is relatively sensitive to the conformation. This is true for the valence orbitals too. The PECD parameter for a Fluorine lone pair of three conformers calculated in [43] is shown in Fig. 12. In agreement with previous works, the PECD parameter is more sensitive to the effective chiral potential in the near threshold region. For photoelectrons of high kinetic energies, the PECD signal for all the conformers converges to zero, as at such energies the photoelectrons are so fast that their outgoing wave packets are not seriously affected.

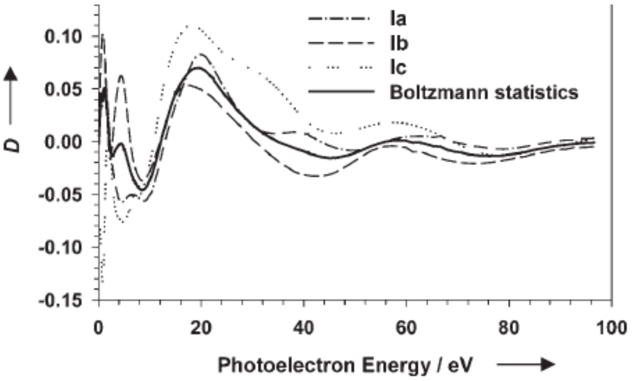

Fig. 12: Cross section σ, asymmetry parameter β and PECD parameter D of a valence orbital, fluorine lone pare, of (1R, 2R)-1,2-dibromo-1,2-dichloro-1,2-difluoroethane stable conformers. The figure is taken from Ref. [43].

In terms of (S)-methyloxirane, the authors of [43] were wondering about the effects of $-\mathrm{CH_3}$ group rotations on the PECD signal, which previously was assumed to have no effect on dichroic parameter. In their work, they reported an unexpectedly huge sensitivity of the PECD for both core and valence orbitals. Here, the results they obtained for the orbital 14a, which is quite delocalized on the whole molecule with a significant contribution from the H 1s orbitals of the methyl moiety, are presented in Fig. 13.

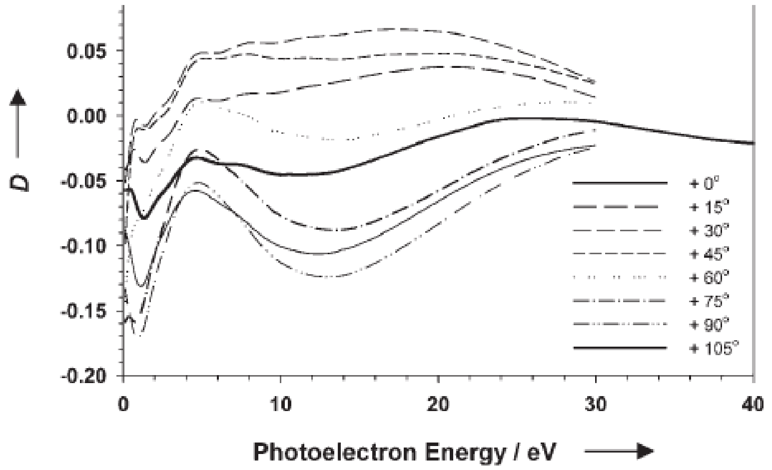

Fig. 13: Dichroic parameter D of 14a orbital of different conformers of (S)-methyloxirane. Different conformers here are different internal rotations of $-CH_3$ group. The figure is taken from Ref. [43].

The averaged PECD based on Boltzmann statistics over all the different conformers presented in Fig. 13 is what can be compared to the experimental results on methyloxirane. The Boltzmann averaged PECD for orbitals 11a-16a are obtained for methyloxirane and are compared to some experimental data [44] available for this molecule, in Fig. 14.

In Ref. [43], the authors used the conformer population obtained theoretically from Boltzmann statistics to average the PECD spectra of different conformers. The aim was to compare the theoretically obtained averaged PECD to the experimental data and prove the principle of conformer dependency of PECD. If the experimental data are confirming the averaged PECD, then it can be said that the PECD signal measured in the lab must depend on the PECD signal of all individual conformers, through a weight which is the conformer population. However, one of the ideas behind research on conformational effects on PECD is to get the conformation population by comparing experimental PECD signal of a mixture of several conformers to the theoretically predicted PECD of individual conformers presented in the mixture. Researchers in this field claim that an experimental/theoretical comparison of PECD can lead to information about the conformation population [45].

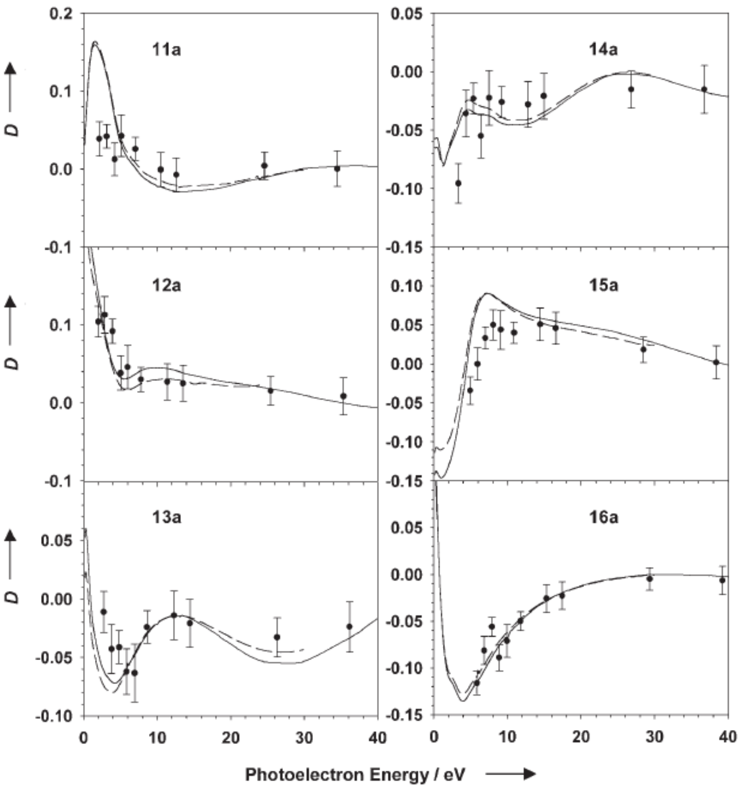

Fig. 14: Dichroic parameter for orbitals 11a-16a of methyl oxirane: the most stable conformer, solid curve, Boltzmann averaged PECD among all conformers presented in Fig. 13, dashed line, and the experimental data from [44], symbols. The figure is taken from Ref. [43].

Garcia et al. have done a theoretical/experimental study on conformer dependency of PECD on terpene endoborneol [45] whose PES spectrum is rather structureless. This precludes any orbital by orbital analysis of PECD, as was the case in the examples mentioned above. However, Garcia et al. showed that a dual theoretical/experimental approach to PECD can help to unambiguously assign the absolute configuration of the molecule under study as well as getting significant information about its conformer population under the experimental conditions. In their work, they calculated the PECD of three individual conformers of endoborneol, which are different in rotation of hydroxyl around the C-O bond axis and compared them to the experimental PECD measured for a sample of endoborneol which is assumed to contain all the three conformers under the condition of the experiment.

Fig. 15 shows a comparison between the theoretical PECD curves of three individual conformers of endoborneol and the experimental PECD signal measured for a mixture of them. The comparison has been made at several photon energies. At each photon energy, an average PECD for three conformers with a presumed ratio of 1:1:1 is calculated and plotted in a solid green line. As this averaged PECD shows a good agreement with the experimental data, Garcia et al, claim that the conformation population in the mixture should be close to what they have assumed, 1:1:1.

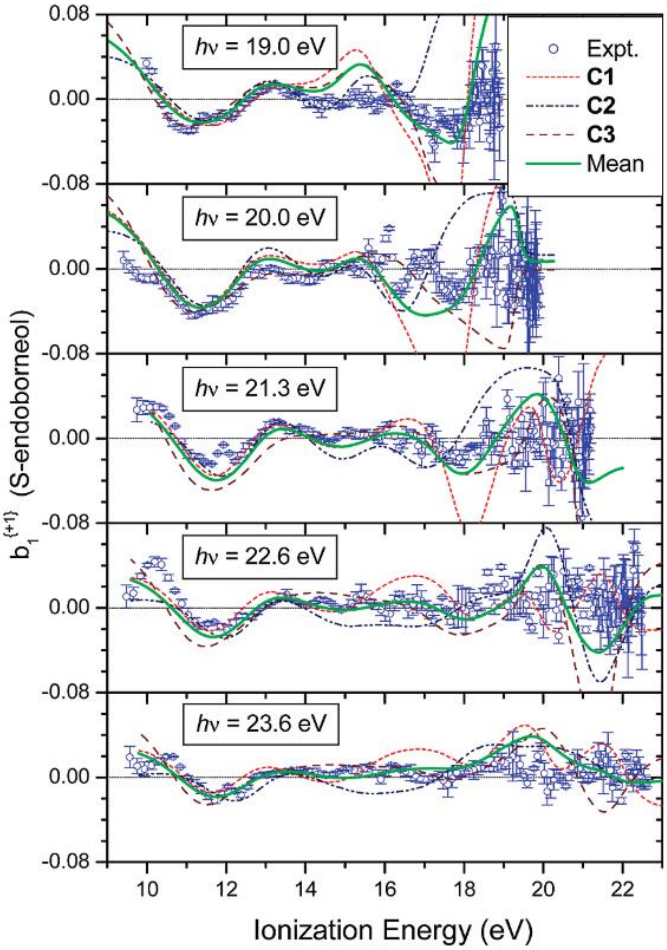

Fig. 15: Theoretical/experimental comparison of endoborneol PECD measurements. The figure is taken from Ref. [45].

Another point that can be realized from Fig. 15 is the convergence of PECD of individual conformers at higher photoelectron energies; this was pointed out previously in the literature, as some examples of that have been already discussed above. However, in their work, Garcia at al. are not presenting such a comparison at photon energies lower than 19.0 eV. The ionization potential of endoborneol is less than 10.0 eV, so it would be interesting to see how the PECD is working at lower photon energies, where the photoelectrons are slower and more sensitive to the chiral potential. But, they are not presenting such a comparison as their theoretical methods are not generating comparable results to the experimental data for PES/PECD at photon energies lower than 18.0 eV. For more examples of conformation effects on PECD, one can look at [42, 46, 47].

1.3.1.3. Dimerization and Clustering

The first investigation on PECD's sensitivity to dimerization was done in 2010 by Nahon et al. [48] in the DESIRS beamline of France synchrotron facility, SOLEIL. With their new PEPICO spectrometer at the moment, DELICIOUS II, they could show that the ionization channels of the camphor monomer and dimer are decoupled in a way so that the ionization of the dimer will not lead to dissociative fragmentation that would lead to some contribution to the monomer ion channel. This can be interpreted as the mass-selected TPES/PES/PECD obtained by their machine being equivalent to size selection of the nascent monomer or dimer species. So by tagging the ToF mass spectrum and filtering the photoelectrons with respect to monomer or dimer masses, one can extract their TPES/PES/PECD separately and compare them together.

In their work, they first showed that the dimerization and generally clustering for the molecule under study, camphor, is happening when the temperature of the beam is down at nearly 10 K. To reach this limit, they increased the backing pressure of the carrier gas, helium, up to 3 bar. Then they showed that the IP of the dimer and trimer is lower than that of monomer, as is obvious from the mass-selected photoelectron images shown in Fig. 16.

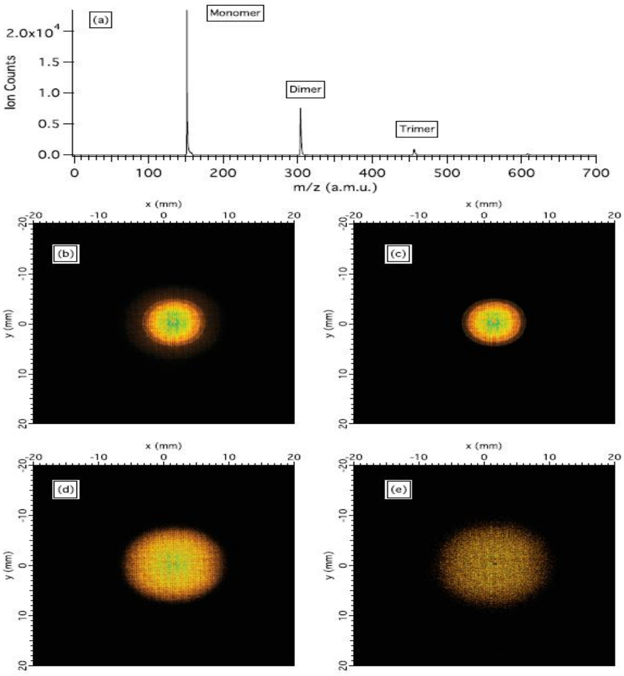

Fig. 16: (a) ToF mass spectrum of (1R)-(+)-camphor, (b) total photoelectron image, (c)-(e) mass-selected photoelectron images for monomer, dimer and trimer, respectively. As it is clear, the radius of images, which is indicative of the energy of the photoelectrons, is increasing as we go from monomer to dimer and then trimer. An immediate result is that the $IP_{trimer} < IP_{dimer} < IP_{monomer}$. *The figure is taken from Ref. [48].*

In the next step, they showed how the onset of the ion yield in the PEPICO spectra of the dimer is shifted to lower energies, with respect to the onset of monomer ion yield. In comparison, the high intensity in the monomer origin band shows that ionization does not change the geometry of monomer too much while in contrast, the flat onset of dimer TPES is indicative of a substantial change in its equilibrium geometry. Finally, Nahon et al. contrasted the usual anisotropy parameter, β, and PECD parameter, b_1, of monomer and dimer. They measured the PECD spectrum of dimer and monomer at different near threshold photon energies; the data presented in Fig. 18 are averaged PECD values across the HOMO band which are already weighted by the corresponding PES signal.

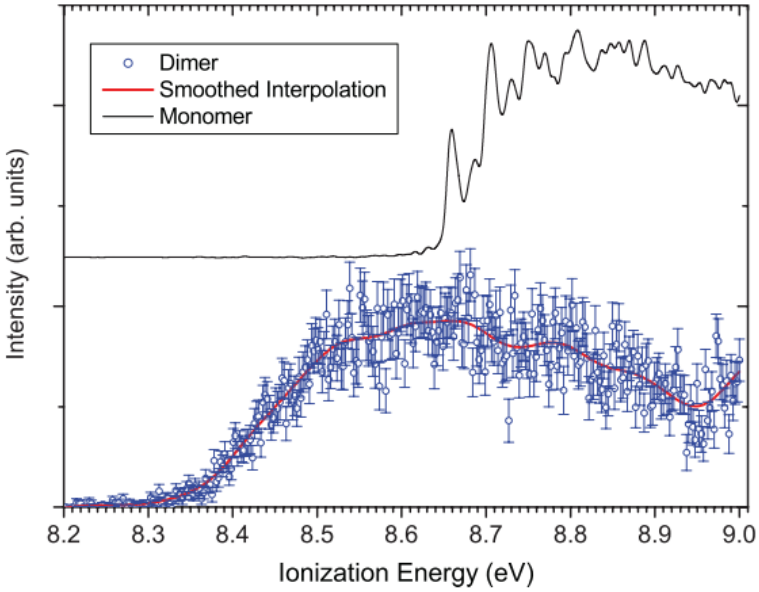

Fig. 17: Experimental dimer and monomer TPES. The dimer TPES is shifted to lower energies as 8.37 eV while the IP of the monomer is 8.66 eV. The figure is taken from Ref. [48].

The first thing that can be inferred from Fig. 18 is that the anisotropy parameter β is roughly the same, within the error bars, for monomer and dimer. So, similar to the case of chemical substitution and conformational effects discussed in previous sections, β is not showing a great sensitivity to dimerization as well. However, the PECD parameter is showing slightly different values for the monomer and dimer. For the monomer, the PECD is uniformly negative in the energy range that the measurement has been done (photon energies have been converted to electron kinetic energies in the figure) while for the dimer it starts from positive values, at lower energy electron kinetic energies, and changes sign to negative values as it goes to higher energies.

As mentioned above, this was the first investigation of dimerization effects on PECD but as is seen in Fig. 18, the quality of the data and the amount of sensitivity (of PECD to the dimerization) they could report are not remarkable. They assumed that the small difference between the monomer and dimer PECD could be because of the existence of different conformers of camphor in the sample. As discussed before, different conformers may possess PECD signals of opposite sign and cancel out each other. However, Nahon et al. suggested further works in this direction on single conformer samples like glycidol might be worthwhile.

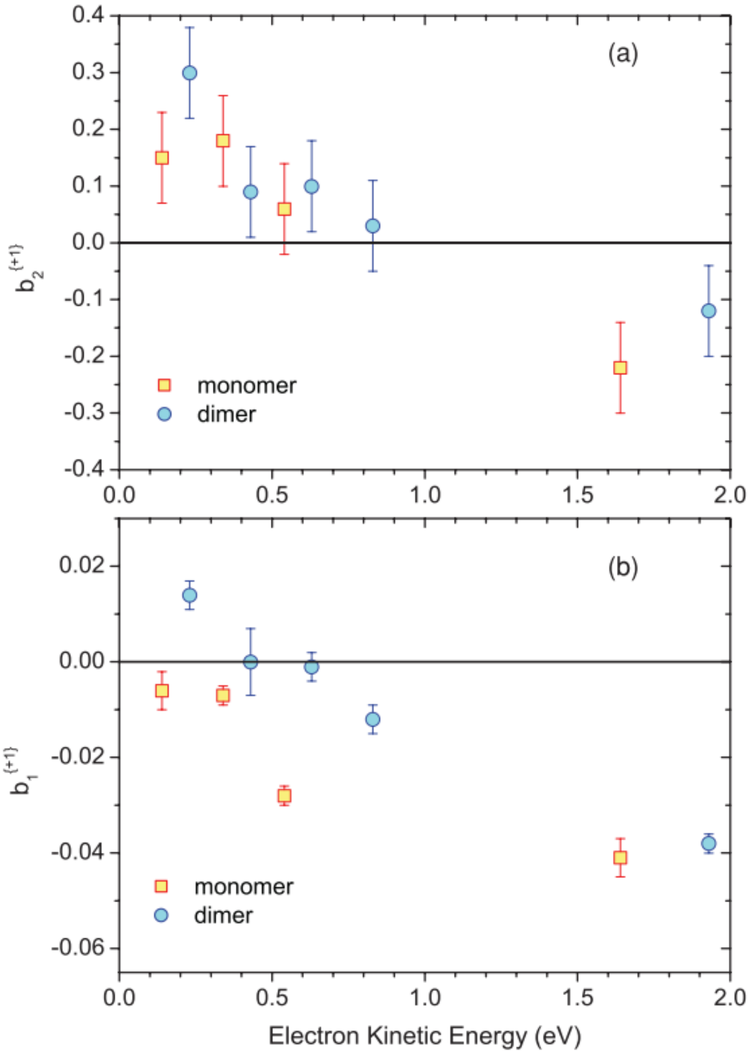

Fig. 18: (top) usual anisotropy parameter, β, and (bottom) PECD parameter, b_1, of (1R)-(+)-camphor monomer and dimer The figure is taken from Ref. [48].

A more comprehensive study on dimerization and clustering effects on PECD was carried out for glycidol [49], as it exists in a single conformer shape, eliminating the complexities due to the conformation. This experiment was also performed with the DELICIOUS II spectrometer at the DESIRS beamline of SOLEIL, which combines an electron VMI setup with an ion ToF mass spectrometer. The technique, as mentioned before, allows PES/TPES/PECD spectra to be recorded in coincidence with any given mass that appeared in the mass spectrum. They examined several clustering conditions which are different in terms of the type and the pressure of the carrier gas, from which strong clustering condition (2 bar Ar) and weak clustering condition (glycidol molecules are expanded through 0.6 bar of He) can be inferred. Using higher pressures of Ar was leading to more clustering rate while lower pressure of He was causing weaker clustering.

In Fig. 19 (a) the mass selected PES and PECD for the first n-mers of glycidol are presented; these results are obtained under strong clustering conditions (2 bar Ar expansion) at a photon energy of 12.1 eV which is above the monomer IP, 9.95 eV. For convenience (easier comparison between S- and R-glycidol enantiomers) the PECD axis of S-glycidol has been reversed. From PES spectra it can be noted that the IP of the clusters is shifted to lower energies while a comparison of monomer and cluster PECD shows an obvious difference; even an opposite sign in the PECD signal can be seen if we go from the monomer to the clusters. However, the PECD of monomer and dimer has been measured at photon energy 9.9 eV, just below the IP of monomer, where the monomer cations in the ToF mass spectrometer must result as a daughter from dissociative ionization of a heavier cluster having itself a lowered IP. In this case, the PECD of monomer and dimer does not show that much difference inducing this meaning that the PECD presents the characteristics of the neutral species from which the photoelectrons are being ejected (dimer in this case).

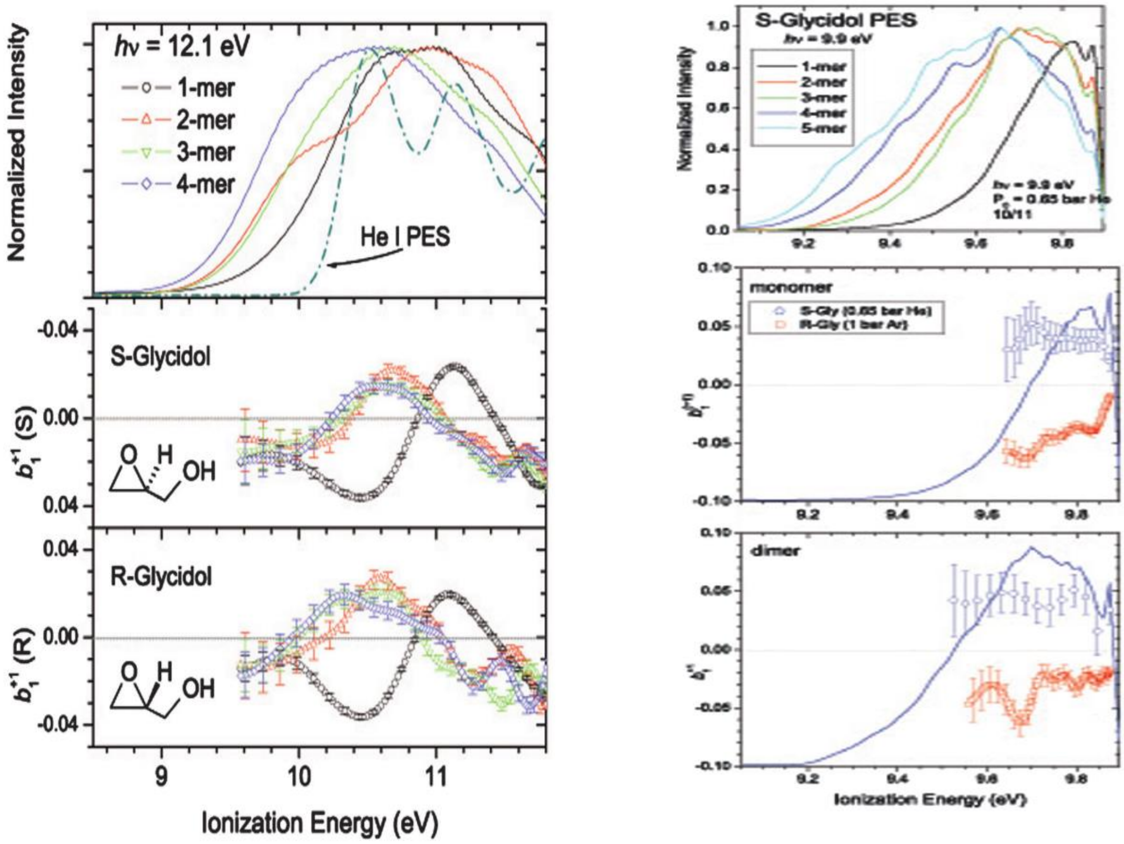

A **B**

Fig. 19: a: Mass selected PES of first n-mers of S-glycidol (top panel) and their corresponding PECD for S-glycidol (middle panel) and R-glycidol (bottom panel), all measured for strong clustering beam using 2 bar Ar expansion at a photon energy of 12.1 eV, above the IP of monomer. b: Mass selected PES of first n-mers of S-glycidol (top panel) and the PECD for S/R-glycidol monomer (middle panel) and S/R-glycidol dimer (bottom panel), all measured at a photon energy of 9.9 eV, below the IP of monomer. The figure is taken from Ref. [49].

As a general conclusion, the authors of [49] say that the PECD of monomers, at photon energies higher than its IP, depends on both the monomer and higher n-mers (from which monomers can be generated as a result of fragmentation in dissociative ionization) while below the monomer IP, the PECD of the monomer is more indicative of the higher n-mers neutral rather than the monomer neutral itself, as the ionization channel from the neutral monomers is being closed below its IP.

In Fig. 20, the PECD of the monomer at two different clustering conditions can be compared. The maximum PECD parameter around 11.25 eV is nearly 8% for weak clustering conditions while it is attenuated down to 5% for strong clustering conditions. In the first regime, where there is a low rate of clustering, the PECD of monomers is expected to have a higher contribution of monomer neutrals since fewer dimers are created and consequently the monomer/dimer ratio is higher. Conversely, in strong clustering conditions, as the number of the n-mers is increased relative to the monomer neutrals, plenty of the monomer cations can be generated from the dissociative ionization of n-mers. As discussed above, in the fragmentation ionization of the n-mers, the daughter monomers carry the PECD of n-mer neutrals which can even have different signs (see Fig. 19 a) and on average cancel the strong PECD of monomer neutrals. Actually, this is why Powis et al. observed an attenuated PECD for S-glycidol monomers at strong clustering conditions.

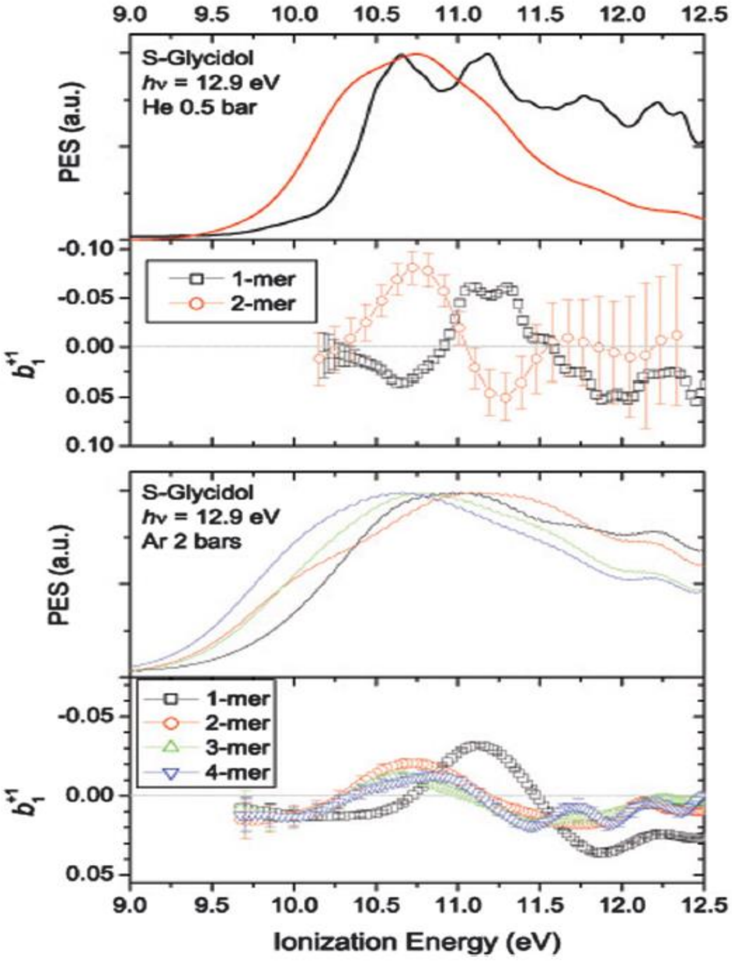

Fig. 20: PES and PECD of S-glycidol monomer and dimer in two clustering condition: top, weak clustering in 0.5 bar He and bottom, strong clustering in 2 bar Ar. The figure is taken from Ref. [49].

To sum up this section, it can be said that PECD shows enhanced sensitivity to dimerization and clustering which makes it a potential candidate to probe such dynamics. Actually, the molecular recognition phenomena (like dimerization and clustering) in the liquid phase are sometimes affected by the molecule-solvent interactions. In contrast, gas-phase PECD analysis is a suitable tool for fundamental studies since it eliminates molecule-solvent interactions.

1.3.1.4. Vibrations

The first experimental evidence of dependency of PECD on the nuclear motion was reported in 2007 by Contini et al. [50]. They showed how the PECD and anisotropy parameter, β, are both depending on the energy content of different vibration states of the molecule. Actually, this phenomena is interesting as it can be considered as evidence of the breakdown of the Frank Condon (FC) secondary assumption. The first assumption in the FC approach, separation of electronic and nuclear motion (in light of their very different mass), is widely accepted. However, the FC approach also assumes that the transition matrix elements between two electronic states are independent of the nuclear geometry during the transition. This means that in the case of molecular photoionization, the electronic wavefunction in the continuum state must be independent of the vibrational dynamics of the cation left behind.

Contain et al. studied the PECD of methyloxirane with a vibrational resolution at the ELETTRA synchrotron, Italy. Although their work was limited to the photoionization of HOMO orbital at a single photon energy, 22.0 eV, the results were convincing and were set as the baseline of further works in this direction. Included in Fig. 21 is the summary of Ref. [50], which in one frame shows how the asymmetry parameters, $\beta, A_{CDAD}$and D are modulated by vibrational states of the cation.

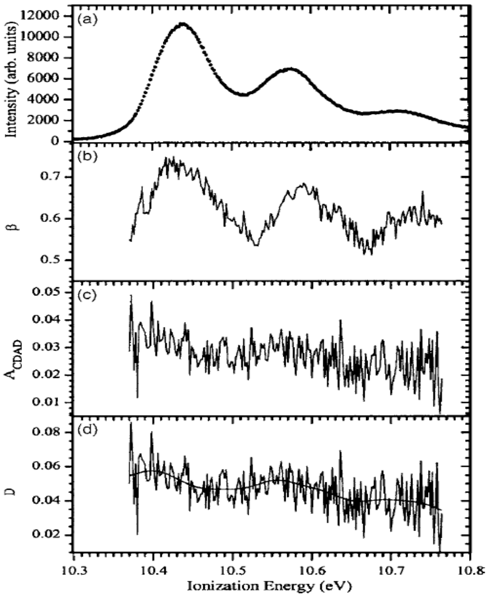

Fig. 21: Dependency of anisotropy parameter, β, and PECD parameter, D, on cation vibrational states in methyloxirane. (a) is the PES of HOMO orbital of methyloxirane and (b)-(d) are respectively showing how β, A_{CDAD} and D are modulated with different peaks in PES. The figure is taken from Ref. [50].

However, in their experiment, Contini et al. used a single photon energy 22.0 eV, which is nearly 12.0 eV above the IP of methyloxirane. The photoelectrons created at this energy would be fast; and, the sensitivity of photoelectrons to the effective chiral potential diminishes at higher energies. So, Garcia et al. [51] reinvestigated the same phenomena for the same molecule but at a photon energy 10.4 eV, less than 1.0 eV above the IP of methyloxirane, where the dichroic parameter is expected to show higher sensitivity.

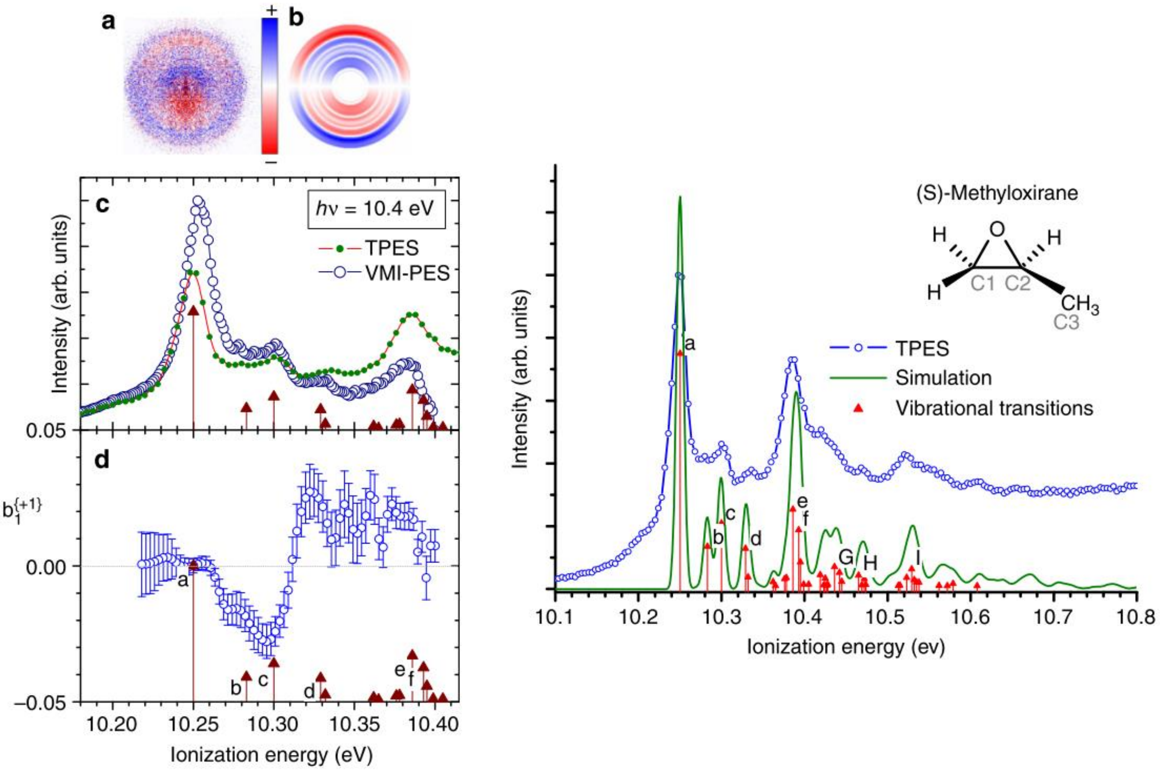

Fig. 22: Right: TPES of S-methyloxirane plotted together with FC simulation to assign the different peaks in TPES (see text). Left: (a) and (b) ar the differential image (RCP-LCP) before and after the able inversion, respectively; (c) is the VMI-PES plotted in top of the TPES and (d) is the dichroic parameter, b_1. The arrows in all plots are the vibrational states whose length is proportional to the corresponding FC factors. The figure is taken from Ref. [51].

Included in the right hand side of Fig. 22 is the TPES of S-methyloxirane on top of the FC simulation, which helps to assign the different peaks in TPES. The features at lower energies (peaks a, b, c, and d in the simulated spectrum on the right hand side of Fig. 22) are assigned to be single quantum excitations from the vibrationless neutral ground state to different normal vibrational modes of the cation. Going from peak a to c, as can be seen from Fig. 22 (b), the PECD takes different values: nearly zero for peak a, negative values for peaks b and c, and a positive value for peak d. The most dramatic change of the PECD is when we go from peak c to d where the PECD switches sign. The PES recorded for methyloxirane is not showing such a visual demarcation for these two peaks, while their PECD is strictly distinct. This enhanced sensitivity of PECD to the adjacent vibrational states makes it a potential analytical tool for studying vibrational dynamics.

Let's finish this section with another example demonstrating the intense modulation of the PECD with respect to the vibronic states. This is a work done by Fanood et al. [52] on monoterpene limonene molecule, from a different class of molecules in comparison to the showcase chiral molecule methyloxirane. In their work, Fanood et al. studied PECD of limonene in a wide photon energy range, from near threshold to 19.0 eV, from which those at lower energies are plotted all together in Fig. 23.

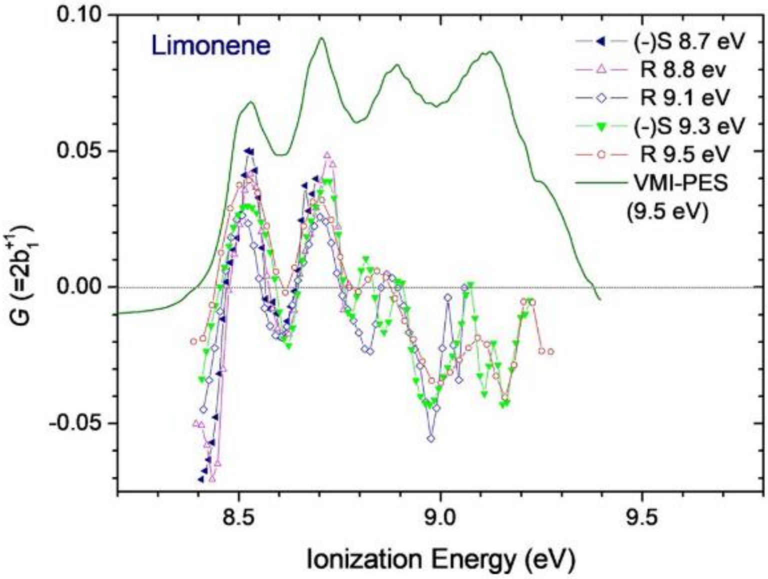

Fig. 23: PECD of limonene over the X-band (an overlap of the HOMO and HOMO-1) at different photon energies between 8.7 eV to 9.5 eVA VMI-PES measured at 9.5 eV is also plotted to see how intensively the PECD is modulated by vibronic structures (see main text). The figure is taken from Ref. [52].

Thanks to their nice calculations, the authors could assign different structures in the PES (over the X-band) to specific vibrational excitations. The first three peaks are assumed to be vibrational excitation from the HOMO orbital while the last peak was assigned to excitation from the HOMO-1 orbitalAs can be clearly seen from Fig. 23, the PECD signal is oscillating in accordance with the minor peaks in PES in this energy range.

1.3.2. Laser Based MP-PECD

1.3.2.1. Pioneering REMPI-PECD experiments

Since 2000, all the PECD measurements were being done in a single-photon ionization scheme using synchrotron radiation until Lux et al. published the first laser-based multiphoton PECD measurement results in 2012 [53]. In their work, they used a fs laser (1 kHz repetition rate, 25 fs pulse duration) to study the PECD of camphor and fenchone in resonantly enhanced multiphoton ionization (REMPI). Three photons of 398 nm, with a total energy of 9.35 eV, were used to eject the electrons from the HOMO orbital of these molecules. Two photons excite the molecules up to an intermediate state; then, the electrons are ionized by the third photon. Because of occurring of a resonance with the intermediate state of the ionization pathway, the measured PECD is called REMPI-PECD. The VMI images published by Lux et al. for different enantiomers of camphor are shown in Fig. 24. It is clear from this figure thatthe mirroring behaviour can be seen when keeping the enantiomer the same and changing the polarization of the light from LCP to RCP or when keeping the polarization of the light the same (LCP or RCP) and changing the enantiomer.

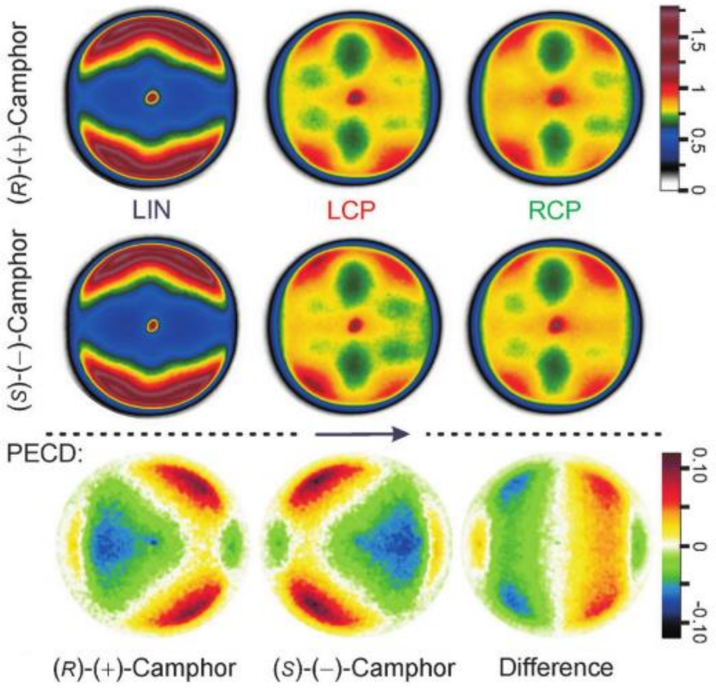

Fig. 24: First row: VMI images recorded for (R)-(+)-camphor using linear (left), LCP (middle) and RCP (right). Second row: VMI images recorded for (S)-(-)-camphor using linear (left), LCP (middle) and RCP (right). Third row: differential image (LCP-RCP) for (R)-(+)-camphor (left) and (S)-(-)-camphor (middle) and their subtraction (right). Figure taken from Ref. [53].

REMPI-PECD is interesting particularly when the laser wavelength is tuned to excite the molecule to one of its high level intermediate states. In such cases, the geometry of the excited neutral is roughly the same as that of the cation because the electrons in high level excited states are relatively far from the molecular nuclei and their ejection does not affect the nuclear motion that much. This is known as a non-rigid selection rule called a propensity rule, which makes us able to compare the REMPI spectrum of a molecule to its PES obtained from a VMI image. In other words, the vibrational states observed in PES are representing the vibrational states obtained excited through the pumping stage. In this way, one can tune the laser wavelength properly to pump some specific vibronic states and measure the PECD for them.

It should also be noticed that in multiphoton PECD measurements, unlike single-photon ones, the higher odd Legendre polynomials also contribute. So, in REMPI-PECD the PECD is not simply presented by $PECD = 2 \times b_1$; the proper expression for MP-PECD is given in (Eq. 6) and will be discussed more in detail later.

Simultaneous to Lux and his co-workers, Lehmann et al. published a more comprehensive laser multiphoton PECD on camphor [30]. They used a fs laser (pulse duration of 150 fs) at two different wavelengths, 380 nm and 400 nm, to pump different intermediate vibronic states and measure the PECD. Actually, with the help of theoretical calculations, they could assign different intermediate states that can get pumped using these wavelengths. This enabled them to study the dependence of the PECD on the intermediate vibronic states for the first time. The assignment of the peaks present in camphor's PES recorded at 380 nm is shown in Fig. 25. Peak I is supposed to be a vibrationally excited level of the 3s Rydberg state while peak II is a vibrationless 3p Rydberg state. Lehmann et al. reported different values of averaged PECD over these two peaks, 5.1% for peak I and 3.5%, for peak II. The averaged PECD at 400 nm was also reported as 7.9%.

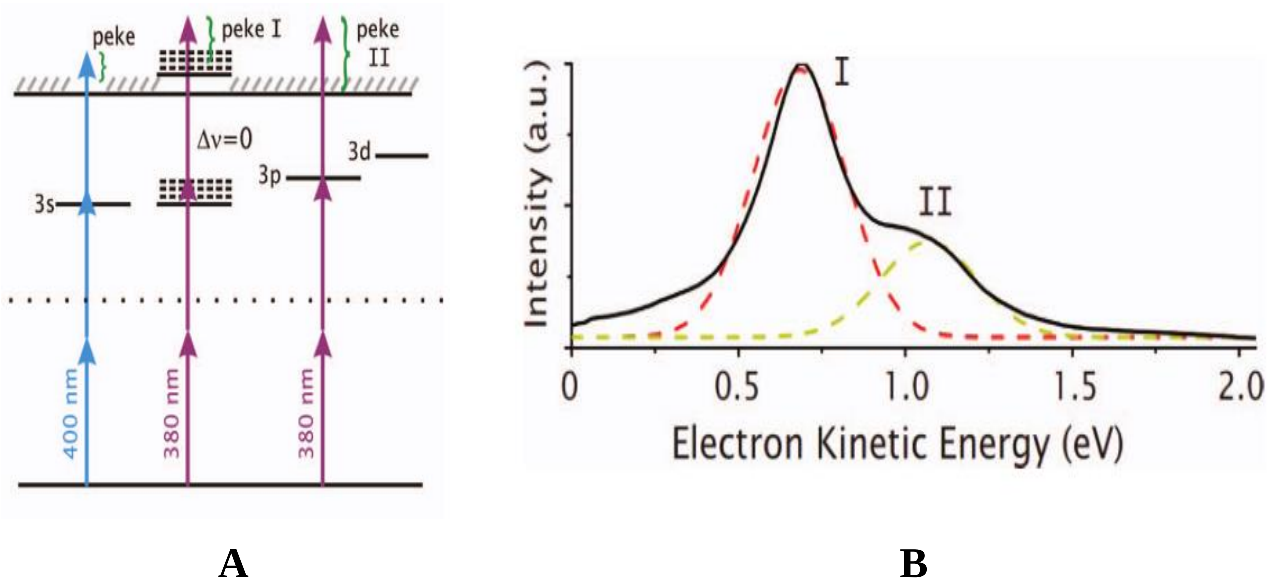

Fig. 25: (a) Schematic of intermediate states getting pumped in (2+1) REMPI of camphor at 400 nm and 380 nm (b) Recorded camphor PES and assigning its peaks at 380 nm. The figure is taken from Ref. [30].

It is also worth noting that Lehmann et al. provided a systematic way to define the PECD in single- and multi-photon schemes. They presented two different but equal ways to express the PECD asymmetry. The first way was to record the LCP and RCP images and fit the normalized differential image given by

$$Diff = \frac{LCP - RCP}{LCP + RCP} \qquad \text{(Eq. 11)}$$

to odd Legendre polynomials, compute the coefficients of the fit, and then use (Eq. 6) to get the PECD. The second way was to count the total number of the photoelectrons ejected into the forward and backward hemispheres (with respect to the direction of the light propagation) using left and right circular polarization and apply the below equation

$$MP - PECD = \frac{I_{+1,f} - I_{-1,f}}{I_{tot}/2} - \frac{I_{+1,b} - I_{-1,b}}{I_{tot}/2} \qquad \text{(Eq. 12)}$$

where $I_{p,f}$ and $I_{p,b}$ are respectively the forward and backward integrated intensities for each polarization ($p = 1$ for right polarization and $p = -1$ for left polarization) and I_{tot} is the total intensity. This technique works because of the time-sensitive detectors, delay-line detectors in their work. Thanks to time-sensitive detectors which generate (x, y, t) information, one can get the full 3D momentum of the photoelectrons. They also showed that these two approaches are theoretically equivalent; actually, they obtained the averaged PECD values for camphor by applying both of these methods to their experimental data and showed that there is good consistency between them.

In the continuation of establishing REMPI-PECD, Lux et al. published another, more comprehensive paper [54] investigating the PECD of three chiral molecules camphor, fenchone and norcamphor, whose chemical structure is approximately the same. They first tried to define the PECD of chiral molecules in a single quantity in a systematic way and applied it to camphor case to show how their method is consistent with the previous work of Lehman et al. (Ref. [30]) discussed above. They also studied the effects of the ellipticity of the light on the PECD signal and found that the PECD shows nonlinear behaviour with respect to S_3, the third Stokes parameter. To this end, they had to retrieve the PECD signal through a tomographic reconstruction method as the commonly used pBASEX algorithm is not working for the case of elliptical polarization, where the 2D VMI images lack a cylindrical symmetry.

They also studied the dependency of the PECD signal on the laser intensity and realized that the total energy and angular distribution of the PECD are not changed significantly by the intensity of the laser while the fragmentation of the parent chiral molecules increases by increasing the laser intensity. As can be seen from Fig. 26, the PECD images are roughly the same at all the laser intensities they applied.

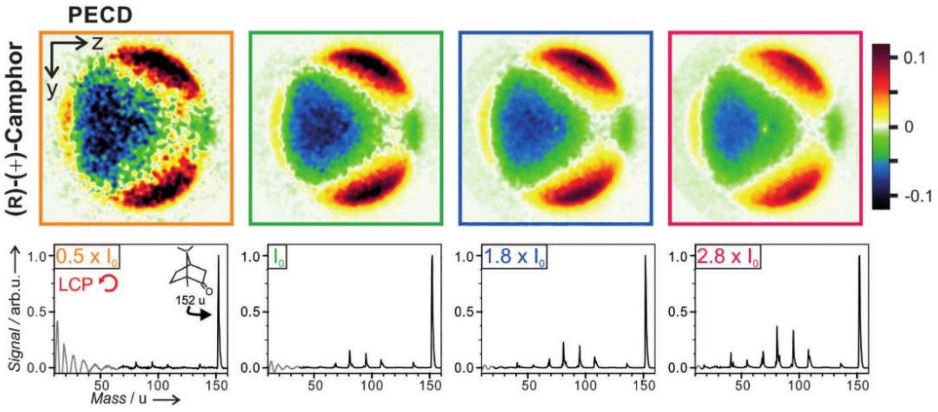

Fig. 26: Top row: the PECD images of (R)-(+)-camphor at different intensities ($I_0 = 4 \times 10^{12}\ W/cm^2$). Bottom row: ToF mass spectrum at different intensities recorded with LCP. The figure is taken from Ref. [54].

In another report, this group showed that the PECD effect can be seen in Above Threshold Ionization (ATI) as well [55]. They just consider the same bicyclic ketones (camphor, fenchone, and norcamphor) but looked at their PAD at higher electron kinetic energies. The photoelectrons observed with higher kinetic energies (with a gap which is roughly equal to the energy of a single photon) can be attributed to the ATI. This was confirmed in their experiment by observing the non-vanishing contribution of higher Legendre polynomials to the PAD and PECD of the chiral molecules.

1.3.2.2. *Vibronic intermediate state dependency of PECD*

In recent years, two interesting REMPI-PECD experiments have been reported. The first one was done by Fanood et al. [56] on the limonene molecule considering a combination of electronic and vibrational intermediate states. They showed how by tuning the wavelength of a fs laser can pump different vibronic intermediate states and measure the PECD associated with those states.

Presented in Fig. 27 is a summary of their REMPI-PECD measurements at the three laser wavelengths 420 nm, 412 nm and 392 nm reported by Fanood et al. They use their calculation to assign different peaks in the PES, as shown on the top axis of the figure. To realise the dependency of the PECD on the vibrationally excited state, one can consider the case of 412 nm where the laser is pumping different vibrational levels of the 3s intermediate electronic state. Going from $v^+=0$ to $v^+=1$ and then to $v^+=2$ one can see an inversion in the PECD signal, from positive to negative values. A similar behaviour that is the inversion of the PECD induced by different cation vibration levels, was previously reported in a single-photon ionization regime [51], already discussed above, and now can be seen in the case of multiphoton ionization. So, a conclusion might be that the PECD intensively depends on the vibrations in both single- and multi-photon ionization regimes. However, this is not surprising as the propensity rule relates the vibrational levels of the intermediate state to those of the cation.

Using 392 nm, the channel for excitation to the higher electronic Rydberg states opens. At this wavelength, one can also expect ionization from the HOMO-1 orbital of the limonene. There is a difference between the PECD signal observed at a longer wavelength than that observed at 392 nm. This difference can be attributed to both different electronic and vibrational levels.

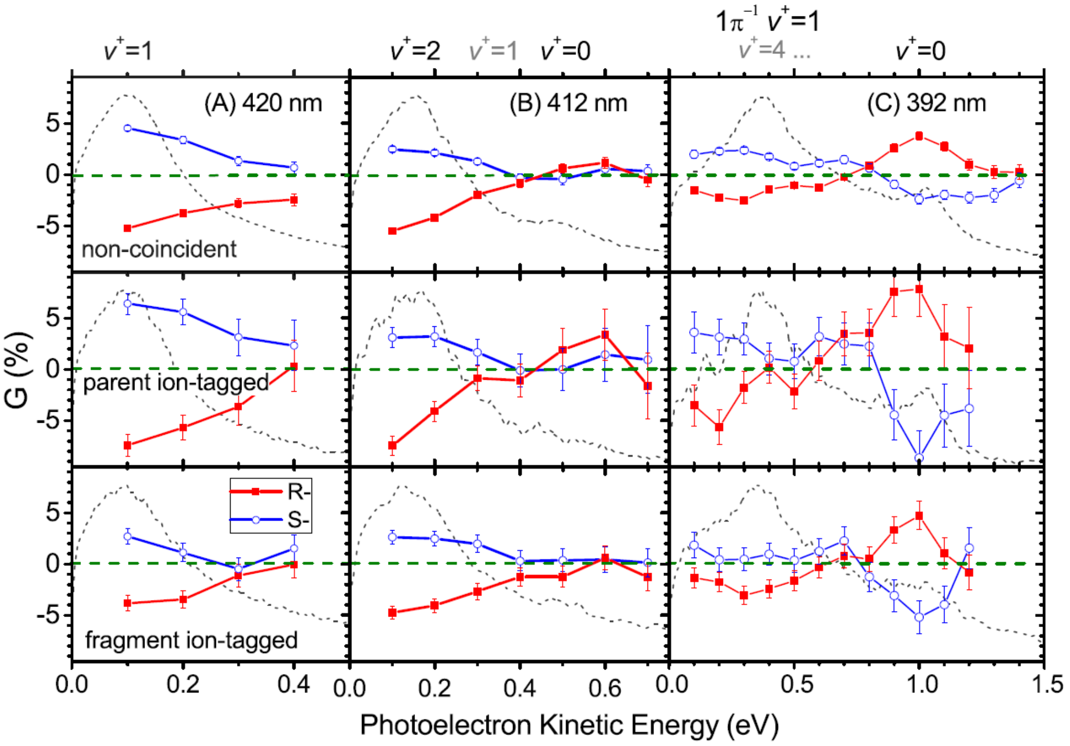

Fig. 27: REMPI-PECD of limonene enantiomers measured at three laser wavelengths 420 nm (left column), 412 nm (middle column) and 392 nm (right column). The top row is the results for the whole photoelectrons while the middle and the bottom rows are showing the results in coincidence with the parent and the fragment ion, respectively. Included in the figures are the black dotted line which is the corresponding PES. The figure is taken from Ref. [56].

In the other interesting work in this direction, Kastner et al. focused just on the role of the Rydberg intermediate states [57]. They decomposed the PECD signal to the contribution of associated Rydberg states disregarding the vibrational excitations. The molecule under study in their work was fenchone whose 3s, $3p_1$ and $3p_2$ Rydberg state can be pumped when scanning the wavelength of a 25 fs laser from 359 nm to 431 nm. In this work, they used a high-resolution ns REMPI technique to assign the peaks in the PES properly. The REMPI-PECD of fenchone with respect to electronic intermediate states reported by Kastner et al is presented in Fig. 28. For comparison, the result of a single photon synchrotron-based PECD measurement on fenchone is also included in the figure.

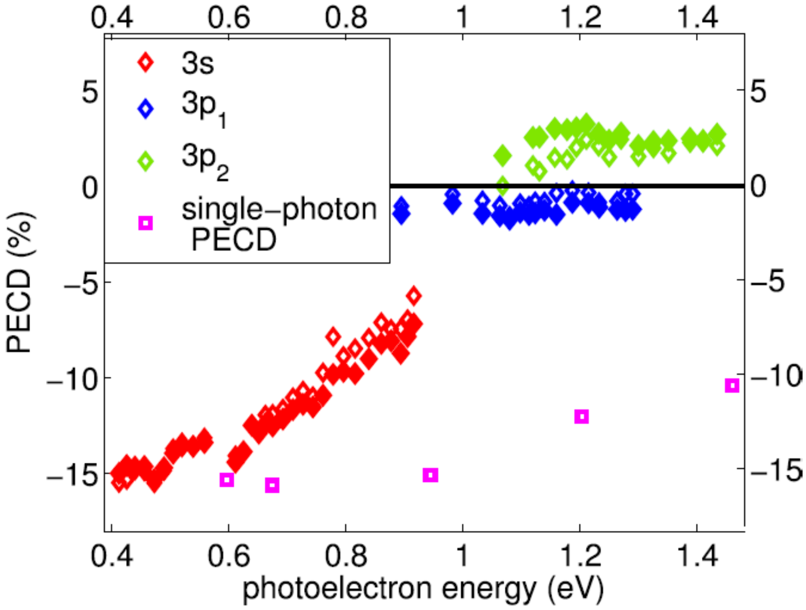

Fig. 28: REMPI-PECD of fenchone for different intermediate states: 3s (red), $3p_1$ (blue) and $3p_2$. A single-photon PECD of fenchone is also plotted for comparison (pink). The figure is taken from Ref. [57].

1.3.2.3. Enantiomer-specific analysis

Toward another direction, researchers in this field were looking for any potential of the PECD to be used as an analytical tool in enantiomer excess (ee) determination. The first suggestion was made by Powis [33]. Later on, several PECD experiments were done using synchrotron radiation dealing with different enantiomerically pure samples. All of these experiments were trying to establish the concept of the PECD experimentally and hence demonstrate that the PECD signal must show a mirroring behaviour when the target chiral molecules are switched from one enantiomer to the opposite one. However, such experiments paved the way for the upcoming laser experiments. When people started to study PECD using the REMPI technique, they were aware of the mirroring behaviour of the PECD signal of the enantiomerically pure samples of opposite shape; but there was no research done yet to discover how exactly the PECD would behave for a compound which is not enantiomerically pure.

Baumert and his co-workers found that the PECD signal for S- and R-enantiomers of fenchone are slightly different. For S-fenchone they obtained an averaged PECD of -13.8% while the PECD measurements for S-fenchone result +10.9%. They knew from the gas chiral chromatography that the enantiomer excess of their samples is 99.8% for the S-enantiomer and 84.0% for the R-enantiomer. Therefore, they attributed this difference in absolute PECD signal to the difference in the ee of their R and S enantiomers.

In a more systematic study, subsequently, they showed that the PECD is dependent on the ee linearly [58]. They prepared samples of fenchone with different ee and measured their PECD. In Fig. 29, the linear relation between the PECD of specimens and their ee can be seen. They also successfully measured the ee of a specimen of unknown ee with less than one percent error.

Another experiment on camphor molecules was done later by Miles et al [59] confirming the linear relation between PECD and ee of the sample. They were using a new technique relying only on the electron counts in the forward and backward hemispheres (disregarding angular and energy distribution of the photoelectrons). They could also reduce the time of ee measurement of the target molecules down to a few minutes.

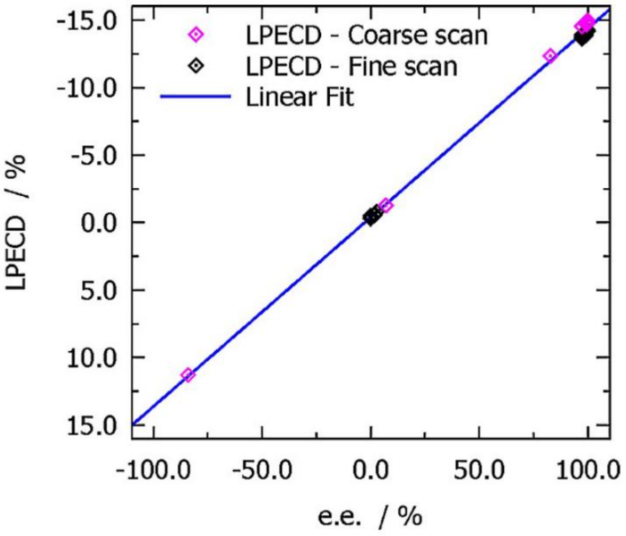

Fig. 29: Linear relation of the PECD and ee The figure is taken from Ref. [58].

In parallel to the Baumert group, Fanood et al. reported their first experiment on enantioselective fs laser experiments on limonene [60]. More interestingly, they proposed the idea of simultaneous ee determination of all the chiral molecules in a multicomponent mixture [61] with taking the advantage of recording the PECD in PEPICO scheme. As a proof of concept, they showed how the ee for limonene and camphor can be measured simultaneously in a mixture of them. To test their proposal, they prepared different mixtures of enantiomerically pure limonene and camphor; in two of the mixtures, they mixed the R-enantiomer of limonene with the R- or S-enantiomer of camphor. When they measured the ee of the mixtures using mass-selective PECD measurement, they found the PECD of the limonene to be the same in the two mixtures but the PECD value for the camphor showed a change in sign from one mixture to the other, as can be seen from the results in Fig. 30. They also could successfully measure the ee of the camphor in a mixture which was composed of only R-limonene but both R- and S-camphor with a ratio of 3:1. The ee of camphor in such a mixture is expected to be 50%; the result of their measurement showed the same amount of ee (although with a relatively large error bar, 0.5±0.2).

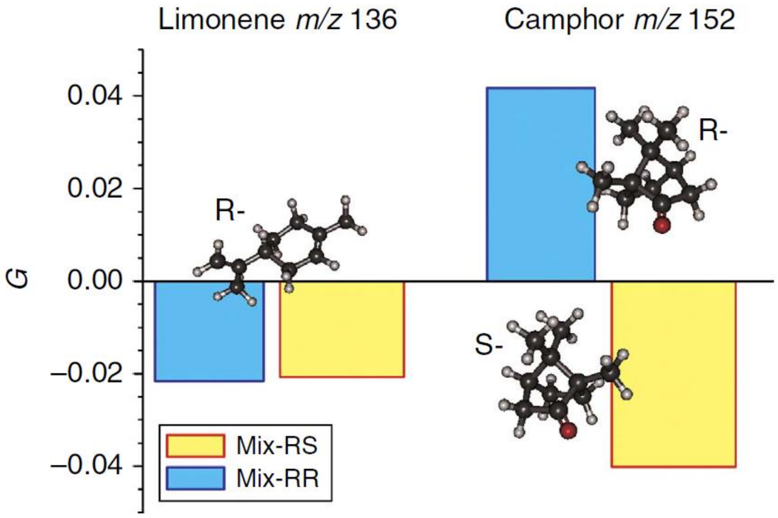

Fig. 30: Mass-selected PECD asymmetry parameter, G, measured in the PEPICO scheme for two mixtures of enantiomerically pure limonene and camphor. Mixture RR contains R-limonene and R-camphor while mixture RS contains R-limonene and S-camphor. The figure is taken from Ref. [61].

1.3.2.4. Time-resolved PECD

Laser pump-probe experiments can be considered as a nice tool to study the evolution of the PECD signal of the chiral molecule as a function of time. If the probe wavelength in a REMPI-PECD experiment is sent with a delay relative to the pump wavelength, the molecule can experience some dynamics before the photoelectrons are ejected from the intermediate resonance state. These dynamics can include the rotational and vibrational motions of the nuclei as well as the evolution in the intermediate electronic states. It has been discussed above how the PECD is sensitive to different vibronic intermediate states; therefore, one may expect the PECD to change over the delay time between the pump and probe. If such a delay pump-probe experiment is repeated with several different delay times between the pump and the probe wavelength, one can see the evolution of the PECD signal as a function of time.

In 2016, Comby et al. published the first experimental work on time-resolved PECD (TR-PECD) [62]. They used linearly polarized light at 201 nm with an 80 fs pulse duration as the pump, and CPL at 403 nm with 70 fs pulse duration as the probe. The pump wavelength excites the fenchone molecule (the experiment was done using R- and S-fenchone) up to its 3s Rydberg state and then the ionization occurs with the probe wavelength. They repeated the experiment with several time delays recording the angular resolved PAD using a VMI setup. The schematic of the experiment and some VMI images they obtained are presented in Fig. 31.

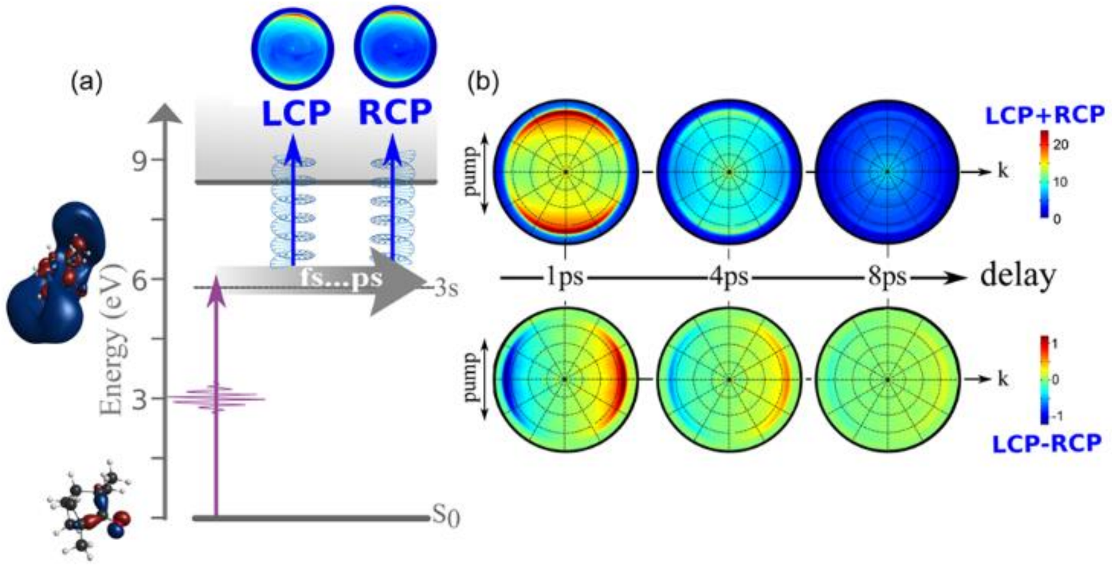

Fig. 31: Schematic of the TR-PECD measurement (a) and photoelectron image recorded at different delay timesin Ref. [62]. A linearly polarized light of 201 nm excites fenchone enantiomers up to its 3s Rydberg state while the photoelectrons are taken out from the intermediate state by CPL. The direction of laser propagation is shown by ***k*** *in the figure. The figure is taken from Ref. [62].*

To reconstruct the 3D photoelectron images and calculate the Legendre polynomials, they used the p-BASEX algorithm requiring a cylindrical symmetry in the plane of the image. But, their 2D VMI images did not possess such a symmetry, as the polarization direction of their linear pump was perpendicular to the direction of their CPL probe, which breaks the cylindrical symmetry. So, the results coming out from the pBASEX algorithm are not exactly the Legendre polynomial, and hence are not referring to the actual PECD. They used a "~" sign on top of the results to distinguish them with the actual quantities. However, the time evolution of the output $\widetilde{\text{PECD}}$ would reflect the time dependency of the actual PECD, which was what they were focused on.

Included in Fig. 32 is the summary of their results showing the time dependency of $\tilde{b}_i$ on delay time between the pump and probe wavelength. The decay in $\tilde{b}_0$ reflects the life time of the intermediate Rydberg state. The drop in $\tilde{b}_2$ is also inferred as the decay in the asymmetry of the photoelectron angular distribution induced by the pump wavelength; actually, the photoelectrons are ejected more along the direction of the polarization of the pump wavelength. The anisotropy induced through the excitation step by the pump wavelength can also affect the higher odd Legendre coefficients like $\tilde{b}_3$. Although $\tilde{b}_3$ can exist intrinsically as a result of two-photon ionization, its evolution observed in their work was attributed to the anisotropy induced by the pump wavelength. This was concluded since the lifetime of the $\tilde{b}_3$ is similar to that of $\tilde{b}_2$ and shorter than that of $\tilde{b}_0$. $\tilde{b}_1$ is showing more interesting behaviour; it experiences a drop firstly followed by rising to a constant value. Comby et al. interpreted this behaviour as a result of Intramolecular Vibrational Relaxation (IVR) that can happen in this time scale. The total $\widetilde{PECD}$ signal is showing the same behaviour as $\tilde{b}_1$ meaning that the most dominant term in $\widetilde{PECD}$ in this ionization pathway for fenchone is $\tilde{b}_1$.

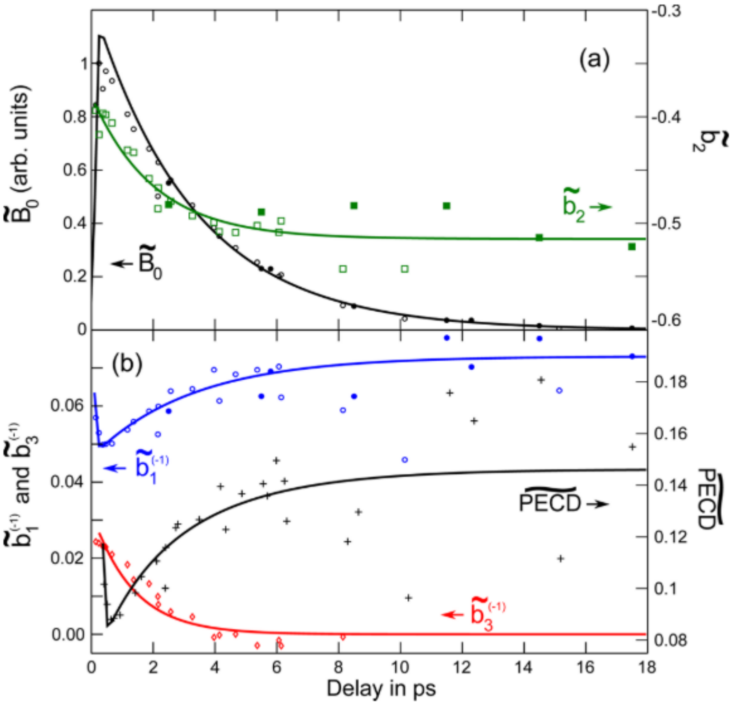

Fig. 32: Dependency of $\tilde{b}_i$ coefficients on the delay time between the pump and probe in a 1+1' REMPI for fenchone. The quantities are calculated as the average of $\tilde{b}_i(eKE)$ around eKE=0.52 (the peak in PES) eV over 30 meV normalized by $\tilde{b}_0(eKE)$ treated in the same way. The figure is taken from Ref. [62].

Recently, Beaulieu et al have done another PECD experiment on the limonene molecule to decouple the role of excitation and ionization steps in REMPI-PECD measurements [63]. They did the experiment using two-colour pump-probe scheme with independent control on both pump and probe polarization. They measured and compared the PECD signal of the limonene molecule in four different setups: (i) both the pump and probe were Circularly Polarised Light (CPL) with the same helicity meaning that the helicity of the pump was switching by changing the helicity of the probe, (ii) the pump was linearly polarized and the probe was CPL, (iii) both the pump and probe were CPL, the helicity of the pump was kept the same as LCP during switching the helicity of the probe and (iv) both the pump and probe were CPL and the helicity of the pump were kept the same as RCP during the switching of the helicity of the probe.

Table 1: Asymmetry parameters and PECD of (+)-R-limonene measured in 1+1' (199 nm+402 nm) REMPIs with different polarization(see main text) for ionization from HOMO and HOMO-1 orbitals

		(i)	(ii)	(iii)	(iv)
HOMO	b1/b0 (%)	-1.6	-2.5	-1.2	-1
	b3/b0 (%)	1	2.5	1	1
	PECD (%)	-3.7	-6.3	-2.9	-2.5
HOMO-1	b1/b0 (%)	-1.1	-1.8	-1.1	-1.5
	b3/b0 (%)	1.4	2.5	1.4	1.3
	PECD (%)	-2.9	-4.9	-2.9	-3.7

Included in Table 1 are the asymmetry values adopted from Ref. [63] for (+)-R-limonene PECD measurements. The first point is that when going from scheme (i) to (ii), the PECD is remarkably increased, from -3.7% to -6.3% for the HOMO orbital and from -2.9% to -4.9% for the HOMO-1 orbital. This huge change in PECD is interpreted as the effect of the linearly polarized pump wavelength as it breaks the isotropy of the target molecules. The induced anisotropy increases the amount of the observed PECD. Also, we can see that to observe the PECD effect, we do not need the pump to be CPL; it is sufficient just to have the probe wavelength circularly polarized. The last point is that the helicity of the pump, when we switch it from LCP to RCP, hardly affects the PECD signal. This can be realized by comparing the PECD values in columns (iii) and (iv) columns, which are respectively for the LCP and RCP pumps.

1.3.2.5. Universality of PECD

In 2015, for the first time, Lux et al. showed that the PECD can be observed at above threshold ionization [55]. The molecules under their study were camphor, norcamphor and fenchone whose vertical IPs are respectively 8.7 eV, 9.17 eV and 8.6 eV. The wavelength they were using was generated by a laser system as the second harmonic of the fundamental, set at 398 nm with a repetition rate of 1 kHz and pulse duration of 25 fs. They increased the intensity of a fs laser up to $I = 1 \times 10^{13}\mathrm{cm}^{-2}$ to get the ATI-PECD effect. As can be seen from Fig. 33, in addition to the threshold photoelectrons (electron kinetic energies below 0.6 eV) an extra region in the PAD and PECD images appears at electron KE above 3.2 eV for all three chiral molecules. The energy difference between the two regions is equivalent to a single photon energy for all the molecules confirming that these photoelectrons have been created just by absorbing one more photon above the ionization threshold.

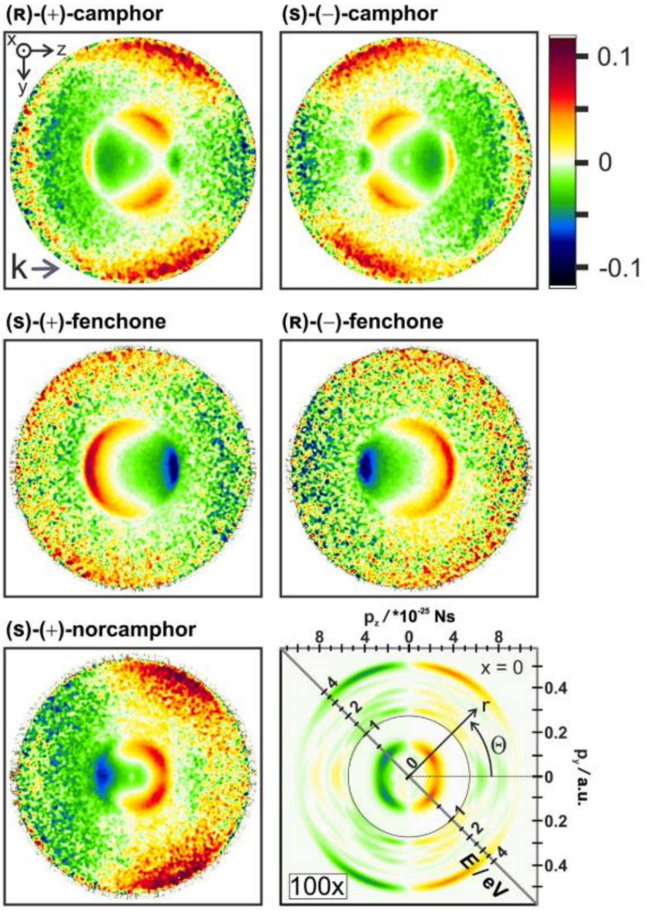

Fig. 33: PECD row images for R- and S-cmphor (top row), R- and S-fenchone (middle row) and S-norcamphor (bottom row, left). The p-BASEX results for S-norcamphor are shown on the right hand side of the bottom row. The radius of the images is presenting the electron kinetic energy with the scan presented in the p-BASEX results of norcamphor. The propagation direction of the light is from left to right in all images. The figure is taken from Ref. [55].

Lux et al. in their work fitted the able inverted PECD images to the first ten Legendre polynomials and saw that as the laser intensity increases, the higher Legendre polynomial coefficients like b_7 and b_8 acquire non-zero values. This means that at higher intensities, as $I = 1 \times 10^{13}\mathrm{Wcm}^{-2}$, four photons are absorbed. They also showed that the PECD signal for ATI could be even larger than that of threshold ionization. For example, the PECD of norcamphor in the threshold and above threshold ionization regions was reported as 9% and 14%, respectively.

Simultaneously, Beaulieo et al. published two papers showing that PECD is a universal effect happening in all ionization regimes: single photon ionization (SPI), REMPI, ATI and tunnel ionization [64, 65]. They used High Harmonic Generation (HHG) to generate the photons in the VUV to X-VUV range required for ionization of the molecules with a single photon. Actually, this method was first applied to the PECD measurement experiments successfully in 2014 [66]. However, there is a limitation to this method as the polarization of the HHG output light cannot be perfectly circular. In HHG, if the pump laser is totally circularly polarized, the probability of recombination of the accelerated electrons to their parent reduces, leading to a reduction in HHG yield. So, inevitably, HHG provides us with elliptical photons instead of perfectly circular ones and this, as it was discussed before, affects the p-BASEX algorithm and the final PECD signal as well.

Fenchone was studied as well as limonene to show how PECD can be measured in all of these ionization schemes. The REMPI threshold ionization for these molecules can be done by the second harmonic of their fundamental wavelength. The second harmonic of the fundamental wavelength (cantered around 800 nm) was generated using a BBO crystal at 400 nm. The laser intensity was set as $I = 2 \times 10^{13}\mathrm{Wcm}^{-2}$ for threshold REMPI ionization. To access ATI, they kept the wavelength roughly the same (402 nm) and just increased the laser intensity up to $I = 4 \times 10^{13}\mathrm{Wcm}^{-2}$. To go to the tunnel ionization regime, they did the measurement using the fundamental wavelength, 800 nm, with an intensity of $I = 1.3 \times 10^{13}\mathrm{Wcm}^{-2}$ and reported 5% of PECD for fenchone. Observing a PECD signal at such high intensities can be considered as a failure of the strong-field approximation. In strong-field approximation, it is assumed that the external field effect is much stronger than the effect of the molecular potential. So, the PECD signal, as a result of the scattering from the chiral molecular potential, should be negligible in the presence of the strong fields; but, it is not.

1.3.3. Conclusion

In this section the state of the art of the PECD research was reviewed. A number of factors affecting the PECD of a chiral molecule were discussed and potential applications of PECD for analytical purposes were pointed out. For example, the sensitivity of the PECD to the vibrational quantum states could make PECD a suitable candidate to probe such dynamics. In Chapter 5 we investigate the dependency of the PECD on vibrational states in detail and propose how the PECD signal recorded for a molecule can reveal some information about its vibrational dynamics.

In addition, as discussed above, the PECD shows a linear relation to the enantiomer excess of a chiral molecule. We use this idea in Chapter 4 to build up a new method based on photoelectron spectroscopy to obtain the enantiomer excess of gas phase mixtures of several chiral molecule.

We also reviewed the pump-probe laser experiments carried out so far for PECD to show how the intermediate vibronic quantum states can affect the PECD signal of a chiral molecule. In Chapter 7 we will report the results of a fs laser experiment we carried out at the Artemis beamline of Central Laser Facility (CLF) on α-pinene to investigate the dependency of the PECD on intermediate vibrational and electronic states.

2. Experimental and Theoretical Methods

2.1. Velocity Map Imaging (VMI)

As discussed before (Sec. 1.2.2), to measure the PECD of molecules we can look at their photoelectron angular distribution. But, we need some techniques to record PAD in photoionization. Velocity map imaging is a technique that enables us to record high-resolution images. Using VMI, it is possible to record energy-resolved and/or angular-resolved PAD images of molecular photoionization; as we will see soon, the angular resolved PAD can be obtained if we are doing PECD for aligned molecules (if we are recording photoelectrons in the molecular frame) or we are using polarized light.

Let us have a look at the processes which happen from the moment of creation of the photoelectrons up to the time when they are detected. In the first step, we have a beam of light and a molecular beam, any of which can have a circular cross-section (in general their cross-section profile can be given by more complicated geometries and also can be non-uniform in terms of intensity). The intersection of these two beams is not simply a point, but rather has an extended profile (Fig. 34). At any point inside the region of intersection of the two beams, photoelectrons can be created and start to expand into space. We can apply an electric field to this cloud of electrons to direct them to the place where the detector is located. If this cloud of electrons hit the detector, a blurred image will be recorded, due to the spatially-extended source. In reality, this fact that the molecular beam and the beamline do not have a point intersection cannot be disregarded but thanks to VMI we tune the electric field used to project the electrons to the detector in order to improve the resolution of the final recorded image.

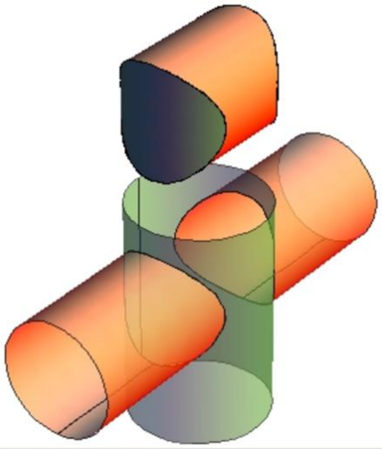

Fig. 34: Intersection of a cylindrical beam line and a cylindrical molecular beam which is an extended interaction area(extended source of photofragments)

What VMI does is to use a certain configuration of electrodes to move the photofragments toward the detector. The configuration consists of three electrodes one of which, the repeller, is a circular plate and the two others, the extractor and the ground, are ring-shaped electrodes. If we calculate the electric potential lines around these three electrodes, it can be found that they penetrate the holes in the middle of ring-shape electrodes and create an electric lens [67]. What this electric lens does is to *map* all the electrons with the *same velocity vector* into the same point on the detector *irrespective of their initial location of creation*. More precisely, although at any point in the intersection area the interaction of the molecular beam and beamline is happening and many electrons with different momenta are being created, the electrons with the same momentum from different points will go to the same point on the detector. To illustrate this, we can look at Fig. 35 taken from reference [67]. In Fig. 35(a) the potential lines around the three electrodes are calculated creating an electric lens in the area between the extractor and the ground electrode. In Fig. 35(c) three points at different locations are shown where the photoelectrons with the *same energy* initially are created. Subfigure (b) zooms in on of the points at which electrons are ejected from the molecules and subsequently are expanding under the effect of the external electric field. For this 2-D schematic picture, let us consider three different electrons in a way that in their initial locations they make the angle $0/180^{\circ}$ $45/135^{\circ}$ and 90° with respect to the horizontal line. If we name the electrons with these angles as 1, 2, and 3 respectively, all the electrons making the angle $0/180^{\circ}$ will go through the line 1 in the Fig. 35(d), all the electrons making the angle $45/135^{\circ}$ will go through the line 2 in the Fig. 35 (d) and all the electrons making the angle 90° will go through the line 3 in the Fig. 35 (d). The main properties of VMI are that this mapping is completely independent of the initial location of electrons.

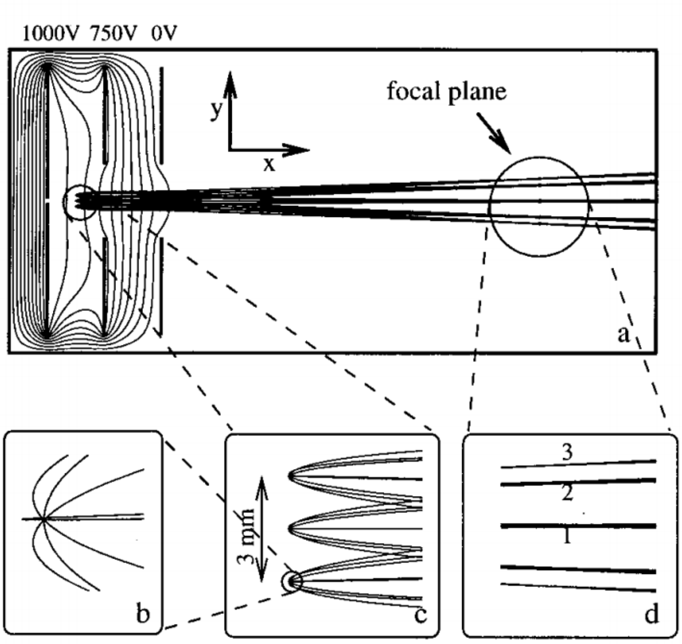

Fig. 35: (a) Electric potential lines calculated around the electrodes, (b) Initial direction of a group of electrons of the same energy, (c) Three groups of electrons with the same energy, but the different initial location and (d) Trajectory of three groups of electrons with angles$0/180^{\circ}$, $45/135^{\circ}$ *and* $90\ ^{\circ}$*with the axis of the detector. The image is taken from Ref. [67].*

In Fig. 36 (a) the points where three trajectories 1, 2, and 3 arrive at the detector are shown. If the problem has a cylindrical symmetry around the axis of the detector, we can rotate these points around that axis to obtain the whole image recorded by the detector, which would be Fig. 36 (b). Note that, such images like Fig. 36 (b) will be created during a period of data acquisition. In other words, all the electrons recorded in VMI images are not created instantaneously and even for those electrons which are created in the same time, the flight time may be different due to their different initial direction.

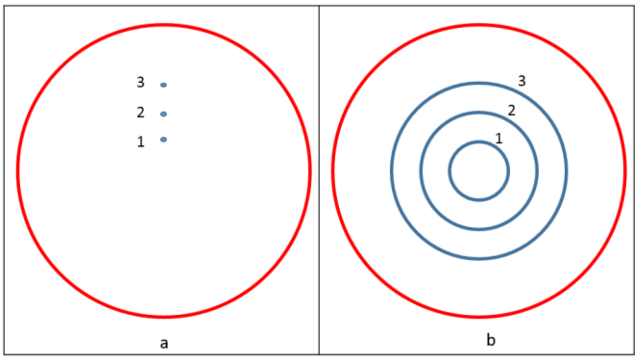

Fig. 36: (a) The points that three groups of electrons, initially making angles $0/180^{\circ}$, $45/135^{\circ}$ *and* $90\ ^{\circ}$, *hit the detector and (b) The total image of these three groups of electrons when the problem has cylindrical symmetry around the detector axis.*

There are two important points about VMI and the images, like Fig. 36, obtained from this technique. As we mentioned before, this figure is obtained by two assumptions: 1) all the electrons have the same energy and 2) the problem has cylindrical symmetry around the axis perpendicular to the detector screen. Below, we explain a little about what happens if these conditions are not the case, but before that, we need to recall the concept of the Newton sphere and its projection to a 2-D plate.

In any given point of the interaction region, a cloud of electrons is created and starts to expand due to the radial speeds of electrons. If we consider all the electrons to carry the same energy, their speed is the same, but along different directions. Therefore the cloud of electrons, in this case, will be the surface of a sphere with an increasing radius. This sphere is called the Newton sphere which finally will be projected to a 2D detector by applying proper electric potentials to the VMI electrodes. In Fig. 37 we can see a schematic view of a typical Newton sphere and its projection on the detector.

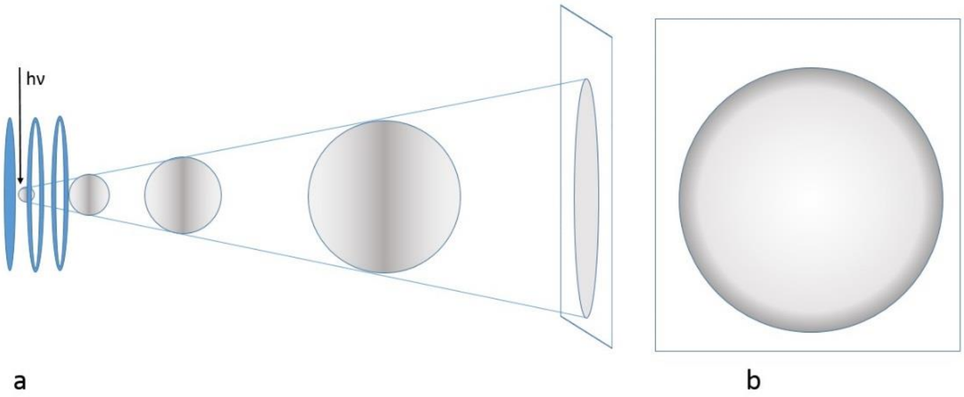

Fig. 37: schematic view of a typical Newton sphere (a) and its projection on a 2-D detector (b)

Now, suppose that the electron cloud consists of two groups of electrons with different kinetic energies, T_1 and T_2. According to $T = mv^2/2$, the radial speed of electrons in the two groups would be v_1 and v_2 which in return gives different final radii on the detector, R_1 and R_2, respectively. In this case, we can say that there are two surface spheres with the same centre (here we considered all the electrons to be created in the same point) any of which is expanding through space and finally will be projected to the detector, as shown in Fig. 38.

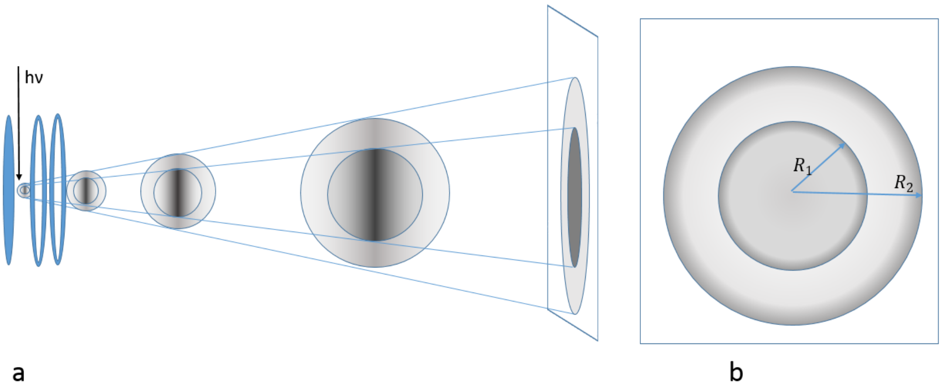

Fig. 38: A Newton sphere with two shells (a) and its projection to a 2-D detector (b)

Now, we can figure out what happens if the electron cloud includes electrons with several different energies. In such a case, the Newton sphere will be like an onion consisting of several shells and its 2-D projection is created by the superposition of the 2-D projection of any of these shells. The schematic view of a Newton sphere containing several shells and its 2-D projection is shown in Fig. 39.

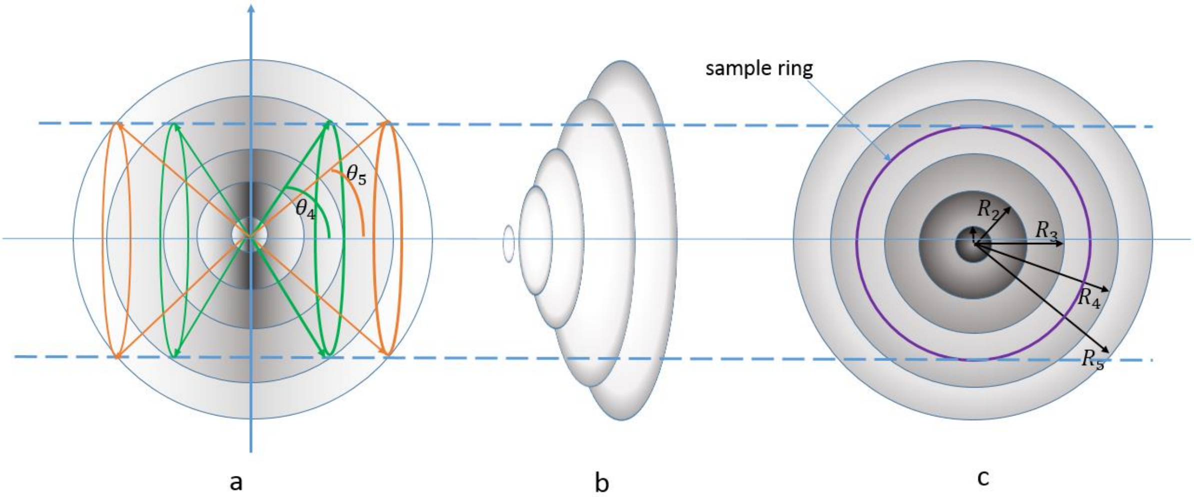

Fig. 39: Onion model of Newton sphere (a), 2-D projection of different shells (b) and the total 2-D image created by the superposition of all single 2-D projections (c).

The ambiguity about the VMI images like Fig. 39 (c) comes when we are looking at some parts inside it. For example, consider the sample ring in Fig. 39 (c). This ring can be a part of the 2-D projection of the shell with radius R_4 or can be a part of the 2-D projection of the shell with radius R_5. But, as we discussed, the two different 2-D projections correspond to electrons with different energies, T_4 and T_5. Based on what we discussed about the projection of electrons of different angles on top of each other on the detector screen, we can say that if the electrons on the sample ring have kinetic energy T_4, their initial direction has been closer to the vertical axis and if they have kinetic energy T_5, their initial direction makes a larger angle with the vertical axis of the Newton spheres. This can be expressed as $\theta_5 > \theta_4$. A single ring on the detector screen can represent the electrons of different energies, and even in a given energy, there are two groups of electrons which can be projected on the same ring, the electrons which are initially going in forward and backward direction but making supplementary angles with the axis perpendicular to the detector screen. In this example, there would be four groups of electrons represented by the same ring on the detector screen. The kinetic energy and direction of these four groups are given by (T_4, θ_4), $(T_4, 180 - \theta_4)$, (T_5, θ_5) and $(T_5, 180 - \theta_5)$. The situation can be even worse if we are looking at the rings very close to the centre of the image. At such a ring, the electrons possessing several different kinetic energies are present making analyses of the VMI images complicated. If we need to look at a group of energy selected electrons we need to use the onion-peeling algorithm which is usually used in analysing VMI images [68, 69].

The second important thing influencing VMI images is the cylindrical symmetry of the problem. If the angular distribution of photoelectron is symmetric around the axis perpendicular to the detector screen, electrons with the same energy will create uniform rings on the detector, see Fig. 36; otherwise, asymmetric shapes will appear on the detector. The more the asymmetry of the PAD, the more asymmetric the shape on the screen. In some cases, we may see the trace of the rings, but non-uniform. For example, if the photoionization is induced by a linearly polarized laser light and the direction of polarization is perpendicular to the axis of the detector screen, the intensity of the rings will be more along the direction parallel to the polarization direction. Another setup that may cause the creation of non-uniform rings on the detector is when we are imaging the photoelectrons ejected from aligned molecules. If a molecule has an axis of symmetry (usually present in molecules with a permanent electric dipole), we can first align the molecules then ionize them. In such cases, there is also the possibility of recording non-uniform VMI images. In Fig. 40, taken from Ref. [70], we can see the asymmetry of photoelectrons ejected from aligned $\mathrm{CO_2}$ molecules which is obviously asymmetric.

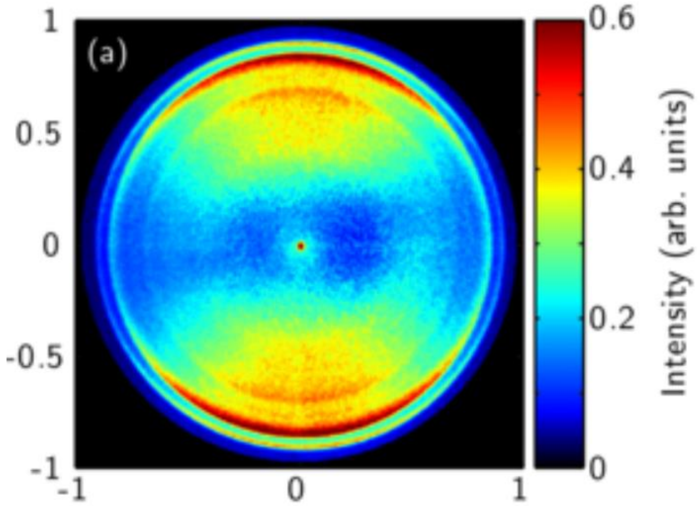

Fig. 40: Photoelectron image of CO_2 molecules aligned with a free-electron laser, taken from Ref. [70]. The x- ad y-axis are respectively the pixel position along the x- and y- directions in arbitrary units

There is a point that is worthwhile to mention here; when we are using a beam of light to ionize the molecules, at some photon energies, a molecular bond may be broken and results in fragmentation of molecule. In some other cases, there may be some impurities in the medium and photoelectrons may be ejected from them. So, the raw PAD images contain electrons coming from several species inside the ionization chamber. In such cases, if somebody is interested in the electronic structure of only some certain species, it is better to find a way to filter the raw photoelectron images. There are several techniques to achieve this goal one of which is setting up time of flight (ToF) mass spectroscopy for the ions as well as a time-sensitive detection for the electrons. In this way, one can select a mass (or some masses) from the ToF spectra and filter the photoelectrons with respect to those that are in coincidence with the selected mass. Further details on coincidence spectroscopy will be presented in Sec. 2.3.

2.2. Time of flight mass spectroscopy (ToFMS)

2.2.1. Basic ToFMS

The beginning of Time-of-Flight Mass Spectroscopy (ToFMS) can be traced to a paper published in 1953 [71]. ToFMS is a technique to detect species with different masses and distinguish them from each other. The most basic ToFMS instruments consist of an acceleration region with a uniform electric field and a field free drift region, as is shown in Fig. 41.

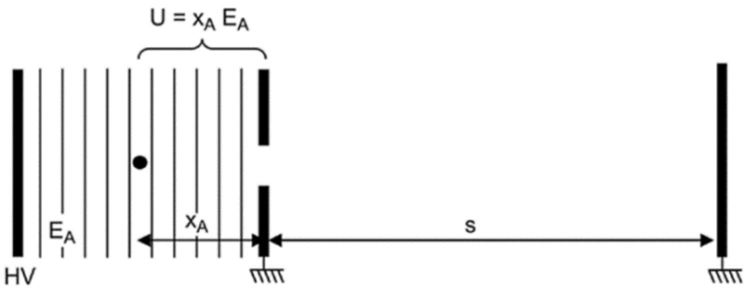

Fig. 41: Schematic view of a basic ToFMS

The total time of flight for a particle to arrive at the detector can be calculated as the sum of the time of flight in the acceleration region and the time of flight in the drift region, $t = t_{acc} + t_{drift}$. If a uniform electric field E_A is applied to the acceleration region, the acceleration will be constant, given by $a = qE_A/m$ in which q and m are the charge and the mass of the particle, respectively. The distance from the initial location of the particle to the end of the acceleration region is X_A so the time of passing this distance with a constant acceleration, a, will be (the initial velocity of the particle is considered to be zero):

$$t_{acc} = \sqrt{\frac{2X_A}{a}} = \sqrt{\frac{2X_A m}{qE_A}} = X_A\sqrt{\frac{2m}{U}} \qquad \text{(Eq. 13)}$$

The particle initially has a potential energy of $U = qE_A X_A$ which at the end of the acceleration region is changed to kinetic energy. Therefore, the equality $1/2\, mv^2 = U$ will give us the velocity of the particle at the beginning of the drift region as

$$v = \sqrt{\frac{2U}{m}} = \sqrt{\frac{2qE_A X_A}{m}} \qquad \text{(Eq. 14)}$$

This velocity will remain constant over the drift region as there is no force applied to the particle in this region. The time of flight in the drift region is then given by

$$t_{drift} = \frac{S}{v} = S\sqrt{\frac{m}{2U}} = S\sqrt{\frac{m}{2qE_A X_A}} \qquad \text{(Eq. 15)}$$

The total time of flight now can be written as

$$t = t_{acc} + t_{drift} = \sqrt{\frac{2X_A m}{qE_A}} + S\sqrt{\frac{m}{2qE_A X_A}} = X_A\sqrt{\frac{2m}{U}} + S\sqrt{\frac{m}{2U}} \qquad \text{(Eq. 16)}$$

If we have several charged particles and record the time of their arrival to the detector, t, their mass can be calculated from (Eq. 16). However, this is the most basic type of ToFMS in which the simplest possible geometry as well as a uniform field in the acceleration region has been taken into account. In addition, we used three assumptions in the above calculation: 1- the initial location of all particles is the same, $\Delta X_A = 0$, 2- the initial creation time of all particles is the same, $\Delta t = 0$ and 3- all the particles initially have the same velocity $\Delta v = 0$. These three assumptions can be related to each other by $\Delta v = \Delta X_A / \Delta t$ (disregarding the thermal velocity of the ions and any possible fragmentation) so we usually need to compensate only two of these uncertainties: spatial spread and velocity spread of particles. The resolution of ToFMS, $m/\delta m$, is limited by uncertainty in initial spatial and velocity distribution of species. In the next section, the Wiley & McLaren ToFMS and how it compensates for uncertainty in initial spatial is explained.

2.2.2. Wiley & McLaren ToFMS

Wiley and McLaren overcame the limitations caused by initial spatial distribution and invented their version of ToFMS, the so called Wiley & McLaren ToFMS [72]. Later, several improvements have been added to this type of ToFMS, but based on the same principles [73, 74]. Moreover, another kind of ToFMS was invented by Mamyrin [75], called as reflection ToFMS. mechanism description of reflection ToFMS can be found elsewhere [76, 77], but here, we explain more about the Wiley & McLaren ToFMS and how it increases the resolution. Suppose that lots of atoms with the same mass are produced not exactly at the same point, but with a spatial spread of ΔX_A. Some of these ions are created at $X_A - \Delta X_A$ while some others may be created at $X_A + \Delta X_A$. We know that the initial electric potential depends on the horizontal coordinate X and is different for the particles created at different points. It can be said that the electric potential at $X = X_A + \Delta X_A$ is more than that at $X = X_A - \Delta X_A$. This will cause the ions created at $X = X_A + \Delta X_A$ to have a larger velocity at the beginning of the drift region, relative to ions created at $X = X_A - \Delta X_A$ (see (Eq. 14)). Although, the ions with the initial location $X = X_A - \Delta X_A$ arrive at the end of the acceleration region sooner, the ions created at $X = X_A + \Delta X_A$ will overtake them at some point in the drift region, called the space focus. If we place the detector at the space focus, the resolution will increase because the uncertainty in the initial position is compensated at this point; the ions with the same mass generated at $X = X_A \pm \Delta X_A$ will hit the detector at the same time.

As is obvious from (Eq. 16) the total time of flight for ions from their initial location to the detector placed at distance S in the drift region depends on the initial location (or it depends on the initial location and the potential energy experienced by the particles at their initial location). We can use this equation to find the location of the space focus by setting the first derivative of (Eq. 16) with respect to X_A equal to zero. This will give us the value of S, matching to the space focus,

$$X_{SF} = 2X_A \qquad \text{(Eq. 17)}$$

in which X_{SF} refers to space focus. By locating the detector at the distance $X_{SF} = 2X_A$ from the ground electrode, we can reach the best resolution for detecting the ions with the same mass. However, the aim in ToFMS is not to detect only one mass; in ToFMS we need to detect several ions with different masses. If we put the detector at such a short distance, the length of the drift region will not be long enough to allow the separation of different masses. The longer the length of the drift tube, the more the separation of different masses. This is the point where Wiley & McLaren's version of ToFMS comes in. Wiley and McLaren solved this problem by considering two different stages for the acceleration region, although their main motivation was to improve the energy focusing. They applied two different potentials to create two different uniform electric fields. The ions are supposed to accelerate by passing through these two electric fields and then enter the drift region, as shown in Fig. 42 (b).

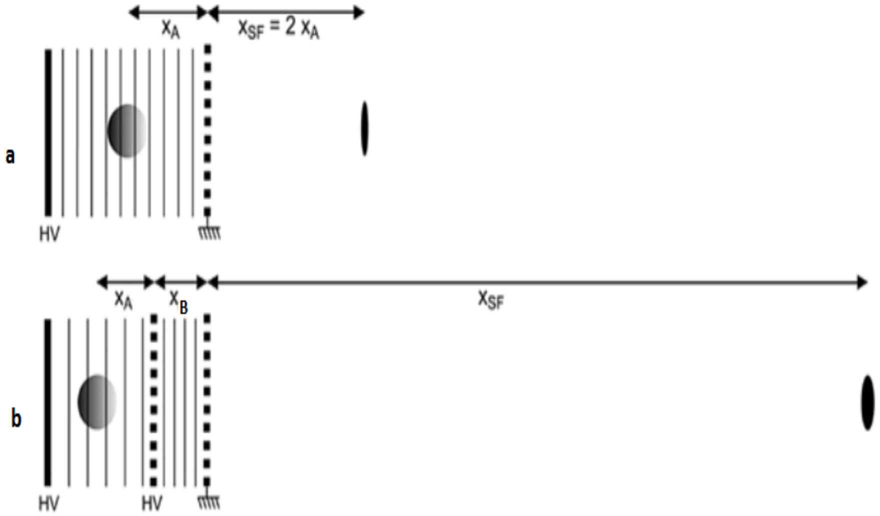

Fig. 42: A basic ToFMS (a) versus a Wiley & McLaren ToFMS (b)

The total time of flight for ions from X_A to the detector can be written as $t = t_A + t_B + t_{drift}$. If we assume that in regions A and B electric field and electric potential energy are given by E_A, E_B, $U_A = qE_AX_A$ and $U_B = qE_BX_B$, respectively, one can calculate the total flight time as:

$$t = \sqrt{\frac{2X_Am}{qE_A}} + \frac{\sqrt{\frac{2q}{m}(E_AX_A + E_BX_B)}}{\frac{qE_B}{m}} + \frac{S}{\sqrt{\frac{2q}{m}(E_AX_A + E_BX_B)}} \qquad \text{(Eq. 18)}$$

To minimize the effects of initial spatial distribution ΔX_A we can set the derivative of (Eq. 18) with respect to X_A equal to zero. One can find the proper distance for S where the detector can be located to get the highest possible resolution. If we again name this value as the space focus, X_{SF}, we have:

$$X_{SF} = 2X_A\left\{(1 + \frac{U_B}{U_A})^{3/2} + \frac{E_A}{E_B}(1 + \frac{U_B}{U_A})\right\} \qquad \text{(Eq. 19)}$$

This relation is completely different from the expression of X_{SF} in basic ToFMS given by (Eq. 17). In (Eq. 19) there are some parameters, all dependent on electric potentials applied to different electrodes, by which we can increase X_{SF} for the same geometry parameters X_A and X_B. In Fig. 42 (from reference [78]) a Wiley & McLaren ToFMS is compared with a basic ToFMS. In the case of Wiley & McLaren ToFMS, the space focus is increased remarkably up to large distances in the drift region. This space focus is now large enough to let the ions with different masses to be separated from each other.

2.3. Photoelectron photoion coincidence spectroscopy (PEPICO)

There is much information in the photoionization process that cannot be seen by doing photoelectron spectroscopy and photoion mass spectroscopy separately while doing both of them in coincidence with each other lets us know more about the photoionization dynamics. PEPICO is a technique in which, after ionization, both the electron and the cation are extracted by applying proper electric potentials and are detected with time-sensitive detectors. Much information like energy, time, and angle-resolved distribution of the fragments can be simultaneously obtained by PEPICO. The first study on PEPICO was published by Brehm and von Puttkammer in 1967 [79]. In a typical PEPICO experiment, the photoelectrons are detected by a VMI technique while a ToFMS is used to detect the ionic fragments, as shown in Fig. 43 taken from Ref. [80]. If the detectors used in ToFMS and VMI are both time-sensitive, we can record the time correlation between the electrons and cations. This helps us to filter the photoelectron images with respect to one or more masses appearing in ToFMS. In this way, we can improve our knowledge about the molecular structure of any certain cation.

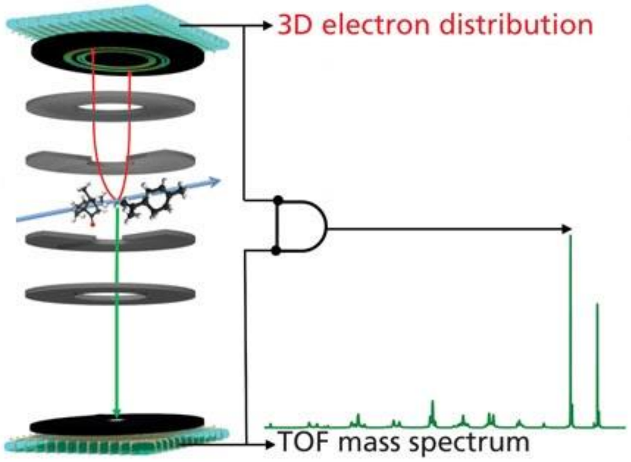

Fig. 43: A typical PEPICO experiment. Photoelectrons are detected by a VMI technique while a ToFMS is used to detect the ionic fragments. The image is taken from Ref. [80].

When the energy of the light source used in PEPICO is fixed [79, 81] the electrons can have different kinetic energies, each of which referring to a unique initial quantum energy level. If we have filtered the photoelectron spectra with respect to one mass, the kinetic energy of electrons then can be translated to the molecular structure of that mass. In several cases, the resolution of the electron kinetic energy is high enough to determine the vibrational structure of the cations as well.

Moreover, there is another version of PEPICO in which the energy of the light source is variable and only the slow electrons are detected. This kind of experiment is called threshold photoelectron photoion coincidence spectroscopy (TPEPICO) and has some advantages over the usual PEPICO experiments. For instance, the efficiency of electron collection and the energy resolution are relatively high [82]. More detailed information on this technique is provided later on in Chapter 3.

2.4. PES, PECD, and SPES

All the single-photon experiments reported in the following chapters are done in the DESIRS beamline of the SOLEIL synchrotron. In DESIRS, an undulator is producing fully variable polarized light over the energy range of 5-40 eV. The photons are passed through a gas filter (filled by Kr) followed by a monochromator to cut off the high harmonics from the undulator and optimize the flux and resolution of the beam, respectively. DELICIOUS III double imaging (i^2PEPICO) spectrometer [24], equipped with a VMI setup for electron imaging and a time of flight Wiley and McLaren mass spectrometer for coincidence ion imaging, was used to record the PEPICO and PECD measurements.

Actually, DELICIOUS III is designed to acquire data in two modes. Its first mode of operation is data acquisition at fixed photon energies which is suitable for PES and PECD measurements. In this mode, for any given photon energy, the photoelectron images were recorded using the VMI technique (in coincidence mode) from which the PES and PECD spectrum could be extracted through the procedure explained in Sec. 1.2.2. For each PES/PECD measurement, the polarization of the light was switched every 15 minutes from RCP to LCP. In the end, all the images recorded by the same polarization were summed up to create the LCP and RCP images. Finally, the total image, LCP+RCP, and the differential image normalized by the total image, $\frac{\mathrm{LCP}-\mathrm{RCP}}{(\mathrm{LCP}+\mathrm{RCP})/2}$, was Abel inversed using the pBASEX algorithm to get the PES and PECD signals, respectively. As the undulator emission polarization were highly pure, $|S_3| > 97\%$, no correction for the degree of circular polarization is made (S_3 is the Stokes parameter indicating the absolute degree of circular polarization).

The second mode of operation is when a range of photon energies is being scanned. In this mode, the monochromator is changing the photon energy by step sizes as short as 5 meV and at each step a VMI image of the photoelectrons is recorded in coincidence with photoions over a short period of time, say one minute. Therefore, for each photon energy, we would have an array containing the PES vs the electron kinetic energy. Adding the PESs recorded in all the steps together in a 2D colour mapped matrix, we can make PES matrices in which every pixel is representing the intensity of the photoelectrons vs the photon energy and photoelectron kinetic energy.

A typical PES matrix is shown in Fig. 44. The diagonal structures correspond to different ionization pathways matching with the unity slope line

$$eKE = h\nu - IE_i \qquad \text{(Eq. 20)}$$

where IE_i is the ionization energy of the i^{th} state.

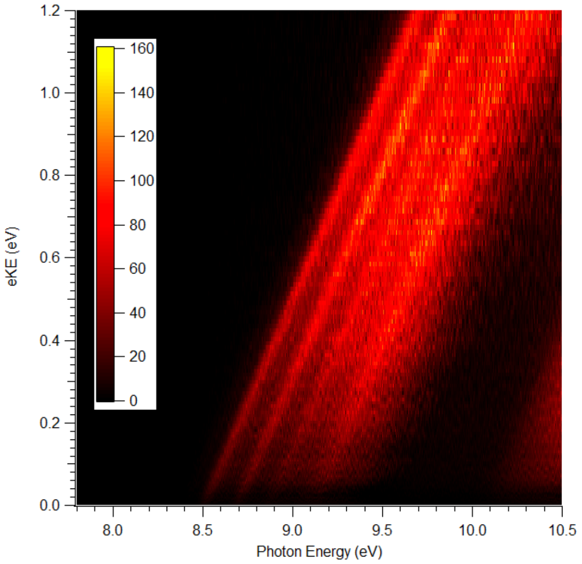

Fig. 44: A typical PES matrix composed by adding all the one dimension PES arrays recorded for any photon energy during the photon energy scan. Using a suitable colour mapping, the photoelectron intensity is presented as a function of photon energy (x-axis) and photoelectron kinetic energy (y-axis).

The information embedded in a PES matrix can be reduced in different ways. For example, one can extract the traditional PES spectrum at a given photon energy by a vertical cut at that photon energy. The other useful kind of spectrum that can be extracted from a PES matrix is the threshold photoelectron spectrum (TPES). This can be obtained by projecting the integrated values in the PES matrix up to a low eKE along the *y*-axis. The resolution of TPES is much better than that obtained in VMI-PES done at a fixed photon energy but is not perfect yet. One can improve the resolution of TPES by integrating the photoelectron intensity of PES matrices along a diagonal direction, parallel to the ionization channels. The spectrum obtained in that way is called slow photoelectron spectroscopy (SPES) which provides a better compromise between the intensity and the resolution. In practice, we can rotate the PES matrix so that the ionization channels become aligned along the *y*-axis and then do the integration in that direction. This process is shown in Fig. 45 where the better resolution and the higher intensity of SPES relative to TPES can be clearly seen. More details on PES matrices and how SPES and TPES can be extracted from them can be found elsewhere [82-84].

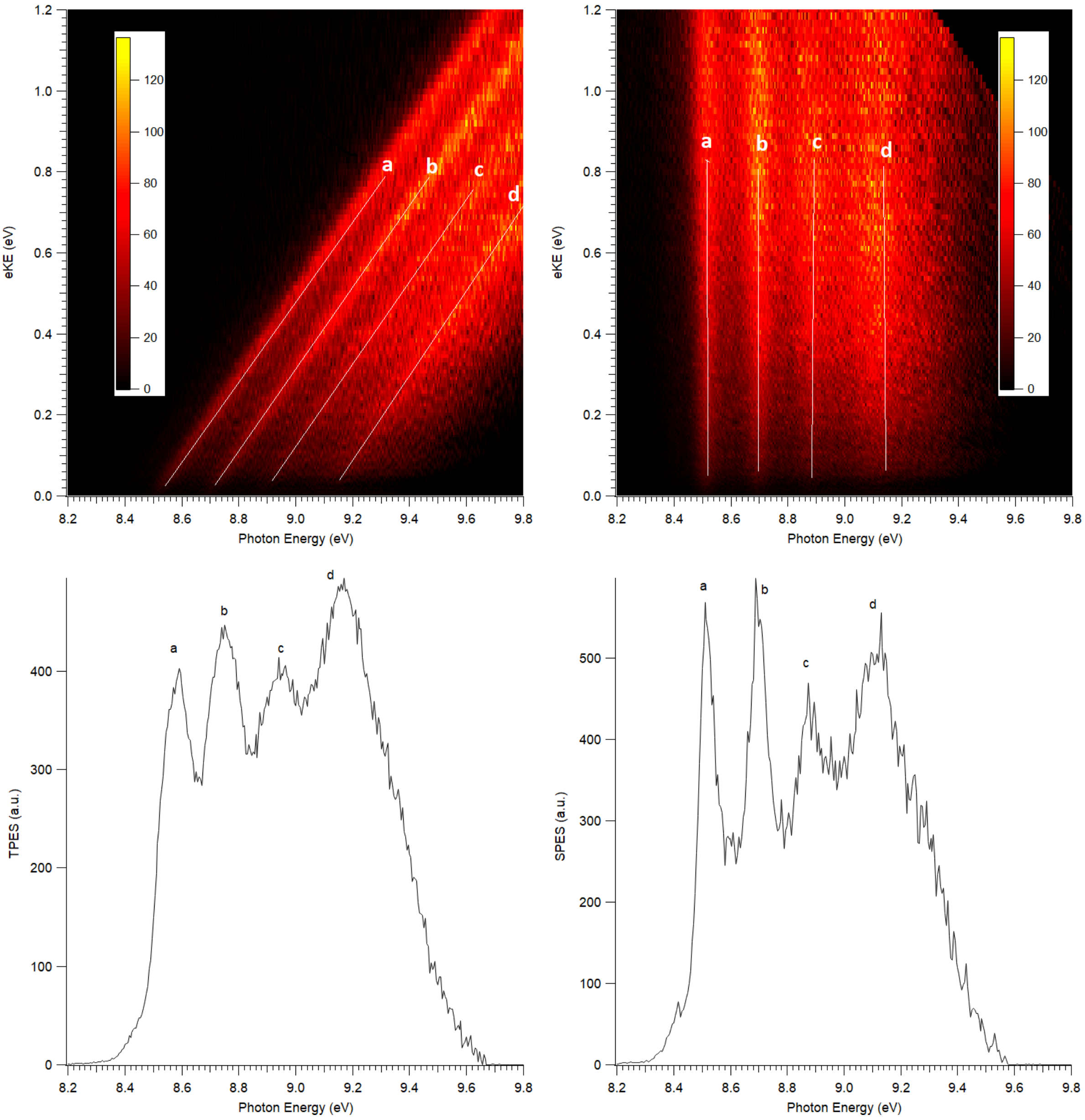

Fig. 45: TPES and SPES of limonene: top left is the normal PES matrix recorded for limonene whose integral up to eKE=100 meV along the y-axis, TPES, is presented in the bottom left; top right is the PES matrix after rotation whose integral up to eKE=100 meV along the y-axis, SPES, is presented in the bottom right. Some white lines labelled a, b, c and d are plotted on the PES matrix and its rotation to show different ionization pathways. The peaks in TPES and SPES corresponding to these channels are determined by the same labels in TPES and SPES spectra as well.

The other advantage of scan mode is that it can be used to monitor the fragmentation dynamics. As the parent cation of some of the samples may be unstable above a certain photon energy and fragments through different dissociative ionization pathways, one may be interested to know at which photon energies the parent starts to fragment and which fragmentation pathways are available. By plotting the intensity of the photoelectrons tagged with the masses appearing in ToF spectrum as a function of photon energy, one can monitor when a certain fragmentation channel is oppening; once some specific fragmentation channels are open, the intensity of the photoelectrons in coincidence with the given fragment will rise correspondingly. This kind of dynamics for the monoterpenes has been studied as well and will be reported in Chapter 3.

For each PECD measurement, the polarization of the light was switched every 15 minutes from RCP to LCP. In the end, all the images recorded by the same polarization were summed up to create the LCP and RCP images. Finally, the total image, LCP+RCP, and the differential image normalized by the total image, $\frac{\text{LCP}-\text{RCP}}{(\text{LCP}+\text{RCP})/2}$, was Abel inversed using the pBASEX algorithm to get the PES and PECD signals, respectively. As the undulator emission polarization was highly pure, $|S_3| > 97\%$, no correction for the degree of circular polarization is made (S_3 is the Stokes parameter indicating the absolute degree of circular polarization).

2.5. CMS-Xα Method

Continuum multiple scattering-Xα (CMS-Xα) method is used in Chapter 6 to calculate the PECD of α-pinene and 3-carene as a function of electron kinetic energy. CMS-Xα is a method in which the molecule is partitioned into spherical regions (region I in Fig. 46) about each atomic centre, enclosed within an outer, spherically symmetric region (region II in Fig. 46). The electrons are expected to be experiencing a radial potential in any region. Therefore, the angular part of their wave function can be expressed in terms of spherical harmonics. Applying all of the boundary conditions, the continuum wave function of ejected photoelectrons, outside and far from the molecular region (region III in Fig. 46) can be calculated. Using the photoelectron angular distribution obtained in this way, one can compute $b_1^{\{+1\}}$.

More information on the CMS-Xα method and how it can be applied to calculate the electric dipole matrix elements for a single photoionisation process, and consecutively the asymmetry parameter b1, can be found in [33, 36, 85-87]. Multiple scattering equations for the continuum electron are solved in a model potential consisting of overlapping atomic spheres (set at 0.81 of the so-called Norman atomic radius [88]) with a spherical harmonic angular basis truncated normally at l_{max}=18, 6, 3 (referring, respectively to the spherical region outside the molecule, the C atomic regions, and the H atomic regions). For the initial state, a smaller basis (l_{max}=5, 3, 1) sufficed. To verify the results, different reduction factors as well as different l_{max} values have also been tried.

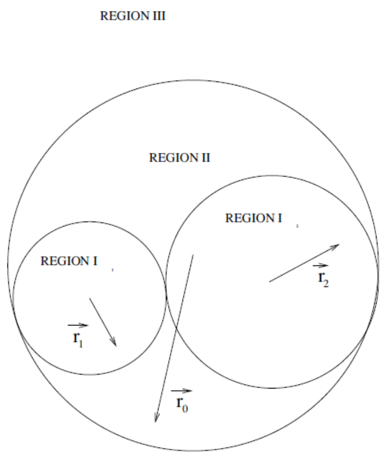

Fig. 46: Partitioning the molecular and out space into spherical regions in CMS-Xα method

2.6. FC and OVGF calculations

Two kinds of simulations were carried out for any molecule studied in this thesis: the vertical ionization energy and the FC simulation. All the calculations have performed using Gaussian 16 software [89] using Density Functional Theory (DFT) with the CAM-B3LYP being used as the functional and the aug-cc-pVDZ as the basis set. FC simulation has been performed in Chapter 3 to simulate the vibrational progression of the cation ground state, while TD-DFT calculations are used in Chapter 7 when we are studying the role of intermediate states on our PECD measurement. For the FC simulation, the geometry of neutral and the cation is optimized and then the vibrational frequencies for both of them are calculated in the harmonic approximation. The results were fed into the FC-Lab II package [90] to get the vibrational spectrum. Only transitions from the ground state of the neutral have been taken into account meaning that the hot bands are neglected here. Once a stick spectrum was obtained, a Lorentzian shaping function has been convoluted to any stick to simulate the vibration spectrum. The cut-off and FWHM of the shaping functions are selected in a way to get the best matching resolution to the experimental data. In the end, the spectrum has been scaled by a factor of 0.93 to compensate for anharmonicity.

To calculate the vertical ionization energies, the outer valence Green's function method [91] was applied using the aug-cc-pVDZ basis set. OVGF calculates the transition energies as the poles of the one electron Greens Function and is more accurate for the outer valance electrons. We have used this method in Chapter 3 to calculate the energy of the cationic excited electronic states. The geometry of the neutral optimized in the FC simulation with the same basis set was used in vertical ionization energy simulation. Like the FC simulation, the OVGF calculation has also been carried out in Gaussian16 software.

3. Near threshold PEPICO and SPES of monoterpenes

One of the main goals of this project is to introduce a new method for simultaneous chemical composition analysis in gas phase mixtures by using photoelectron spectroscopy. To achieve that goal we needed to record the SPES of the mixture and the compounds separately. In this chapter, we report the results of PEPICO and SPES experiments on five of the most interesting monoterpenes (listed below) in conjugation with some FC and OVGF calculations for all of them. The experimental data presented in this chapter (and parts of those which will be used in the following chapters) have been acquired in the DESIRS beamline of the French synchrotron, SOLEIL, in March 2016 by Prof. Ivan Powis, Prof. Laurent Nahon, and Dr. Gustavo Garcia. However, the author has analysed the complete set of the data presented here and has also done the required calculations in order to interpret the experimental results. We have already published the results in Ref. [92], but more details can be found here, particularly, in terms of the assignment of the vibrational structures. The data presented here have also been reanalysed for the purpose of standardising them for the chemical composition analysis presented in the following chapters. More details will be given in Chapter 4 when the chemical composition analysis of the gas phase mixtures are presented.

For any given monoterpene, we will first investigate the fragmentation dynamics regarding the photoionisation from the outermost occupied orbitals (HOMO and HOMO-1). For this step, the OVGF calculation plays a leading role in the interpretation of the experimental data. In the next step, the vibrationally resolved photoelectron spectrum of the monoterpenes of interest, obtained through the SPES technique, will be reported in comparison with the FC simulation. The FC simulation done by the author was crucial in this step to assign the vibrational structures observed in experimental SPES, which itself is very demanding when the vibrational effects on PECD are discussed in the following chapters.

The interesting monoterpenes to us are (+)-(1R,5R)-α-pinene, (-)-(1S,5S)-β-pinene, (+)-(4R)-limonene, (+)-(1S,6R)-3-carene and (-)-(1S,5S)-sabinene (Fig. 47), which will be called as *'standards'* or *'basis'* in the following. All the samples were obtained from Sigma-Aldrich. The enantiomer purity for α-pinene and limonene were specified to be higher than 97% but for the other samples there was no ee information. Using a two-column gas chromatography (GC^2) analysis of the samples, the ee for β-pinene and 3-carene were found to be 94% and >99%, respectively. In the case of sabinene, there was not a pure sample available at the moment; only an extract sample with a purity of >75%. The results of GC^2 on this sample showed that the sabinene chemical composition in the extract is 75.9% with the reminder being β-pinene. The ee of the sabinene compound in the extract was found to be 86.7% while for the β-pinene compound the ee was 80.3%.

All the samples were in liquid phase kept at room temperature in a bubbler through which He gas was flowed with a backing pressure of 0.5 bar. The evaporated samples, carried with He, were then expanded into vacuum through a nozzle with a diameter of 70 μm and after passing through a double skimmer arrangement, entered into the DELICIOUS III spectrometer.

The chemical structure of the monoterpenes are shown in Fig. 47. The chemical formula for all of them is $C_{10}H_{16}$. However, the monocyclic ring structure of limonene, in comparison to the bicyclic ring structure of the other monoterpenes, makes it different. Limonene is less rigid than the other four bicyclic monoterpenes, suggesting the availability of several conformers for it. The possible limonene conformers can be divided into two main groups with respect to the position of the isopropenyl tail relative to the ring. The first group includes those in which the isopropenyl tail is positioned axially relative to the ring while in the second group the tail takes an equatorial position. In each group, there are three possible conformers any of which is distinguished by a different rotation of the tail group. An extensive study on limonene shows that two of the equatorial conformers can be present in the sample (with approximately equal population) even after cooled jet expansion when the sample is originally kept at room temperature [52]. The photoelectron spectrum of the two conformers is expected to be the same, as confirmed by FC simulation, meaning that there would eventually be some uncertainties about the relative contributions of each conformer in the SPES and PECD spectra. In contrast, the other monoterpenes possess a bicyclic structure which makes them more rigid [93, 94] than limonene; as a consequence, there would be only a single conformer for any of them, which therefore reduces the uncertainties in the results.

There is also another difference between limonene and the other monoterpenes studied here. Limonene has two close-lying outer π orbitals: the 2π orbital (HOMO) which is located around the double bond in the ring and the 1π (HOMO-1) which is located at the double bond in the isopropenyl tail. We will shortly show that for limonene the X-band spans both of these orbitals while it is only the HOMO orbital which contributes to the X-band of the other monoterpenes. In fact, the PECD is a phenomenon which depends on the original orbital from which the photoelectrons are ejected. So, as the two outermost orbitals of the other monoterpenes are less overlapping over the most interesting region of the spectrum (X-band), their results will be easier to interprate.

The presence of an endo-cyclic double bound for α-pinene, limonene, and 3-carene is also another important feature providing a structure-full X-band spectrum for them. We will see how the stretching of this double bound produces distinctive vibrational progression in the spectra of these monoterpenes. In contrast, β-pinene and sabinene who lack such an endo-cyclic double bound show a structureless spectrum in terms of both experimental SPES and FC simulation.

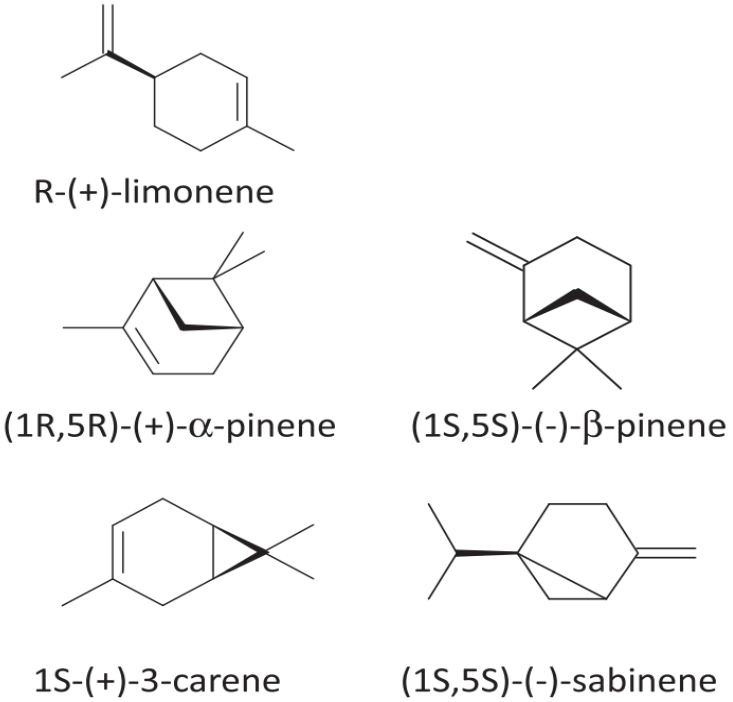

R-(+)-limonene

(1R,5R)-(+)-α-pinene

(1S,5S)-(-)-β-pinene

1S-(+)-3-carene

(1S,5S)-(-)-sabinene

Fig. 47: Chemical structure of the monoterpenes under the study; all have the chemical formula $C_{10}H_{16}$. The main difference is between the limonene and the other monoterpenes; limonene has two double bonds, one in the six-member ring and the other in the isopropenyl tail. The other four monoterpenes have only a double bond but a bicyclic ring structure suggesting more rigidity for them rather than limonene.

3.1. Results

3.1.1. α -pinene

Due to its bicyclic ring structure, α-pinene possesses only one conformer [94]. The geometrical structure of the molecule is shown in Fig. 48 (a). The HOMO orbital of the neutral is a π orbital localized around the C=C double bound, shown in Fig. 48 (b).

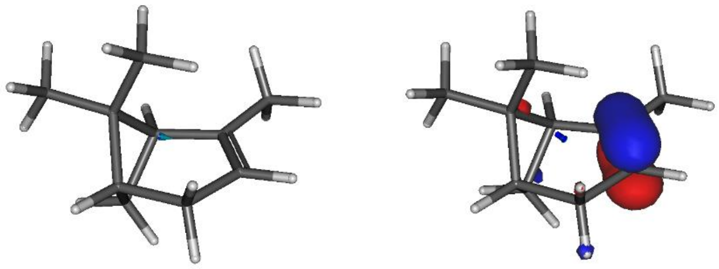

(a) (b)

Fig. 48: Geometrical structure of α-pinene (a) and HOMO orbital of the molecule. The HOMO orbital of the neutral has a π character and is mostly localized around the double bond.

The SPES scan was measured over a photon energy range from 7.8 eV to 10.5 eV with a step size of 5 meV (541 steps). In each step, a VMI image was recorded using a delay-line detector, where the Poisson statistics is assumed to govern the count rate in the image. So, the standard error for each pixel is proportional to the square root of the number of counts in that pixel. The VMI image is then Abel inverted using the pBASEX algorithm to obtain the PES at each photon energy as a function of electron kinetic energy. In pBASEX, the errors in the image pixels are propagated through the whole process to generate the error bars of the output PES. Finally, all the 2D PESs (with their associated errors) are put alongside together to make the PES matrix. In a typical PES matrix, the x- and y-axes represent the photon energy and the electron kinetic energy, respectively. PES matrices need to be rotated and projected onto the x-axis to obtain the SPES as a function of photon energy (for more details see Sec. 2.4). The errors in the PES matrix are propagated through the rotation and projection processes to obtain the final error bars for each data point in the SPES. Briefly, the whole range SPES consist of 541 data points of the form (x, y), where x values are the photon energies and y values are the intensity of the slow photoelectron with the errors calculated through the abovementioned process. The data points are simply linked together with a line to make a spectrum.

Fig. 49 shows the experimental SPES of α-pinene without tagging any mass to the photoelectrons. The results of our OVGF calculation are also plotted in this figure to see where the first transition, expectedly a π-π transition, lies and how much higher in energy the next transition is. Based on the results of the OVGF calculation, the first band expanding from 8.16 eV to 9.0 eV is, therefore, the X-band of the molecule corresponding to the projection of the electronic ground state of the neutral into the electronic ground state of the cation.

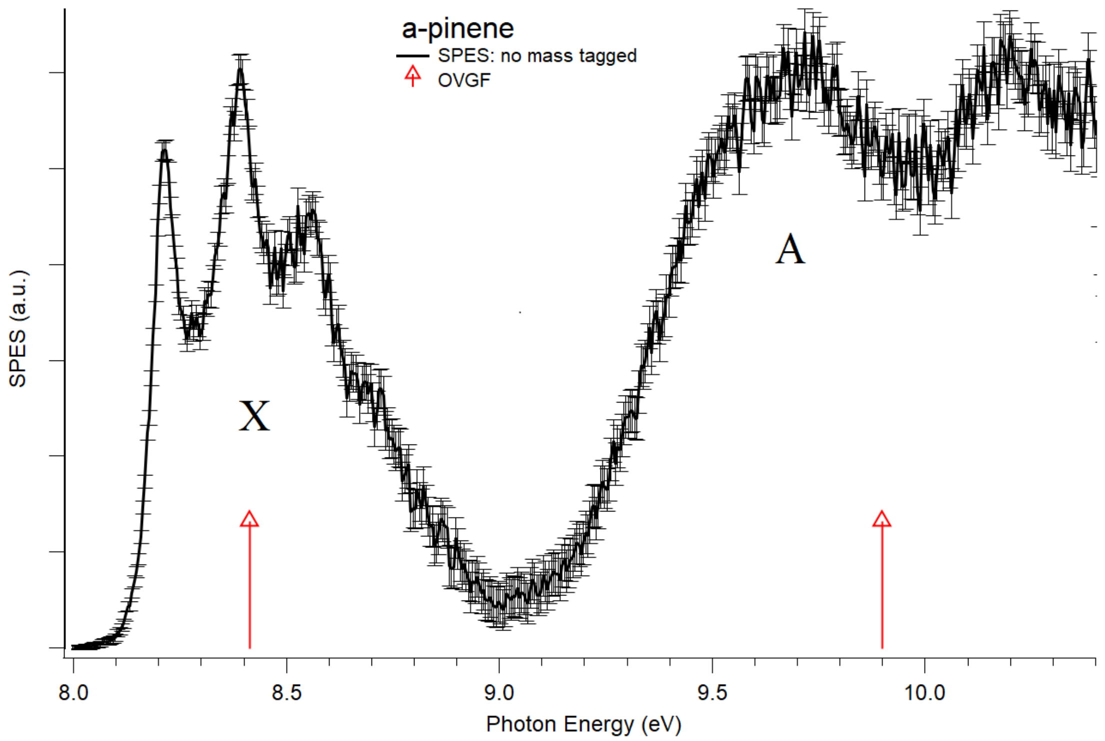

Fig. 49: The high resolution SPES of α-pinene with no mass tagged, the black curve. The maximum eKE considered to get this spectrum was 100 meV. The red arrows are the results of OVGF calculation and show the vertical ionization energies.

The cation state over the X-band region is stable and does not dissociate. However, as we enter into the next band, which is corresponding to the first excited state of the cation, a huge amount of fragmentation can be seen. This fact can be clearly seen in Fig. 50 where the mass-selected total ion yield spectrum is plotted. The fragmentation appears about photon energy of 8.98 eV which is where the X-band ends up and the next band starts. The main fragment is m/z 93 whose abundance overtakes the abundance of the parent ions at 10.18 eV.

The drops in the signal at 8.84 eV, 10.31 eV, and 10.39 eV are due to the shut down of the synchrotron radiation. However, the drop in the signal at 10.03 eV is real and is due to the absorption line of the Krypton gas in the gas filter. This absorption line is useful as it is used to calibrate the x-axis.

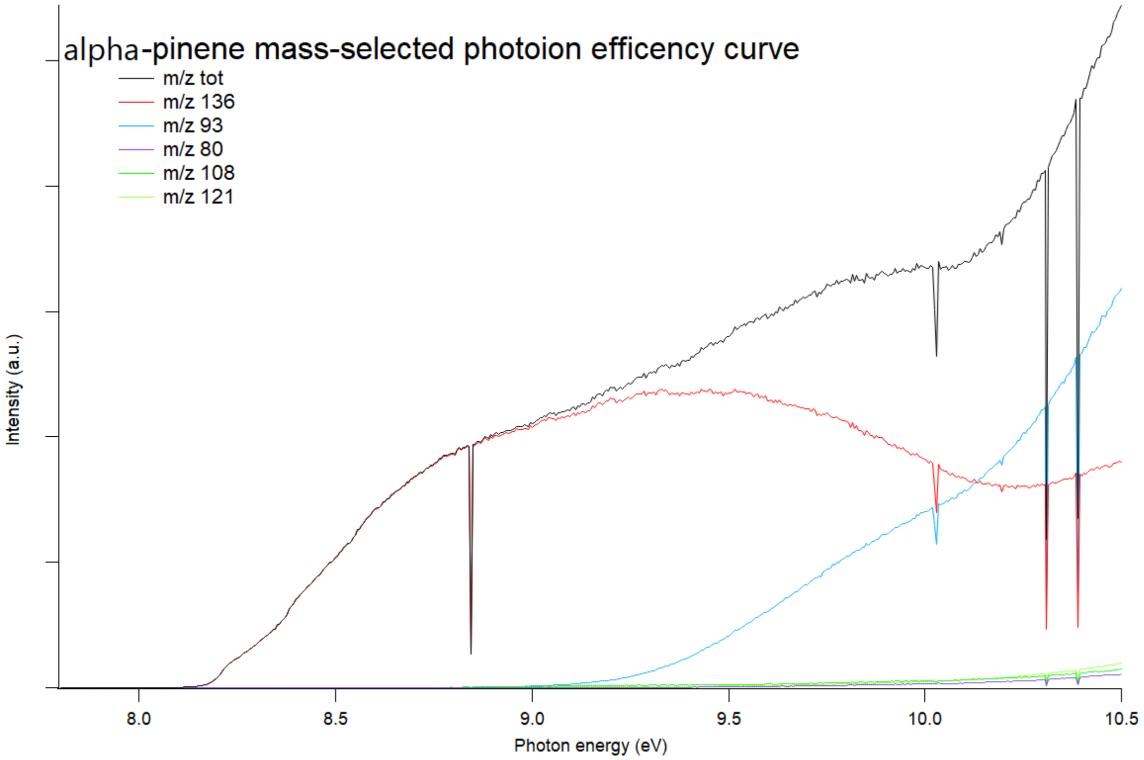

Fig. 50: Mass-selected photoion efficiency curve of α-pinene. The threshold of fragmentation is around 8.98 eV with the main fragmentat being m/z 93.

The ToF spectrum of α-pinene recorded during the scan is presented in Fig. 51 (d). It confirms m/z 93 as the main fragment appearing at higher photon energies. Included in Fig. 51 is also the PES matrix of the total photoelectrons (no mass selection) obtained in coincidence with the parent and the main fragment mass (m/z 136 and m/z 93), respectively. As can be clearly seen, the total PES matrix is composed of two main parts. The first part includes the photoelectrons generated from the ionisation of the parent (before the photodissociation process) while the other part is mostly the photoelectrons generated by ionising the main fragment, m/z 93, (produced after the parent has fragmented). These two parts are well separated from each other with a dark area (see Fig. 51 (a)) which corresponds to the gap between the X and the next band in the spectrum.

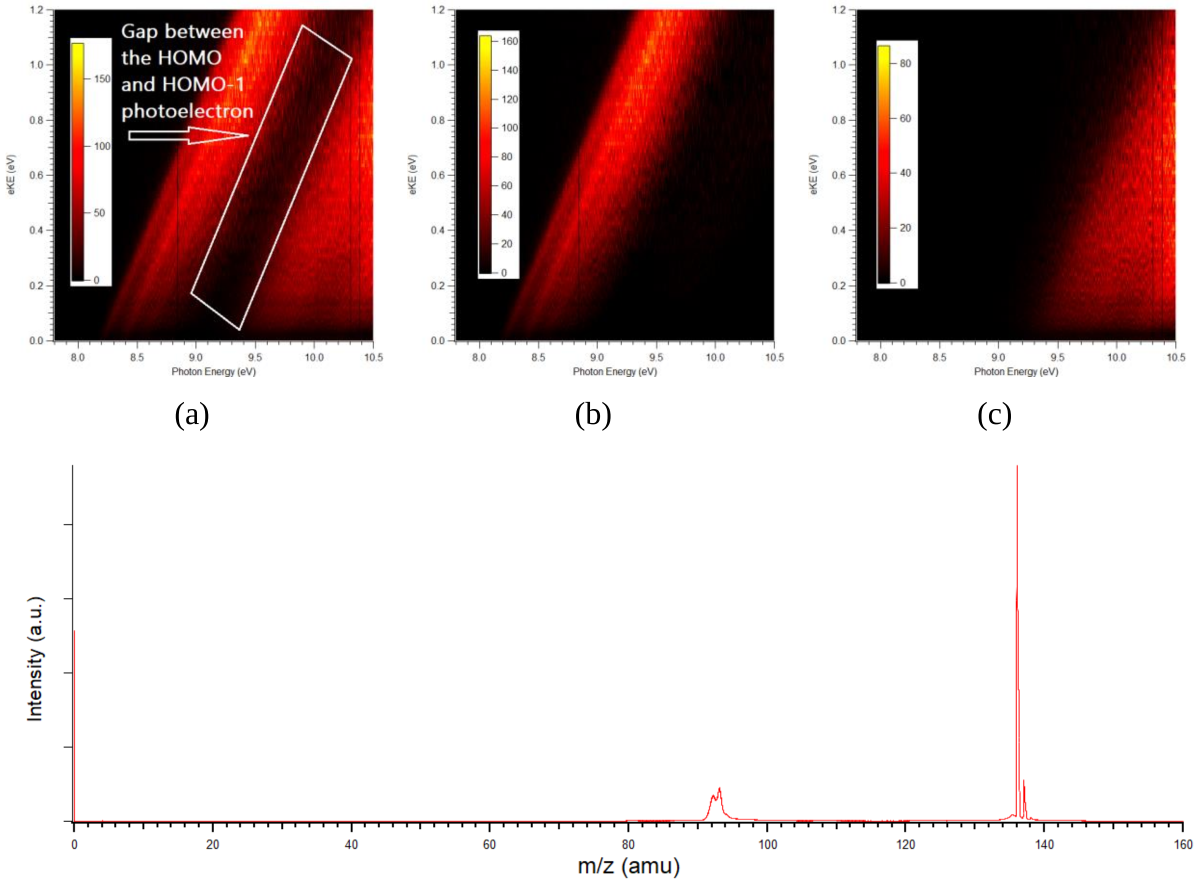

(a) (b) (c)

(d)

Fig. 51: The PES matrix of α-pinene without mass selection (a), tagged with m/z 136 (b) and tagged with m/z 93 (c). The ToF mass spectrum (d) recorded during the scan shows m/z 93 as the dominant fragment.

Fig. 52 shows the mass-selected SPES for the parent and different fragments appearing in the α-pinene scan. Photoelectron energies up to 100 meV have been taken into account to obtain the spectra presented in this figure. The IP of α-pinene is measured to be 8.16 eV in a reasonable agreement with Ref. [95]. The point is that the parent's spectrum falls down to zero around 9.0 eV, which is again an indication of the high dissociation rate for the parent ions above this energy. The other fragments appearing in the scan are m/z=80, 108, 121. These all together contribute to less than 10% of the total fragmentation over the scan energy range measured here.

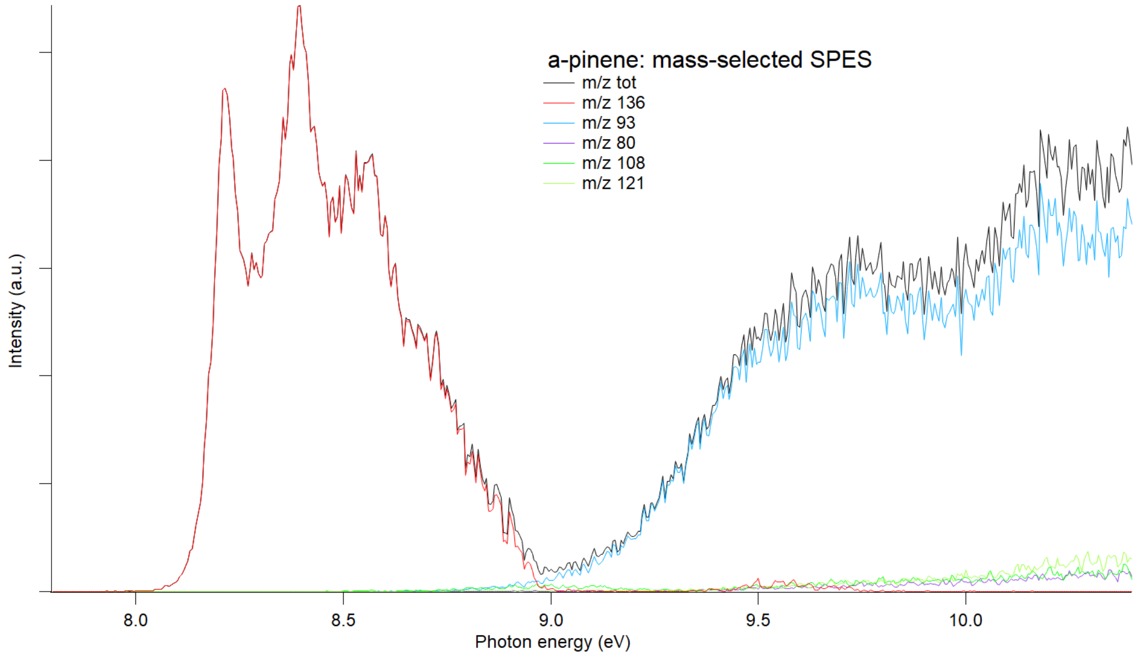

Fig. 52: Mass-selected SPES of the parent and fragments in the α-pinene scan. Fragment m/z 93 is the dominant one above 8.98 eV; however, there are also fragments m/z=80, 108, 121 present in the scan.

We now turn to a more detailed look at the SPES spectrum of the parent. To investigate the identity of different peaks in the X-band region, the most interesting region for us, we have done the FC simulation for neutral to cation transition with the results presented in Fig. 53. After obtaining the stick spectrum, a Lorentzian function has been convoluted with the stick transitions to simulate the spectrum. The cut-off and FWHM of the Lorentzian functions have been set as 1500 cm^{-1}, and 400 cm^{-1} respectively. The SPES of the parent up to photoelectron energy of 100 meV is also plotted on top of the simulation results to show how well the FC simulation matches the experimental results. α-pinene is composed of 26 atoms indicating 72 normal vibration modes for it (number of normal modes=3N-6, where N is the number of the atoms). The frequency of the different normal modes of the neutral and cation ground state, computed using the DFT method with the CAM-B3LYP as the functional and aug-cc-pVDZ as the basis set, are presented in Table 2. Transitions between the vibrational ground state of the neutral into the first and 56th vibrational modes of the cation states make the most outstanding structures in the FC simulation.

Table 2: The calculated frequencies of the vibrational normal modes of the neutral and cation of α-pinene calculated at the CAM-B3LYP aug-cc-pVDZ basis. There are 72 normal modes from which the most interesting ones are mode number one and mode number 56. The transition between the vibrationally ground state of the neutral into the first and 56th modes of the cation makes the most remarkable structures in the FC simulation. See Fig. 53 as well.

normal mode	Frequency (cm^{-1})			normal mode	Frequency (cm^{-1})			normal mode	Frequency (cm^{-1})	
	Neutral	Cation			Neutral	Cation			Neutral	Cation
1	124.39	65.78		25	974.91	962.95		49	1472.29	1443.2
2	175.28	104.09		26	987.93	979.64		50	1474.52	1461.34
3	195.73	182.44		27	1020.13	995.18		51	1477.74	1464.07
4	206.54	191.11		28	1037.4	1006.63		52	1484.12	1474.84
5	227	217.02		29	1062.74	1020.08		53	1492.04	1494.73
6	265.5	240.09		30	1073.34	1051.39		54	1506.42	1497.72
7	310.01	314.08		31	1083.14	1066.04		55	1511.95	1517.99
8	339.64	322.63		32	1113.43	1082.7		56	1761.89	1567.23
9	392.42	385.53		33	1135.26	1120.98		57	3034.55	3012.75
10	401.5	398.91		34	1157.82	1131.81		58	3036.36	3037.16
11	433.16	426.46		35	1197.38	1166.61		59	3045.57	3050.39
12	471.61	451.38		36	1213.8	1206.59		60	3052.47	3061.75
13	492.35	484.07		37	1242.58	1239.64		61	3063.48	3068.05
14	582.26	538.33		38	1258.37	1249.47		62	3080.15	3090.77
15	634.6	586.83		39	1262.37	1262.43		63	3088.14	3116.05
16	685.45	634.23		40	1281.59	1285.87		64	3091.01	3134.04
17	795.2	698.47		41	1315.68	1300.17		65	3102.17	3136.04
18	810.53	731.93		42	1347.86	1349.78		66	3104.86	3138.08
19	843.88	816.75		43	1370.44	1364.03		67	3113.82	3140.84
20	871.65	865.19		44	1379.1	1375.27		68	3136.16	3152.75
21	913.54	875.45		45	1402.35	1401.07		69	3145.02	3169.21
22	932.34	918.74		46	1412.68	1413.82		70	3162.68	3177.81
23	953.83	935.28		47	1416.6	1427.18		71	3165.91	3200.43
24	960.68	951.06		48	1462.87	1438		72	3179.54	3204.95

The first peak in the spectrum shown in Fig. 53, peak a, includes different vibrational levels of the first normal mode. In terms of the stick spectrum, there are three major sticks contributing to peak a. The lowest energetic one is the 0-0 transition, the transition between the vibrational ground state of the neutral into that of the cation. The second and the third transitions in that region are between the ground state of the neutral and the first vibrational mode, ν1, with respectively one and two quanta excitations. The second peak in the spectrum, peak b in Fig. 53, is exactly composed of the same transitions mentioned for peak a, but in combination with one quanta excitation of the normal mode number 56. Similarly, peak c and d are the same but for higher excitation levels of normal mode 56. In other words, major peaks in the X-band, are mainly the vibrational progression of the first normal mode modulated on to the vibrational progression of mode 56.

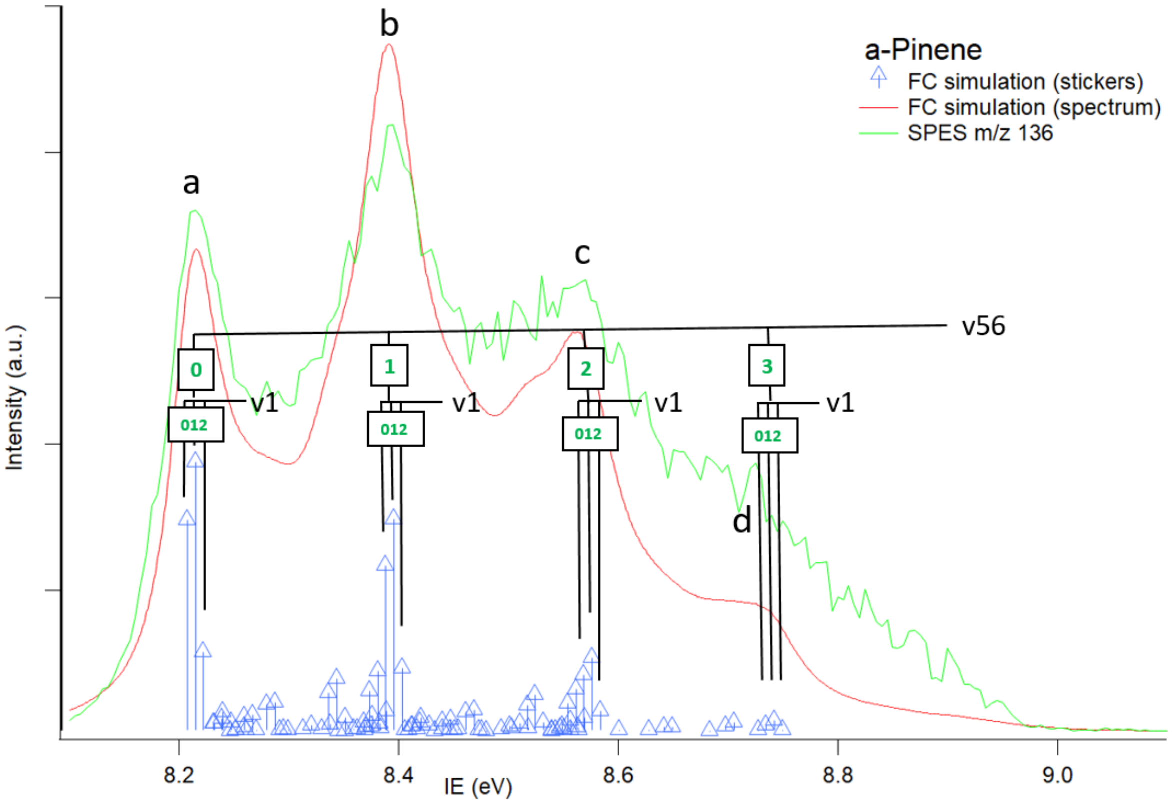

Fig. 53: SPES spectrum of the parent over the X-band (green curve) together with the results of the FC simulation. The blue sticks are showing the FC factors for transitions from the vibrationless state of the neutral, from which only 100 of the most dominant transitions are plotted here. The red solid curve is the simulated FC spectrum obtained by convoluting a Lorentzian shaping function (cutoff=1500 cm^{-1} and FWHM=400 cm^{-1}) to any of the sticks. Peak a is almost a vibrational progression of the firs normal mode while the subsequent peaks in the SPES can be attributed to the vibrational progression of the normal mode v1 modulated on the vibrational progression of the normal mode v56.

Normal mode 1 of the cation can be attributed to the ring bending, while normal mode 56 is mostly the double bound stretching. Included in Fig. 54 is the displacement of different atoms in α-pinene with respect to each other in these two modes. The direction and the length of the arrows represents the direction and the amplitude of the vibrations, respectively. Atoms indexed as 0 and 1 in this figure are the carbons of the double bond. For normal mode 56, as the arrows show, the displacement of these two carbons causes the stretching of the double bond in the ring. In normal mode 1, the ring bends and the methyl groups attached to two sides of the molecule get closer to each other.

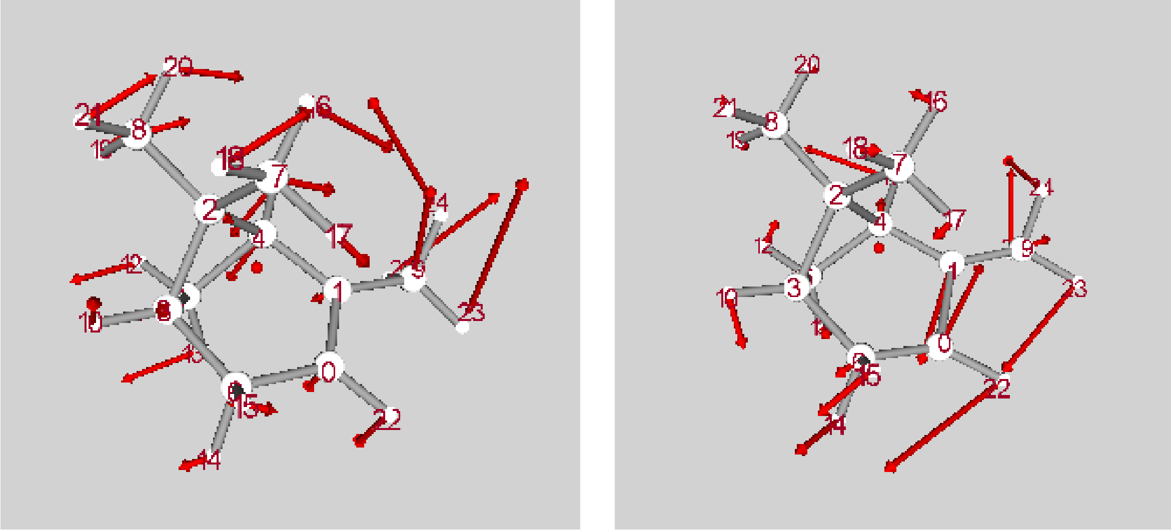

(a) (b)

Fig. 54: Normal modes 1st (a) and 56th (b) of α-pinene cation. The length and the direction of the red arrows are respectively showing the amplitude and the direction of any displacement of atoms within the molecule. The 1st mode is ring bending while the 56th mode is double bound stretching (see the main text).

3.1.2. 3-carene

Similar to α-pinene, 3-carene has also a rigid bicyclic ring structure, giving a single conformer. The geometrical structure of 3-carene is shown in Fig. 55 (a). The HOMO orbital of the neutral is also shown in Fig. 55 (b) and corresponds to a π orbital located around the double bond in the main ring.

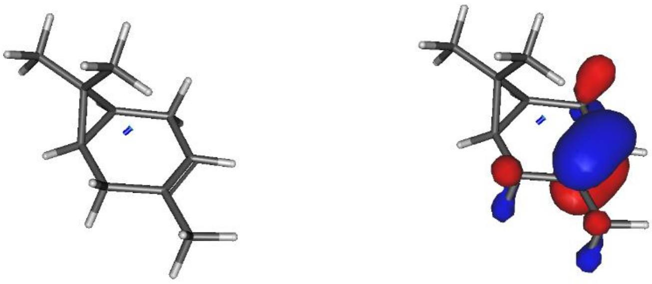

(a) (b)

Fig. 55: Geometrical structure of 3-carene (a) and HOMO orbital of the molecule. The HOMO orbital of the neutral has a π character and is mostly localized around the double bond.

The experimental SPES of 3-carene without tagging any mass to the photoelectrons is plotted on top of the OVGF calculation for this molecule in Fig. 56. The maximum kinetic energy of photoelectrons to get the SPES spectrum is 100 meV. Unlike α-pinene, the next vertical ionization energy calculated via the OVGF method are close to the origin transition. In the α-pinene case, the next transition was predicted to be 1.5 eV above the origin, and confirmed by the experimental SPES of α-pinene where the X-band was well separated from the next band.

However, the next transitions for 3-carene are closer to the origin with a gap of 1.13 eV. Actually, as can be seen from the SPES shown in Fig. 56, the X- and A- band are overlapping and the intensity does not fall down to zero over the 9.0-9.5 eV region.

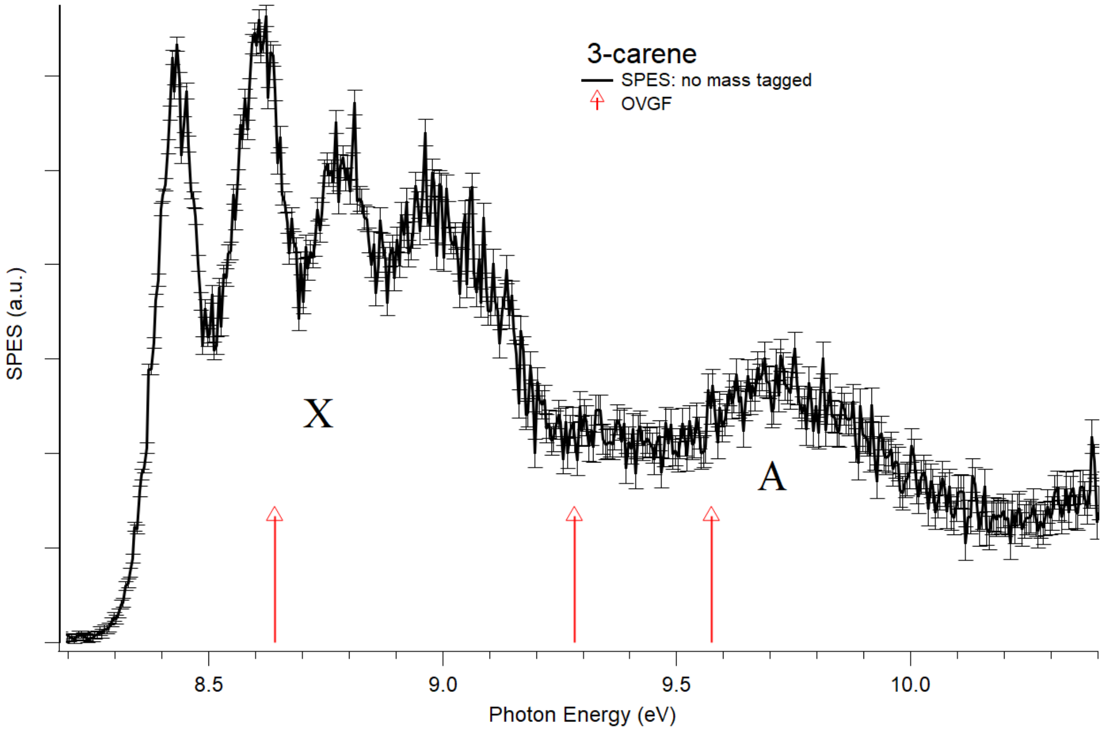

Fig. 56: The high resolution SPES of 3-carene with no mass tagged, the black curve. The maximum eKE considered to get this spectrum was 100 meV. The red arrows are the results of OVGF calculation and show the vertical ionization energies.

Above 9.0 eV, at the edge of the X-band where the A-band is beginning, the cation starts to fragment. The main fragment is m/z 93, with small amounts of m/z 80 and 121 as well. Included in Fig. 57 is the mass tagged total ion yield curves for the parent and the fragments. In comparison to α-pinene for which the abundance of fragment m/z 93 was overtaking the abundance of the parent ions, we can say that fragmentation of the 3-carene cations is less. Actually, through the whole range of the scan, the parent remains the most dominant species despite decay due to fragmentation.

The PES matrix with no mass tagging of the photoelectrons as well as the PES matrices in coincidence with m/z 93 and 136 are presented in Fig. 58. It can be seen that the total PES matrix is roughly the sum of the other two matrices as they are the most dominant species in the ToF mass spectrum. It is interesting that the photoelectrons in coincidence with the fragments are all lying above the onset of the A-band ionization channel and also that there is only a small amount of photoelectrons coming from the parent ions over that region. This means that the excited cations of the parent are highly dissociative.

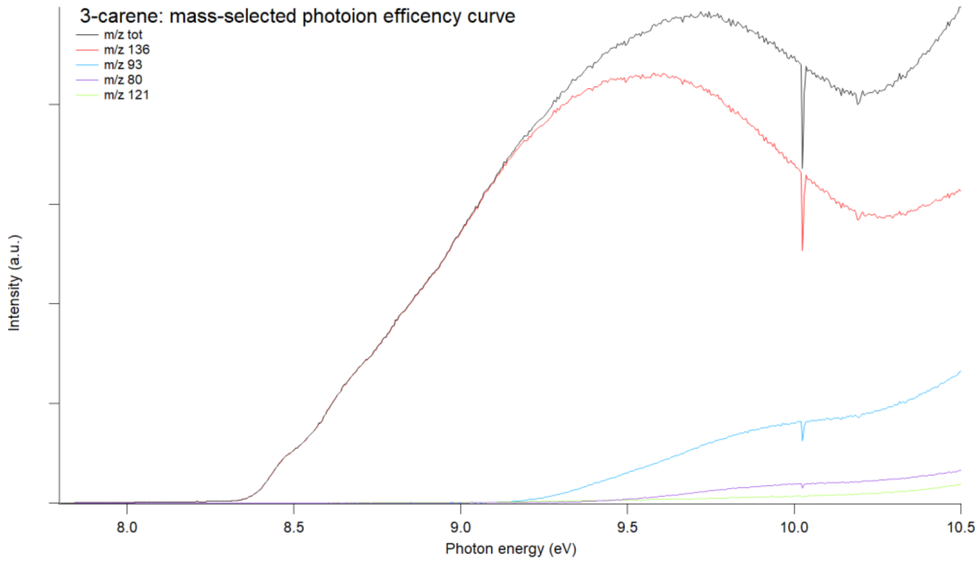

Fig. 57: mass-selected photoion efficiency curve of 3-carene. The thresholds of fragmentation are around 9.05 eV with the main fragmentation being m/z 93. The drop happening for all the species at 10.03 eV is due to the Kr absorption line in the gas filter, which can be used in monochromator calibration.

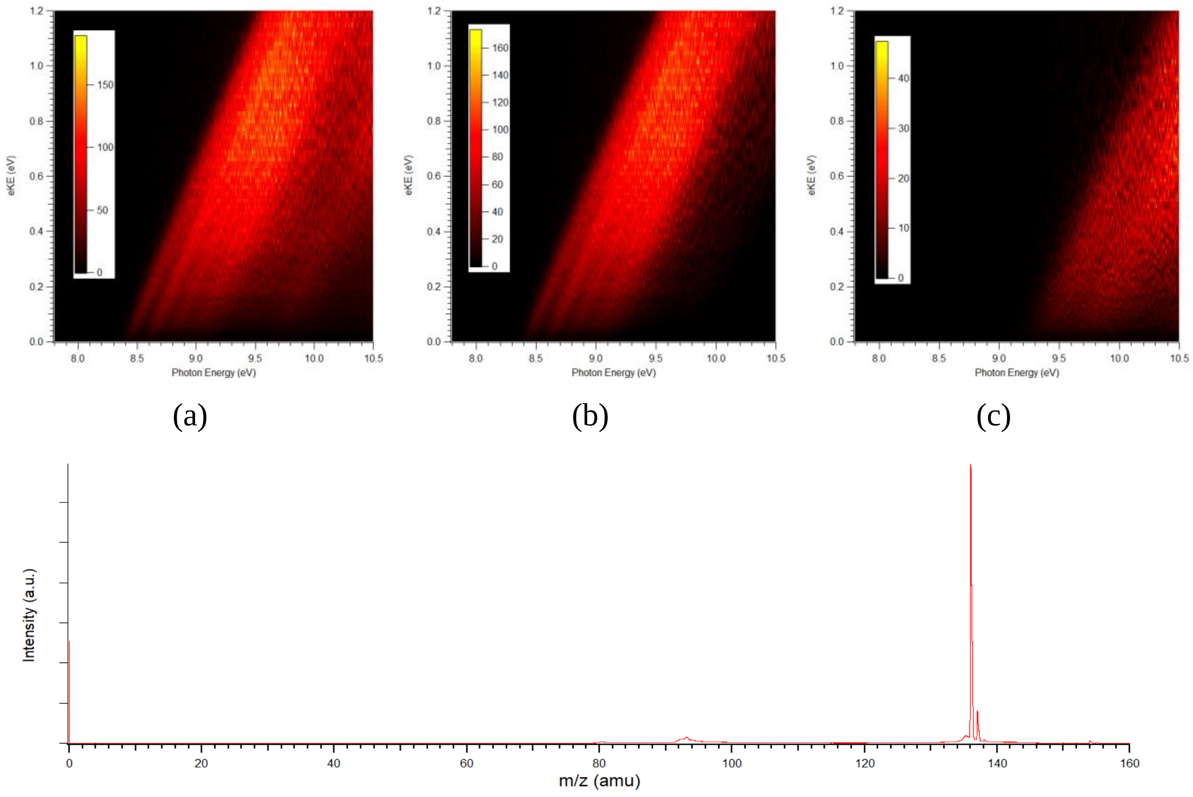

(a)

(b)

(c)

(d)

Fig. 58: The PES matrix of 3-carene without mass selection (a), tagged with m/z 136 (b), and tagged with m/z 93 (c).The ToF mass spectrum (d) recorded during the scan is showing m/z 93 as the dominant fragment.

To see more details, we have extracted the mass-selected SPES of any species present in the ToF mass spectrum as well as the SPES of the total photoelectrons, plotted in Fig. 59. The IP of 3-carene is recognised to be 8.38 eV. Similar to α-pinene, the 3-carene parent has four major vibrational structures; however, in this case, the fourth peak is not as stable as it was for α-pinene. In fact, for 3-carene, fragmentation is starting from the middle of the fourth peak. There are two possible explanations for this: fragmentation might simply be due to instability in the cation ground state over this region or it can be the cause of entering into the A-band region. The latter is particularly plausible if we look at the results of the OVGF calculation again, included in Fig. 56. The OVGF calculation predicts the onset of the second ionization channel very close to the fragmentation threshold we see here. If we assume the second option to be true (or more possible), some part of the parent SPES above 9.05 eV can be attributed to the excited cation states. In other words, the fourth peak in the parent's SPES is where the ground and the first excited state of the cation overlap. We will shortly see how this argument makes sense when we do the FC calculation for the ground state of the cation.

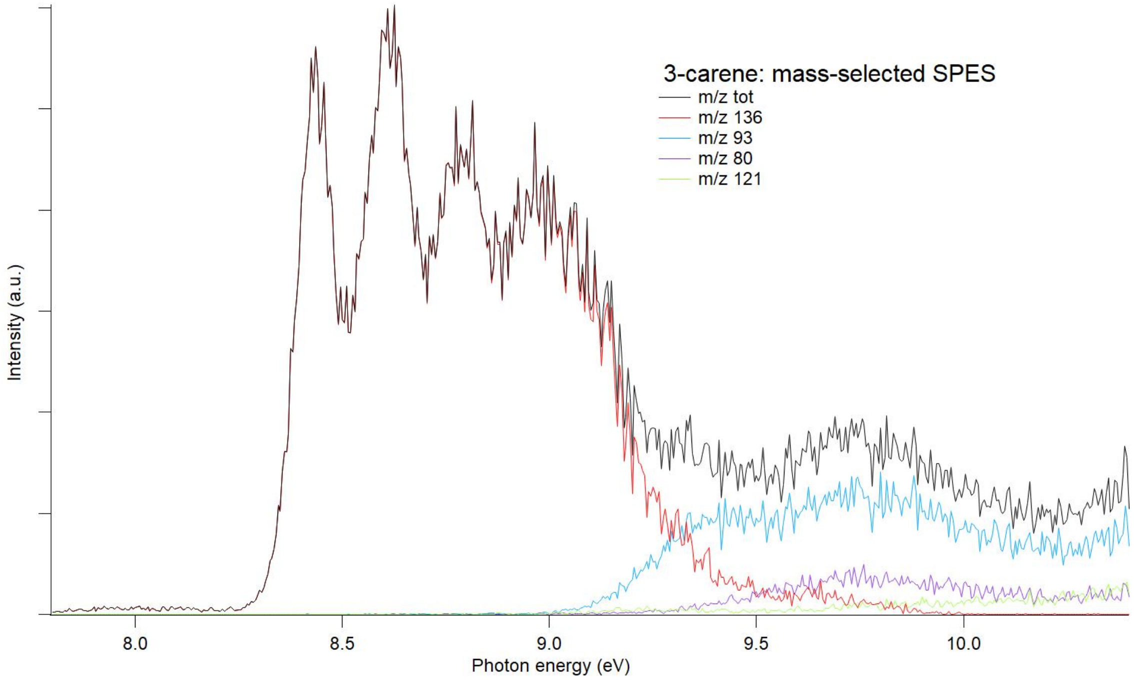

Fig. 59: mass-selected SPES of the parent and fragments present in the 3-carene scan. m/z 93 is the dominant fragment, however, there are some other fragments like m/z 80 and m/z 121 present in the scan.

To obtain more information on the identity of the different peaks in the X-band, FC simulations for the transition were performed between the electronically ground state of the neutral and that of the cation. To this aim, the geometry optimization and frequency calculations of the neutral and the cation have been done using the DFT method with the CAM-B3LYP as the functional and aug-cc-pVDZ as the basis set, in Gaussian 16. The output files were fed to the FC lab II to calculate the FC factors as a stick diagram. A Lorentzian shape function, cut off=1500^{-1} cm and FWHM=400 cm^{-1}, was convoluted to any stick to get the FC spectrum. In this calculation, the hot integrals (FC factors from vibrationally excited states of the neutral) are ignored and only the transitions from the vibrationless state of the neutral are taken into account.

3-carene is composed of 26 atoms giving 72 vibrational normal modes for the molecule. A list of these normal modes and their frequencies for the neutral and the cation can be seen in Table 3. Only transitions from the vibrationless state of the neutral are considered into account. The most important cation's normal modes involved in the transitions are highlighted in the table.

Table 3: The calculated frequency of vibrational normal modes of the neutral and cation of 3-carene calculated using basis set aug-cc-pVDZ. There are 72 normal modes from which the most interesting ones are v1, v2, v3, v56, v60, and v65. The transition between the vibrationless state of the neutral into these modes of the cation makes the most remarkable structures in the FC simulation. See Fig. 61 as well.

normal mode	Frequency (cm^{-1})			normal mode	Frequency (cm^{-1})			normal mode	Frequency (cm^{-1})	
	Neutral	Cation			Neutral	Cation			Neutral	Cation
1	78.25	75.06		25	977.05	964.38		49	1473.78	1455.84
2	160.59	114.96		26	1001.71	982.07		50	1475.6	1463.54
3	184.85	153.41		27	1022.15	987.7		51	1479.93	1468.38
4	193.9	169.47		28	1032.43	1003.45		52	1481.66	1474.48
5	208.44	187.56		29	1060.08	1023.77		53	1483.49	1480.09
6	235.73	214.83		30	1068.99	1048.36		54	1495.28	1484.03
7	254.92	232.75		31	1104.29	1088.98		55	1522.99	1507.58
8	273.2	268.66		32	1128.19	1109.92		56	1785.4	1600.28
9	342.13	348.23		33	1174.52	1135.5		57	3017.16	2959.02
10	354.97	355.27		34	1186.2	1151.04		58	3023.31	2983.5
11	414.14	387.68		35	1196.02	1170.83		59	3037.41	2999.08
12	433.24	416.56		36	1239.16	1196.15		60	3037.77	3021.5
13	466.19	457.9		37	1248.03	1210.86		61	3047.8	3035.67
14	514.43	502.57		38	1254.95	1237.77		62	3056.73	3041.02
15	580.41	590.09		39	1333.48	1320.6		63	3061.84	3061.32
16	700.49	655.27		40	1348.29	1340.75		64	3090.95	3104.9
17	735.9	699.04		41	1370.1	1349.68		65	3101.03	3111.33
18	786.34	740.76		42	1394.34	1368.83		66	3104.45	3134.08
19	808.62	764.71		43	1405.33	1376		67	3123.53	3137.26
20	842.54	807.75		44	1413.08	1380.76		68	3138.68	3146.09
21	923.54	845.72		45	1420.83	1401.56		69	3152.76	3172.72
22	942.76	876.11		46	1425.51	1414.89		70	3157.05	3194.89
23	958.63	911.5		47	1464.04	1420.84		71	3164.89	3196.84
24	969.04	930.97		48	1468.59	1432.63		72	3168.07	3202.41

To assign the different peaks in the SPES to different excitations, let's firstly just focus on the first peak around 8.43 eV. Included in Fig. 60 is the SPES around this peak plotted together with the FC simulation. Here, only the most dominant sticks are plotted for the clarity and the sticks with the oscillation strength of less than 1% of the most dominant transition are ignored. A label (νx y) is used to show the identity of the transitions, where νx stands for the normal mode number x, and y indicates the level of excitation in that mode. As we can see, the first peak is composed of the origin transition plus a combination of zero or one single quanta excitation of the first three normal modes (ν1, ν2, ν3).

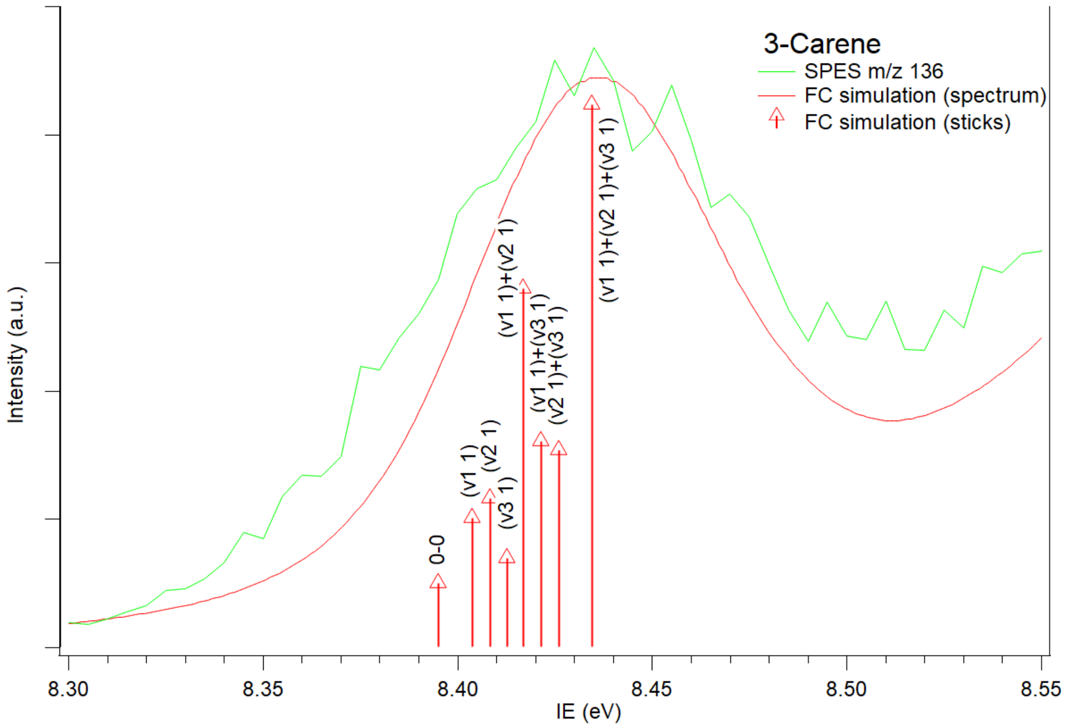

Fig. 60: SPES spectrum of 3-carene (m/z 136) over the first peak in the X-band (green curve) together with the results of the FC simulation. The red sticks are showing the FC factors for transitions from the vibrationless state of the neutral, from which only the most dominant sticks are plotted for the clarity and the sticks with the oscillation strength of less than 1% of the most dominant transition are ignored. The red solid curve is the simulated FC spectrum obtained by convoluting a Lorentzian shaping function (cutoff=1500 cm^{-1} and FWHM=400 cm^{-1}) to any of the sticks. This peak is composed of the origin transition plus a combination of zero or one single quanta excitation of the first three normal modes (v1, v2, v3). A label (νx y) is used to show the identity of the transitions, where vx is standing for the normal mode number x, and y is indicating the level of excitation in that mode.

We call the group of transitions shown in Fig. 60 'pack A'. The other peaks in the 3-carene SPES are mainly composed of pack A plus a combination of zero or single quanta excitation of modes ν56, ν60 and ν65. The peaks around 8.6 eV and 8.68 eV include the same transitions as pack A in addition to a single quanta excitation in modes ν56 and ν60, respectively. One quanta excitation of normal modes ν50 and ν60 are contributing to the next peak at 8.95 eV. Finally, the last peak in our simulation region, at 9.13 eV, is again composed of pack A together with one quanta excitation of normal modes ν60 and ν65. Fig. 61 can help to get a better sense of what is going on with the vibrational levels in the cation state. In this figure, only the most dominant 1000 sticks are plotted.

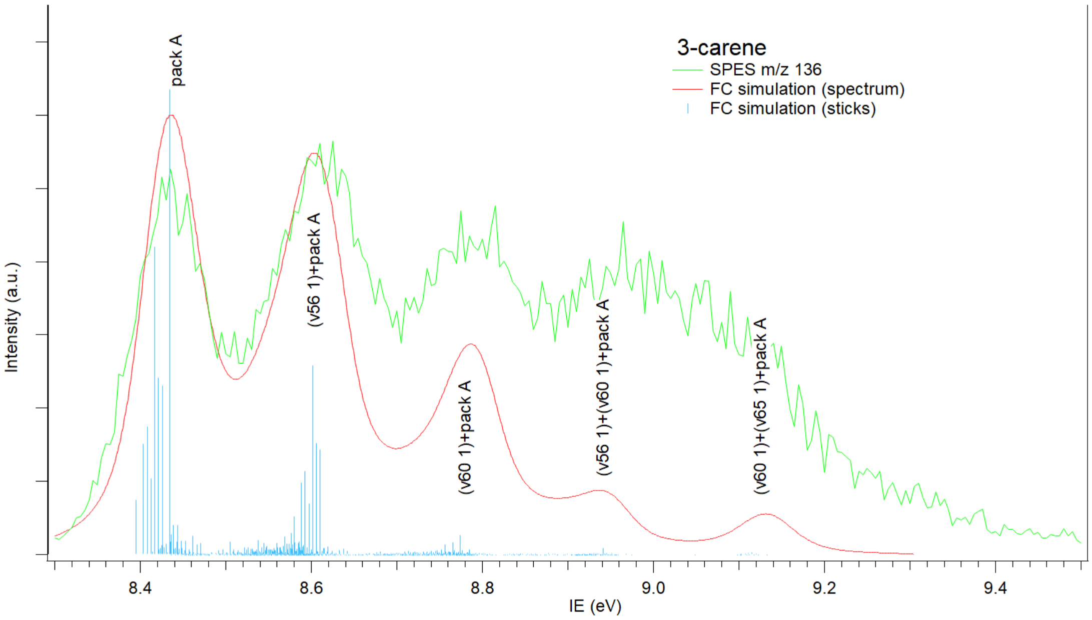

Fig. 61: SPES spectrum of 3-carene (m/z 136) over the X-band (green curve) together with the results of the FC simulation. The blue sticks are showing the FC factors for transitions from the vibrationless state of the neutral, from which only 1000 of the most dominant transitions are plotted here. The red solid curve is the simulated FC spectrum obtained by convoluting a Lorentzian shaping function (cutoff=1500 cm^{-1} and FWHM=400 cm^{-1}) to any of the sticks. For more information see the text.

The FC simulation matches the experimental SPES well for the first three peaks over the region IE=8.3-8.9 eV but fails to reproduce the rest of the spectrum very well. In fact, the discrepancy between the SPES spectrum and the simulation appears around the same energy that 3-carene starts to fragment. We also discussed this position in the energy axis to be potentially where the ionization channel to the first electronically excited state of the cation opens. Now, we can say that the peaks in the SPES, above 9.0 eV, are perhaps due to the vibrational structures of the first excited electronic state of the cation and this is why our FC calculation cannot simulate that region very well. Actually, in our FC simulation, we only have taken the transitions between the neutral and the ground state of the cation into account. So, doing a time-dependent density functional theory (TD-DFT) calculation in conjugation with FC simulation can be helpful to clarify the situation.

The normal modes ν1 and ν56 are more or less the same vibrational motions as they were for the α-pinene; ν1 is a ring bending mode while ν56 is the double bound stretching mode. Normal modes ν2 and ν3 are mainly due to the rotation of the methyl group attached to the main ring and the main ring torsion, respectively. Symmetric and antisymmetric stretching of the methyl group attached to the main ring is almost what contribute respectively to the normal modes ν60 and ν65. Fig. 62 shows the direction and the amplitude of the displacements involved in these key modes.

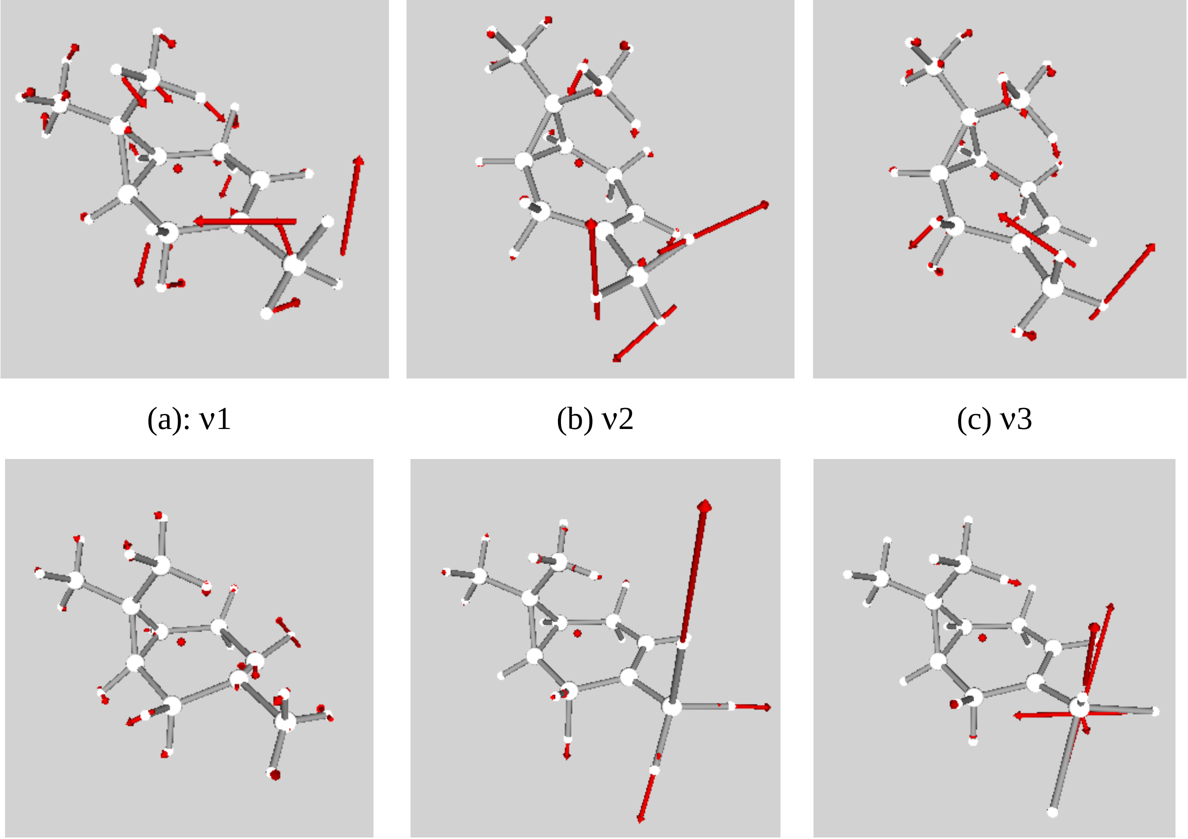

(a): ν1 (b) ν2 (c) ν3

(d) ν56 (e) ν60 (f) ν65

Fig. 62: Normal vibrational modes ν1 (a), ν2 (b), ν3 (c), ν56 (d), ν60 (e) and ν65 (f) of the 3-carene in the cation state. The length and the direction of the red arrows are respectively showing the amplitude and the direction of any displacement of atoms within the molecule.

3.1.3. Limonene

Previously, we mentioned that limonene has a less rigid structure than the bicyclic monoterpenes. The other difference between limonene and the other monoterpenes is that the limonene molecule possesses an extra double bond located on its tail. The HOMO-1 orbital of limonene is a π orbital located on this double bound with an ionisation energy much closer to the ionization energy of the HOMO orbital (in comparison to the gap between the first and the second vertical ionization energies for cases of α-pinene and 3-carene). As can be seen from Fig. 64, both the first two vertical ionization energies are now positioned within the X-band region. This adds complexity to the problem; for limonene, transitions from the HOMO-1 can definitely contribute to the second half of the X-band, above IE=8.8 eV. So, we should not expect the result of our FC simulation, which is only considering the HOMO orbital, to match with the experimental SPES well. The broader shape of the two peaks on the right hand side of the X-band, in comparison to the narrower shape of the two peaks in the left hand side of it, might also be a consequence of the opening of the second ionization channel.

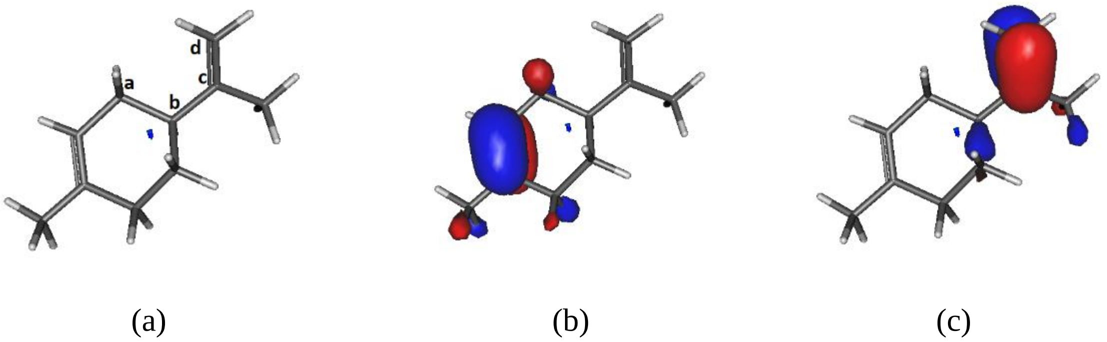

(a) (b) (c)

Fig. 63: Geometrical structure of the limonene (a), HOMO (b), and HOMO-1(c) orbitals. The HOMO orbital of the molecule has π character and is mostly localized around the double bond. The HOMO-1 orbitalis also a π orbital located around the double bond in the isopropenyl tail.

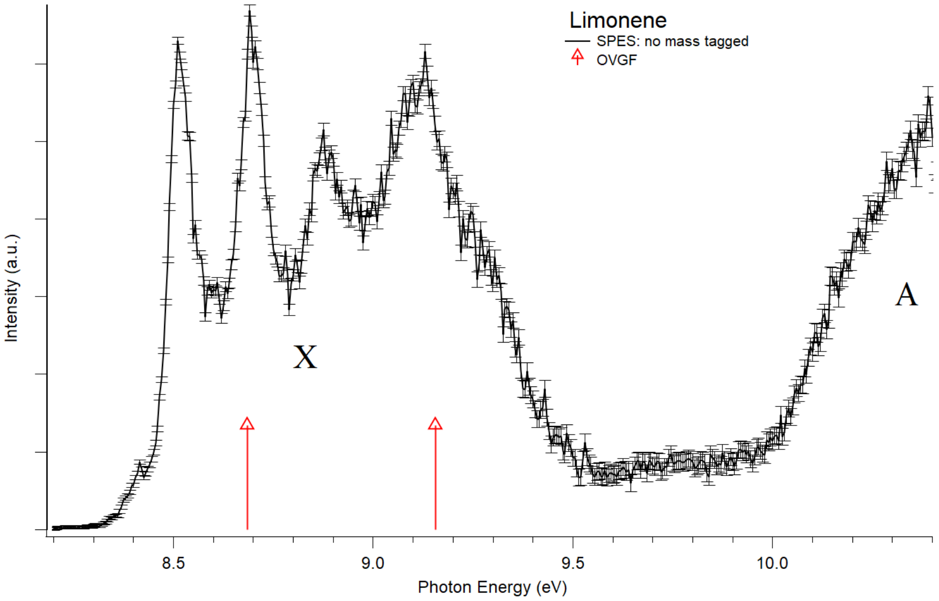

Fig. 64: The high resolution SPES of limonene with no mass tagged, the black curve. The maximum eKE considered to get this spectrum was 100 meV. The red arrows are the results of OVGF calculation and show the vertical ionization energies.

Mass selected ion efficiency curves for limonene scan is presented in

Fig. 65. The fragmentation starts at 9.1 eV with the fragments observed having m/z=80, 93, 108, and 121. Similar to 3-carene and α-pinene, the main fragment is m/z 93, but the amount of fragmentation is less for limonene in comparison to those two monoterpenes. Actually the total ion yield curve of the parent is not decaying as much as it was in the cases of α-pinene and 3-carene. So, it can be said that the limonene, despite its less rigid structure, has more stable cations.

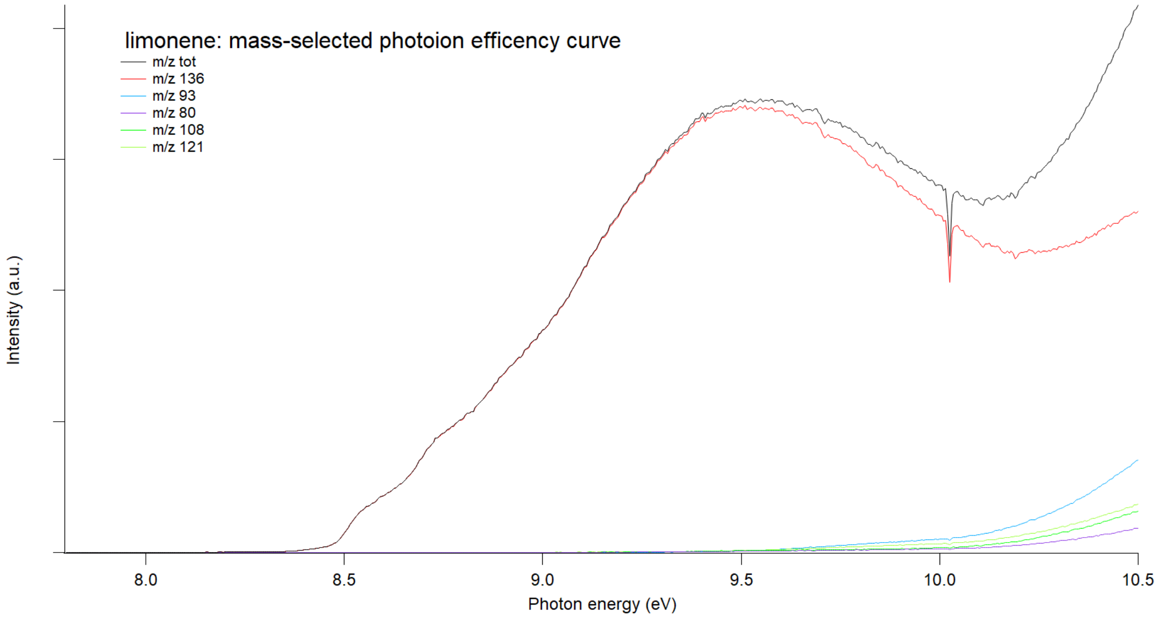

Fig. 65: Mass-selected photoion efficiency curve of limonene. The threshold of fragmentation is around 9.1 eV, with the main fragment being m/z 93.

To see how the fragmentation of the limonene is less than that of α-pinene, one can also compare the ToF mass spectrum recorded during the scan of these two molecules, as presented in Fig. 52 (d) and Fig. 66 (d). In Fig. 66, we have presented the total PES matrix as well as the PES matrices tagged with the parent, m/z 136, and the main fragment, m/z 93. The four vibrational structures in the X-band can even be easily seen from the PEX matrices. More detailed information about how different tracks in the PES matrix can be assigned to certain peaks in the SPES spectrum is provided in Fig. 45 as well.

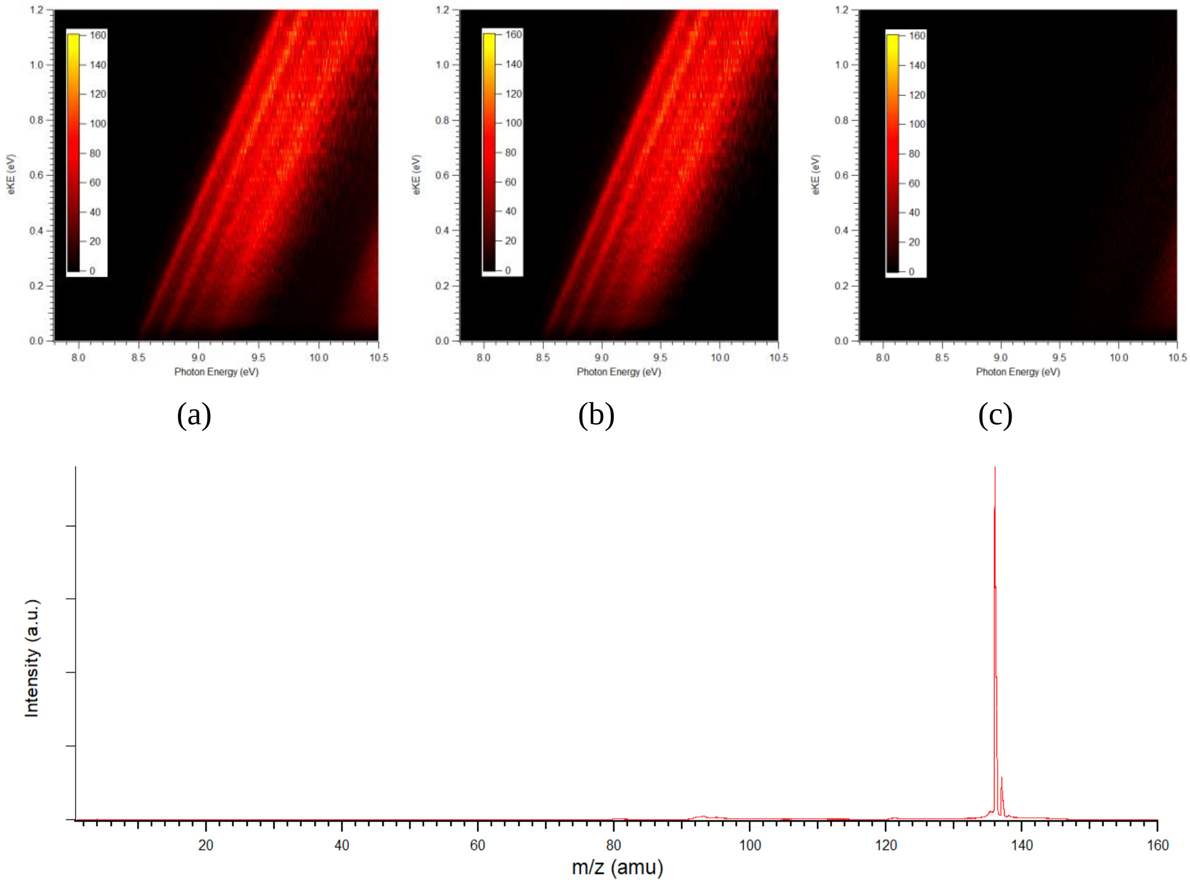

(a) (b) (c)

(d)

Fig. 66: The PES matrix of limonene without mass selection (a), tagged with m/z 136 (b), and tagged with m/z 93 (c). The ToF mass spectrum (d) recorded during the scan shows m/z 93 as the dominant fragments.

The SPES spectra in coincidence with any species present in ToF mass spectrum are plotted in Fig. 67. The photoelectron kinetic energies up to 100 meV have been taken into account to extract these spectra. Within this kinetic energy range and for photon energies above 9.6 eV, there are clearly no photoelectrons in coincidence with the parent mass. On the other side, as we go higher in photon energy, the SPES of the fragments become more intense. The same argument we used to explain the reason for fragmentation in the 3-carene case can be applied here. The fragmentation is due to entering into the second ionization channel as its onset matches with the position of the second vertical ionization energy. The IP of the molecule is measured as 8.47 eV in a good agreement with the literature [96, 97].

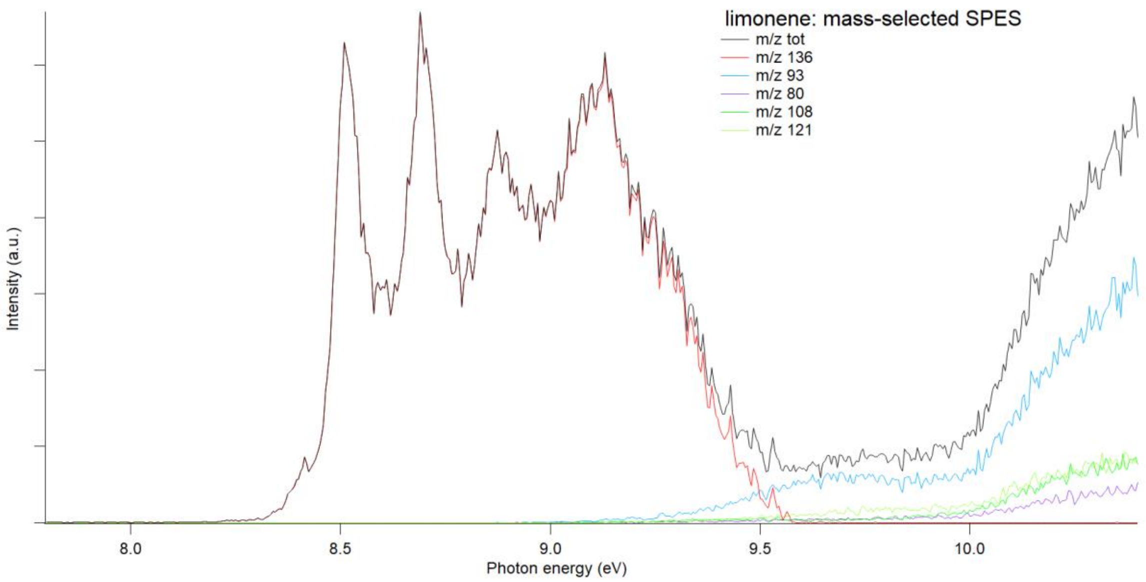

Fig. 67: Mass-selected SPES of the parent and fragments present in the limonene scan. m/z 93 is the dominant fragment, however, there are some other fragments m/z=80, 108, 121 present in the scan.

Now, let's focus on the SPES of the parent and compare it with the FC simulation to assign the different peaks over the X-band. The geometry optimization and frequency calculation of the ground state of the neutral and the cation have been done using the DFT method with the CAM-B3LYp as the functional and aug-cc-pVDZ as the basis set, in Gaussian 16 [89]. The output files were fed into the FC lab II to calculate the FC factors as a sticks diagram. A Lorentzian shaping function, cut off=1500^{-1} cm and FWHM=400 cm^{-1}, was convoluted to any stick to get the FC spectrum. In this calculation, the hot integrals are ignored and only the transitions from the vibrationless state of the neutral are taken into account. In other words, a 0°K FC simulation has been done.

A list of the vibrational normal modes and their frequencies for the neutral and the cation are given in Table 4. As we will see shortly, the most important transitions in the case of limonene are ν1, ν2, ν3, ν18, ν55, and ν59. These are highlighted in the table.

To assign the different peaks in the SPES, just similar to 3-carene, we firstly focus on the first peak around 8.50 eV. Included in Fig. 68 is the SPES around this peak plotted together with the FC simulation. Here, only the most dominant sticks are plotted. As we can see, the first peak is composed of the origin transition plus a combination of zero or one or two single quanta excitation of the first three normal modes (ν1, ν2, ν3).

Table 4: The frequency of normal vibrational modes of the neutral and cation of limonene calculated using basis set aug-CC-pVDZ. There are 72 normal modes from which the most interesting ones are v1, v2, v3, v18, v55, and v59. The transition between the vibrationless states of the neutral into these modes of the cation makes the most remarkable structures in the FC simulation. See Fig. 69 as well.

normal mode	Frequency (cm^{-1})			normal mode	Frequency (cm^{-1})			normal mode	Frequency (cm^{-1})	
	Neutral	Cation			Neutral	Cation			Neutral	Cation
1	28.77	37.55		25	979.45	966.31		49	1465.43	1450.87
2	81.66	66.21		26	1008.87	969.12		50	1470.16	1461.74
3	162.75	107.95		27	1017.38	1011.8		51	1476.28	1470.49
4	172.87	161.39		28	1042.35	1019.87		52	1479.45	1475
5	190.73	179.03		29	1046.89	1040.15		53	1483.59	1487.12
6	201.22	184.14		30	1065.24	1047.59		54	1491.67	1493.06
7	275.24	206.05		31	1082.79	1067.66		55	1743.5	1591.81
8	314.06	312.64		32	1105.85	1075.8		56	1777.07	1736.75
9	327.1	327.56		33	1149.15	1107.91		57	3014.04	2912.23
10	345.46	352.15		34	1171.9	1142.93		58	3023.83	2971.11
11	441.57	405.75		35	1191.5	1191.96		59	3037.8	3006.66
12	460.45	451.01		36	1234.2	1211.05		60	3043.56	3023.57
13	505.48	497.5		37	1257.6	1256.16		61	3047.47	3054.07
14	513.13	510.53		38	1287.21	1271.65		62	3054.73	3074.82
15	565.66	556.81		39	1317.79	1311.67		63	3070.15	3077.3
16	653.15	629.9		40	1338.29	1331.87		64	3086.23	3083.79
17	722.25	693.5		41	1343.77	1348.26		65	3091.54	3110.31
18	780.16	707.51		42	1371.33	1358.35		66	3104.29	3112.54
19	815.09	741.43		43	1403.12	1360.44		67	3114.99	3158.21
20	821.27	793.55		44	1404.86	1374.46		68	3138.45	3164.72
21	918.77	846.71		45	1419.61	1380.46		69	3145.22	3174.45
22	933.83	899.65		46	1425.39	1407.34		70	3166.63	3182.81
23	943	916.96		47	1446.32	1411.23		71	3172.02	3189.49
24	944.09	942.69		48	1463.31	1420.3		72	3259.64	3266.2

We call the group of transitions shown in Fig. 68 as 'pack A'. The other peaks in the limonene SPES are mainly composed of the pack A plus a combination of zero or single or double quanta excitation of modes ν18, ν55, and ν59. The second major peak, peak b, is mostly the pack A transitions in addition to one quanta excitation of ν55. The next major peak, peak c, is assigned to two quanta excitation of ν55 or single quanta excitation of ν59 in addition to pack A. Peak d is one quanta excitation in both ν55 and ν59 together with transitions in pack A. Finally, peak c is two quanta excitation in ν59 combined with pack A transitions.

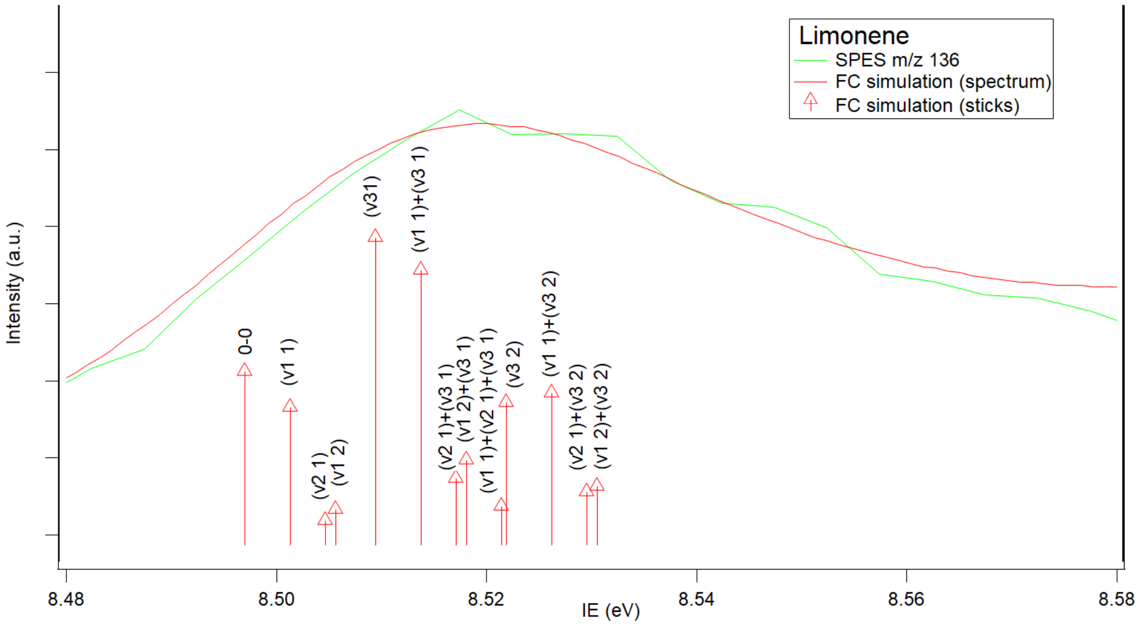

Fig. 68: SPES spectrum of limonene (m/z 136) over the first peak in the X-band (green curve) together with the results of the FC simulation. The red sticks are showing the FC factors for transitions from the vibrationless state of the neutral, from which only the most dominant sticks are plotted for the. The red solid curve is the simulated FC spectrum obtained by convoluting a Lorentzian shaping function (cutoff=1500 cm^{-1} and FWHM=400 cm^{-1}) to any of the sticks. This peak is composed of the origin transition plus a combination of zero or one or two single quanta excitation of the first three normal modes (v1, v2, v3). A label (νx y) is used to show the identity of the transitions, where vx is standing for the normal mode number x, and y is indicating the level of excitation in that mode.

In the case of limonene, there are some minor vibrational structures between the major ones evident in Fig. 69. With the help of our calculations, we can assign these minor structures as well. In fact, each of the minor peaks is composed of the same transitions making the immediate previous major peak in addition to one quanta excitation of ν18. The identity of some of the minor peaks is also shown in Fig. 69 where the vibrational levels in the cation state are shown clearer. In this figure, only the most dominant 3300 sticks are plotted.

The FC simulation matches with the experimental SPES very well below 9.0 eV but it shows some discrepancy above this energy with the experiment. It was mentioned above that the next ionization channel opens around 9.15 eV (Fig. 64). The FC simulation presented here only considers transitions from the vibrationless ground state to the vibrational levels of the electronical ground state of the cation. So, the reason for the mismatch between the FC simulation and the experimental SPES might be due to entering an energy range where the vibronic levels of the next electronic state of the cation are contributing.

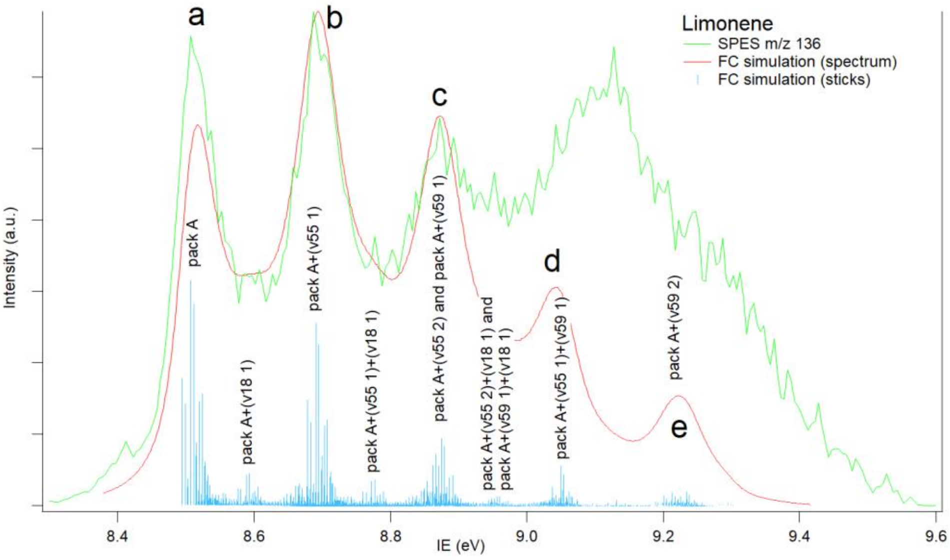

Fig. 69: SPES spectrum of limonene (m/z 136) over the X-band (green curve) together with the results of the FC simulation. The blue sticks are showing the FC factors for transitions from the vibrationless state of the neutral, from which only 3300 of the most dominant transitions are plotted here. The red solid curve is the simulated FC spectrum obtained by convoluting a Lorentzian shaping function (cutoff=1500 cm^{-1} and FWHM=400 cm^{-1}) to any of the sticks. For more information see the text.

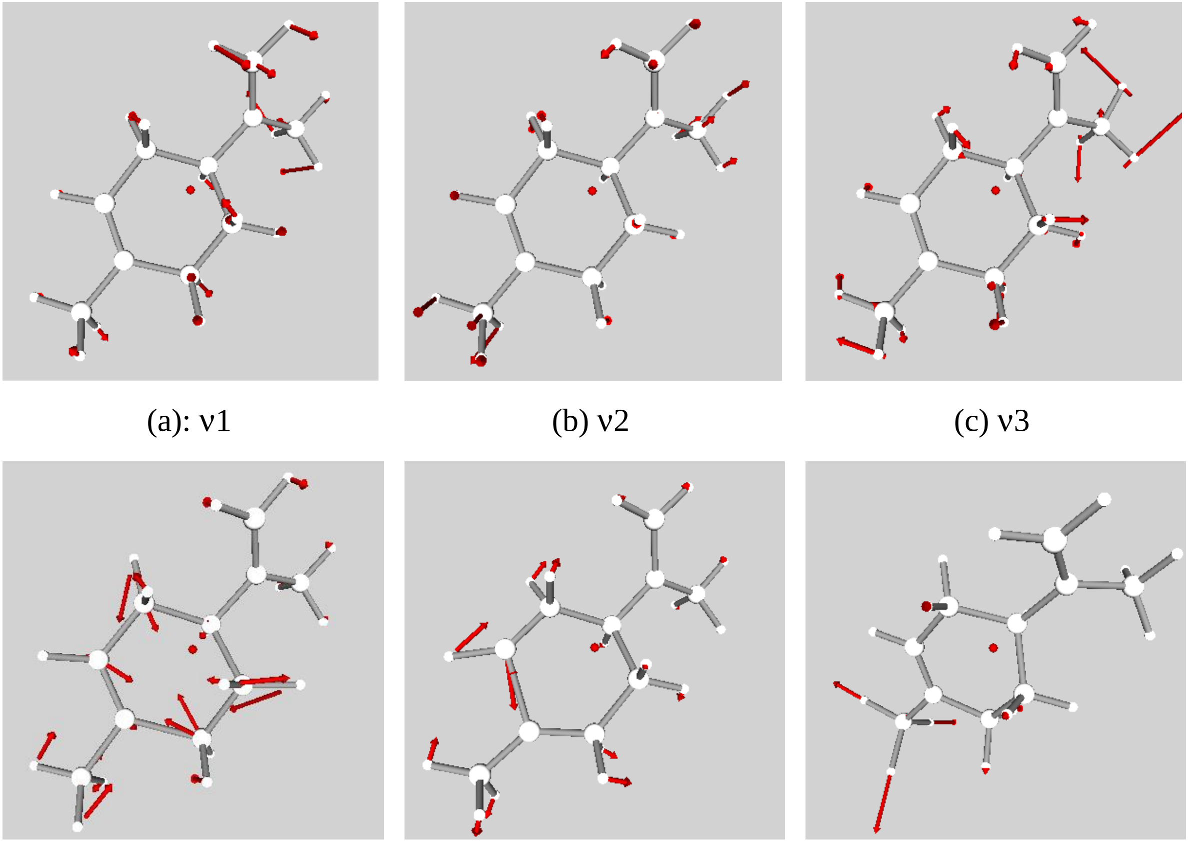
(a): ν1

(b) ν2

(c) ν3

(d) ν18

(e) ν55

(f) ν59

Fig. 70: Normal vibrational modes v1 (a), v2 (b), v3 (c), v18 (d), v50 (e) and v59 (f) of the limonene in the cation state. The length and the direction of the red arrows are respectively showing the amplitude and the direction of any displacement of atoms within the molecule.

At the end of this section, we will discuss what kind of motions are contributing to the most important vibrational modes discussed above. The modes ν1-ν3 are respectively rocking, symmetric ring bending and ring torsion motions. 0-3 quanta excitation of these modes creates the transitions in pack A, which corresponds to the first major peak in the SPES. Modes ν55 and ν59 are the double bound (in the ring) stretching mode and a symmetric stretching of the methyl group attached to the ring, respectively, which produce the progression from the first major peak to the next ones. Mode ν18 is the ring breathing mode whose frequency is 707.51 cm^{-1} and if it is added to transitions involved in any major peak, the next minor peak is created.

3.1.4. β-pinene

β-pinene is another bicyclic ring structure monoterpene [98-100] studied here. As can be seen from Fig. 71 (a), it has two rings, a six and a four-membered ring. However, there are two main differences between the β-pinene and the other monoterpenes discussed so far in this chapter. The first difference is that β-pinene lacks any endo-cyclic double bond. There is only one double bond in the case of β-pinene located out of the ring. We will see in the following how this fact makes a significant difference in the SPES of β-pinene in comparison to that of the other monoterpenes, α-pinene for example. The HOMO orbital of the neutral is a π one located around the double bond, as can be seen from Fig. 71 (c). The other difference appears when we ionize the molecule. Based on our calculation, the four-membered ring in β-pinene opens during the ionization from the HOMO orbital; the geometrical structure of the cationic state of β-pinene is shown in Fig. 71 (b) where it can be seen that the four membered ring has been opened. Such a big change in the geometry may also make our FC simulation inefficient; we postpone detailed discussion on that to later.

Similar to α-pinene, the OVGF calculation for β-pinene shows a big energy gap between the first and the next ionization channels. This is confirmed by the experimental SPES recorded for β-pinene, shown in Fig. 72, where all the photoelectrons up to eKE=100 meV have been taken into account. Like α-pinene, the X- and A-band are fairly separated at 9.7 eV. However, as the signal at this energy does not drop entirely to zero, we can assume that these two bands are slightly overlapping.

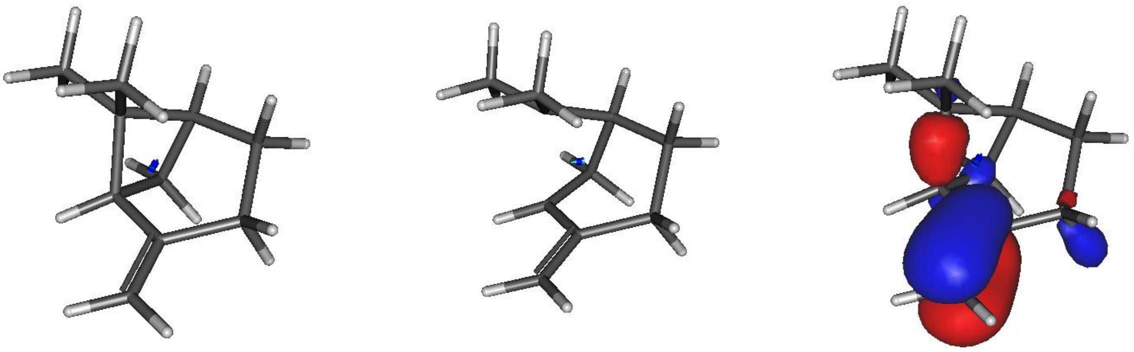

(a) (b) (c)

Fig. 71: Geometrical structure of β-pinene in its neutral (a) and cationic (b) ground state. (c) is the HOMO of the molecule in its neutral state. The HOMO orbital of the neutral is mostly a π orbital located around the exo-cyclic double bound.

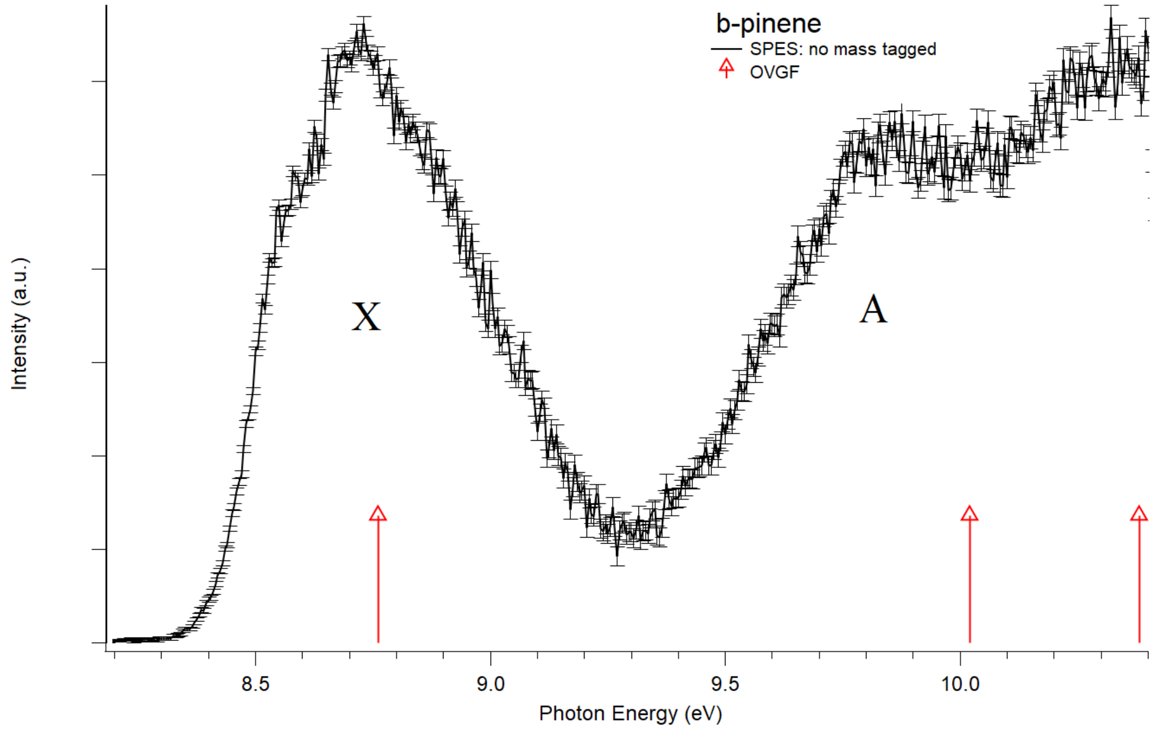

Fig. 72: The high resolution SPES of β-pinene with no mass tagged, the black curve. The maximum eKE considered to get this spectrum was 100 meV. The red arrows are the results of OVGF calculation and show the vertical ionization energies.

To get an insight into the possibility and the strength of the fragmentation pathways, we have extracted and plotted the mass tagged photoion efficiency curves for all the species seen in the ToF mass spectrum. The results are presented in Fig. 73. The fragmentation starts around 9.1 eV with the main fragment being m/z 93. Fragmenting to mass 93 amu gets more and more significant in a way that above 9.3 eV the abundance of the fragment m/z 93 overtakes the abundance of the parent. There are some other fragments possible, m/z=80, 108, and 121, but they all together contribute to less than 20% of the total fragmentation. The drop in the intensity observed at 10.03 eV is due to the absorption line of the Kr present in the gas filter while the other drop at 9.9 eV was due to a sudden synchrotron shut down.

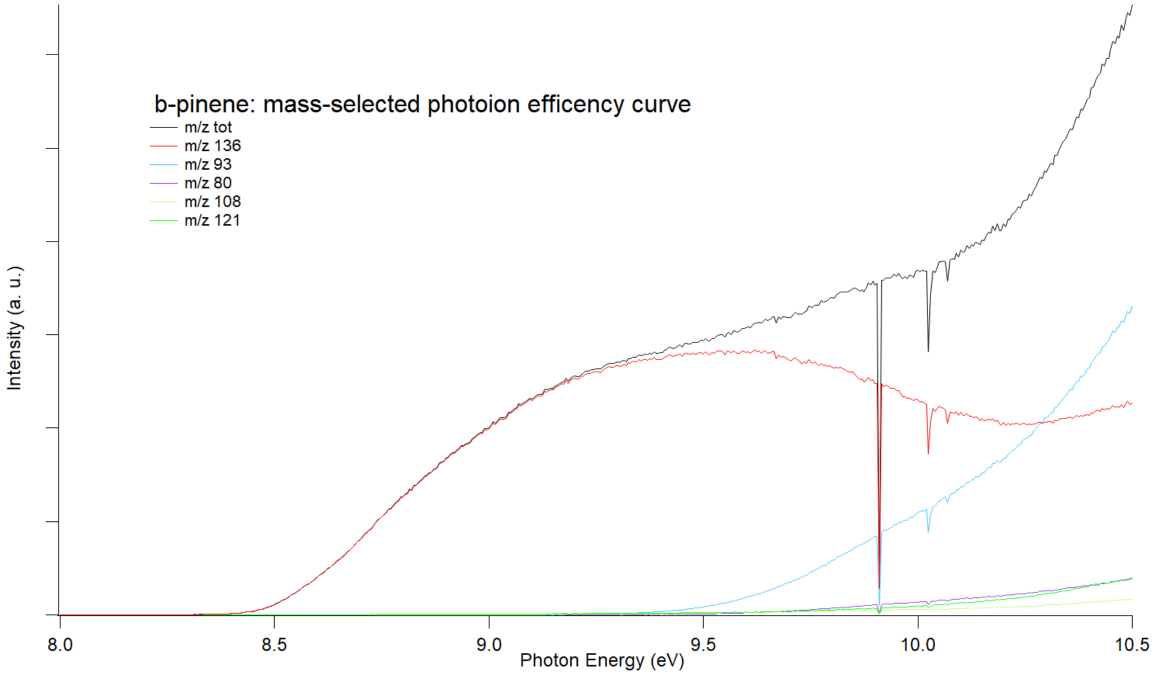

Fig. 73: Mass-selected photoion efficiency curve of β-pinene. The thresholds of fragmentation are around 9.1 eV with the main fragmentation being m/z 93.

Included in Fig. 74 is the total PES matrix as well as the PES matrices in coincidence with the parent and the main fragment, m/z 93, ions. The gap between the X-band and the next band can be clearly seen. It can also be said that the photoelectrons in coincidence with the parent mass are corresponding to the first band while the photoelectrons coming from m/z 93 are mainly producing the rest part of the total PES matrix. In the case of β-pinene, the X-band is rather structureless and looks more like a bump (see Fig. 72); this fact can even be seen from the total PES matrices which lack any sharp traces over the first ionisation channel (in comparison to the other terpenes studied so far in this chapter).

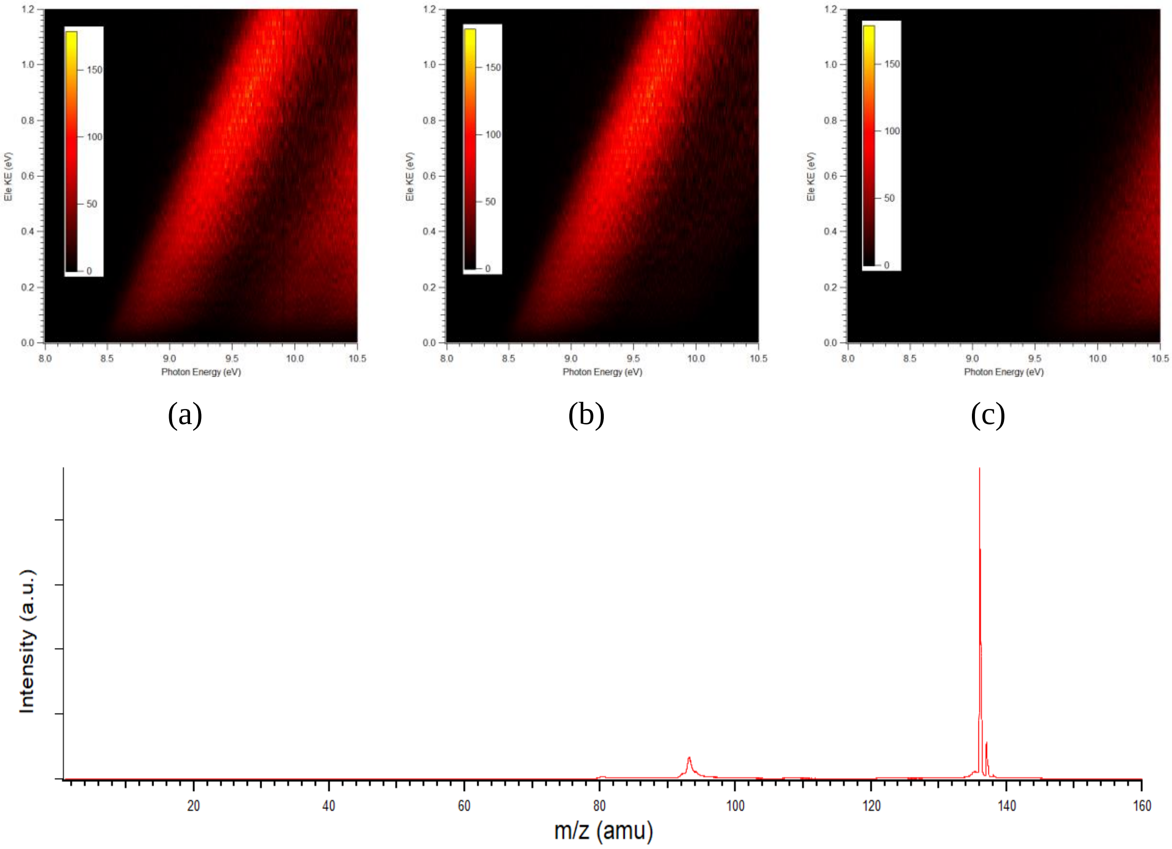

(a) (b) (c)

(d)

Fig. 74: The PES matrix of β-pinene without mass selection (a), tagged with m/z 136 (b), and tagged with m/z 93 (c).The ToF mass spectrum (d) recorded during the scan is showing m/z 93 as the dominant fragments.

Mass-selected SPES can tell us more about the fragmentation pathways. The IP of the molecule is determined to be 8.38 eV in good agreement with the literature [100]. Fig. 75 shows the mass-selected SPES for any species present in the ToF mass spectrum over the scan range, where only photoelectrons up to kinetic energy of 100 meV are taken into account. At this resolution, we can easily see that the fragmentation threshold is around 9.1 eV. However, the parent ions are not entirely dissociating at this energy. Actually, for β-pinene, the parent ions are more stable and a considerable amount of them remain unfragmented up to 10.05 eV. Looking back to the result of our OVGF calculation presented in Fig. 72, one can find that the energy at which all the parent ions dissociate (10.05 eV) is matching the photon energy needed to exceed the next ionization channel. So, we can assume that ionization from the HOMO-1 is totally dissociative.

The other point we can get from Fig. 75 is the swap between the intensity of two of the fragments, m/z 80 and m/z 121. The abundance of m/z 80 is more than that of m/z 121 from the onset of the fragmentation till 10.05 eV, which we assume to be the energy at which the next ionization channel is being opened. As we pass this energy, the fragmentation dynamics are changing and the cations are dissociating more to m/z 121 rather than to m/z 80.

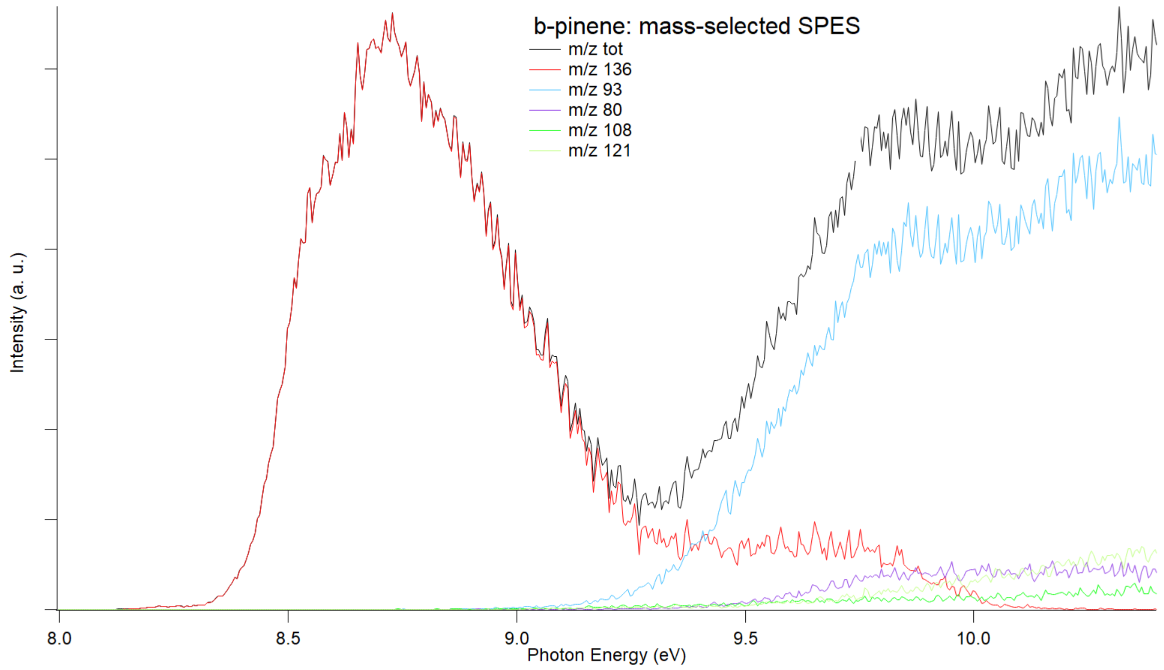

Fig. 75: Mass-selected SPES of the parent and fragments present in the β-pinene scan. m/z 93 is the dominant fragment, however, there are some other fragments m/z=80, 108, 121 present in the scan.

Like the other monoterpenes, the β-pinene molecule is composed of 26 atoms giving 72 normal vibrational modes. The list of these modes for both the neutral and the cation is given in Table 5. The modes which contribute to the most significant transitions are highlighted in the table. In this case, simultaneous excitation of modes ν2, ν5, and ν6 plays the major role in combination with some other modes like ν10, ν24, ν56.

Table 5: The frequency of normal vibrational modes of the neutral and cation of β-pinene calculated using the DFT method with the CAM-B3LYP as the functional and aug-cc-pVDZ as the basis set. There are 72 normal modes from which the most interesting ones are v2, v5, v6, v10, v24, and v56.

normal mode	Frequency (cm^{-1})			normal mode	Frequency (cm^{-1})			normal mode	Frequency (cm^{-1})	
	Neutral	Cation			Neutral	Cation			Neutral	Cation
1	105.02	115.69		25	962.33	960.84		49	1470.23	1468.33
2	164.58	132.15		26	981	974.54		50	1475.11	1468.66
3	187.12	154.22		27	995.5	985.61		51	1476.92	1470.89
4	211.29	191.7		28	1011.59	992.24		52	1493.91	1487.82

5	231.72	204.43		29	1038.97	997.29		53	1496.15	1494.87
6	300.72	237.94		30	1077.36	1057.31		54	1509.68	1506.27
7	361.51	313.83		31	1085.08	1065.16		55	1519.58	1519.6
8	389.35	367.04		32	1102.19	1075.7		56	1747.05	1547.03
9	397.18	384.67		33	1141.97	1106.38		57	3047.21	3037
10	423.15	398.11		34	1176.48	1124.06		58	3052.85	3046.73
11	460.58	415.16		35	1214.72	1168.13		59	3060.75	3074.33
12	483.57	432.41		36	1229.29	1214.05		60	3069.85	3078.95
13	537.35	485.98		37	1247.67	1229.79		61	3082.28	3101.38
14	621.75	542.26		38	1258.95	1262.58		62	3092.5	3106.58
15	659.24	568.72		39	1266.9	1285.34		63	3100.4	3127.21
16	739.25	585.15		40	1290.28	1298.26		64	3102.1	3134.64
17	786.85	704.65		41	1303.78	1305.42		65	3109.88	3138.62
18	806.54	783.1		42	1328.2	1331.48		66	3116.44	3152.74
19	845.17	817.57		43	1334.78	1353.76		67	3118.26	3171.47
20	885.18	851.15		44	1363.95	1359		68	3141.54	3185.28
21	905.67	884.1		45	1372.06	1395.28		69	3154.99	3193.45
22	923.07	897.31		46	1405.3	1403.13		70	3155.21	3199.46
23	929.54	918.95		47	1418.53	1427.4		71	3164.86	3200.27
24	955.5	945.57		48	1451.83	1437.49		72	3243.94	3280.62

Included in Fig. 76 is the SPES of β-pinene plotted on top of the results of the FC simulation. The point is that there are no pronounced vibrational peaks seen in either the SPES or FC simulation. Unlike the other monoterpenes, the β-pinene SPES and FC simulations are just looking like a structureless bump. As we saw before, in the case of α-pinene, 3-carene, and limonene, the stretching of the endo-cyclic double bond was almost responsible for the major structures over the X-band; lacking such a vibrational mode causes a rather structureless X-band for β-pinene.

The FC stick spectrum of β-pinene is also shown in Fig. 76 where we only have plotted one hundred of the most significant transitions. All the dominant transitions include one or two quanta excitation of modes ν5 and ν6. The combination of these two modes with modes ν2, ν10, ν24, and ν56 makes mainly the rest of the spectrum. The deformations happening within the normal modes ν2, ν5, ν6, ν10, ν24, and ν56 are all shown in Fig. 77.

Finally, we should notice that in our calculation for β-pinene, the four-membered ring is opened in the cation state making the geometry of the cation dramatically different from that of the neutral. Such a huge difference might be the reason why the FC simulated spectrum is not in a very good agreement with the experimental SPES.

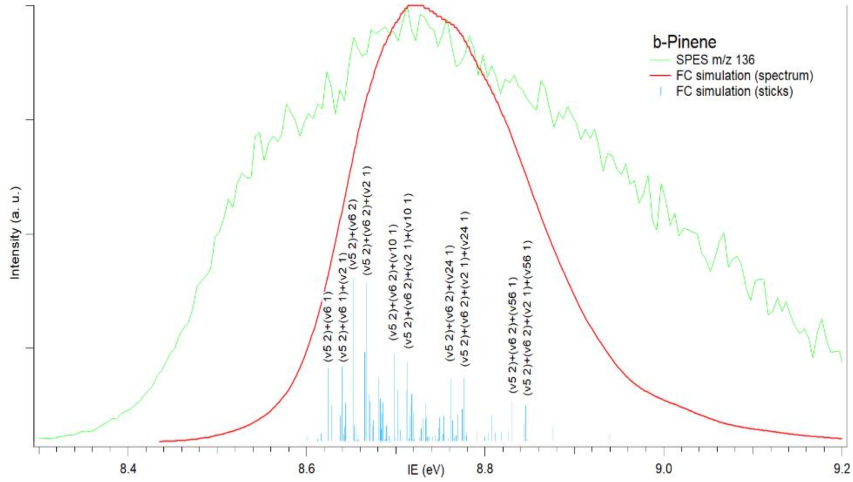

Fig. 76: SPES spectrum of β-pinene (m/z 136) over the X-band (green curve) together with the results of the FC simulation. The blue sticks are showing the FC factors for transitions from the vibrationless state of the neutral, from which only 100 of the most dominant transitions are plotted here. The red solid curve is the simulated FC spectrum obtained by convoluting a Lorentzian shaping function (cutoff=1500 cm^{-1} and FWHM=400 cm^{-1}) to any of the sticks. For more information see the text.

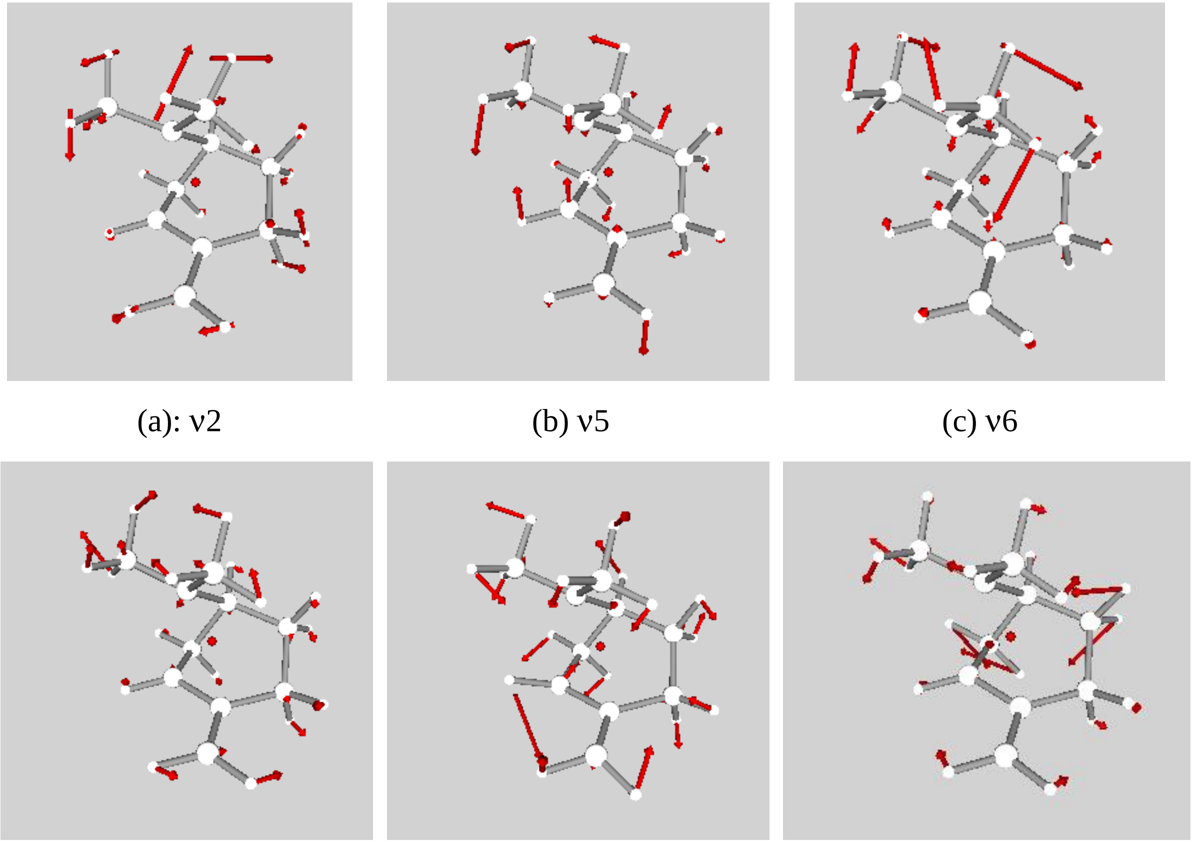

(a): ν2 (b) ν5 (c) ν6

(d) ν10 (e) ν24 (f) ν56

Fig. 77: Normal vibrational modes v2 (a), v5 (b), v6 (c), v10 (d), v24 (e) and v56 (f) of the β-pinene in the cation state. The length and the direction of the red arrows are respectively showing the amplitude and the direction of any displacement of atoms within the molecule.

3.1.5. sabinene

Sabinene also has a bicyclic ring structure composed of a three- and a five-membered ring. Similar to β-pinene, one of the bonds stretches due to ionization. This suggests a huge change in the geometry which may make the FC calculation less efficient in this case as well. The other similarity between sabinene and β-pinene is the lack of any endo-cyclic double bond. The double bond of the sabinene is also located outside of the ring. So, based on what we discussed previously in this chapter, it is not far unexpected that sabinene shows a structureless SPES over its X-band. The HOMO orbital of the neutral is π in character, partially localized around the double bond and the three-membered ring. The LUMO orbital of the cation also has almost the same shape, see Fig. 78 (c) and (d).

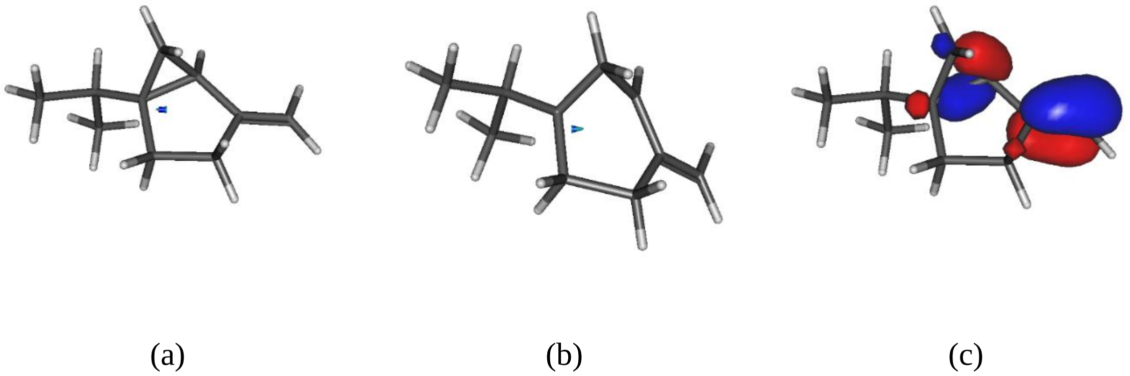

Fig. 78: Geometrical structure of sabinene in its neutral (a) and cationic (b) ground state. (c) is showing the HOMO of the molecule in its neutral state. Which shows mostly a π character and is located mostly around the exo-cyclic double bound.

Included in Fig. 79 is the SPES recorded for the sabinene without any mass tagging to the photoelectrons. The maximum kinetic energy of the photoelectrons taken into account to obtain the SPES spectrum is 100 meV, just the same condition as the other monoterpenes studied so far. In this case, although the X- and A-band can be distinguished easily, they are not well separated and there is some overlap between them around 9.25 eV. We have plotted the result of our OVGF calculation in the same figure to get a sense of where the next ionization channel is opened. From the first look, one can see how poor the vibrational structures are over the X-band, in comparison to α-pinene, limonene, and 3-carene. We will discuss this later when we present the FC simulation results.

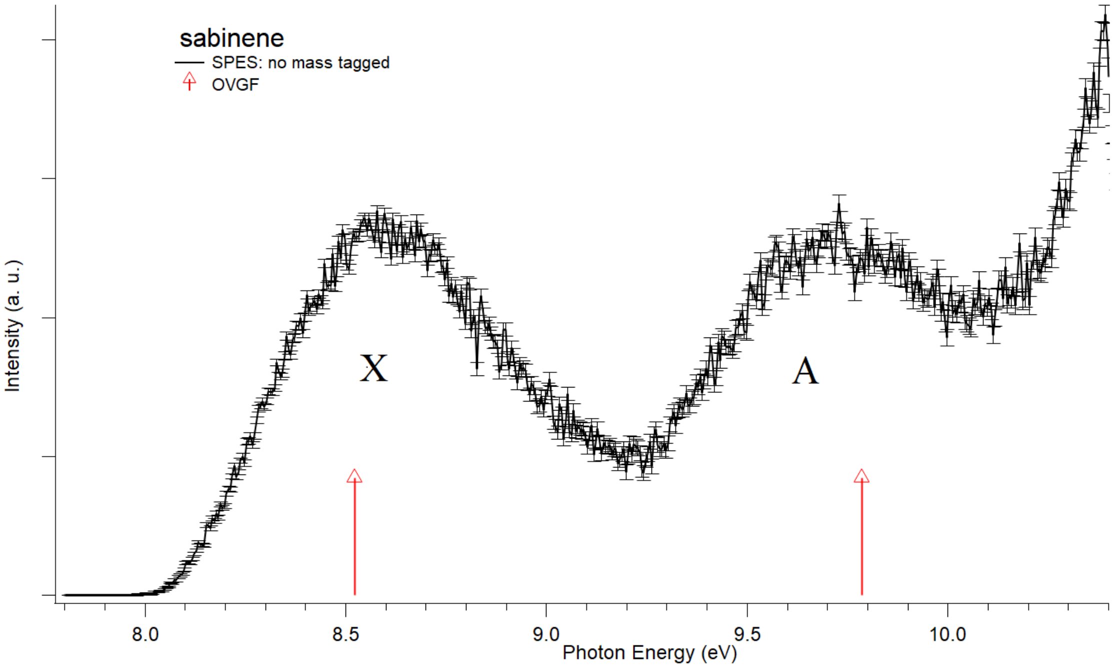

Fig. 79: The high resolution SPES of sabinene with no mass tagged, the black curve. The maximum eKE considered to get this spectrum was 100 meV. The red arrows are the results of OVGF calculation and show the vertical ionization energies.

To see the relative amount of the fragments, we have plotted the mass-selected total ion yield curves for the sabinene scan in Fig. 80. The fragmentation seems to starts at 9.1 eV with the main fragment being m/z 93. The fragment with m/z 93 is overtaking the parent, in intensity, at 10.3 eV; so, it can be said that the fragmentation, in this case, is also considerable at photon energies above 10.0 eV. There are also some other masses seen in the ToF like m/z 80, 108, and 121 who all together contribute for no more than 20% of total fragmentation. Like the other scans, the drop at 10.03 eV is due to the Kr absorption line while the other drop at 9.85 eV was caused by instabilities in the synchrotron radiation.

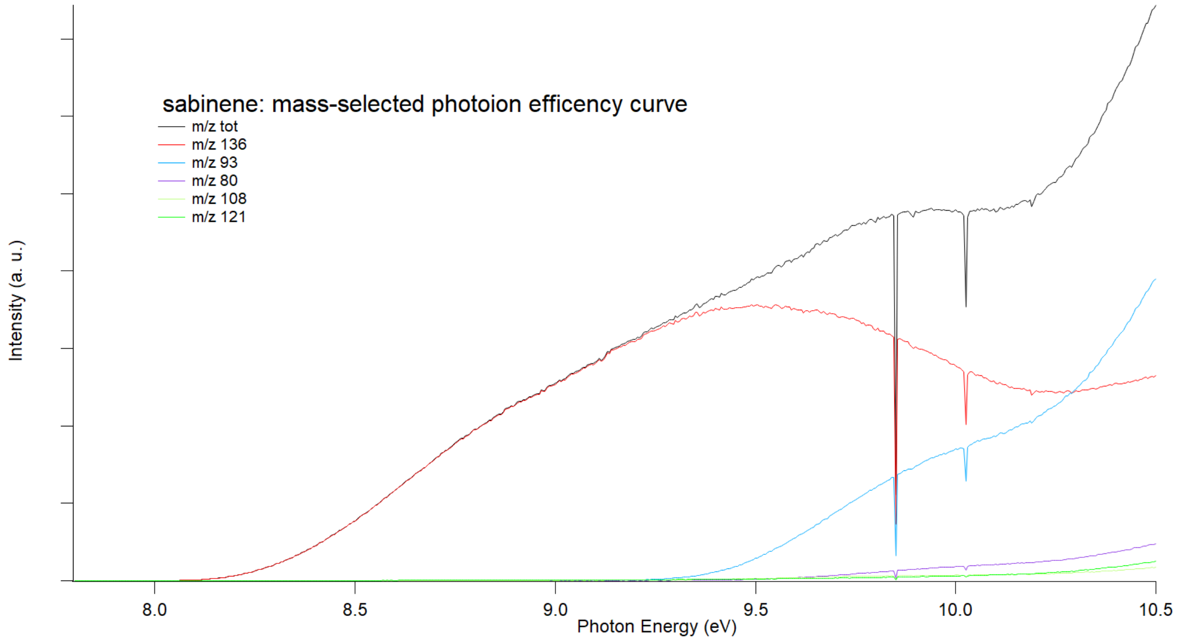

Fig. 80: Mass-selected photoion efficiency curve of sabinene. The thresholds of fragmentation are around 9.1 eV with the main fragmentation being m/z 93.

We can also look at the PES matrices as well as the mass-selected SPES graphs to see how different species contribute to the total photoelectron signal on the detector. Shown in Fig. 81 (a), (b), and (c) are the total photoelectron matrix and the PES matrices in coincidence with the parent and the main fragment (m/z 93), respectively. The ToF mass spectrum is also plotted in Fig. 81, which is more and less similar to that of the other monoterpenes. Comparing the total PES matrix to the PES matrices tagged with m/z 136 and 93, one can say that the photoelectrons making the X-band are mostly coming from the parent mass, m/z 136, while the A-band region is almost covered by the m/z 93 contribution.

Considering only the photoelectron kinetic energies up to 100 meV, we have extracted the mass-selected SPES for any of the masses observed in ToF spectrum the results of which are plotted in Fig. 82. By looking at the SPES curves, we can see the fragmentation thresholds easily. Actually, the fragmentation threshold can be read from the mass-selected total ion yield curves presented in Fig. 80 too, but such curves are showing the total ions making the resolution worse. So, this can be considered as one of the advantages of the SPES technique that we can get better insights about the fragmentation dynamics.

The black curve in Fig. 82 is the total slow photoelectrons (up to 100 meV); just look at how it matches with the parent SPES, the red curve, over the XD-band and how it is close to the SPES of the fragment m/z 93 over the next bands. This confirms the conclusion we made just above by comparing the PES matrices; the photoelectrons coming from the parent are almost responsible for the X-band while those coming from the fragments are covering the next bands.

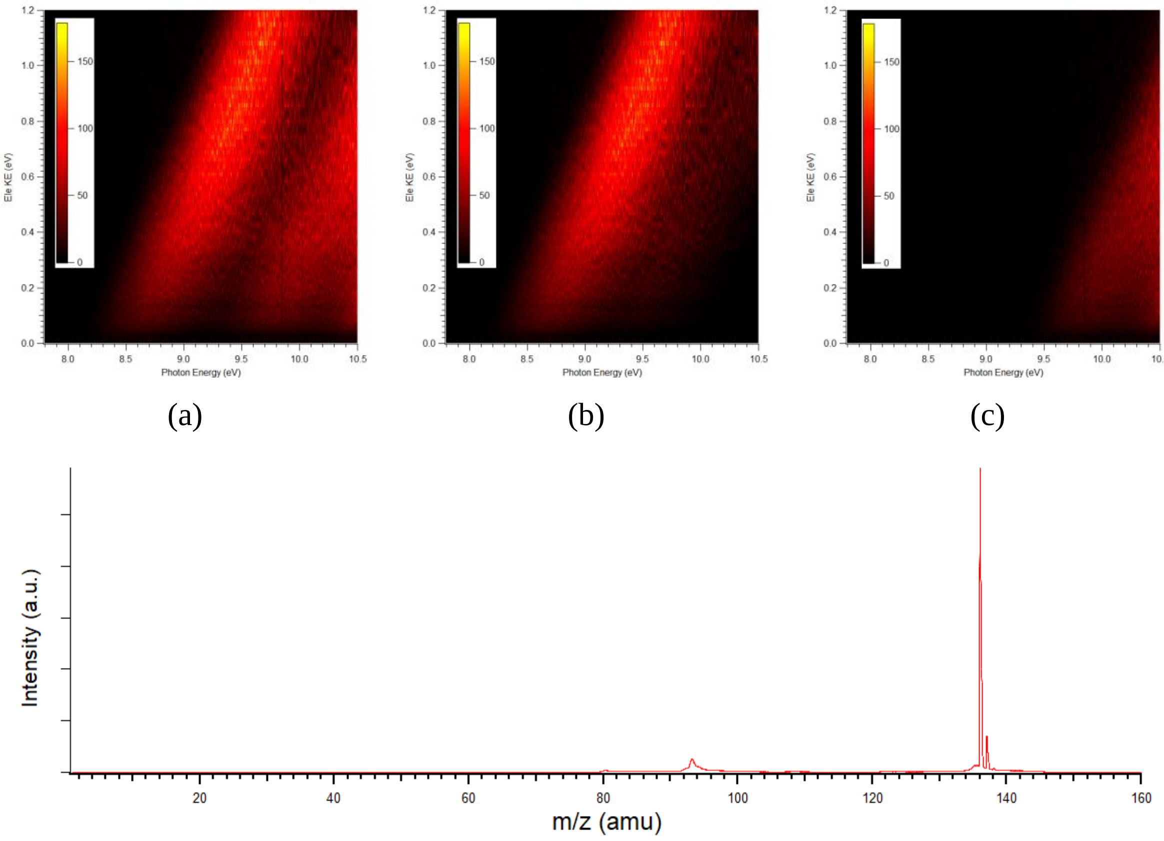

(a) (b) (c)

(d)

Fig. 81: The PES matrix of sabinene without mass selection (a), tagged with m/z 136 (b), and tagged with m/z 93 (c). The ToF mass spectrum (d) recorded during the scan is showing m/z 93 as the dominant fragments.

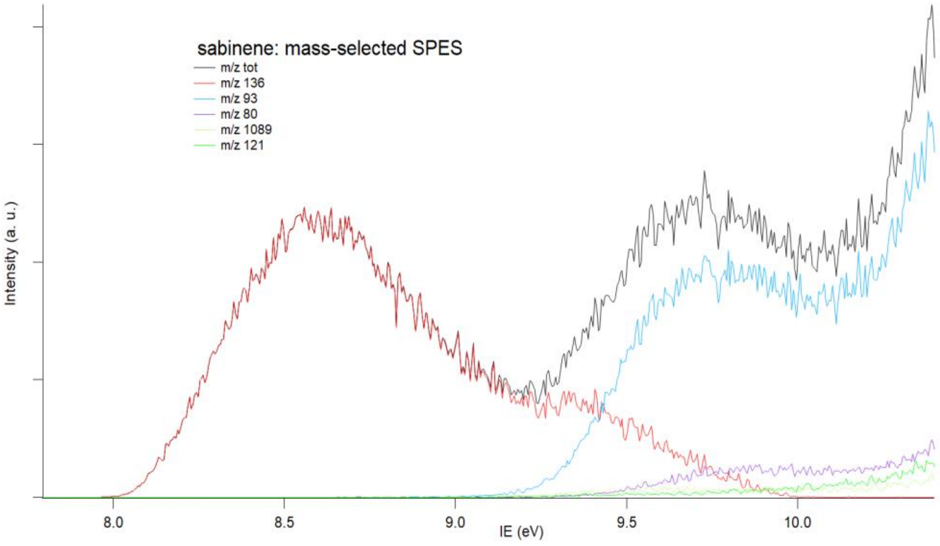

Fig. 82: mass-selected SPES of the parent and fragments present in the sabinene scan. m/z 93 is the dominant fragment, however, there are some other fragments m/z=80, 108, 121 present in the scan.

The other point is the expansion of the parent SPES to photon energies above the fragmentation threshold. In fact, the slow photoelectrons in coincidence with parent mass are lasting up to 10.0 eV which is even above the second vertical ionization energy calculated using the OVGF method (see Fig. 79). This means even the second ionization channel is not totally dissociative in the case of sabinene.

The other thing we need to do with the sabinene SPES is to correct it for the impurity. Earlier in this chapter, we mentioned that the results of the GC^2 analysis showed that our sabinene was not pure; the present compounds in the sample were sabinene and β-pinene with 75.9% and 24.1 % abundance, respectively. We can simply apply (Eq. 40) to do the correction, replacing the SPES to PES in this case. Included in Fig. 83 is the SPES of the β-pinene and extract sabinene as well as the corrected SPES which should be considered for pure sabinene.

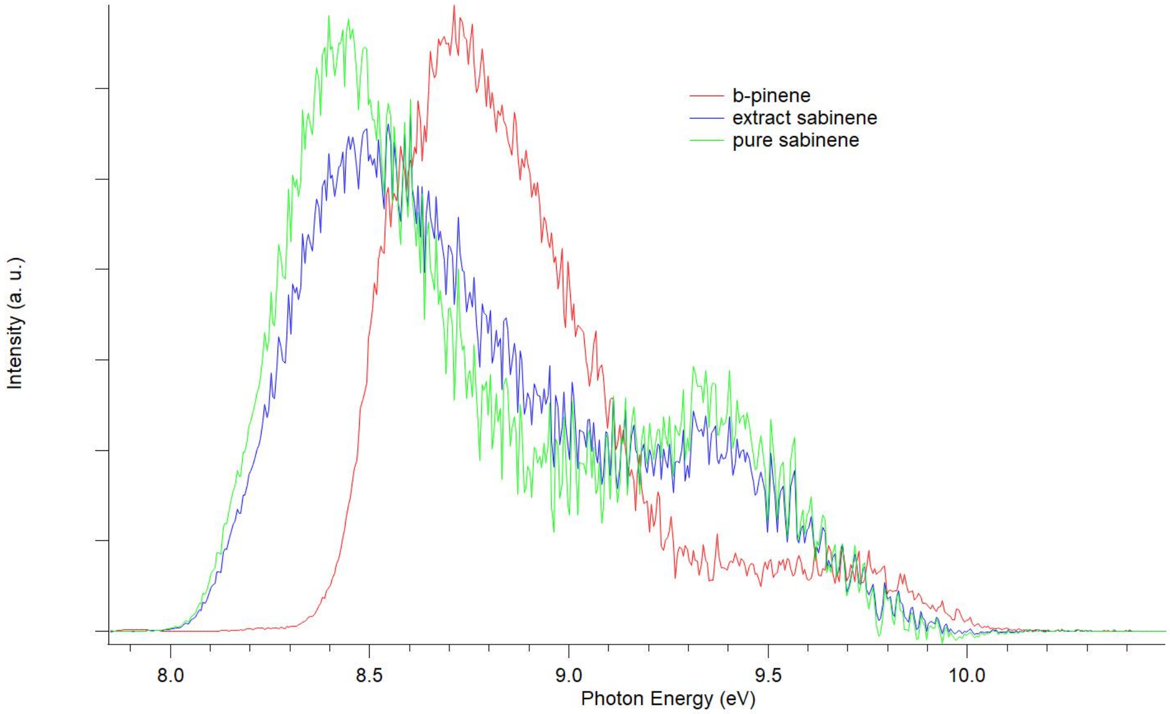

Fig. 83: Correction of the sabinene SPES with respect to the β-pinene impurity.

The frequency calculations for the neutral and cationic states of the molecule are presented in Table 6. The most significant modes contributing to the FC simulated spectrum are highlighted among which we can infer to ν1, ν2, ν3, ν4, ν6, and ν15. The higher frequencies are not involved in the dominant simulated sticks. This might be the reason for the small range progression of the total FC simulation, from 8.3 eV to 8.7 eV which obviously is not in good agreement with the experimental SPES. The SPES is plotted together with the results of the FC simulation in Fig. 84 to show the discrepancy between the simulation and the experiment in the case of sabinene. In fact, the experimental SPES is expanding over a broad range from 8.0 eV to 10.0 eV while our FC simulated sticks spectrum is only covering a small range of that.

Table 6: The frequency of normal vibrational modes of the neutral and cation of sabinene calculated using the DFT method with CAM-B3LYP as the functional and aug-cc-pVDZ as the basis set. There are 72 normal modes from which the most interesting ones are v1, v2, v3, v4, v6, and v15.

normal mode	Frequency (cm^{-1})			normal mode	Frequency (cm^{-1})			normal mode	Frequency (cm^{-1})	
	Neutral	Cation			Neutral	Cation			Neutral	Cation
1	62.76	47.18		25	951.98	950.83		49	1470.89	1466.3
2	102.52	87.64		26	976.78	965.59		50	1478.86	1470.87
3	156.66	154.75		27	992.24	976.42		51	1481.86	1477.72
4	207.73	192.04		28	996.64	1004.41		52	1490.25	1487.58
5	224.56	209.4		29	1026.92	1014.26		53	1491.7	1491.36
6	256.84	228.24		30	1050.61	1046.02		54	1501.34	1498.38
7	270.56	253.57		31	1060.33	1064.84		55	1514.63	1511.66
8	301.38	275.92		32	1069.34	1094.95		56	1759.53	1549.74
9	364.23	340.49		33	1091.7	1110.38		57	3042.64	3067.49
10	380.67	369.13		34	1152.33	1139.56		58	3048.74	3069.23
11	449.59	404.42		35	1179.96	1161.61		59	3053.96	3074.51
12	496.86	455.49		36	1191.71	1188.47		60	3066.4	3078.65
13	521.51	510.42		37	1230.99	1214.51		61	3072.85	3079.78
14	575.4	523.58		38	1247.87	1260.78		62	3111.76	3125.46
15	652.79	567.24		39	1271.63	1283.38		63	3120.04	3144.71
16	671.76	590.58		40	1308.18	1287.5		64	3125.85	3151.5
17	750.1	642.79		41	1316.42	1309.68		65	3128.93	3152.45
18	801.98	743.19		42	1346.09	1334.36		66	3131.67	3156.61
19	830.09	807.27		43	1352.71	1389.79		67	3133.19	3159.09
20	880.44	846.41		44	1378.97	1400.04		68	3148.54	3163.29
21	909.48	870.43		45	1396.54	1415.8		69	3161.1	3175.39
22	917.94	885.12		46	1412.35	1424.48		70	3194.41	3223.58
23	927.18	933.84		47	1426.57	1427.25		71	3235.23	3234.05
24	939.41	942.55		48	1453.28	1459.9		72	3250.53	3285.37

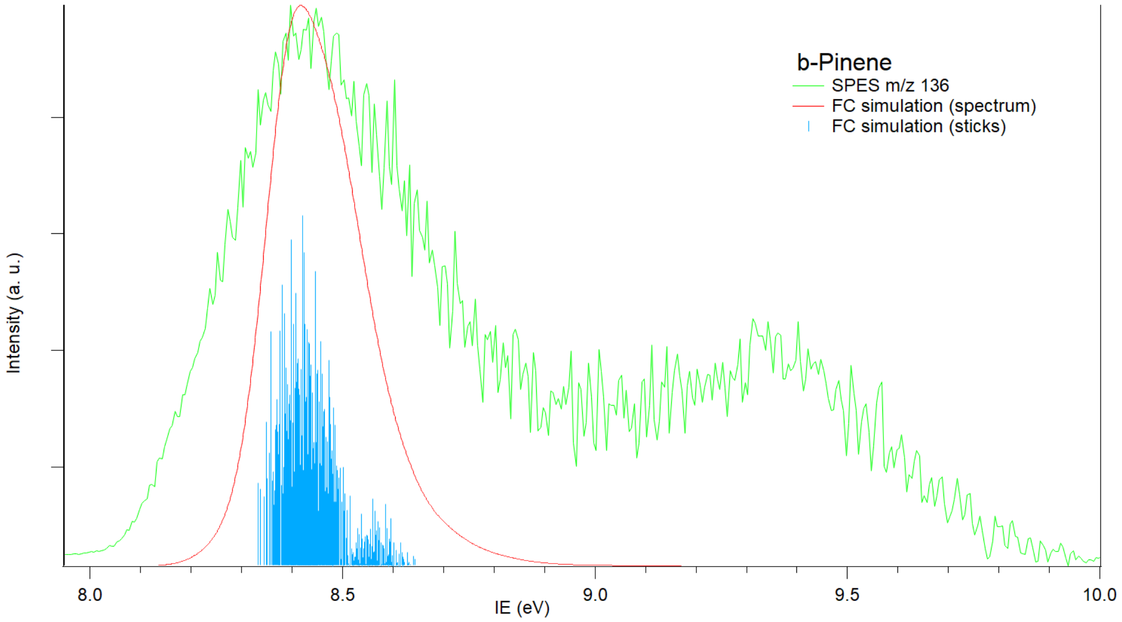

Fig. 84: The corrected SPES spectrum of sabinene (m/z 136) over the X-band (green curve) together with the results of the FC simulation. The blue sticks are showing the FC factors for transitions from the vibrationless state of the neutral, from which only 500 of the most dominant transitions are plotted here. The red solid curve is the simulated FC spectrum obtained by convoluting a Lorentzian shaping function (cutoff=1500 cm^{-1} and FWHM=400 cm^{-1}) to any of the sticks. For more information see the text.

3.2. Conclusion

Photoelectron-Photoion coincidence spectroscopy techniques like PEPICO and SPES enabled us to study the fragmentation dynamics of the monoterpenes. Particularly, comparing the mass-selected SPES with the OVGF calculation for any molecule reveals the dissociative or non-dissociative character of ionisation pathways from the HOMO and HOMO-1 orbitals. In most of the cases studied here, the ionisation from HOMO orbital was quite stable while the ionisation from HOMO-1 orbital was recognised to be the very dissociative. The fragmentation threshold for five monoterpenes was specified precisely thanks to the high resolution of the slow photoelectron spectroscopy technique. The comparison between the experimental results and the theoretical calculation was also helpful to declare the contribution of the HOMO and HOMO-1 to the X-band region. For example, for limonene the HOMO-1 is also contributing to some parts of the X-band region while for the other monoterpenes the majority of the X-band only corresponds to ionisation from the HOMO orbital. This point will be valuable in the following chapters when we will be studying the PECD of each molecule.

The other achievement was the assignment of the vibrational structures observed in the X-band of the monoterpenes using FC simulations. The frequency calculation we did here was helpful to clarify the kind of nuclear motions that can affect the photoelectron spectrum of the molecules. For example, in the case of α-pinene, stretching of the double bond in the main was recognised to be responsible for the main structures in the photoelectron spectrum. This kind of information is key for interpreting the vibrational dependency of PECD. In fact, assigning the vibrational structures in the photoelectron spectrum enables us able to investigate the vibrational dependency of PECD more precisely as we will see in Chapters 5, 6 and 7.

Here, we not only reported the experimental/theoretical results for five of the most interesting members of the monoterpene family but also pointed out some of the similarities or differences between them. It was discussed that how some differences in their geometrical structure can lead to different photoelectron spectra. For example, α-pinene, 3-carene, and limonene who possess a double bound in their 6-membered ring are showing a more vibrationally structured SPES rather than β-pinene and sabinene. In addition, limonene was realised to have a less rigid geometry rather than the other bicyclic monoterpenes allowing it to take various conformers. We also showed how the assignment of the four main vibrational structures observed in α-pinene SPES could be different from those in 3-carene SPES; in the case of α-pinene the four main vibrational peaks were assigned to a regular progression in normal mode ν56 (endo-cyclic double bound stretching) while in the case of 3-carene some of the vibrational peaks were assigned to excitations of normal modes ν60 and ν65 (symmetric and antisymmetric stretching of the methyl group attached to the main ring, respectively).

4. Chemical Composition and Enantiomer Excess Analysis Using Photoelectron Spectroscopy

4.1. Introduction

Essential oils (EOs) obtained from aromatic plants have found a variety of applications in pharmacology, food science and the cosmetic industry [101-108] demanding their composition to be fully characterized in the purpose of determining the quality, geographical origin and genuineness of the oils as well as revealing any possible contamination. Among the EOs, the black pepper oil and Mexican lime were selected for investigation in this study. Massive and comprehensive reviews on these oils are available describing their chemistry, analytical tools, extraction methods, applications, etc. [109, 110]. Over 100 compounds have been found in black pepper oil [111] while the citrus oils are even more complex matrices that are composed of about 400 different chemicals [112]. The composition of the EOs depends on several factors like geographical origin, adulteration, and storage conditions as well as the cultivation, extraction, and separation methods [113, 114].

Volatiles are the dominant species in EOs, ranging from 85% to 99% of the total compounds in citrus oils for example. Monoterpene and sesquiterpene hydrocarbons, their oxygenated derivatives, as well as aliphatic aldehydes, alcohols, and esters create the majority of the volatiles in black pepper and citrus oils [114-116]. Monoterpenes, including α-pinene, β-pinene, limonene, 3-carene, sabinene, γ-terpinene and α-phellandrene, contribute from 88% to 98% of the total volatile compounds in citrus oils [112, 117] and from 30% to 70% of the total volatile compounds in black pepper oil [115, 116].

The authentication and quality control of EOs [112, 118, 119] places a huge importance on their chemical composition (cc) and enantiomer excess (ee) analysis. Currently, the main analytical tool to study the cc and ee of volatile compounds of the EOs is Gas Chromatography (GC) with a variety of methods such as conventional and comprehensive GC as well as fast and very fast GC [120]. In well-established GC methods, mass spectroscopy information, linear retention indices (LRIs) and commercial standards are applied to identify the compounds present in the mixture, while a flame ionization detector (FID), considering the relative peak areas generated by the specific GC-FID software, is used to quantize the analysis [120].

Depending on the complexity of the mixtures, two- or multi-dimensional GC (MDGC) may be needed [121]. Normally, in the first capillary, non-polar column, most of the compounds and their enantiomers can be separated; however; if there are any overlapping peaks remaining at the end of the first column, the second apolar column/dimension will separate them. In terms of EOs analysis, the second column often is added in order to determine the ee of the compounds. The most popular material used as the stationary phase in the second column is derivatized cyclodextrins [122].

Many studies on EOs ee analysis have been done in the past two decades using multidimensional enantioselective gas chromatography [123-125]. However, all of them suffer from the shortcomings of the GC method. The first limitation of GC methods in determining the ee of the EOs is that "a universal selective chiral capillary is not available" [120]. In complex mixtures, there might be plenty of chiral standards to which the response of the column would be different or a single column may not be able to separate them at all. So, for a given sample, in order to get a complete set of analysis, several different columns should be used, reducing the certainty of the results. In addition, in many cases, a mass spectrometer is added to the line to discriminate against the remaining overlapping peaks coming out from the columns which itself decreases the reliability of the qualitative/quantitative information [120]. The other drawback of GC methods is that the sample needs to be injected into the column at a relatively high temperature in order to vaporize. On the other hand, to increase the separation power of the columns, a temperature ramp is applied; the temperature of the columns is increased up to a few hundred degrees through several steps. Experiencing such a high temperature can be destructive to the initial sample in terms of causing fragmentation for some standards or inducing chemical reactions between different compounds. Both fragmentation and chemical reactions will change the composition of the sample, making the results less reliable. Actually, the compounds that are coming out from the columns might not be exactly those present in the initial mixture injected into the columns. The other disadvantage of GC methods is that the sensitivity of the detection system, normally a Flame Ionisation Detector (FID), could be different for different compounds. In an FID system, the ions created for each compound are being counted and integrated as the area under the corresponding peak. Firstly, in the flame, it could be possible to get a different level of ionisation for different samples. This could be pronounced in the case of non-volatile samples that can reside or stick to the column more easily. Secondly, the outcome of FID would be several peaks whose relative area to be considered as the composition of the mixture. In this case, the question is how well related are the relative peak area of a compound to its abundance in the mixture?

As "there appears to be little room for future improvement in the MDGC instrumental field" [120], people have started looking for other possible alternatives. Fourier Transform Infrared (FTIR) spectroscopy, as well as FT-Raman spectroscopy, have been shown to be powerful analytical tools in both qualitative and quantitative composition analysis of the EOs [126-128]. These methods are finding application in quick quality control of the EOs [129-134], removing the need for relatively time-consuming MDGC methods. The limitation of such techniques is that they just can be applied to get the composition of the oils, but cannot provide any information about the ee of the chiral compounds, which contribute for the most part of the oils. So, switching from GC methods to spectroscopic techniques, there is still some technique needed to provide both the cc and the ee information of the sample simultaneously.

In this chapter, we are introducing a new method, based on photoelectron spectroscopy, to measure both the cc and ee of the volatiles in multi-compounds EOs simultaneously. The idea is to get the composition of the oils by comparing the photoelectron spectrum of the oil to that of the pure compounds and extract the ee of each compound by comparing the PECD spectrum of the oil to that of the enantiomerically pure compounds. In terms of cc, we can use either the normal VMI photoelectron spectrum (VMI-PES) measured at fixed photon energies or the high-resolution Slow Photoelectron Spectrum (SPES), while for the ee analysis, the PECD spectrum measured at fixed photon energies are used. For more detailed information on measuring SPES, VMI-PES, and PECD spectra see Chapters 3 and 5. Black pepper oil is mainly composed of the five standards mentioned in the abovementioned chapters and there might be some amount of γ-terpinene in Mexican lime oil. It has been tried to keep most of the experimental conditions the same for all the measurements. However, normalisation with respect to the experimental parameters which have been set differently for different species will be applied, as discussed below.

4.2. Theoretical Approach

4.2.1. SPES and VMI-PES fitting: cc analysis

Suppose that the molecular beam is crossed by the radiation beam creating an interaction volume V with a cross section A, as shown in Fig. 85. As the detector system we are using, a delay-line detector, is a counting system, the photoelectron spectra for each sample (both the

VMI-PES and the SPES) are proportional to the ionization rate r^i, acquisition time t^i and the interaction volum V^i for that sample. The latter is limited mostly by the cross section of the radiation beam used for any sample, A^i, because the molecular beam geometry is supposed to be roughly the same for all the measurements, as all of the molecular beam experimental parameters (including carrier gas, backing pressure, and skimmer diameter) have been kept the same for different measurements.

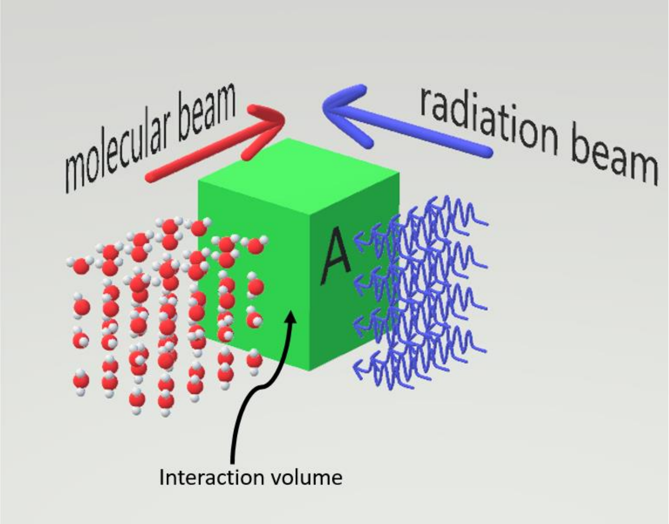

Fig. 85: Simplified schematic of interaction volume and its cross section to the radiation beam. For a more realistic interaction volume see Fig. 34.

So, the SPES of a pure sample can be given by:

$$SPES^i = (r^i t^i A^i) s^i \qquad \text{(Eq. 21)}$$

where s^i is the instrumental sensitivity factor and will be applied later on if different measurements have been done in different runs of the experiment. For example, as the detector systems get older, their sensitivity can decrease or any change in the electronics can increase or decrease the detection threshold affecting the final intensity of the spectrum. The ionization rate itself depends on the photon flux (number of photons per unit time per unit area) at the time of measurement, φ_{ph}^i, the number of molecules present in the interaction volume n^i as well as the interaction cross section σ^i for the given sample. Therefore, we can obtain:

$$SPES^i = \varphi_{ph}^i n^i \sigma^i t^i A^i s^i \qquad \text{(Eq. 22)}$$

The number of the molecules in the interaction volume is proportional to the gas phase mole fraction of the sample which itself, by assuming ideal liquids, would be equal to the mole fraction of the sample in the liquid phase:

$$n^i = ax^i \qquad \text{(Eq. 23)}$$

where x^i is the mole fraction of the sample in the liquid phase and a is a constant relating the n^i and x^i together. For pure samples, x^i is equal to one; we can also absorb the constant a into the cross-section as $\sigma'^i = a\sigma^i$, and call the σ'^i as the effective cross section. These lead us to:

$$SPES^i = \varphi^i_{ph}\sigma'^i t^i A^i s^i \qquad \text{(Eq. 24)}$$

The SPES of a mixture of several pure compounds can be obtained through a similar procedure. Actually, the spectrum of a mixture is a sum over all the compounds as below:

$$SPES^{mix} = \sum_i (r^i t^{mix} A^{mix}) s^{mix} \qquad \text{(Eq. 25)}$$

where t^{mix}, A^{mix} and s^{mix} are respectively the acquisition time, the cross section of the radiation beam, and the instrumental sensitivity factor at the time of measuring the spectrum of the mixture. We also should notice that the ionization rate for any compounds present in the mixture is a function of photon flux at the time of measuring the mixture's spectrum, φ^{mix}_{ph}, as well as the mole fraction and the effective cross section of that specific compound. So, one can write:

$$SPES^{mix} = \sum_i \varphi^{mix}_{ph}\sigma'^i x^i t^{mix} A^{mix} s^{mix} \qquad \text{(Eq. 26)}$$

By multiplying $\varphi^i_{ph} t^i A^i s^i$ to the (Eq. 26) and using (Eq. 24) we can obtain:

$$SPES^{mix} = \sum_i x^i \left(\frac{\varphi^{mix}_{ph} t^{mix} A^{mix} s^{mix}}{\varphi^i_{ph} t^i A^i s^i} SPES^i\right) \qquad \text{(Eq. 27)}$$

or simply

$$SPES^{mix} = \sum_i x^i SPES'^i \qquad \text{(Eq. 28)}$$

where $SPES'^i$ is the spectrum of each pure compound after being normalized with respect to the experimental parameters including the photon flux, the acquisition time, the cross section of the radiation beam and the instrumental sensitivity factor. The normalisation factor for each compound is defined as the coefficient of $SPES^{i}$ inside the parentheses in (Eq. 27). The same expression can be obtained similarly for the VMI-PES as:

$$PES^{mix} = \sum_{i} x^{i} PES'^{i} \qquad \text{(Eq. 29)}$$

In practice, the photon flux and the cross section of the radiation beam are tuned by caches setting and the exit slit in the monochromator. The cross-section of the beam is linearly proportional to the exit slit while the photon flux is reported by the DESIRS beamline scientists to be a function of photon energy showing a nonlinear relation with the caches settings, as shown in Table 7. In all the SPES measurements, the cache value has been set as 1 mm while in the VMI measurements, the photon flux has been controlled by adjusting the cache to take values such as 1.0 mm, 1.1 mm, 1.2 mm and 1.3 mm. So, we do not need to normalise the SPES data with the cache settings, but we use the values in Table 7, wherever needed, to normalise the VMI-PES.

Table 7: Relation of the photon flux with the cache setting with the photon flux being normalised to one at a cache value of 1 mm.

Caches (mm)	Photon Flux at hv=9.0 eV	Photon Flux at hv=9.0 eV
1	1	1
1.1	1.08	1.08
1.2	1.15	1.14
1.3	1.2	1.19

Based on (Eq. 28) and (Eq. 29), we can try to get the chemical composition cc^{i} (equivalent to the mole fraction x^{i}) of the compounds in a mixture by making a linear combination of the individual spectra of the pure compounds and fit it to the spectrum of the mixture. The coefficient of the fits would be directly equal to the cc of the pure compounds.

We use linear least square regression in MATLAB R2016a [135] to obtain the fit. In terms of SPES and VMI-PES fitting, a built-in function called *lsqnonneg* has been used, which uses linear least square regression but constraining the coefficient to the positive values. At the end of the fitting process, the coefficients are normalised to sum up to one. These constraint on the coefficients in SPES and VMI-PES fittings are compatible with the fact that the cc of any compound in a mixture should be a positive value ranging between zero to one, $0 \leq cc^i \leq 1$, with the sum of all of them to be one, $\sum cc^i = 1$.

Another point we take into account in the fitting process is that the intensity of the spectra, and consequently the error bars, are not the same over the whole scan range. Our standard range to record the SPES of all the oils is [7.8 eV, 10.5 eV] but, for example, black pepper oil SPES shows considerable intensities just within [8.1 eV, 9.8 eV], as we will see later on in this chapter. In addition, the error bars are not the same for the entire scan range. So, we must weight the data points in a way to highlight those with a higher intensity but smaller error bars. The following expression is then a suitable function to weight the data points properly:

$$w_a^{SPES} = \frac{SPES_a^{mix}}{dSPES_a^{mix}} \qquad \text{(Eq. 30)}$$

where $dSPES$ is the error bars on SPES and the subscript a is an index for individual data points in the fitting range. The same kind of weighting is considered in VMI-PES fitting as below:

$$w_a^{PES} = \frac{PES_a^{mix}}{dPES_a^{mix}} \qquad \text{(Eq. 31)}$$

4.2.2. PECD fitting: ee analysis

In Sec. 1.3.2.3, we reviewed the research work carried out so far in terms of the relation of the PECD signal observed for a sample with the ee of its components. The first point was that for the single component mixtures, the PECD signal is linearly dependent on the ee of the sample and varies between plus and minus of the PECD of the enantiomerically pure sample. This implies that for a single component mixture:

$$PECD^{mix} = ee^i PECD^i \qquad \text{(Eq. 32)}$$

where the $PECD^i$ is the PECD of the enantiomerically pure sample. However, if the mixture is a multicomponent one, some modification to the equation above is needed. Let's consider an extreme case where a mixture is composed of two chiral molecules with the cc of the compounds being 99% and 1%. It is expected for the PECD of the mixture to be dominated by the PECD of the first compound, whose abundance is higher than the other. For this reason, we need to weigh the PECD of the compounds by their cc and photoelectron spectrum. A weight function having such properties and summing up to one is:

$$\overline{W^{\iota}} = \frac{cc^{i}PES^{i}}{\sum_{i} cc^{i}PES^{i}} \qquad \text{(Eq. 33)}$$

where the denominator of the right hand side is just the photoelectron spectrum of the mixture, based on (Eq. 28) or (Eq. 29). On the other hand, in less extreme cases, the PECD of every significant chiral compound should contribute to the PECD of the mixture. So, the expression relating the PECD of a multicomponent mixture to the PECD of its enantiomerically pure compounds can be written as:

$$PECD^{mix} = \sum_{i} \overline{W^{\iota}} ee^{i} PECD^{i} \qquad \text{(Eq. 34)}$$

or

$$PECD^{mix} = \sum_{i} ee^{i} \left(\frac{cc^{i}PES^{i}}{\sum_{i} cc^{i}PES^{i}} PECD^{i}\right) \qquad \text{(Eq. 35)}$$

where in the last step we have used (Eq. 33).

The expression given in (Eq. 35) is what we use to get the ee of each monoterpene present in the sample. To that aim, a MATLAB built-in function called *lsqlin* was used, which applies linear least square regression but with some constraints on the lower and upper limits of the coefficients. Since the ee of each compound naturally must be a value ranging in [-1, +1], the lower and upper limits for ee in the PECD fitting have been set as -1 and +1, respectively.

Similar to the SPES and VMI-PES fitting, we need to weight the data points in the fitting range to highlight the meaningful and less noisy data points of the spectra. The weight function that we use to weight the PECD data is:

$$w_{a}^{PECD} = \frac{PES_{a}^{mix}}{dPECD_{a}^{mix}} \qquad \text{(Eq. 36)}$$

where $dPECD$ stands for the error bars of the PECD spectrum of the mixture and the subscript a is an index for individual data points in the fitting range. This means that the data points wherever the intensity of the oil's VMI-PES is stronger and also the oil's PECD is less noisy, should be considered as the most important parts of the fitting range.

It should be noticed that we need to do the VMI-PES or SPES fitting to get the chemical composition of the mixture before applying (Eq. 35) to reveal the ee of each compound present in the mixture. The other point is that there might be some achiral compounds in the mixture contributing to the photoelectron spectrum, but not to the PECD. In such cases, $\overline{W^{\iota}}$ will sum up to one only if all the compounds including achiral ones are taken into account. So, wherever there are some achiral compounds in our mixtures, we will consider a zero PECD spectrum for them and then apply (Eq. 35 with the achiral species to be involved.

4.3. Experiments

In this chapter, we will report the results of chemical composition and enantiomer excess analysis for two EOs purchased from Sigma Aldrich: black pepper oil and Mexican lime oil with their main monoterpene components being α-pinene, β-pinene, limonene, 3-carene, sabinene, γ-terpinene. A detailed explanation of the experimental setup and the methodology as well as the technical information about the pure compounds is given in chapters 3 and 5. For cc analysis, we need the SPES or VMI-PES of the oils as well as those of the chemically pure compounds while for the ee analysis we need the VMI-PES and VMI-PECD spectra of the oils and the compounds (except the VMI-PECD of γ-terpinene as it is achiral). We have done the VMI measurements at two photon energies just to find out what effects the photon energy could have on the analysis. So, in total, we have five oils and seven compounds for each of which we had to measure a SPES spectrum as well as two VMI-PES, requiring plenty of time which is not easy to obtain in synchrotron facilities. Doing all the measurements in a single beamtime was not possible as each beamtime is consistent of maximum six working days; so, the measurements had to be done in three different beamtimes in March 2016, March 2017, and June 2019. We also needed to repeat some certain measurements in two beamtimes to check the instrumental sensitivity, which is essential in normalization of the data set. Table 8 shows the dates when each measurement was made.

Table 8: list of al SPES and VMI measurements done for the EOs and their compounds; for more details, see the text.

	SPES	VMI measurement at hν=9.0 eV	VMI measurement at hν=9.5 eV
March 2016	black pepper oil α-pinene β-pinene limonene 3-carene sabinene	black pepper oil α-pinene β-pinene Limonene 3-carene	black pepper oil α-pinene β-pinene limonene 3-carene

March 2017	Mexican lime oil	Mexican lime oil sabinene	Mexican lime oil sabinene
June 2019	γ-terpinene	γ-terpinene	γ-terpinene

In the first beamtime, March 2016, the aim was to collect all the data needed for the cc and ee analysis of black pepper oil, as it is mostly composed of only five of the monoterpenes. SPES and VMI measurements for the oils and all the compounds were done successfully except the VMI measurements for the sabinene which was postponed to March 2017 due to the shortage of time. In March 2017, the SPES and VMI measurements for the other oil, Mexican lime oil, were done as well as the VMI measurements of the sabinene and. Finally, in June 2019, the SPES of γ-terpinene was measured. Since γ-terpinene is not a chiral species, there was no need to measure the PECD of it; however, we made a couple of VMI measurement at fixed photon energies of 9.0 eV and 9.5 eV on this sample, using linear horizontal polarization, just to get the VMI-PES of the sample for cc analysis.

As mentioned above, one of the issues when comparing data from one run of the experiment to another is the instrumental sensitivity which does not remain the same from one beamtime to another. Indeed, the intensity of the VMI-PES, as discussed above, depends on several factors. We have control over some of these like exit slit and the caches in the monochromator, as well as the data acquisition time. However, there might be other factors out of our control like the current of the storage ring of the synchrotron, the threshold of the electronics, the gain of the detector, etc.; we group all of those parameters and call them instrumental sensitivity. Our procedure to get the instrumental sensitivity factor is to record the VMI-PES of the same sample in two beamtimes and normalize them with the experimental parameters under our control. If there is any difference remaining in the intensity of the VMI-PES spectrum we consider that as the instrumental sensitivity factor. To illustrate this, look at the VMI-PES recorded for β-pinene at hν=9.5 eV in March 2016 and June 2019 shown in Fig. 86. The two spectra are quite similar to each other in structure, showing the reproducibility of our experiments. However, the intensity of them is not identical which is due to different experimental conditions. We can compare the two spectra using the following:

$$\frac{PES_{2019}}{PES_{2016}} = \frac{(cache \times ex\_slit \times acq\_time)_{2019}}{(cache \times ex\_slit \times acq\_time)_{2016}} \times \frac{s_{2019}}{s_{2016}} \qquad \text{(Eq. 37)}$$

where $cache$, ex_slit and acq_time are standing for cache setting, exit slit setting and the acquisition time, respectively, and s is the instrumental sensitivity factor. The subscript 2016 or 2019 refers to different runs of the experiment, March 2016 and June 2019, respectively. We select the intensity of the spectra at their peak position to enter as PES_{2019} and PES_{2016} into the (Eq. 37). After putting the values of other experimental parameters inside the parenthesis in (Eq. 37), we obtain $\frac{s_{2019}}{s_{2016}} = 0.93$.

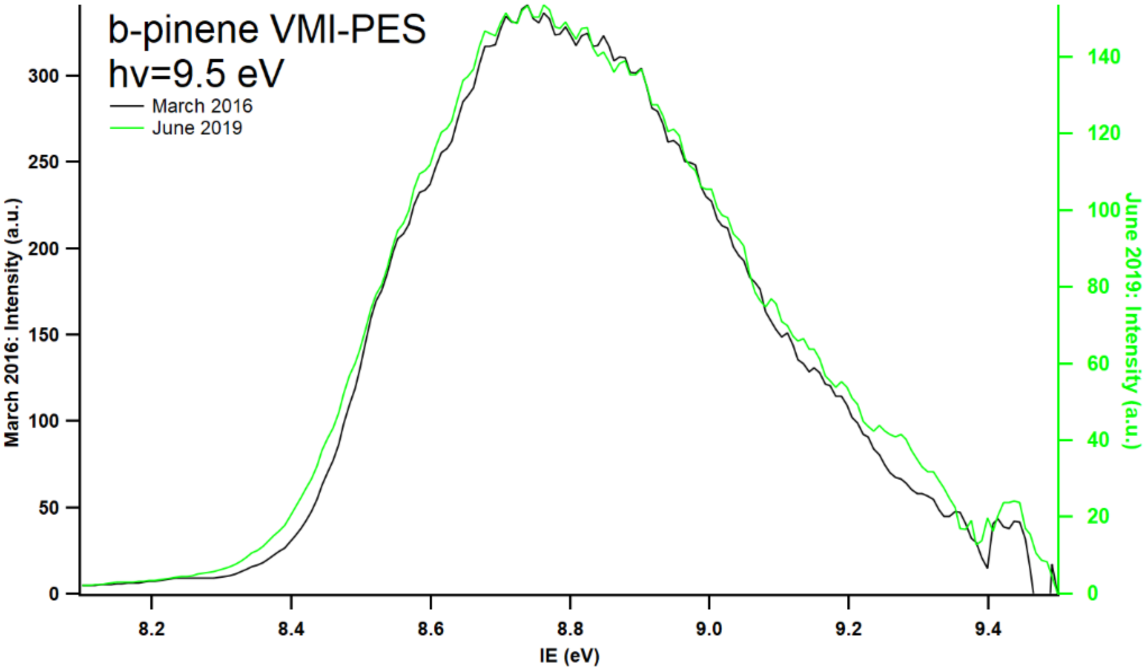

Fig. 86: VMI-PES of b-pinene recorded in March 2016, black, and June 2019, green.

The same procedure can be followed to get the ratio of the sensitivity factors of March 2017 and June 2019. Actually, sabinene is the species whose VMI-SPES at hν=9.5 eV in these two runs were recorded, not shown here; applying an equation like (Eq. 37) leads us to $\frac{s_{2019}}{s_{2017}} = 0.45$. To get the sensitivity factor ratio between March 2016 and March 2017 we can just use the below cyclic relation, connecting the three different beamtime together:

$$\frac{s_{2017}}{s_{2016}} = \frac{s_{2017}}{s_{2019}} \times \frac{s_{2019}}{s_{2016}} \qquad \text{(Eq. 38)}$$

which gives us $\frac{s_{2017}}{s_{2016}} = 2.06$.

The black pepper oil, and five of the monoterpenes constituents, were also sent to the gas chromatography analysis to get the cc and the ee of the compounds as a reference to which we can compare the results of the fittings. The cc and ee analyses were done in Nice using a GC*GC machine coupled with a ToF mass spectrometer. The primary column was Chirasil-Dex CB (24.540 m × 0.25 mm ID, 0.25 μm film thickness) modulator-coupled to a DB Wax secondary column (1.40 m × 0.1 mm ID, 0.1 μm film thickness). Helium was used as the carrier gas at a constant flow of 1 mL min^{-1}. Sample volumes of 1 µL were injected in the split mode at an injector temperature of 230 °C. The primary oven was operated as follows: 40 °C for 1 min, the temperature increase of 5°C min^{-1} to 80 °C and held for 5 min, followed by 0.5 °C min^{-1} to 100 °C, then temperature increase of 20 °C min^{-1} to 180 °C and an isothermal hold at 180 °C for 2 min. The secondary oven used the same temperature program with a constant temperature offset of 30 °C. A modulation period of 3 seconds was applied. The TOF-MS was operated at a storage rate of 150 Hz, with a 25−500 amu mass range. Data were acquired and processed with LECO Corp ChromaTOF$^{\text{TM}}$ software.

4.4. Black Pepper Oil

Black pepper is a significant agricultural crop with high nutritional, health, and medicinal benefits [136-138]. The plant is native to South East Asia and China but it is being cultivated in tropical regions ranging from many parts of India, Brazil, Indonesia, Sri Lanka, Vietnam, to Malaysia [139]. Several studies have shown that the major components present in black pepper oil are the volatile monoterpenes ranging from 60% to 80% of the total composition [111, 116, 140]. However, the cultivation, storage, and extraction conditions are likely to affect the individual percentage of any of these monoterpenes [110, 139, 141]. In this section, we will report the results of the SPES, VMI-PES, and VMI-PECD of the black pepper oil sample we had and will perform the cc and ee analysis on it based on the method explained above.

The SPES of the black pepper oil was measured over the photon energy range [7.8 eV, 10.5 eV] with steps of 5 meV. All the experimental conditions were kept similar to those for the monoterpenes reported in Chapter 3, except the acquisition time for each step and the exit slit setting, for which we will normalize the data. The experimental setup for the VMI measurements was also the same as that for the standard monoterpenes reported in Chapter 5 although the exit slit, acquisition time, and the cache settings were individually adjusted to control the count rate and prevent detector saturation.

Fig. 87, Fig. 88 and Fig. 89 show the results of SPES fitting, VMI-PES fitting at hν=9.5 eV and VMI-PES fitting at hν=9.0, respectively, for black pepper oil. Fitting a linear combination of all the seven basis mentioned in Sec. 4.3 revealed that there is no γ-terpinene and α-phellandrene present in the oil; so, in these figures, only the compounds contributing to the black pepper oil composition are plotted.

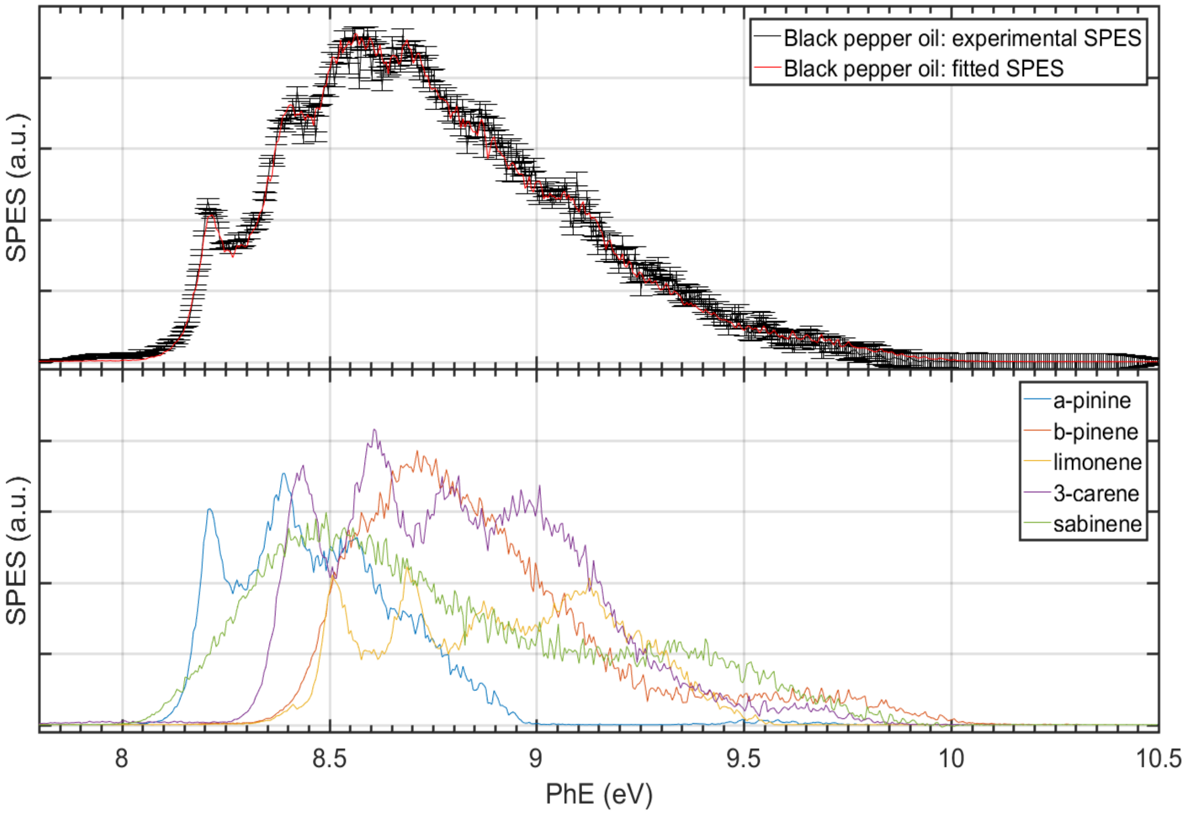

Fig. 87: Black pepper oil SPES fitting. Top: the fit, red, on top of the experimental SPES of the oil, black. Bottom: the experimental SPES of individual basis present in the oil. All the data shown in this figure have been measured in March 2016 with the same experimental setup. The same experimental parameters have been applied except the exit slit and the acquisition time for which the data have been already normalized.

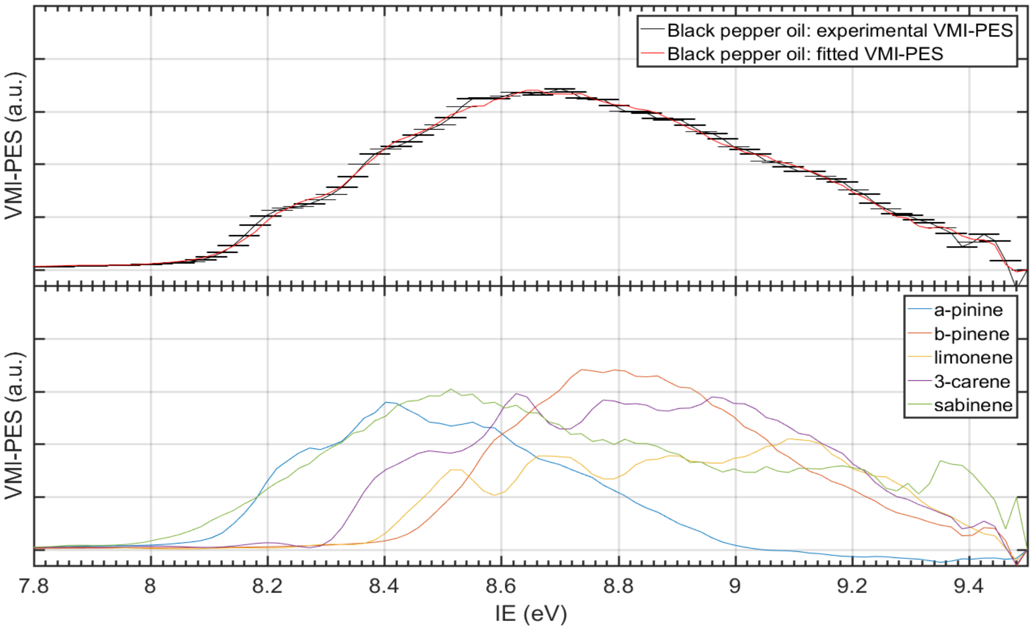

Fig. 88: Black pepper oil VMI-PES fitting at hν=9.5 eV. Top: the fit, red, on top of the experimental VMI-PES of the oil, black. Bottom: the experimental VMI-PES of individual basis present in the oil. All the data shown in this figure have been measured in March 2016 with the same experimental setup, except the VMI-PES of the sabinene which has been measured in March 2017. The correction for sabinene impurity has already been done, see Sec. 3.1.5 and Sec. 5.2.5. The same experimental parameters have been applied except the exit slit, cache setting, and the acquisition time for which the data have been already normalized.

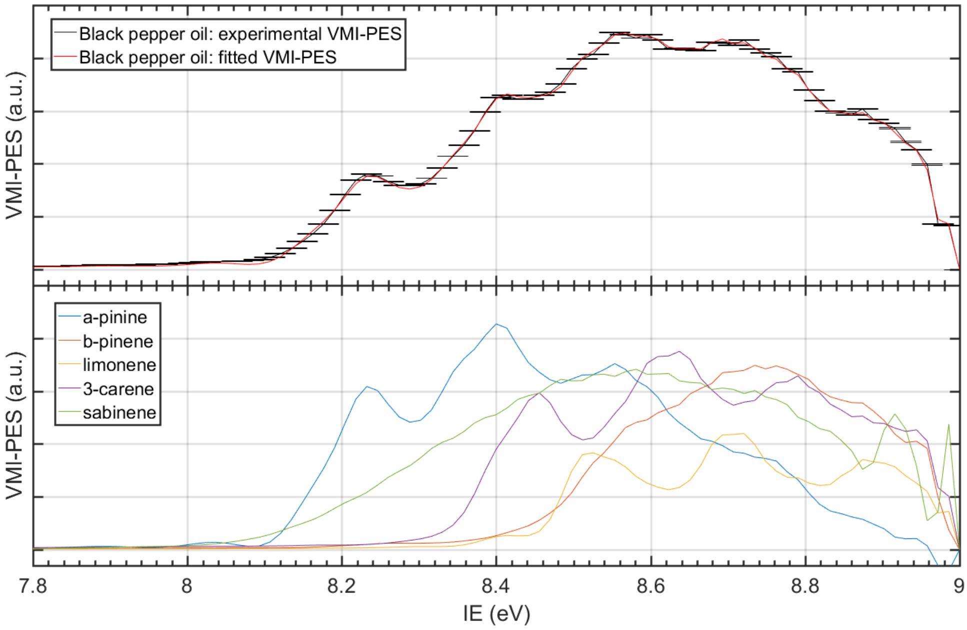

Fig. 89: Black pepper oil VMI-PES fitting at hν=9.0 eV. Top: the fit, red, on top of the experimental VMI-PES of the oil, black.Bottom: the experimental VMI-PES of individual basis present in the oil. All the data shown in this figure have been measured in March 2016 with the same experimental setup, except the VMI-PES of the sabinene which has been measured in March 2017. The correction for sabinene impurity has already been done, Sec. 3.1.5 and Sec. 5.2.5. The same experimental parameters have been applied except the exit slit, cache setting, and the acquisition time for which the data have been already normalized.

The results of the black pepper oil composition obtained through the SPES and VMI-PES fittings are presented in Table 9, in comparison with the results of the GC*GC analysis. The best agreement can be seen between the results of VMI-PES fitting at hν=9.5 eV which is predicting the abundance of α-pinene, β-pinene and sabinene within 1% accuracy and the abundance of limonene and 3-carene within 5% accuracy if the GC*GC results are taken as the reference. However, the result of the SPES fitting and VMI-PES fitting at hν=9.0 eV are also very close to the GC*GC results. The SPES results for all the compounds, except limonene, are within 5% accuracy. In the first look, the SPES could be nominated as the best method for fitting, compared to the VMI-PES, since the resolution of SPES is higher with more vibrational structures being resolved in it; but, as can be seen from Table 9, the VMI-PES fittings are leading to roughly the same results (or even better results when compared to GC*GC analysis). Nonetheless, any deviation between the results of our method and the GC*GC analysis can be attributed to the different detection systems and different levels of sensitivity that GC*GC shows to different compounds, see Sec 4.1 and Sec 4.2.1.

*Table 9: Pepper oil composition obtained through the SPES and VMI-PES fitting in comparison with the results of the GC*GC analysis.*

method compound	SPES	VMI-PES at hν=9.0 eV	VMI-PES at hν=9.5 eV	Average of SPES and VMI fittings	GC*GC
α-pinene	30.99±0.88	28.95±0.65	29.35±3.70	29.76	29.37
β-pinene	20.70±0.60	18.34±0.64	23.98±1.10	21.01	23.56
Limonene	21.27±1.07	28.83±0.98	18.50±3.04	22.87	13.65
3-carene	13.97±0.62	17.13±0.75	11.38±2.14	14.16	16.65
Sabinene	13.07±1.44	6.73±1.32	16.79±5.08	12.20	16.42

The error bars we obtain by fitting the SPES and VMI-PES at hν=9.0 eV are reasonably small; however, the error bars obtained in VMI-PES fitting at hν=9.0 eV are less good. This could be due to the detector gain loss problem that we had, causing the spectra of some basis, α-pinene for example, to become negative in the central parts of the detector. In Fig. 88, it can be seen how the PES of α-pinene becomes negative for energies above 9.0 eV.

The results that we obtained here are also compatible with the GC results for the black pepper oil in the literature, although the two methods are not strictly comparable due to the difference in their mechanism; as a matter of fact, our analysis is done in headspace while the GC results are obtained with the total injection. Actually, for the standards mentioned in Table 9, the range of cc reported in the literature is: (0.3-13) for a-pinene, (2-15.8) for b-pinene, (8.7-26%) for limonene, (0.2-38%) for 3-carene and (0.2-29%) for sabinene [111].

To get the ee of each compound, the PECD fitting at two photon energy was done. Fig. 90 and Fig. 91 show the VMI-PECD spectra of the basis and the oil at photon energies hν=9.5 eV and hν=9.0 eV, respectively. The PECD spectra has been plotted over the region where the intensity of the photoelectron spectrum of the oil is significant, and consecutively, the error bars on the oil's PECD are reasonably small.

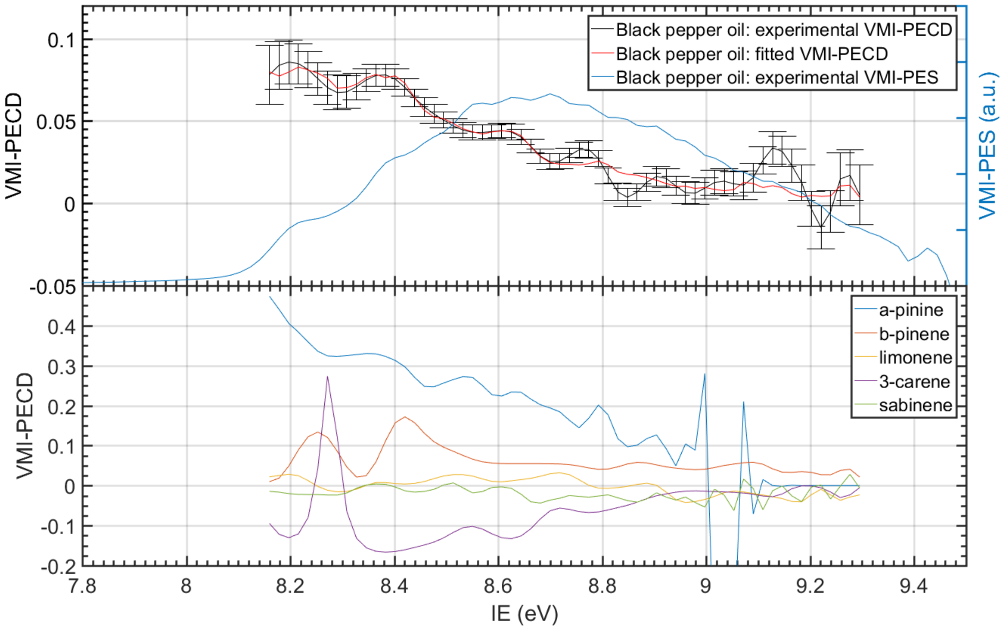

Fig. 90: Black pepper oil VMI-PECD fitting at hν=9.5 eV. Top: the fit, red, on top of the experimental VMI-PECD of the oil, black. The VMI-PES of the oil is also plotted just to have a track of the region where there is a significant photoelectron signal. Bottom: the experimental VMI-PECD of individual basis present in the oil including (+)-(1R,5R)-α-pinene, (-)-(1S,5S)-β-pinene, (+)-(4R)-limonene, (+)-(1S,6R)-3-carene and (-)-(1S,5S)-sabinene. All the data shown in this figure have been measured in March 2016 with the same experimental setup, except the VMI-PECD of the sabinene which has been measured in March 2017. The correction for sabinene impurity has already been done, see Sec. 3.1.5 and Sec. 5.2.5. The same experimental parameters have been applied except the exit slit, cache setting, and the acquisition time for which the data have been already normalized.

The first point about the plots is that at hν=9.5 eV, the PECD of α-pinene shows a dramatic, unrealistic behaviour around the IE of 9.03 eV. This behaviour is just the effect of the pBASEX algorithm when applied to get the PECD signal out of the photoelectron images recorded by a detector with a gain loss in the central part. Actually, there was a gain loss in the detector causing the VMI-PES of α-pinene to become negative at the IE above 9.0 eV, which can be seen clearly in Fig. 88. When VMI-PES changes sign (requiring the VMI-PES to be nearly zero), the pBASEX algorithm results in such a dramatic PECD signal. The same kind of unrealistic PECD signal can be seen for 3-carene around IE=8.25 eV at hν=9.5 eV measurement. However, these problematic PECD values do not contribute to the fitting; they are automatically filtered out since the PECD of each individual compound is being weighted by its corresponding PES, see (Eq. 35). The second point is that the fitted function lies within the error bars of the experimental PECD signal of the oil for most of the data points which is a very good achievement for our method. However, there are some regions such those around IE=9.15 eV at hν=9.5 eV where the PECD signal cannot to be fitted properly. This could be attributed to the presence of some other chiral monoterpenes in the black pepper oil, but not available in the basis set we have considered here. Based on the literature, the other possible monoterpenes are camphene, α-thujene, β-phellandrene etc. with the abundance of less than few percent [111, 116, 140-142]. So, more works in this direction can be done by completing the basis data set and making a more comprehensive library for the analysis to improve the fit.

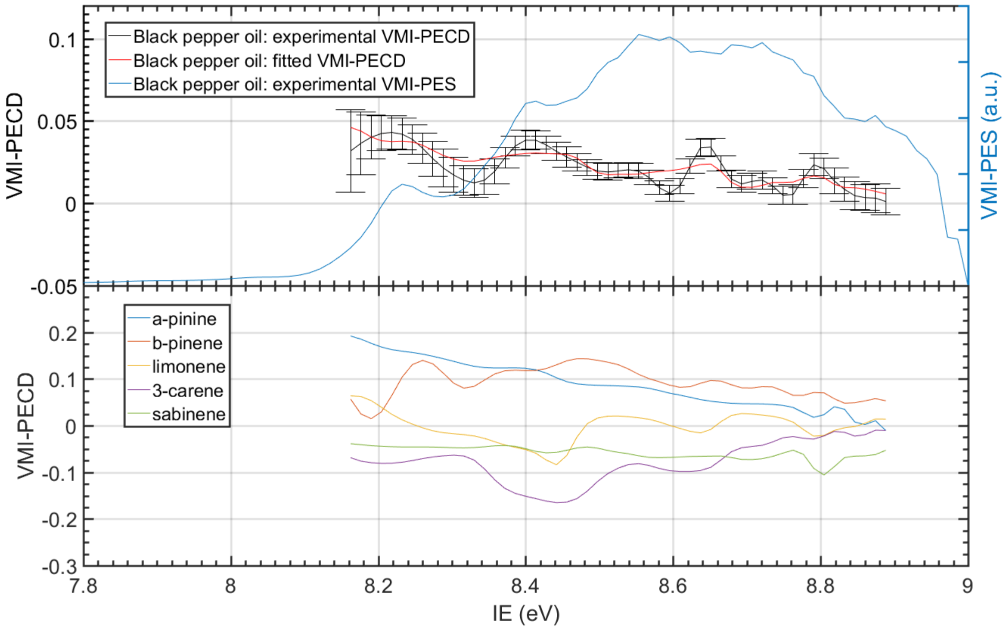

Fig. 91: Black pepper oil VMI-PECD fitting at hν=9.0 eV. Top: the fit, red, on top of the experimental VMI-PECD of the oil, black.The VMI-PES of the oil is also plotted just to have a track of the region where there is a significant photoelectron signal. Bottom: the experimental VMI-PECD of individual basis present in the oil including (+)-(1R,5R)-α-pinene, (-)-(1S,5S)-β-pinene, (+)-(4R)-limonene, (+)-(1S,6R)-3-carene and (-)-(1S,5S)-sabinene. All the data shown in this figure have been measured in March 2016 with the same experimental setup, except the VMI-PECD of the sabinene which has been measured in March 2017. The correction for sabinene impurity has already been done, see Sec. 3.1.5 and Sec. 5.2.5. The same experimental parameters have been applied except the exit slit, cache setting, and the acquisition time for which the data have been already normalized. The PECD curves have not been plotted over regions where the error bars of the oil's PECD are enormously large.

The results of the fittings are presented in Table 10. A very good agreement with the GC*GC results is obtained for α-pinene, β-pinene and sabinene using hν=9.0 eV measurements. The results obtained for α-pinene and limonene using hν=9.5 eV data are also in agreement with the GC*GC results. Additionally, the average of ee obtained at two photon energies for all the compound is roughly matching with the GC*GC results. Just similar to the cc analysis, any difference in the results obtained through our method with those of GC*GC can be attributed to different detection systems as well as to the different sensitivity of the GC*GC method to different compounds. See Sec 4.1 for more details.

The error bars obtained for the VMI-PECD fittings at both the photon energies are relatively large. This could be due the fact that we are using the results of our VMI-PES fitting in the VMI-PECD fitting (see (Eq. 35); so, any uncertainty in the cc values, obtained through the VMI-PES fitting, can propagate into the ee values obtained from the VMI-PECD.

*Table 10: The ee of the pepper oil's compounds obtained through the VMI-PECD fitting in comparison with the results of the GC*GC analysis.*

method / compound	VMI-PECD at hν=9.0 eV	VMI-PECD at hν=9.5 eV	Average of VMI-PECD fittings	GC*GC
a-pinene	28.51±9.55	34.80±3.54	31.66	32.00
b-pinene	82.09±51.99	37.83±21.42	59.96	81.48
Limonene	-99.84±63.42	-21.27±40.60	-60.56	-22.97
3-carene	-26.69±18.99	-86.82±27.58	-56.76	-56.34
Sabinene	97.57±84.98	24.70±59.28	61.14	87.80

As can be seen, the ee obtained with the hν=9.0 eV is in some cases different from those obtained from hν=9.5 eV measurements. The same thing happens for the cc analysis as well. In addition, for a given compound, hν=9.5 eV data set might give more accurate results, if compared with the GC*GC output. For example, the hν=9.0 eV measurements overestimate the abundance of limonene, 28.83%, while hν=9.5 eV measurements lead to 18.50% as the abundance of limonene, which is more comparable to the results of GC*GC. One possible explanation for this is the higher IP of limonene relative to that of the other compounds. Indeed, limonene shows a significant photoelectron signal from 8.45 eV to 9.5 eV(Fig. 87). Obviously, hν=9.5 eV measurements include that range but the hν=9.0 eV one does not. On the other hand, the significant photoelectron signal of α-pinene happens between 8.1 EV to 9.0 eV, included in both the hν=9.0 eV and hν=9.5 eV measurements. For this reason, the abundance of α-pinene obtained through both of these data sets are very compatible, 28.95%, and 29.35% for hν=9.0 eV and hν=9.5 eV measurements, respectively. Looking at Table 10, we found that hν=9.5 eV is the better choice for the limonene ee as well. It gives the ee of the limonene to be -21.27, very close to the results of the GC*GC analysis, -22.97, while hν=9.0 eV measurement leads to -99.84 which is quite far from GC*GC results. So, the conclusion could be that for the fitting process to give more accurate results, it would be prefrable to do the VMI measurements at a photon energy (or over a scan range, for SPES) that includes the whole significant spectrum of all the standards.

4.5. Mexican Lime Oil

The volatile fraction of the lime oil has been reported to be more than 85% of the total mixture [117, 143]. Like most of the EOs, the volatiles included in lime oil are monoterpenes, inparticular, the basis mentioned in 4.1. Some GC analyses on lime oil samples of different origins have shown that 3-carene has no contribution in the lime oil composition, while there are about 5-20% of γ-terpinene present in this oil [109, 117, 118]. So, for the Mexican lime oil, we add the γ-terpinene to the five standards we had in Sec. 4.4.

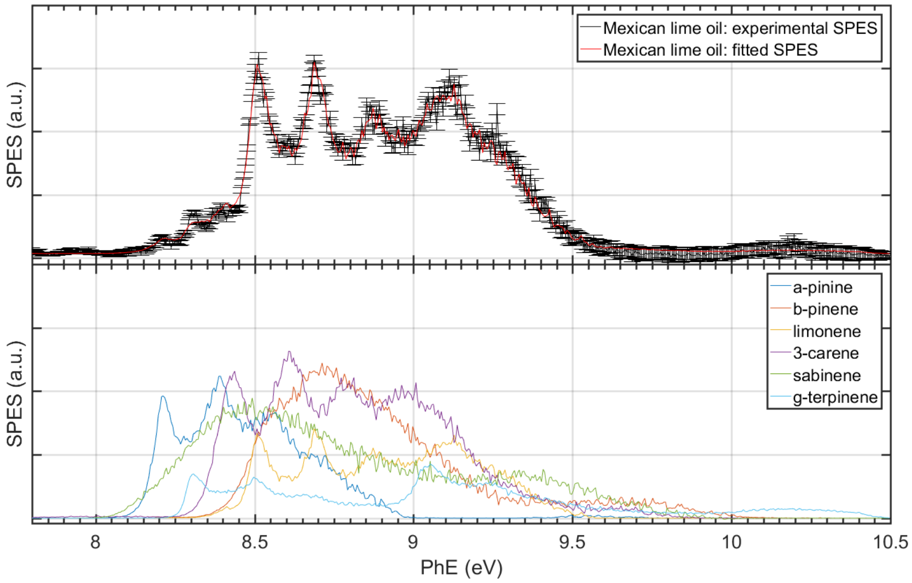

Fig. 92: Mexican lime oil SPES fitting. Top: the fit, red, on top of the experimental SPES of the oil, black. Bottom: the experimental SPES of individual basis present in the oil. All the data shown in this figure have been measured in March 2016 with the same experimental set up except the SPES of the oil, measured in March 2017, and the SPES of γ-terpinene, measured in June 2019. The same experimental parameters have been applied except the exit slit and the acquisition time for which the data have been already normalized. The data have been normalised with respect to the instrumental sensitivity factor from beamtime to beamtime as well.

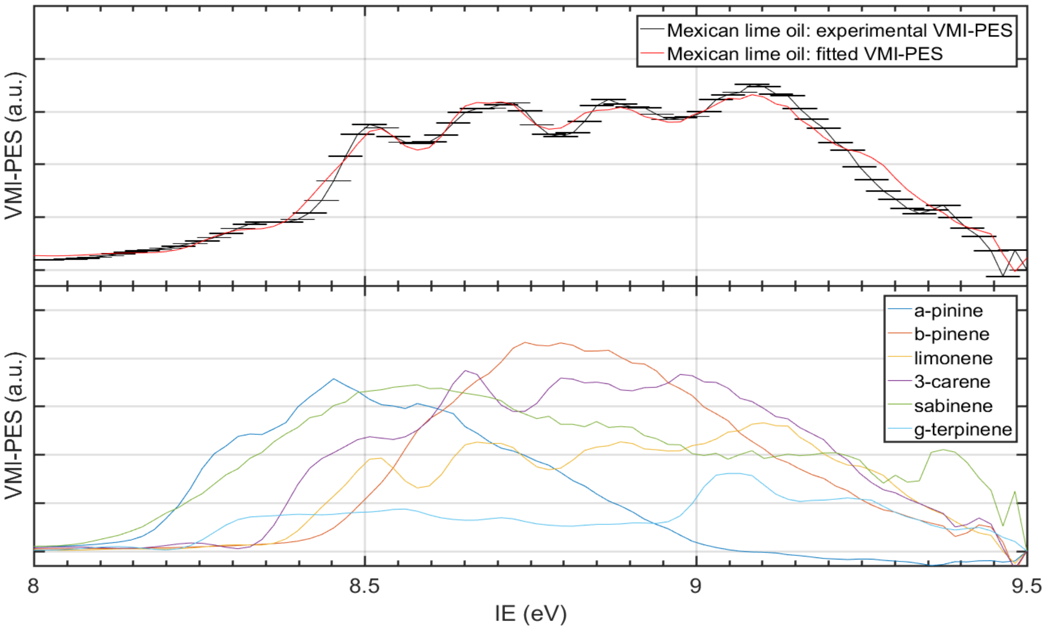

Fig. 93: Mexican lime oil VMI-PES fitting at hν=9.5 eV. Top: the fit, red, on top of the experimental VMI-PES of the oil, black. Bottom: the experimental VMI-PES of individual basis present in the oil. All the data shown in this figure have been measured in March 2016 with the same experimental setup, except the VMI data of the sabinene and the oil which have been measured in March 2017 and the VMI data of γ-terpinene which has been measured in June 2019. The correction for sabinene impurity has already been done, see Sec. 3.1.5 and Sec. 5.2.5. The same experimental parameters have been applied except the exit slit, cache setting and the acquisition time for which the data have been already normalized.

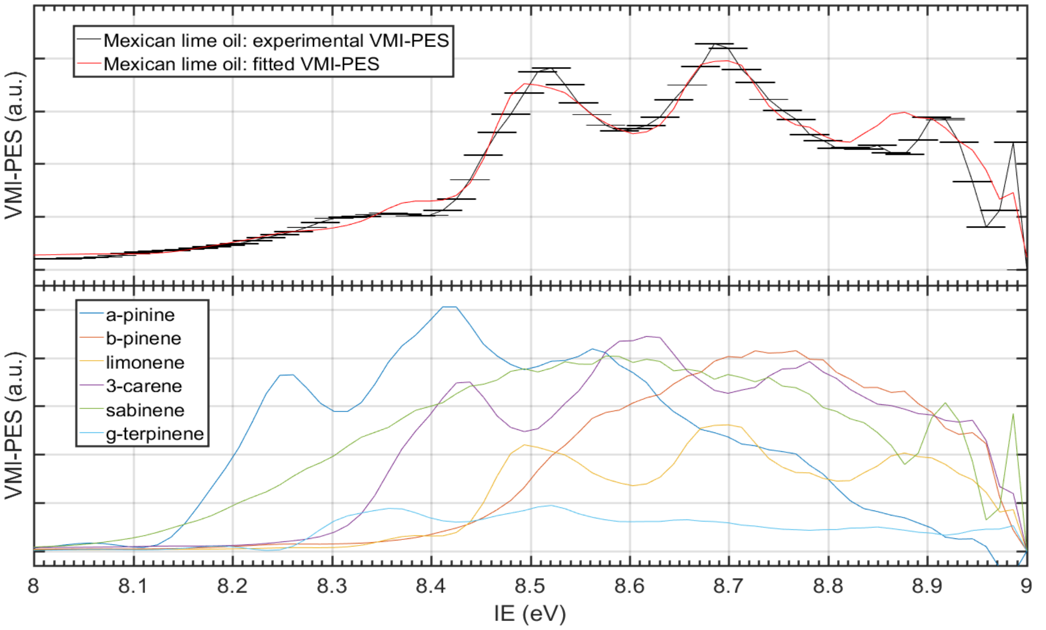

Fig. 94: Mexican lime oil VMI-PES fitting at hν=9.0 eV. Top: the fit, red, on top of the experimental VMI-PES of the oil, black. Bottom: the experimental VMI-PES of individual basis present in the oil. All the data shown in this figure have been measured in March 2016 with the same experimental setup, except the VMI data of the sabinene and the oil which have been measured in March 2017 and the VMI data of γ-terpinene which has been measured in June 2019. The correction for sabinene impurity has already been done, see Sec. 3.1.5 and Sec. 5.2.5. The same experimental parameters have been applied except the exit slit, cache setting, and the acquisition time for which the data have been already normalized.

Fig. 92, Fig. 93 and Fig. 94 are showing the SPES, VMI-PES at hν=9.5 eV and VMI-PES at hν=9.0 eV, respectively. All the spectra shown in these figures have not been measured in the same beamtime, so, wherever needed, the data have been normalised by an instrumental sensitivity factor. The results of the fittings are presented in Table 11, wherein all the cases, the cc of the compounds have been already normalised to sum up to 100%.

All three fittings lead to similar results. Limonene is found to be the most dominant component (71.5 on average) with the γ-terpinene to be the second major component (15.64% on average). Our method is also resulting in 0% contribution for 3-carene and just a few percent for α-pinene, β-pinene, and sabinene, on average. Actually, based on the literature review conducted prior to this work, we knew that 3-carene is not present in the lime oil; however, we included it in the basis set to check if our method is leading to a cc= 0% for 3-carene or not. As can be seen from Table 11, in all three fittings that we have done, the cc of 3-carene is obtained to be 0%.

Our results are in an excellent agreement with the GC analysis in the literature [109, 118, 127, 128]. For instance, some data reported in Ref. [109] for Mexican lime oil composition are retrieved and shown in Table 12, where four industrial and three laboratory samples of the Mexican lime oil have been studied. The laboratory samples have been purified either by Cold Pressed or Hydro Distillation techniques. As mentioned before, the extraction techniques affect the composition of the EOs, and this is what can be seen from Table 12. The composition of α-pinene, β-pinene, limonene, and sabinene obtained through our method are matching very well with those presented in Table 12, with less than 3% error on average. The cc we obtain for β-pinene and γ-terpinene also lie between the min and max cc values reported in the literature for these two compounds; our fittings lead to cc=5.33%, in average, for β-pinene while the min and max cc presented in Table 12 for different Mexican lime oil samples are 1.09% and 23.69%, respectively. In the case of γ-terpinene, we obtained cc=15.64%, on average, while the corresponding min and max values in Table 12 are 5.38% and 20.25%, respectively.

We should also mention that error bars we obtain for SPES and VMI-PES fittings are all reasonable in this case, smaller than 2% for all the components. This makes us confident in the fitting method we are using to extract the chemical composition of the monoterpenes.

Our results are also in a good match to those reported in [128]. Using a GC machine equipped with an FID, the authors of [128] obtained the cc of the standards as: α-pinene 2.05%, β-pinene

6.15%, limonene 73.06%, 3-carene 0%, sabinene 0.73% and γ-terpinene 18.01%. These all matchvery well with our averaged results, presented in Table 11, within a few percent.

Table 11: Mexican lime oil composition obtained through the SPES and VMI-PES fitting. In each fitting, the cc of the six compounds has been normalised to sum up to 100%.

method compound	SPES	VMI-PES at hν=9.0 eV	VMI-PES at hν=9.5 eV	Average of SPES and VMI fittings
α-pinene	3.71±0.29	5.36±0.64	6.95±0.59	5.34
β-pinene	2.75±0.87	3.02±0.72	10.24±1.01	5.33
limonene	74.56±1.02	75.08±0.98	64.76±1.35	71.47
3-carene	0.00±0.01	0.00±0.01	0.00±0.01	0.00
sabinene	3.45±1.08	3.21±0.81	0.00±0.83	2.22
γ-terpinene	15.53±1.14	13.33±1.62	18.06±1.65	15.64

Table 12: Mexican lime oil composition taken from Ref. [109] and references therein. The values in each column have been normalised to 100.

	Industrial				Laboratory			Average
					cold-pressed		Distilled	
a-pinene	2.45	2.35	2.31	2.29	4.13	2.41	1.09	2.43
b-pinene	23.69	25.34	21.93	24.13	15.33	6.99	1.19	16.94
limonene	60.07	60.23	61.23	59.54	57.65	76.52	92.15	66.77
3-carene	0.00	0.00	0.00	0.00	0.00	0.00	0.00	0.00
sabinene	2.88	2.91	2.78	3.63	2.64	6.19	0.18	3.03
g-terpinene	10.91	9.17	11.76	10.42	20.25	7.90	5.38	10.83

In terms of the PECD fitting and ee analysis, we only use the measurements we have at hν=9.0 eV, for which the PECD fitting is shown in Fig. 95. We should notice that in this case, unlike the case of black pepper oil, the VMI-PES and PECD of the oil have been measured in separate beamtimes. This can potentially cause some serious issues, particularly when the angular response of the detector changes overtime. In such cases, one solution is to record a photoelectron image of Xenon, using vertical polarization of light at a relatively high photon energy, at each beamtime. That image should look isotropic in principal; so, any artificial anisotropic response generated by the detector would be compensated by normalising all the photoelectron images recorded at a given beamtime with respect to the corresponding calibration Xenon image for that beamtime. Unfortunately, we have not measured such a calibration image for our first runs done in March 2016 and March 2017, when we measured the PECD of most of the standards and the oils under the study. However, based on the Xenon images we recorded in some of our later experiments (whose results are not shown here), we have seen that there is an anisotropy in the detector response changing over time. We also have observed that this detector anisotropy affects the VMI measurements done at hν=9.0 eV less than those measured at hν=9.0 eV.

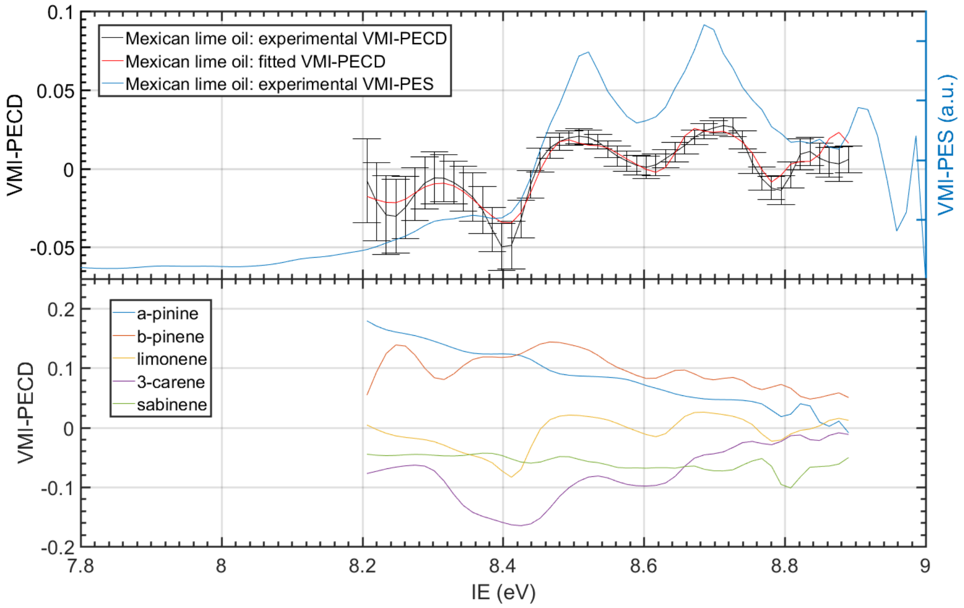

Fig. 95: Mexican lime oil VMI-PECD fitting at hν=9.0 eV. Top: the fit, red, on top of the experimental VMI-PECD of the oil, black. The VMI-PES of the oil is also plotted just to have a track of the region where there is a significant photoelectron signal. Bottom: the experimental VMI-PECD of individual chiral basis present in the oil including (+)-(1R,5R)-α-pinene, (-)-(1S,5S)-β-pinene, (+)-(4R)-limonene, (+)-(1S,6R)-3-carene, (-)-(1S,5S)-sabinene and γ-terpinene. All the data shown in this figure have been measured in March 2016 with the same experimental setup, except the VMI data of the sabinene and the oil which have been measured in March 2017. The correction for sabinene impurity has already been done, see Sec. 3.1.5 and Sec. 5.2.5. The same experimental parameters have been applied except the exit slit, cache setting, and the acquisition time for which the data have been already normalized. The PECD curves have not been plotted over regions where the error bars of the oil's PECD are enormously large.

Table 13 shows the result of the PECD fitting for Mexican lime oil at hν=9.0 eV in comparison to some results reported in the literature. As can be seen, our method is leading to roughly matching results for the first four compounds mentioned in Table 13, while completely diverging in the case of sabinene. The divergence in sabinene ee can be due to several reasons. First, the lime oil sample we have used here and its extraction method is not exactly the same as those in literature. Actually, one of the main goals in the Ref. [125] is to show how the ee of different compounds in a given citrus oil varies over seasons. So, the ee of the chiral compounds in a citrus oil is a quite sensitive quantity and even using the same extraction method cannot guarantee that to be the same for a given citrus. Second, the sabinene was minority component in our lime oil sample, as confirmed by the results of our cc analysis giving the cc of the sabinene to be cc=2.22%, on average. The result of the VMI-PES fitting at hν=9.5 eV was also giving cc=0% for sabinene, putting doubt on its presence in our lime oil sample. So, it seems that our method could not be quite determinative for ee of the samples with a very low abundance. Third, there might be more chiral monoterpenes present in lime oil, like a-thujene and camphene [109, 125], that we have not taken them into account here. This could manipulate the ee of our basis in a way that compensates for the other not-considered compounds. This is happening during the least square fitting when the optimisation functions to try minimize the residuals. Finally, we should also remember that the VMI data of the lime oil has not been measured at the same beamtime with the VMI data of the standards. As mentioned above, if there is an artificial anisotropy in the response of the detector changing over time, the fitting could lead to incorrect results in ee analysis.

The VMI-PECD fitting gives large uncertainties for ee values in this case as well. One reason could be that the PECD of the lime oil was recorded in a different experimental run, with a possible anisotropy in the detector response. Any anisotropy in the detector response could artificially change the recorded PECD and hence place more uncertainties on the results. The second reason could be the MATLAB routine we are using in PECD fitting. It would be worth using different linear and non-linear regression functions in MATLAB, such as *fitlm* or *lsqcurvefit,* to see if the uncertainties can be improved or not. Finally, as mentioned before, this this may be a limitation of our method, since the uncertainties on cc values, obtained through VMI-PES fitting, propagate forward and add more uncertainty in the ee values.

This is emphasising the need for further works on the fitting process to improve the results. For example, using different MATLAB routines

Table 13: The ee of the Mexican lime oil's compounds obtained through VMI-PECD fitting at hν=9.0 eV in comparison with those taken from Ref. [109] and Ref. [125]and references therein.

	VMI-PECD fitting at hν=9.0 eV	Ref. [109]				Ref. [125]	
		Two industrial samples of Mexican lime oil Type A		Two industrial samples of Mexican lime oil Type B		Range of ee for three Cold Pressed samples of Mexican lime oil Type A	Range of ee for three Cold Pressed samples of Mexican lime oil Type B
(+)-a-pinene	-35.8±4.20	-54.9	-55.46	-54.56	-45.16	[-55.00, -56.4]	[-53.6, -55.4]
(-)-b-pinene	100±56.25	93.54	93.54	92.8	86.96	[91.0, 93.0]	[91.0, 92.6]
(+)-limonene	100±23.85	95.06	95.04	95.06	93.38	[94.2, 94.4]	[94.0, 94.4]
(+)-3-carene	nt	nt	nt	nt	nt	nt	nt
(-)-sabinene	-100±68.25	71.24	70.76	70.78	57.2	[69.2, 69.6]	[69.2, 69.6]

In this chapter, we introduced the theoretical and experimental basis of a new method based on photoelectron spectroscopy to simultaneously measure the cc and ee of multicomponent gas-phase mixtures. The idea of the chemical composition analysis was that the photoelectron spectrum of a mixture must be a linear combination of the photoelectron spectra of its compounds, with the coefficients of the linear combination representing the chemical composition (cc). Similarly, the PECD spectrum of the mixture can be represented as a linear combination of the weighted PECD spectra of the compounds, with the coefficients being the enantiomer excess for each compound in this case.

The mixtures selected for this study were black pepper oil and Mexican lime oil. Based on the literature, a set of monoterpenes including α-pinene, β-pinene, limonene, 3-carene, sabinene, and γ-terpinene are supposed to constitute the majority of the volatile compounds in the two selected oils. So, we measured the high-resolution photoelectron spectrum of these two essential oils as well as that of their compounds using the SPES technique at the DESIRS beamline of the SOLEIL synchrotron in order to obtain the cc. We also measured the VMI-PES and VMI-PECD of the oils and their compounds at two fixed photon energies, hν=9.0 eV and hν=9.5 eV, from which the VMI-PES results were used to obtain the cc in a similar way to the SPES technique. The cc obtained using VMI-PES were in an excellent agreement with those obtained using the SPES technique, which verified the validity of our method. The VMI-PECD spectra weighted by the corresponding VMI-PES then were used to obtain the ee of each compound. As an interesting result, our method could successfully reveal that the lime oil sample is composed mainly of limonene and there is no 3-carene present in the oil, which is what we expected from the majority of literature works on this sample.

5. Vibronic modulation of PECD in monoterpenes

5.1. Introduction

For the first time in 2007, Contini et al. showed that in the photoionization of methyloxirane, the PECD depends on the vibrational states of the cation left behind [50]. This can be considered as a breakdown of the FC secondary assumption, which assumes the transition moments between two electronic states is independent of the nuclear motion as the time scale for the electron transition is much faster than that of nuclear motions. Continuing the research on PECD for the purpose of studying its dependency on the cation vibrational states, therefore, can help in refining the theoretical FC assumptions. The other motivation for experiments on the vibrational dependency of PECD is the insight that such experiments can give us about vibrational dynamics. In other words, if the relation of the PECD with the vibrational states in the cation is well known, one can use PECD as a tool to probe the vibrational states, particularly where the vibrational structures cannot be seen in the PES easily due to the low resolution. Below, we will see that due to the limitation of the VMI technique, the resolution of PES becomes worse at higher photoelectron kinetic energies. However, the resolution of PECD is less affected by increasing eKE.

In this chapter, we will only see how PECD is highly sensitive to the vibrational structures in the cation state using VUV synchrotron-based single photon ionization. However, the dependency of PECD on vibration states of the intermediate state in REMPI-PECD has been recently observed [56] followed by Time Resolved (TR)-PECD experiments [62]. So, studying the vibrational dependency of PECD in a time-resolved scheme can enable us to get information about vibrational dynamics like IVR happening in the intermediate excited states.

Here, the molecules under study are exactly those mentioned in Chapter 3. Actually, the aim of this chapter is to report the results of the PECD measurements on five monoterpenes whose SPES were studied in Chapter 3. The PECD measurements for all of the standards presented in this chapter have been recorded in the same experimental run (done in March 2016). So, the details on the experimental setup as well as the specific information of the samples can be found in Chapters 2 and 3. In this chapter, I will describe the way I have analysed the data and will provide some discussion on how PECD can be a better tool to probe the vibrational quantum levels rather than PES, particularly, when the higher photoelectron energies are concerned.

Two series of PECD measurements were carried out for all the mentioned terpene isomers, one at photon energy 9.0 eV and the other at photon energy 9.5 eV; in addition, for α-pinene, β-pinene and 3-carene two more photon energies, 10.5 eV and 12.0 eV, were tried. As described in chapters 2 and 3 all the experimental conditions were kept the same for each series of experiments; the liquid samples were kept at room temperature in a bubbler through which He gas was flowed with a backing pressure of 0.5 bar. The evaporated samples, carried with He, were then expanded into vacuum through a nozzle with a diameter of 70 μm and after passing through a double skimmer arrangement, entered into the DELICIOUS III spectrometer.

As mentioned before, among the five monoterpenes chosen for this experiment, limonene is a little bit different. Firstly, the ionization from its X-band includes both the HOMO and HOMO-1 orbitals while the X-band of the other samples only includes the ionization from the HOMO orbital. Secondly, limonene has six distinct conformers three of which can be present in the sample at room temperature. So, the PECD of limonene over the X-band region is slightly harder to interpret. However, an extensive study on limonene, published by the Powis group, can be found as a guideline to further studies [52]. The reader is also referred to our recently published paper on these monoterpenes [92] for more detailed information.

The other important factor that makes a huge difference is the chemical structure of the monoterpenes. In particular, three of the monoterpenes, α-pinene, limonene and 3-carene, possess an endo-double bond around which the HOMO orbital is located. The stretching of this chemical bond is what makes the PES of these three monoterpenes have such rich structure. In contrast, the PES of β-pinene and sabinene do not show any significant vibrational peak due to the lack of such an endo-double bond in their geometry. Consequently, the PECD of the monoterpenes is expected to behave differently. For those monoterpenes with an endo-double bond in their geometry, a significant modulation of the PECD is observed while in the cases of β-pinene and sabinene the PECD spectra do not change dramatically.

5.2. Results

5.2.1. α-pinene

As mentioned above, for α-pinene four PECD measurements were done at photon energies 9.0 eV, 9.5 eV, 10.5 eV and 12.0 eV. As one of the objectives of these measurements was to investigate the dependency of PECD on vibrational structures, the photon energies were chosen to be close to the IP of the molecule in order to get the highest possible resolution. The IP of α-pinene as we saw in Chapter 3 is about 8.16 eV, so, we expect to see higher resolution in the PES at lower photon energies like 9.0 eV and 9.5 eV rather than 10.5 eV and 12.0 eV. Furthermore, as the photon energy increases, it is more likely for the molecule to be fragmented. Shown in Fig. 96 is the ToF spectrum of α-pinene at selected photon energies. At 9.0 eV no fragmentation is observed. At 9.5 eV a tiny amount of fragmentation can be seen while at 10.5 eV and 12.0 eV the fragmentation can be seen obviously. Particularly, at 12.0 eV, the number of main fragment's ions overtakes the number of the parent ions. Our results show the mass 93 amu as the main fragment in the ToF mass spectrum in agreement with the literature [144, 145]. This fragment is created by separating the isopropenyl group from the parent by absorbing an extra photon after the ionisation [97]. Detailed discussions on the fragmentation dynamics were presented in the previous chapters where we reported the TPEPICO results supported by FC and OVGF calculations.

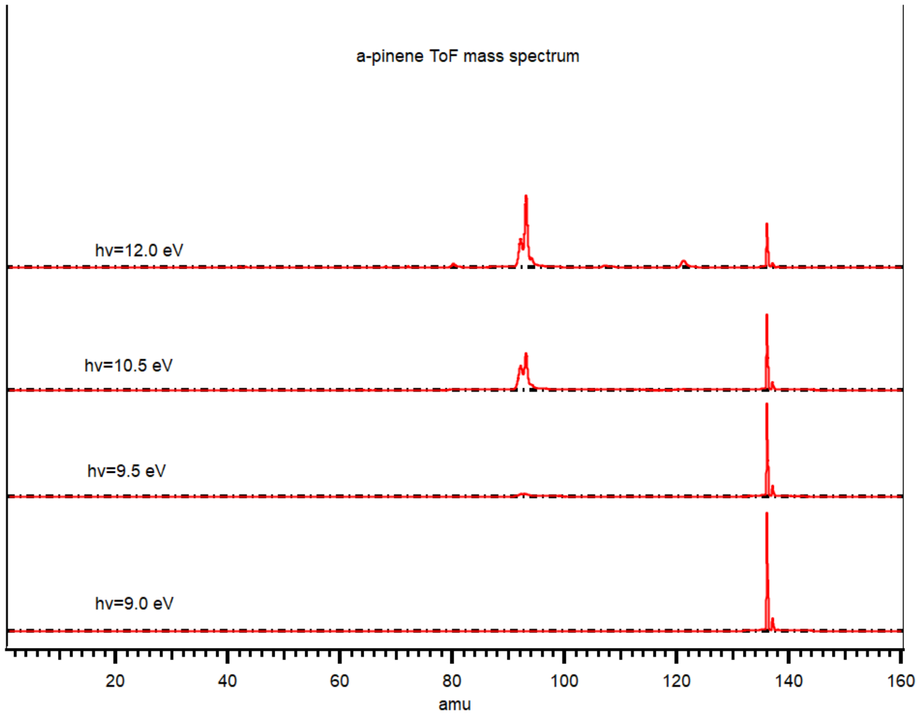

Fig. 96: ToF spectrum of α-pinene at photon energies 9.0 eV, 9.5 eV, 10.5 eV and 12.0 eV. At 9.0 eV the only mass observed in ToF is the parent, 136 amu. As the photon energy increases, the parent molecules start to fragment. The main fragment is mass 93 amu whose counts overtake the parent at 12.0 eV.

As the experimental setup was designed for coincidence measurements, one can decompose the total photoelectrons image into a series of images corresponding to any masses tagged to the ToF spectrum. Here, we are interested only in the photoelectrons who are in coincidence with parent mass, 136 amu. So, the rest of the photoelectrons corresponding to any fragmentation are filtered out. The most important reason why we consider only the photoelectrons in coincidence with the parent mass is that the fragmentation is not happening with the same rate at all the photon energies; the two lower photon energies, 9.0 eV and 9.5 eV, are showing nearly zero fragmentation while the two higher photon energies, 10.5 eV and 12.0 eV, are showing a massive fragmentation, see Fig. 96. We have looked at the PES extracted from the photoelectrons in coincidence with the parent and the main fragment, m/z=93 amu, and saw that they are totally different. This means that the fragmentation is happening before ionisation, which in return can lead to different PECD signals for the parent and the fragments. So, if we had considered all the photoelectrons, the PECD signal at lower photon energies was mostly coming from the parent mass while the PECD signal at higher photon energies could be a mix of the PECD of the parent and that of the fragments. In such a case, the comparison between the PECD at different photon energies could not be very useful, with some confusion remaining on the problem.

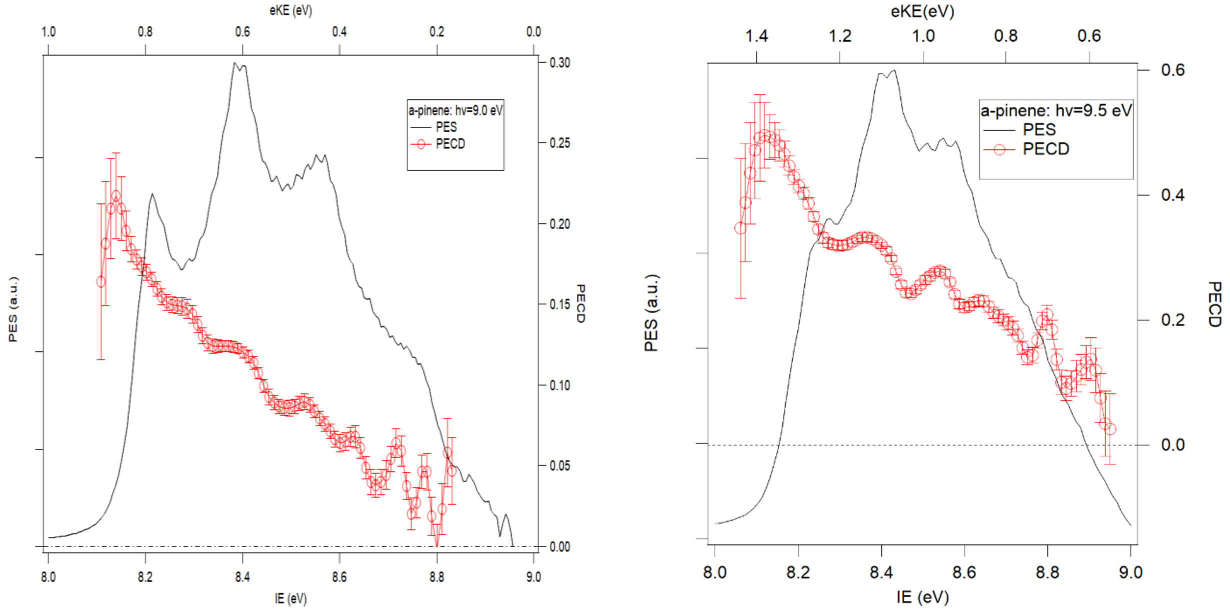

(a) (b)

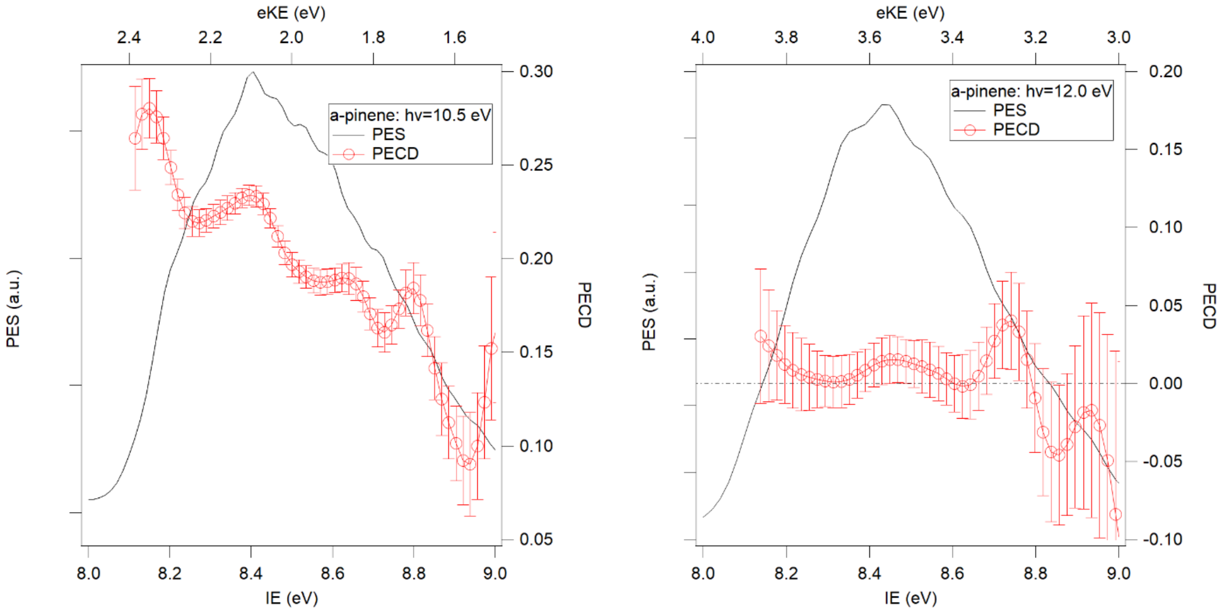

(c) (d)

Fig. 97: PES and PECD of (+)-(1R,5R)-α-pinene at photon energies 9.0 eV (a), 9.5 eV (b), 10.5 eV (c) and 12.0 eV (d) over the same ionization energy range, IE between 8.0 eV to 9.0 eV. In all cases, the PECD is showing modulation with respect to the vibrational structures in PES. As we go from lower to higher photon energies, the resolution of PES gets worse but the oscillations in PECD signal are survived and can still indicate the location of the vibrational structures. Both the PES and PECD spectra are in coincidence with the parent mass, m/z=136 amu.

PES and PECD spectra of α-pinene at different photon energies are presented in Fig. 97 a-d. At 9.0 eV and 9.5 eV where the vibrational structures are well resolved in the PES, we can see that the PECD signal is modulated with them. An important point can be figured out by comparing the PES and PECD spectra of α-pinene at lower photon energies, 9.0 eV and 9.5 eV, with those at higher photon energies, 10.5 eV and 12.0 eV. Particularly, at 10.5 eV, one can see that the poor resolution of the PES does not allow the vibrational structures to be seen very well while the PECD signal is still showing very clear oscillations; as such oscillations in the PECD are due to vibrational dynamics of the cation state [52] one can get information about the vibrational states by looking at the PECD spectrum even where it is not possible to see the vibrational structure in PES clearly.

There are two more points in Fig. 97 when we compare different photon energies together. The first is an increase in the size of errors in the PECD signal as we go from 9.0 eV to 12.0 eV. This can be realised as a consequence of a higher fragmentation rate at higher photon energies. For example, at 12.0 eV a considerable amount of the ions count rate (and subsequently the photoelectrons) is coming from the fragments, which at the end are filtered out. In other words, the statistics of the photoelectrons who are in coincidence with parent mass drops at higher photon energies and is reflected as the worsening the errors in the PECD of the parent molecule.

The last point is the low PECD signal at 12.0 eV. While the PECD signal at 9.0 eV and 9.5 eV exceeds 20% and 40%, respectively, the PECD signal at 12.0 eV remains less than 5%. This drop in the PECD signal has been discussed in previous chapters as a result of less interaction between the faster photoelectrons and the chiral potential of the molecule. At 12.0 eV, the photoelectrons possess kinetic energies of 3-4 eV over the X-band, which is much higher than the typical photoelectron kinetic energy of the same band at 9.0 eV, 0-1 eV. Although such an argument is valid only when we are comparing very low photon energies with relatively high photon energies, in chapter 6 we will see that even a small change in eKE can affect the PECD signal dramatically. The other factor that can affect the PECD values at different photon energies is the orbital from which the photoelectrons can be ionized. At higher photon energies, the ionization channels from deeper orbitals opens. This can happen if the photon energy is higher than the IP of these orbitals. The observed PECD at ionization energies higher than the IP of deeper orbitals, HOMO-1 for example, would be a combination of the PECD of HOMO and HOMO-1.

5.2.2. 3-carene

The photon energies 9.0 eV, 9.5 eV, 10.5 eV and 12.0 eV were tried in the case of 3-carene. The corresponding ToF spectra are presented in Fig. 98 just to see how the fragmentation is increasing with photon energy. The main fragment, in this case, is m/z=93 again. However, the number of the parent ions are still more than that of any of fragments even at 12.0 eV. The IP of 3-carene is 8.3 eV (Sec. 3.1.2) and the parent ions would be stable just up to a certain photon energy. There is no fragmentation at 9.0 eV and the fragmentation rate at 9.5 eV is very low; it can hardly be seen in the ToF mass spectrum. At 10.5 eV and 12.0 eV, the parent cations are less stable and fragments to different masses. A detailed study on the fragmentation dynamics of 3-carene can be found in Sec. 3.1.2 as well.

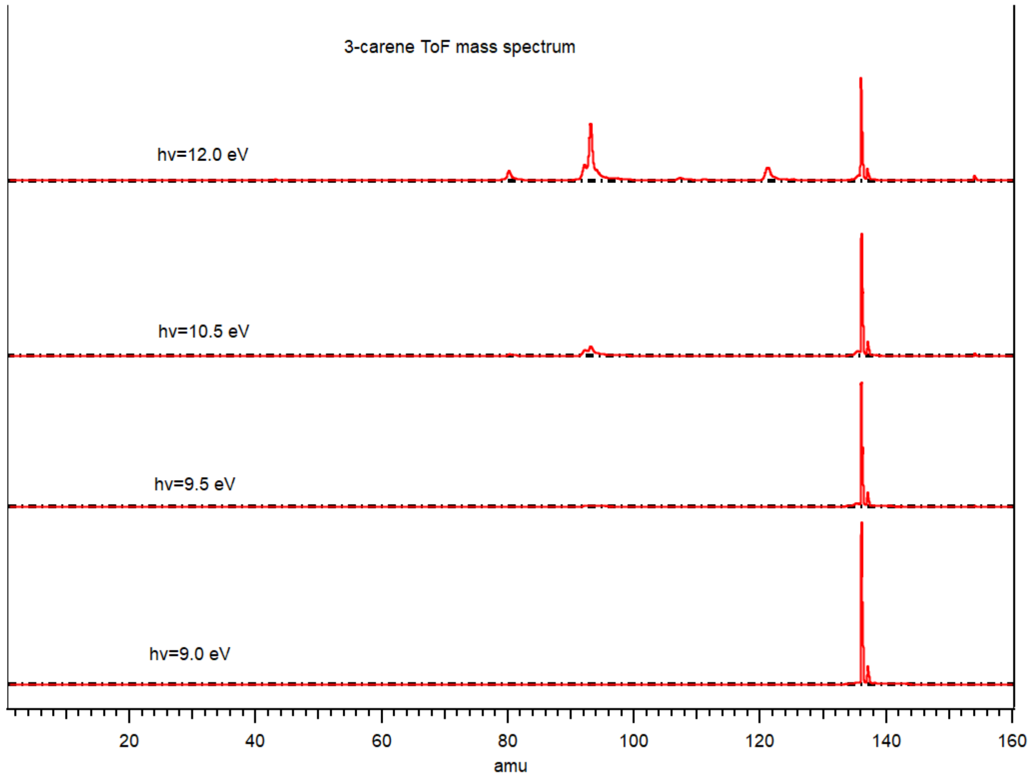

Fig. 98: ToF spectrum of α-pinene at photon energies 9.0 eV, 9.5 eV, 10.5 eV and 12.0 eV. At 9.0 eV the only mass observed in ToF is the parent, 136 amu. As the photon energy increases, the parent molecules start to fragment.

Included in Fig. 99 a-d are the PES and PECD of 3-carene at our interesting photon energies. Similar to α-pinene, we can see the intensive PECD modulation with respect to PES peaks. It is happening at higher photon energies as well. The PECD absolute values decrease at 12.0 eV while the error bars get larger. The reason for that is the same as it was in the case of α-pinene.

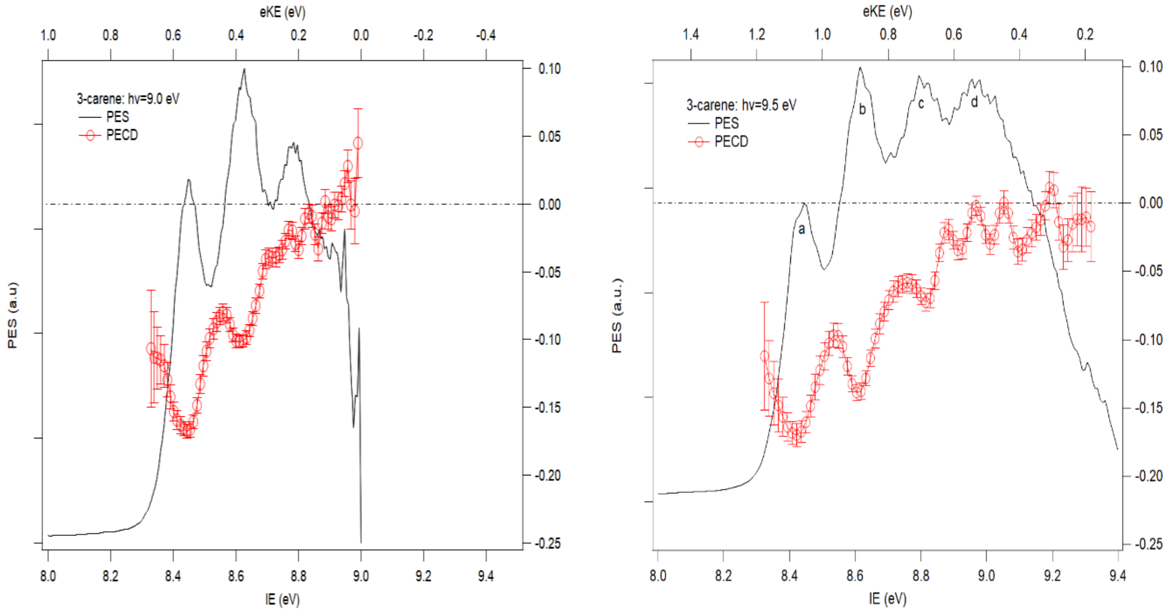

(a) (b)

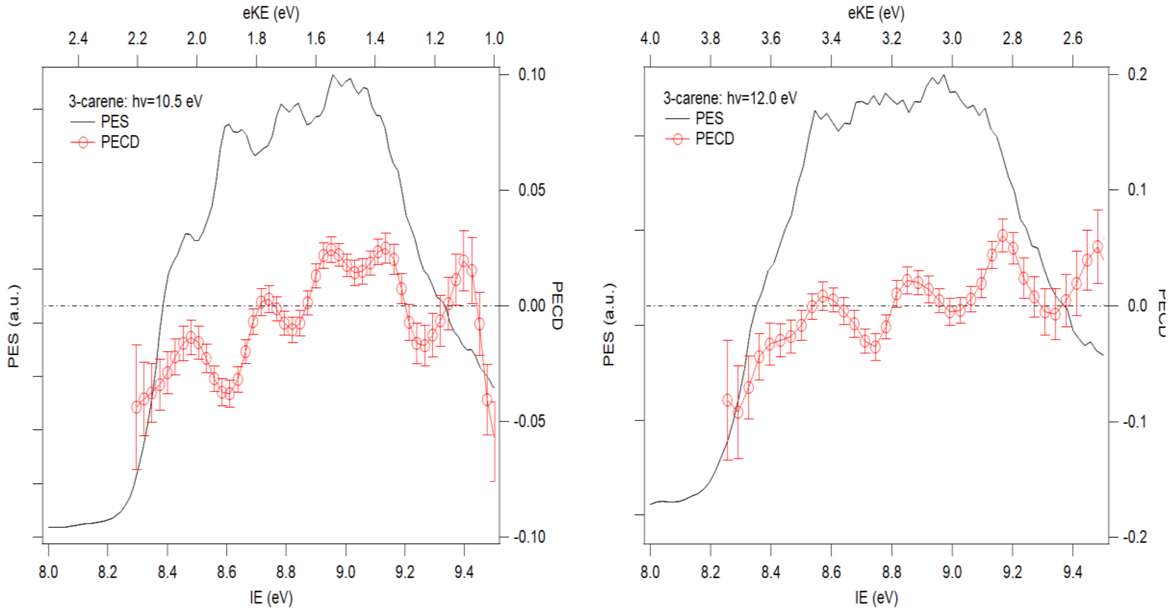

(c) (d)

Fig. 99: PES and PECD of (+)-(1S,6R)-3-carene at photon energies 9.0 eV (a), 9.5 eV (b), 10.5 eV (c) and 12.0 eV (d) over the same ionization energy range, IE between 8.0 eV to 9.5eV. In all cases, the PECD is showing modulation with respect to the vibrational structures in PES. Both the PES and PECD spectra are in coincidence with the parent mass, m/z=136 amu.

The resolution of a typical VMI setup is limited by the photoelectron kinetic energy; the higher the photoelectron kinetic energy, the worse the resolution. This can affect the PES resolution even at small energy differences like 0.5 eV. One can see this fact by looking at the PES of 3-carene recorded at 9.5 eV, Fig. 99 (b); The resolution of two peaks in the right hand side of the spectrum, peaks c and d, is much better than that of the two left hand side peaks, peaks a and b. This can also be a reason for more oscillations of the PECD spectrum over the lower photoelectron energies rather than over the higher photoelectron energies. Indeed, the higher resolution over the lower energetic region is more pronounced in the PECD spectrum as it is more sensitive to the vibrational structure. In the same figure, PECD shows only one oscillation per peak for peaks a and b, but more oscillations per peak for peaks c and d. This effect is clearer when we are comparing two regions very close to the threshold where the relative differential energy between two regions is considerable.

5.2.3. Limonene

In this run of the experiment, only two photon energies for limonene PECD measurement were tried, hν=9.0 eV and hν=9.5 eV. An extensive study on the limonene molecule has been recently reported in which the results of other experiments over a broad photon energy range are presented [52]. However, the current results are in agreement with them and verify them very well.

ToF mass spectrum of limonene at the two photon energies is shown in Fig. 100. The only mass which can be seen clearly at both photon energies is the parent, m/z=136. There is only a negligible amount of fragment m/z=93 at hν=9.5 eV.

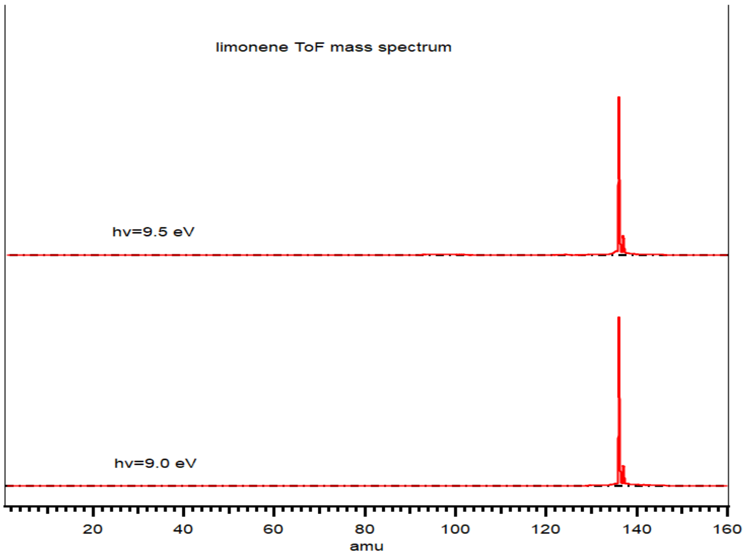

Fig. 100: ToF spectrum of limonene at photon energies 9.0 eV and 9.5 eV. At both photon energies, the only mass observed in ToF is the parent, 136 amu. There is only a tiny, negligible amount of fragment m/z= 93 at 9.5 eV.

The IP of limonene is 8.47 eV (see Sec. 3.1.3) which is slightly higher than that of the other monoterpenes presented here. Although the X-band of limonene includes two outermost orbitals, HOMO and HOMO-1, the ionization from both of them is not dissociative over this range. In fact, the onset of dissociative ionization for limonene is higher than that of the other monoterpenes. We will discuss this more in detail in the following chapters. For this reason, the ToF mass spectrum of limonene is clearer at hν=9.5 eV.

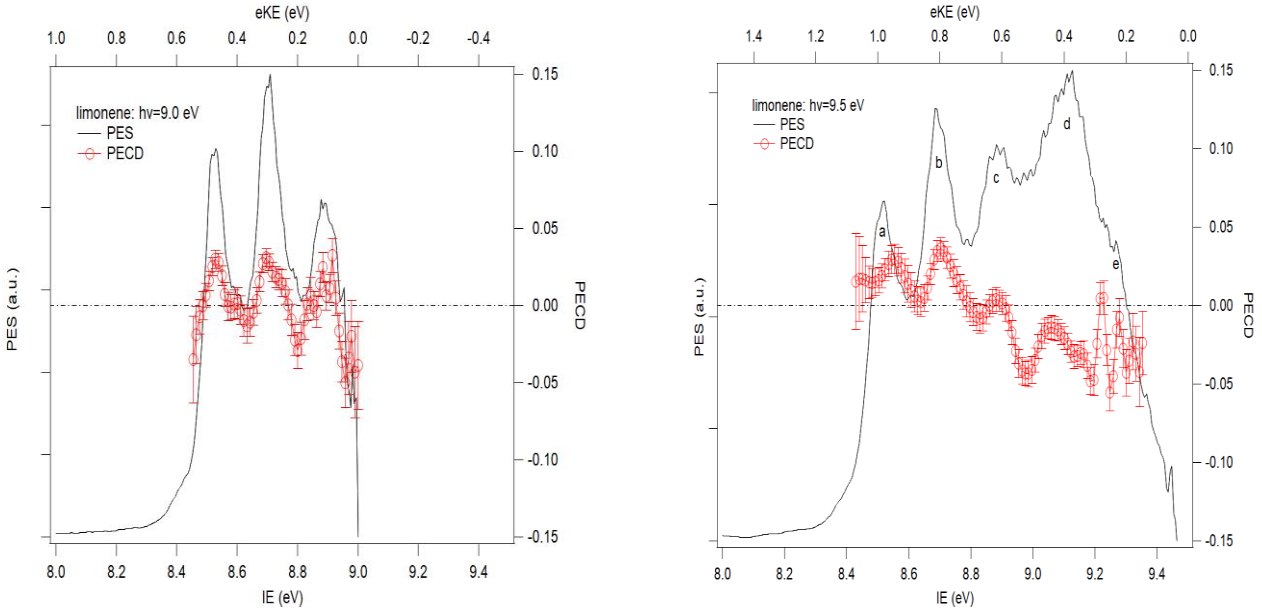

(a) (b)

Fig. 101: PES and PECD of (+)-(4R)-limonene at photon energies 9.0 eV (a), 9.5 eV (b). At hν=9.0 eV the modulation of PECD with PES spectra is beautifully seen here. At hν=9.5 eV, the last two peaks, d and e, include the ionization from HOMO-1 as well [52]. Both the PES and PECD spectra are in coincidence with the parent mass, m/z=136 amu.

The PEs and PECD spectra of limonene at hν=9.0 eV and hν=9.5 eV are presented in Fig. 101. In the case of hν=9.0 eV, a nice modulation of PECD with respect to any vibrational structure in the PES can be seen. The PECD signal changes sign between two peaks of PES meaning that the forward-backward asymmetry in the photoelectron angular distribution is flipping periodically by going from one vibrational structure to another one. At hν=9.5 eV, the same thing is roughly happening over the first three peaks of the PES (peaks a, b, and c); however, for the last two peaks, d and e, the oscillation of the PECD signal do not nicely match with the peaks in PES. This is because of two reasons. The first reason is that at photon energies above 9.0 eV, the ionization channels from HOMO-1 are also open; so, the PECD of photoelectrons ejected from the HOMO-1 orbital would contribute to the total observed PECD. The other reason could be the higher resolution for the lower energetic photoelectrons, as an intrinsic character of VMI imaging. Particularly, in the position of peak e, where the resolution is expected to be higher than the other peaks, the finer vibrational structures can be seen in the PES; this higher resolution is intensively reflected in the PECD spectrum in the form of more oscillations.

5.2.4. β-pinene

All three monoterpenes presented so far in this chapter (α-pinene, 3-carene, and limonene) have well-structured PES spectra. The vibrational peaks over their X-band were clearly visible, particularly at lower photon energies 9.0 eV and 9.5 eV. However, the vibrational structures are less visible in the PES of the other two chosen monoterpenes in this chapter, β-pinene, and sabinene. In this section, we are presenting the result of PECD measurements on β-pinene at four different photon energies 9.0 eV, 9.5 eV, 10.5 eV, and 12.0 eV. In the next section, the results of sabinene PECD measurements will be presented.

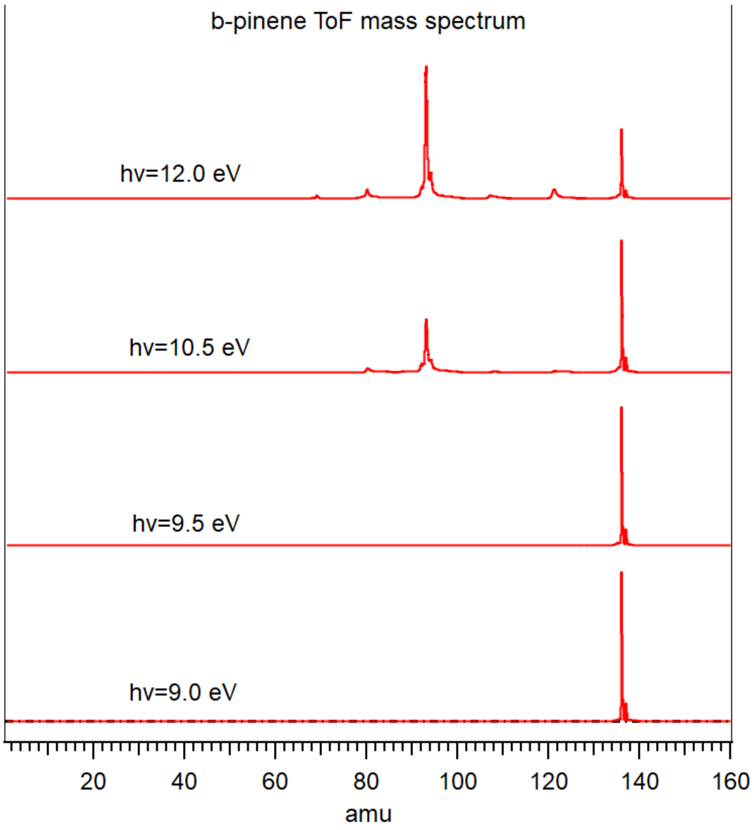

Fig. 102: ToF spectrum of α-pinene at photon energies 9.0 eV, 9.5 eV, 10.5 eV and 12.0 eV. At 9.0 eV the only mass observed in ToF is the parent, 136 amu. As the photon energy increases, the parent molecules start to fragment. The main fragment is mass 93 amu whose counts overtake the parent at 12.0 eV.

Just like before, we firstly show the ToF mass spectrum of β-pinene. The ToF mass spectra at the four photon energies are presented all together in Fig. 102. Again, at 9.0 eV there is obviously no fragmentation. At 9.5 eV there is just a tiny, negligible amount of m/z=93. For higher photon energies, fragmentation become more intensive; m/z=93 is the main fragment whose abundance takes over the parent ion count at 12.0 eV.

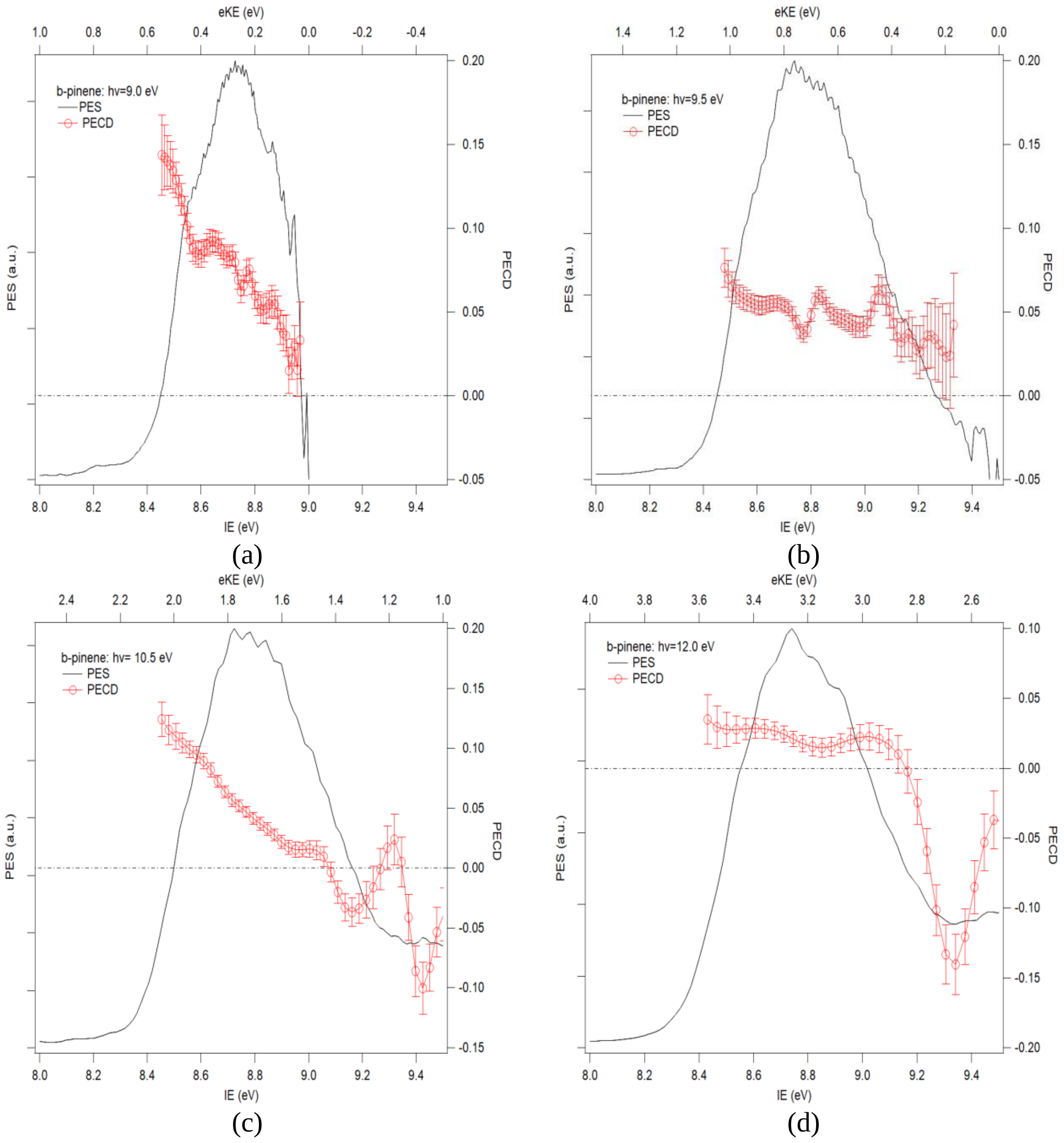

(a) (b)

(c) (d)

Fig. 103: PES and PECD of (-)-(1S,5S)-β-pinene at photon energies 9.0 eV (a), 9.5 eV (b), 10.5 eV (c) and 12.0 eV (d) over the same ionization energy range, IE between 8.0 eV to 9.5 eV. Both the PES and PECD spectra are in coincidence with the parent mass, m/z=136 amu.

Shown in

Fig. 103 is the PES and PECD of β-pinene at the four photon energies, tagged with the parent mass 136 amu. At hν=9.0 eV, everywhere there is even minor structures in the PES, we can see modulation of PECD. The modulation in the middle of X-band at hν=9.5 eV is more interesting. In this region, there is no significant vibrational structure resolved around IE=8.8

eV and IE=9.1 eV but the PECD is showing obvious, visible oscillations. To prove that these oscillations in PECD are due to the vibrational structures we need either a PES with higher resolution or a FC simulation for the transition between the ground state of the neutral to the ground state of the cation.

The PECD signal over the region IE=9.0 eV to IE=9.3 eV is showing totally different behaviours at the three photon energies 9.5 eV, 10.5 eV, and 12.0 eV. At 9.5 eV, the PECD over this region is positive with small fluctuations. Going to 10.5 eV, the amplitude of PECD oscillations gets larger and PECD changes sign several times. At 12.0 eV, the PECD goes from positive to negative values over the mentioned region with a minimum of -15%. The other point rises if we compare the PECD at IE=8.45 eV for the lowest, 9.0 eV, and the highest, 12.0 eV, photon energy. PECD at this ionization energy reaches its own maximum value, 15%, at hν=9.0 eV while for photon energy 12.0 eV, the PECD is less than 5%. This is due to the sensitivity of the PECD to the photoelectron kinetic energy effects that will be discussed in detail in Chapter 6.

5.2.5. Sabinene

Similar to β-pinene, sabinene has no obvious vibrational structure across its X-band. So, it would be interesting to see if PECD of sabinene over that region shows any oscillations or not. For sabinene, only two photon energies were tried, hν=9.0 eV and hν=9.5 eV. The ToF mass spectrum for these photon energies is shown in Fig. 104. There is no fragmentation at 9.0 eV while there is only a negligible amount of fragment m/z=93 at hν=9.5 eV. To get the PES and PECD spectra, the photoelectrons are always filtered by tagging the parent mass to the ToF mass spectrum, even in the cases where there are negligible amounts of fragmentation.

Included in Fig. 105 is the PES and PECD of extract sabinene sample at the two photon energies. It can be seen that the PECD absolute values at 9.0 eV are larger than that at 9.5 eV. However, in both cases, the PECD graph, unlike the PES curve, has again more structures.

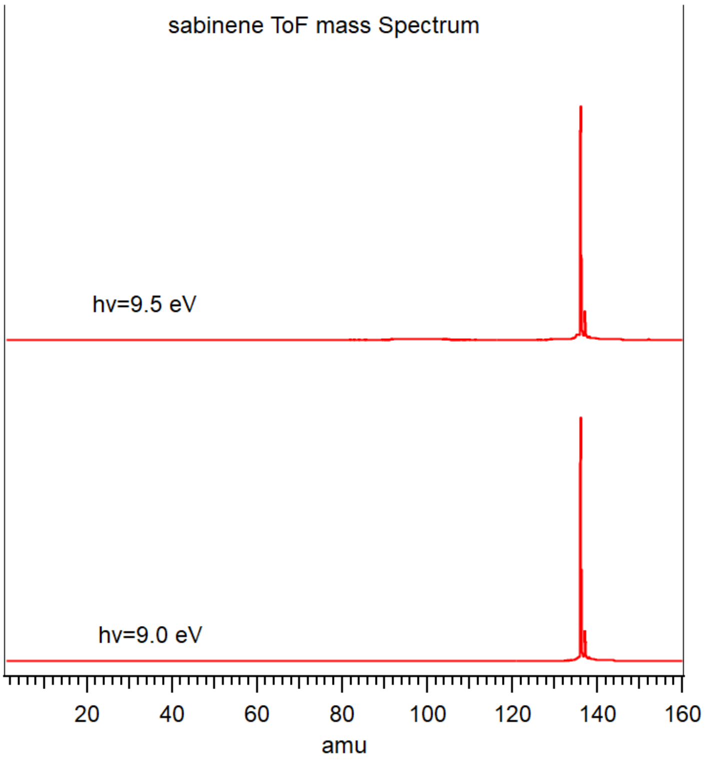

Fig. 104: ToF spectrum of sabinene at photon energies 9.0 eV and 9.5 eV. At both photon energies, the only clearly observable mass in ToF mass spectrum is the parent, 136 amu. There is only a tiny, negligible amount of fragment m/z= 93 at 9.5 eV.

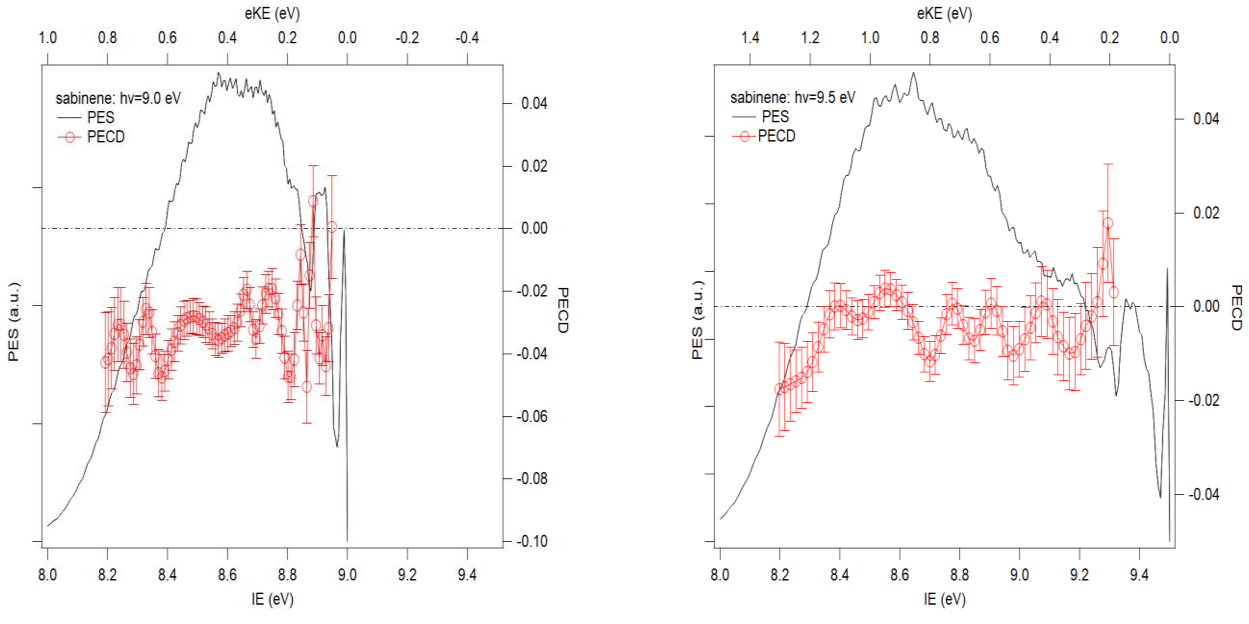

(a) (b)

Fig. 105: PES and PECD of extract (-)-(1S,5S)-sabinene at photon energies 9.0 eV (a), 9.5 eV (b). Both the PES and PECD spectra are in coincidence with the parent mass, m/z=136 amu.

As mentioned earlier, the sabinene sample was neither chemically nor enantiomerically pure. The results of the GC^2 analysis showed that the compounds present in the extract are sabinene and β-pinene with 75.9% and 24.1 % abundance, respectively. We can use this information to correct the PES spectrum of sabinene for the β-pinene impurity. Provided that the vapour pressure of sabinene and β -pinene are equal [146], the PES of the extract can be expressed as:

$$PES_{ex} = c.c._{s}\, PES_{s} + c.c._{\beta p}\, PES_{\beta p} \qquad \text{(Eq. 39)}$$

where c.c. is the chemical composition of compounds in extract sample and subscripts ex, s and βp stand for extract, sabinene and β-pinene, respectively. This leads to the following equation for the PES of pure sabinene:

$$PES_{s} = \frac{PES_{ex} - c.c._{\beta p}\, PES_{\beta p}}{c.c._{s}} \qquad \text{(Eq. 40)}$$

Fig. 106 is showing the PES of β-pinene and extract as well as the PES of pure sabinene obtained through (Eq. 48), for photon energy 9.5 eV.

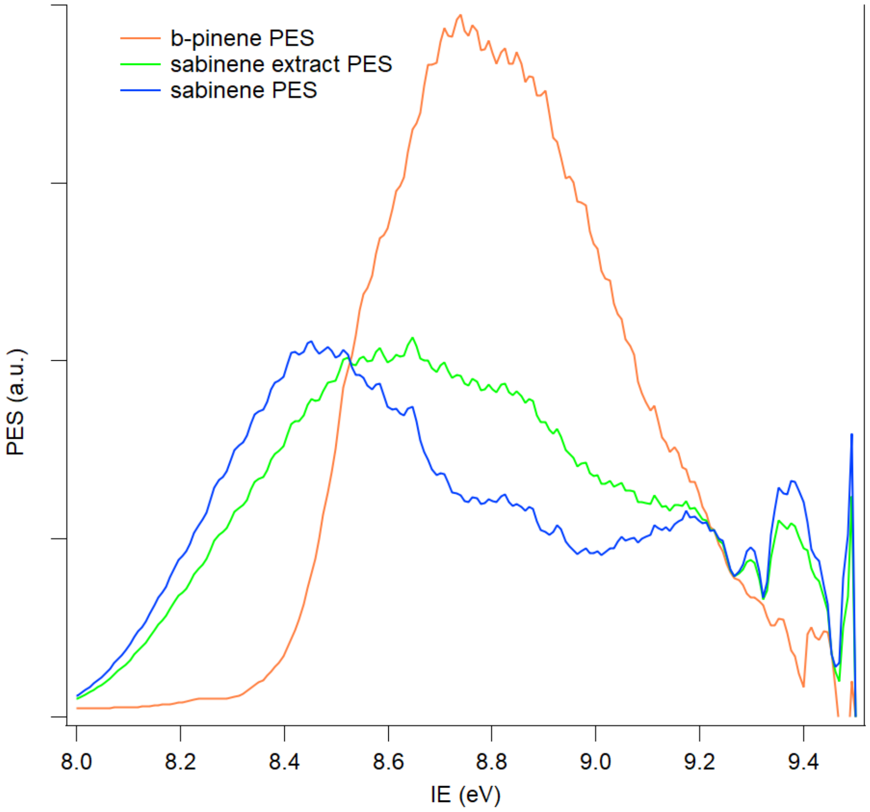

Fig. 106: The correction of sabinene PES for β-pinene impurity at photon energy 9.5 eV. The blue curve can be considered as the PES of pure sabinene. The PES of the extract sabinene and β-pinene (green and orange curves, respectively) are fed to (Eq. 48) to obtain the PES of pure sabinene.

We can also correct the PECD spectrum for both the chemical and enantiomeric impurities. In Sec. 5.2.5, we will see that the PECD of a mixture of molecules can be expressed in terms of the PES and PECD of the compounds as below:

$$PECD_{mix} = \frac{\sum_i (c.c.\times e.e.\times PES \times PECD)_i}{\sum_i (c.c.PES)_i} \qquad \text{(Eq. 41)}$$

where ee is the enantiomer excess of compounds and c.c. would be their chemical composition if they have all the same vapour pressure. Applying the above equation to the case of sabinene extract one can get:

$$PECD_s = \frac{(PES \times PECD)_{ex} - (c.c.\times e.e.\times PES \times PECD)_{\beta p}}{(c.c.\times e.e.\times PES)_s} \qquad \text{(Eq. 42)}$$

The PES_s was calculated in the previous step; so now, it can be used here to calculate the PECD of pure sabinene. The ee of the sabinene and β-pinene compounds in the extract was found to be 86.7% and 80.3%, respectively; these values are used in (Eq. 42). Fig. 107 is showing the PES and PECD of a sabinene sample which is assumed to be both chemically and enantiomerically pure, for photon energy of 9.5 eV.

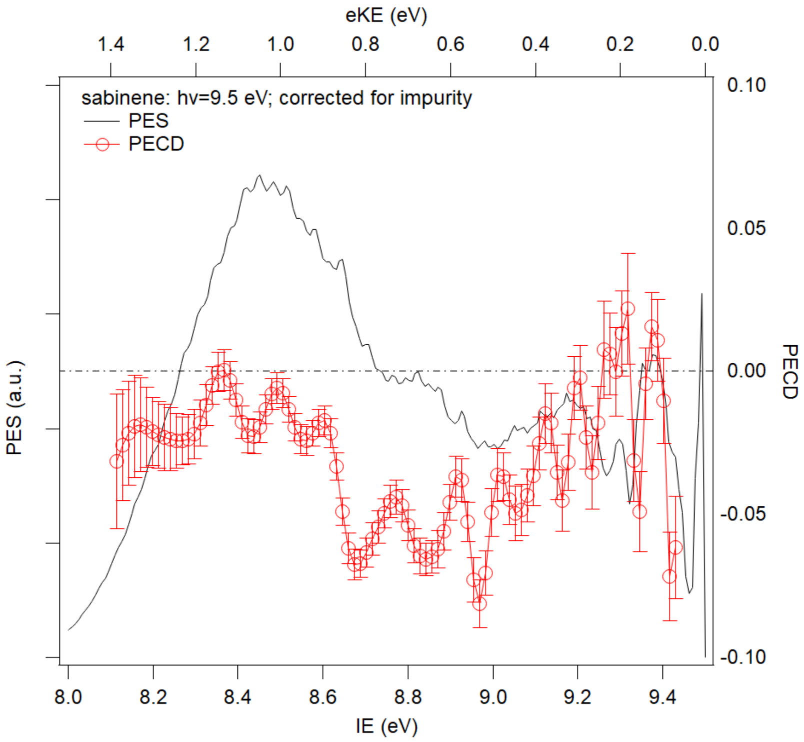

Fig. 107: The corrected PES and PECD of sabinene at photon energy 9.5 eV.

5.3. Conclusion

In this chapter, the PECD of five monoterpenes at different photon energies was studied. One of the achievements was that the PECD is depending highly on the vibrational motions of the molecules. This finding emphasises the potential of PECD to be used as a probe of the vibrational quantum levels. The second, complementary finding was that the resolution of the PECD in a VMI setup is less affected than that of PES when the photoelectron energy is increased. In other words, at relatively higher photon energies, the resolution of PES becomes worse in such a way that the vibrational structures cannot be seen obviously; in contrast, the PECD spectra resolution remains the same over a vast photon energy range. This suggests the PECD as a more sensitive tool in probing the vibrational quantum levels of the molecules, even when the vibrational structures are not resolved in the PES.

We also discussed the PECD spectrum of the monoterpenes in a comparative way to show that the PECD shows a modulated behaviour with respect to the vibrational structures. This modulation is more obvious in the case of the monoterpenes whose PES are rich in terms of vibrational structures. For example, the PESs of limonene, α-pinene and 3-carene are rich in vibrational structure due to the endo-double bond stretching mode. Consequently, the sign and value of the PECD spectra of these molecules change several times. In contrast, in the case of β-pinene and sabinene, the PECD signal is not changing a lot as the corresponding PES does not show significant vibrational structures.

6. Decoupling the effect of vibrations and photoelectron kinetic energy on PECD

In Chapter 5, it was shown how the PECD depends on the vibrational structure of the cation in the single photon ionization of monoterpenes using synchrotron radiation. However, the vibrations are not the only thing on which PECD depends; PECD also depends on the kinetic energy of the photoelectrons, for instance. Recently, we have shown experimentally how the PECD of α-pinene varies as a function of the photoelectron kinetic energy [92]. If we plot the PECD of α-pinene at two photon energies 9.0 eV and 9.5 eV vs the photoelectron kinetic energy, we will clearly see how the PECD strongly depends on eKE for this molecule. Presented in Fig. 108 (taken from Ref. [92]) is the PECD of α-pinene measured at two photon energies 9.0 eV and 9.5 eV plotted vs the kinetic energy of the electrons, showing that the PECD of this molecule is generally growing up when the eKE increases. The main objective in this chapter is to study the dependency of the PECD on two factors, eKE and vibrational motions of the nuclei, in order to decouple them from each other. Here, for the first time, we propose an approach to freeze one of these two effects and study the impacts of the other one on the PECD.

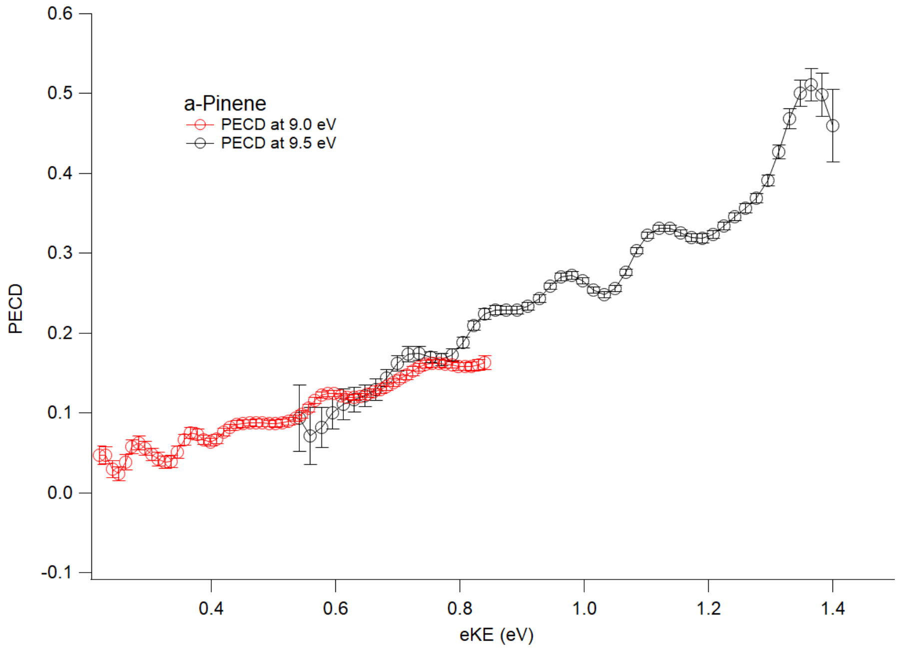

Fig. 108: PECD of α-pinene at photon energies 9.0 eV, red curve, and 9.5 eV, black curve, vs the kinetic energy of the photoelectrons. Although some vibrational modulations can be seen in the form of peaks and valleys in the graphs, the PECD tends to grow up as the eKE increases.

For this reason, we decided to continue our PECD research on monoterpenes over a broader range of photon energies expanding from very near threshold up to 19 eV. Two of the monoterpenes, α-pinene, and 3-carene, were more interesting to us for several reasons. Firstly, they display a more structured PES making it possible to study the vibrational effects in combination with the kinetic energy effects. Secondly, they possess only one conformer making the interpretation the results much easier. Finally, the absolute value of these two monoterpenes PECD is greater than that of the others, at least at 9.0 eV and 9.5 eV, based on the results reported in Chapter 5. As mentioned in Chapter 5, for α-pinene and 3-carene, there were PECD measurements at photon energies 9.0 eV, 9.5 eV, 10.5 eV, and 12.0 eV available from an experimental run done in March 2016. So, we did two complementary runs of experiments in May 2018 and Apr 2019 to expand the PECD measurements over a photon energy range from near threshold up to 19.0 eV. In May 2018, we tried the higher photon energies like 11.0 eV, 13.0 eV, 15.0 eV and 19.0 eV for both α-pinene and 3-carene while in Apr 2019 some lower photon energies (8.35 eV, 8.5 eV and 8.7 eV for α-pinene; 8.55 eV, 8.7 eV and 8.85 eV for 3-carene) were carried out. Actually, the lower photon energy measurements, thanks to their higher resolution, could provide us with a better insight into the vibrational effects while the higher photon energy measurements are good to study the electron kinetic energy dependency of PECD. In all three runs of the experiment we used the same enantiomer of 3-carene, (+)-3-carene. For α-pinene, in 2016 used (+)-α-pinene while we switched to the other enantiomer, (-)-α-pinene, in 2018 and 2019. So, we need to plot the vertically flipped PECD of 2016 α-pinene to make it comparable with those measured in 2018 and 2019. Enantiomerical purity of α-pinene and 3-carene samples in all three runs of the experiment has been higher than 97% and the rest of the experimental setup was kept the same as those mentioned in Chapters 3 and 5.

6.1. Results

6.1.1. 3-carene

In this section, the results of VMI-PES and -PECD of 3-carene at several photon energies expanding from near threshold up to 19.0 eV are reported. The reader is recommended to have read Sec. 3.1.2 and Sec. 5.2.2 for more a detailed discussion of the 3-carene PES/PECD. We are only interested in the photoelectrons in coincidence with the parent mass, m/z=136 amu, and only focus on the X-band region of the spectrum. As mentioned above, there have been 11 photon energies tried for 3-carene in total, hν=8.55, 8.7, 8.85, 9.0, 9.5, 10.5, 11.0, 12.0, 13.0, 15.0, 19.0 eV. As the resolution of the VMI data gets worse with increasing photon energy, we divide the data set into three classes with respect the resolution of the results: high resolution class including photon energies up to 9.5 eV; medium-resolution class including photon energies 10.5 eV, 11.0 eV, and 12.0 eV; and finally low-resolution class including the highest photon energies 13.0 eV, 15.0 eV, and 19.0 eV. To study the effect of the vibrations on the PECD, our focus would be on the high resolution data class, as the vibrational structures are better resolved among this class of the data. On the other side, to study the effect of the photoelectron kinetic energy on PECD the whole set of PECD measurements will be taken into account.

Presented in Fig. 109 is the photoelectron spectrum of 3-carene recorded at five of the lowest photon energies, considered as the high resolution ones. Actually, as shown in Sec. 3.1.2, there are five major vibrational structures in the X-band region of 3-carene; here, we choose the photon energies in a way that in each step one more of those vibrational structures appear in the spectrum. There are two points that we can realize from Fig. 109 first of which is the smaller width of the vibrational peaks at lower photon energies. For instance, between two measurements of hν=8.85 eV and hν=9.5 eV, the first one shows a narrower peak at the same IE, 8.45 eV. This is due to the fact that at lower photon energies, the maximum photoelectron kinetic energy is less, which in turn provides a higher resolution to the VMI data.

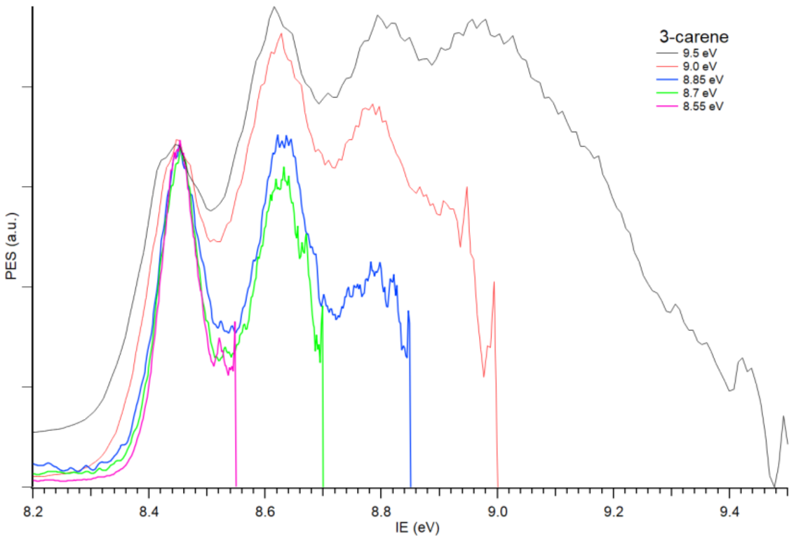

Fig. 109: PES of 3-carene at different photon energies. There are five major vibrational structures in the photoelectron spectrum of 3-carene over the X-band (see Sec. 3.1.2 also); here, it has been tried to choose the photon energies in a way that in each step one more of those vibrational structures appear in the spectrum.

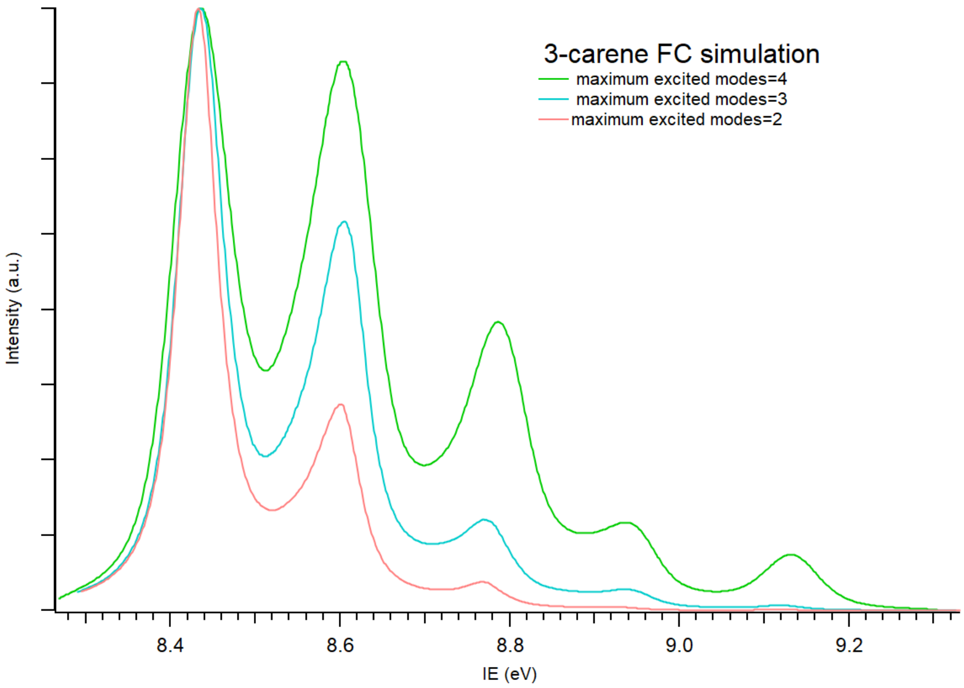

Fig. 110: FC simulation of 3-carene done at harmonic level using basis set aug-cc-pVDZ. When using FC-LabII to simulate the spectrum between the ground and cation state, the number of normal modes that can get excited simultaneously has been set to different values: 2 (red curve),3 (cyan curve) and 4 (green curve). Again, the spectra have been normalized to the height of the first vibrational peak at 8.45 eV.

The other point that we can find out from Fig. 109 is the different ratio between consecutive peaks in the PES when we go to higher photon energies. Indeed, the data plotted in this figure have been normalised in a way that the first peak (in the left hand side of the spectrum, at IE=8.45 eV) for all of the photon energies take the same intensity. Setting the intensity of the first peak to the same value for all the measurements, one can see that, for instance, the second peak in the PES is not appearing to have the same intensity for all the photon energies. The higher the photon energy, the higher the second peak. More generally, if we normalize the X-band spectrum of different photon energies to their left hand side, in the right hand side of the X-band, the PES is taking a higher value for higher photon energies. Looking for some explanation to this, we have performed the FC simulation for the cation state of 3-carene several times allowing different numbers of normal modes to be excited simultaneously in each simulation (the procedure for FC simulation is explained in Sec. 2.6). Here, all of the other parameters in the simulation, the basis set and the level of simulation, for example, are kept the same. One can see from Fig. 110, a similar trend is happening if we normalize all the simulated spectrums to have the same intensity at their first peak, IE=8.45 eV. In general, the more the number of excited normal modes, the higher the right hand side of the spectrum. Therefore, one possible explanation to what we see in the experiment could be that at higher photon energies, more normal modes are excited simultaneously. However, this is not the only possible explanation; we can explain the difference by looking at the ionization energy of HOMO-1 orbital of 3-carene, which is lying between 9.0 eV to 9.5 eV, see Sec. 3.1.2. The intensity of the vibrational peaks in the right hand side of the PES can be higher due to opening the ionization channel from HOMO-1 orbital, as is the case for limonene [52].

PECD data corresponding to our high resolution class of photon energies is presented in Fig. 111 as well as the PES at 9.5 eV which helps in tracking the location of the PECD oscillations with respect to the vibrational structures in the X-band. A very obvious modulation of PECD with vibrational structures can be seen from Fig. 111 at all of the photon energies. This oscillation can be compared to the similar behaviour previously reported for limonene [52]. Below, we will have a closer look at this data in order to decouple the effect of vibrations and the effect of photoelectron kinetic energy on PECD.

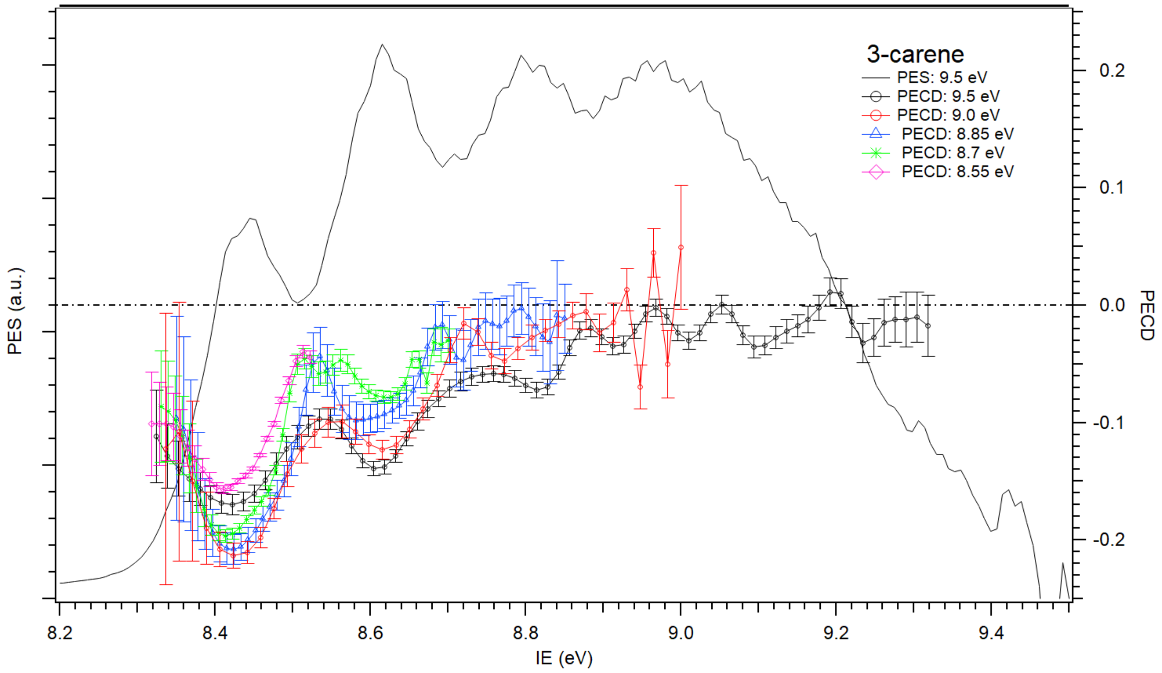

Fig. 111: Experimental PECD results of 3-carene for photon energies equal to and lower than 9.5 eV. The PES recorded at 9.5 eV is also plotted on top of the PECD curves to show the location of the vibration peaks.

Focusing first on the vibrational structure at IE=8.45 eV and its associated PECD, Fig. 111 shows that the PECD follows the same trend over this region for all photon energies, in which, there is a valley in the PEDC curves coinciding with the peak in PES. However, the absolute minimum value in the PECD curves is not exactly the same for all photon energies. This difference can be attributed to the difference in the photoelectron kinetic energies as the vibrational character for all of them is the same (see Sec. 3.1.2). To visualise this point, the PES recorded at different photon energies, as well as the PECD corresponding to only the first vibrational structure, have been plotted in Fig. 112 as a function of their eKE. All the PECD curves show the same modulation to the vibrational structure with a little bit change in the absolute value of a PECD at increasing eKE. Therefore, the PECD of 3-carene is more dependent on the vibrational dynamics rather than on electron kinetic energy, over the discussed energy range.

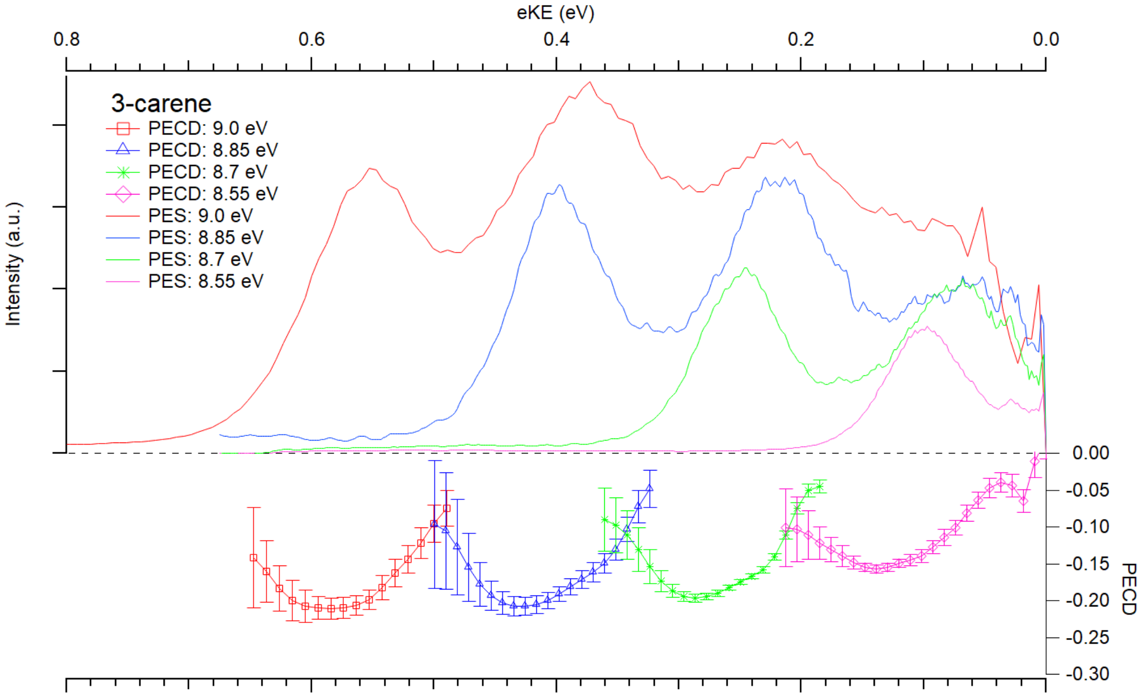

Fig. 112: PES and PECD of 3-carene recorded at different lower photon energies vs eKE, the axis on the top. The PES spectra are rescaled to make the plot clearer. For each photon energy, the PECD corresponding only to the first vibrational peak is plotted here.

Now, we can try to exclude the effect of eKE on PECD in order to see its dependency purely on vibrations. In Sec. 3.1.2, particularly Fig. 60 and Fig. 61, the vibrational character of different peaks in PES was discussed. Briefly, the first peak at IE=8.45 eV was assigned to a combination of origin transition and zero or one single quanta excitation of normal modes ν1, ν2, and ν3. The second and third peaks, at IE=8.60 eV and IE=8.79 eV, were assigned to have the same vibrational character as the first peak, but in addition to one quanta excitation of normal modes ν56 and ν60, respectively. Having that said, one can see from Fig. 112 that the first peak of the PES at hν=8.7 eV is aligned with the second peak of PES at hν=8.85 eV as well as with the third peak of PES recorded at hν=9.0 eV. The PECD of 3-carene corresponding to these interesting different vibrational structures are plotted in Fig. 113. Inside the eKE window expanding from 160 meV to 300 meV, the PECD recorded at hν=8.7 eV is showing the largest average absolute value, around 20%. Based on Fig. 60 and Fig. 61, this is where only the low frequency normal modes (ν1, ν2, and ν3) are involved. Now, look at the PECD recorded at photon energy 8.85 eV just plotted inside the window; its absolute value has been decreased down to about 10% on average. This can be considered purely as the effect of adding one quanta excitation of normal mode ν56, double bound stretching mode. For hν=9.0 eV, the third peak of PES (adding one quanta of normal mode ν60 to the first peak in PES) lies down in the eKE window. It can be seen that adding one quanta of normal mode ν60, symmetric methyl group stretching, is also decreasing the PECD absolute values, down to less than 5%.

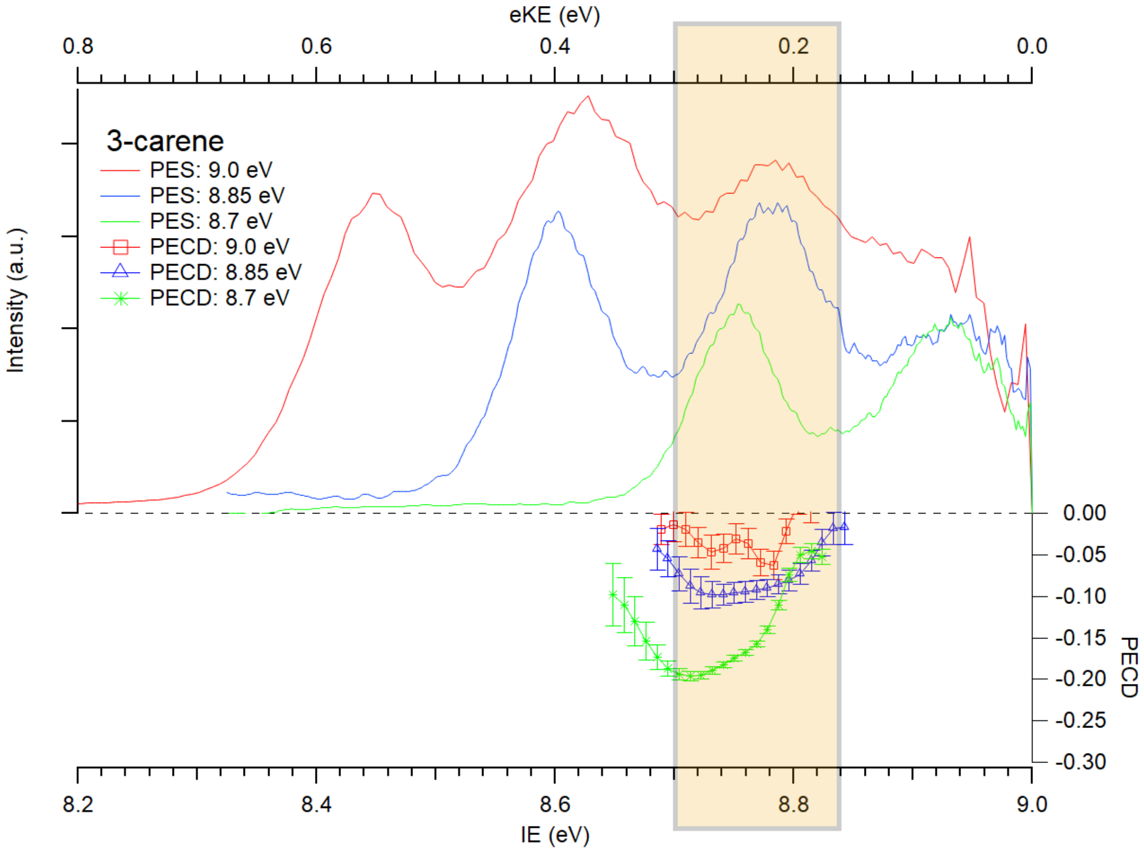

Fig. 113: PES and PECD of 3-carene recorded at different lower photon energies vs eKE, the axis on the top. The PES spectra are rescaled to make the plot clearer. For each photon energy, the PECD corresponding only to the interesting vibrational peaks in the eKE window is plotted here, see the text.

It seems to be a general fact that, at the same eKE window, adding a quanta of higher frequency modes, ν56 and ν60 for instance, causes a decrease in the absolute PECD of 3-carene. To support this idea, we can consider another eKE window expanding from eKE=320 meV to eKE=480 meV where the first vibrational peak at hν=8.85 eV gets aligned with the second vibrational peak of hν=9.0 eV. As shown in Fig. 114, within the eKE window, the PECD recorded at hν=8.85 eV, which is supposed to associate only with low-frequency vibrational modes, takes larger absolute values on average relative to the PECD recorded at hν=9.0 eV, which associates with the one quanta excitation of double bound stretching mode ν56 in addition to the low-frequency vibrational modes.

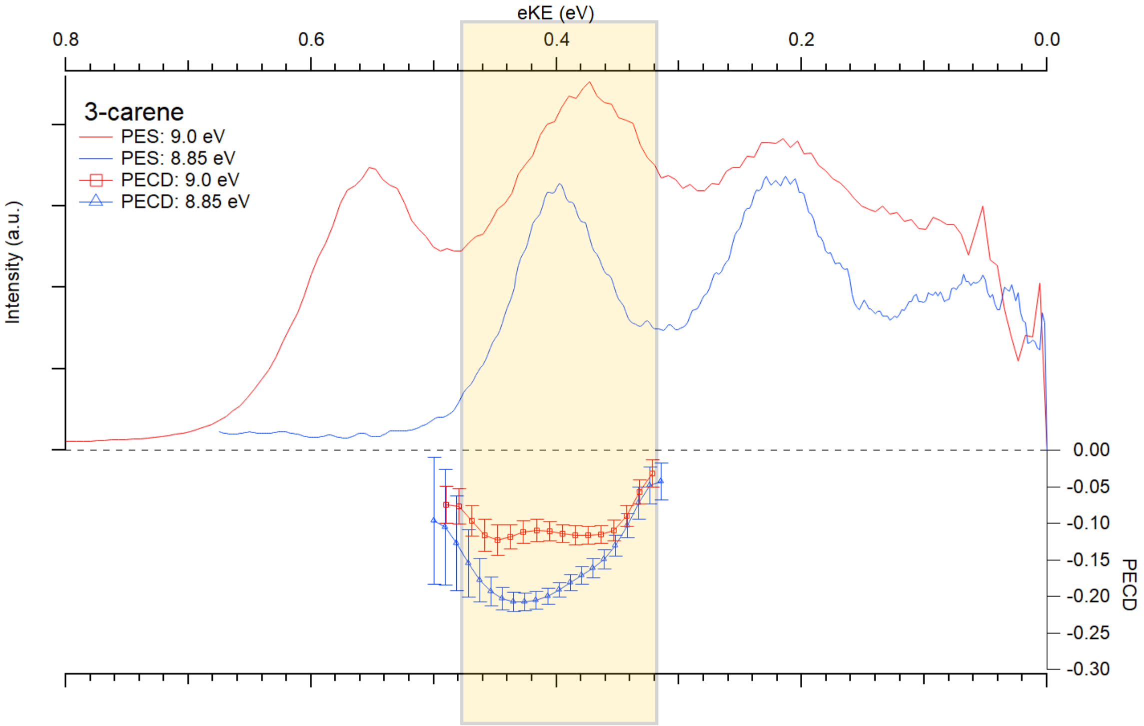

Fig. 114: PES and PECD of 3-carene recorded at hν=8.85 eV and hν=9.0 eV vs eKE, the axis on the top. The PES spectra are rescaled to make the plot clearer. For each photon energy, the PECD corresponding only to the interesting vibrational peaks in the eKE window is plotted here, see the text.

A vibrational modulation of PECD can also be seen in the case of our medium resolution data set as the vibrational structures can still be resolved in the spectrum. The interesting point is the intensive oscillations in the PECD curves, particularly in the case of hν=12.0 eV, where the vibrational structures are not very well resolved in the corresponding PES. In Chapter 5, we argued that this makes PECD a potential probe for the vibrational dynamics wherever the resolution of PES in VMI experiments is not high enough to show them.

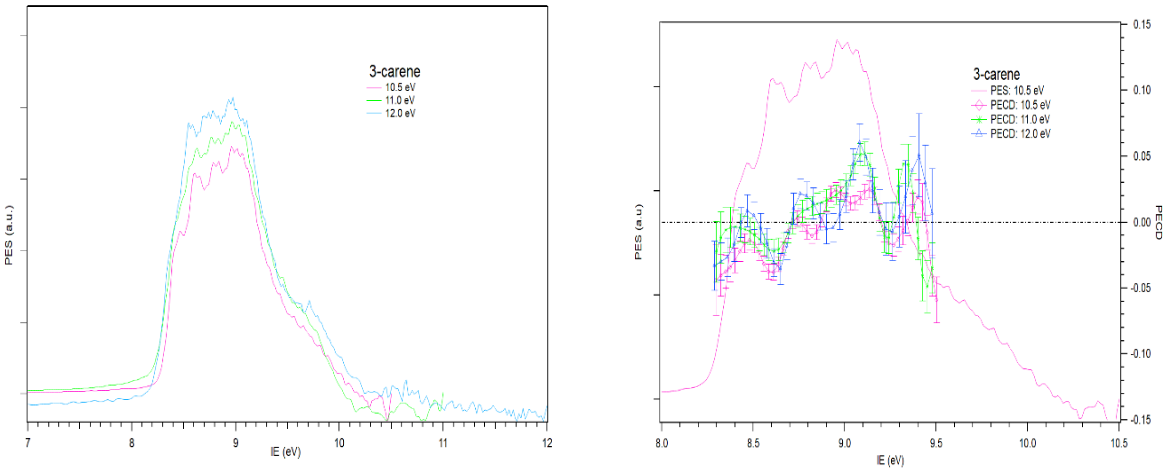

(a) (b)

Fig. 115: PES (a) and PECD (b) of medium resolution data set (hν=10.5, 11.0,12.0 eV) of 3-carene. The PES of hv=10.5 eV has also been plotted on top of the PECD curves in the right just to help to track the location of vibrational structures. The PESs are plotted with different scales just to make them comparable in the same frame as clear as possible.

Our low-resolution data set includes three higher photon energies, h*ν*=13.0, 15.0, 19.0 eV. These measurements are interesting as the PECD for each of them is totally different. As can be seen from Fig. 116, over an IE range from 8.2 eV to 9.0 eV, the PECD recorded at h*ν*=13.0 eV is almost zero, while the PECD of h*ν*=15.0 eV and h*ν*=19.0 eV take totally positive and negative values, respectively. This behaviour cannot be due to the vibrations as it is the same for a range of energy including several vibrational structures, IE=8.2 eV to 9.0 eV. In the following, we will show that such a behaviour can be explained by theory as a result of the eKE dependency of PECD.

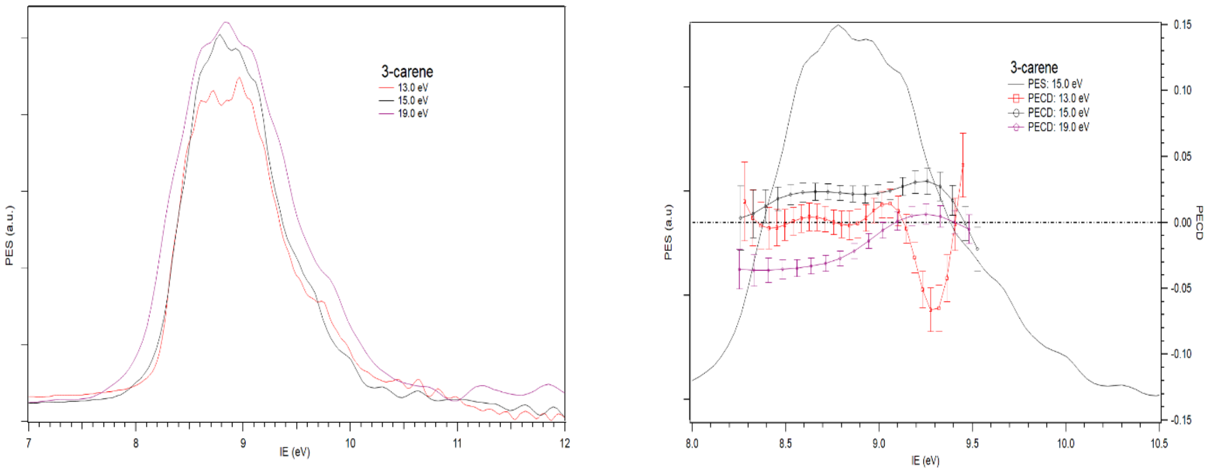

(a) (b)

Fig. 116: PES (a) and PECD (b) of low resolution data set (hν=13.0, 15.0,19.0 eV) of 3-carene. The PES of hv=15.0 eV has also been plotted on top of the PECD curves. The PESs are plotted with different scales just to make them comparable in the same frame as clear as possible.

To verify our experimental results, over the whole range of photon energies we tried, we have performed CMS-Xα calculations. It should be noticed that CMS-Xα considers the fixed geometry for both the ground and the continuum state. So, the results that we are presenting here, are obtained at the fixed, equilibrium geometry of the ground state by which we mean vibrations are ignored. For this reason and to make the results of CMS- Xα calculation comparable to the experimental results, we are just picking up the experimental PECD values at the IP of 3-carene, 8.38 eV, where we believe the origin (vibrationless state) lies down [92]. Fig. 117 shows the CMS-Xα calculation on top of which the experimental values have been plotted, all as a function of eKE. A good agreement can be seen between our calculation and what we observe experimentally.

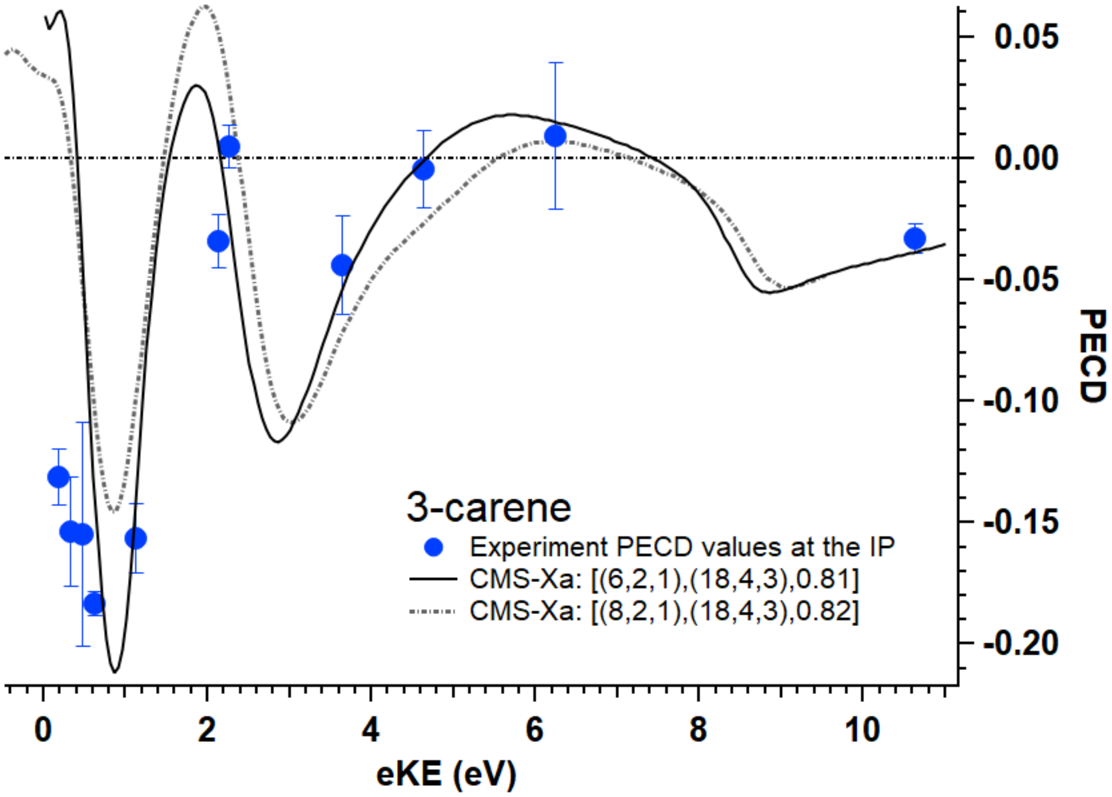

Fig. 117: PECD of 3-carene as a function of electron kinetic energy: the solid black curve is the result of CMS-Xα calculation and each of the blue dots is the PECD value at 3-carene IP for one of the photon energies we tried experimentally. In the CMS-Xa method, we have tried two different sets of Norman reduction factors as well as different lmax values to truncate the spherical harmonic angular basis in either the initial state or the final cation state in order to get a reliable set of results. These are mentioned in the legend as [(lmax for the outsphere in the initial state, lmax for C atoms in the initial state, lmax for H atoms in the initial state), (lmax for the outsphere in the final state, lmax for C atoms in the final state, lmax for H atoms in the final state), Norman reduction factor].

For eKE below 1.5 eV, the CMS-Xα method is predicting PECD values about 20% which is matching with the experimental values. On the other hand, the PECD of 3-carene is changing sign frequently at eKE above 1.5 eV, confirming the dependency of PECD on eKE. Both experimental and theoretical results are showing the same trend for PECD sign change over the whole energy range presented in Fig. 117. Particularly, if we look at the last three experimental data points, corresponding to our low-resolution data set (hν=13.0, 15.0, 19.0 eV), we can verify the PECD results presented in Fig. 116 (b) very well. In figure Fig. 116 (b), we saw zero PECD for hν=13.0 eV while positive and negative PECD values for hν=15.0 eV and hν=17.0 eV, respectively. The same thing now can be seen in CMS-Xα results; at eKE=4.64 eV, which is associated with hν=13.0 eV, the PECD predicted by theory is around zero. CMS-Xα is also resulting a positive value of PECD at eKE=6.25 eV, associating with hν=15.0 eV and a negative value of PECD at eKE=10.62 eV, associating with hν=19.0 eV.

6.1.2. α-pinene

We have measured the PECD of α-pinene over a range of photon energies expanding from near ionization threshold up to 19.0 eV. Like 3-carene, we can classify these photon energies into three groups: high-resolution class involving photon energies equal and below 9.5 eV, medium resolution class including hν=10.5, 11.0, 12.0 eV, and eventually the low-resolution class involving the three highest photon energies hν=13.0, 15.0, 19.0 eV. As a quick reminder, the data presented in this section are the results of three different beamtime at the DESIRS beamline of SOLEIL synchrotron. In the first run, Sep 2016 (photon energies hν=9.0, 9.5, 10.5, 12.0 eV), R-enantiomer of α-pinene has been used while in the other two runs, May 2018 (photon energies hν=11.0, 13.0, 15.0, 19.0) and Mar 2019 (photon energies hν=8.35, 8.5, 8.7), the measurements have been made on S-enantiomer of α-pinene. So, wherever needed, the PECD curves recorded in 2016 using R-enantiomer will be negated to be comparable to those recorded in 2018 and 2019 with S-enantiomer. It should also be noticed that all the graphs presented in this chapter, are in coincidence with parent mass, m/z=136 amu. The interesting region of the spectrum to us is the X-band, where there is no significant amount of fragmentation. The X-band region is also interesting as it only corresponds to the photoelectrons being ejected from the HOMO orbital, reducing the complexity of interpreting the results, see Sec. 3.1.1 for more information.

We start by looking at α-pinene PES recorded at photon energies that belong to the high resolution class. Within this class, the PES of α-pinene shows a high resolution since the photon energies are all relatively close to the IP of the molecule, 8.16 eV, resulting in lower kinetic energies of the photoelectrons which itself is leading to higher resolutions in a typical VMI imaging setup. However, the resolution of a specific peak in all of them is not the same; again, the lower the photon energy, the higher the resolution. This can be easily seen from Fig. 118 where the spectra recorded at lower photon energies are plotted on top of each other. Here, all the spectra have been normalized in a way that the intensity of the first vibrational peak at 8.22 eV takes the same value for all of them. Firstly, we can see the first major vibrational peak at 8.22 eV is narrower at hν=8.35 eV that that at hν=9.5, for example. Just like 3-carene, the other point is the different relative ratio between the first two consecutive vibration peaks, one at 8.22 eV and the other at 8.4 eV, for different photon energies. At hν=8.5 eV and hν=8.7 eV, those peaks have the same intensity while at hν=9.0 eV and hν=9.5 the origin is shorter than the next one. The same kind of argument provided for 3-carene could be true here; briefly, at higher photon energies, more normal modes are being excited simultaneously (see Sec. 6.1.1).

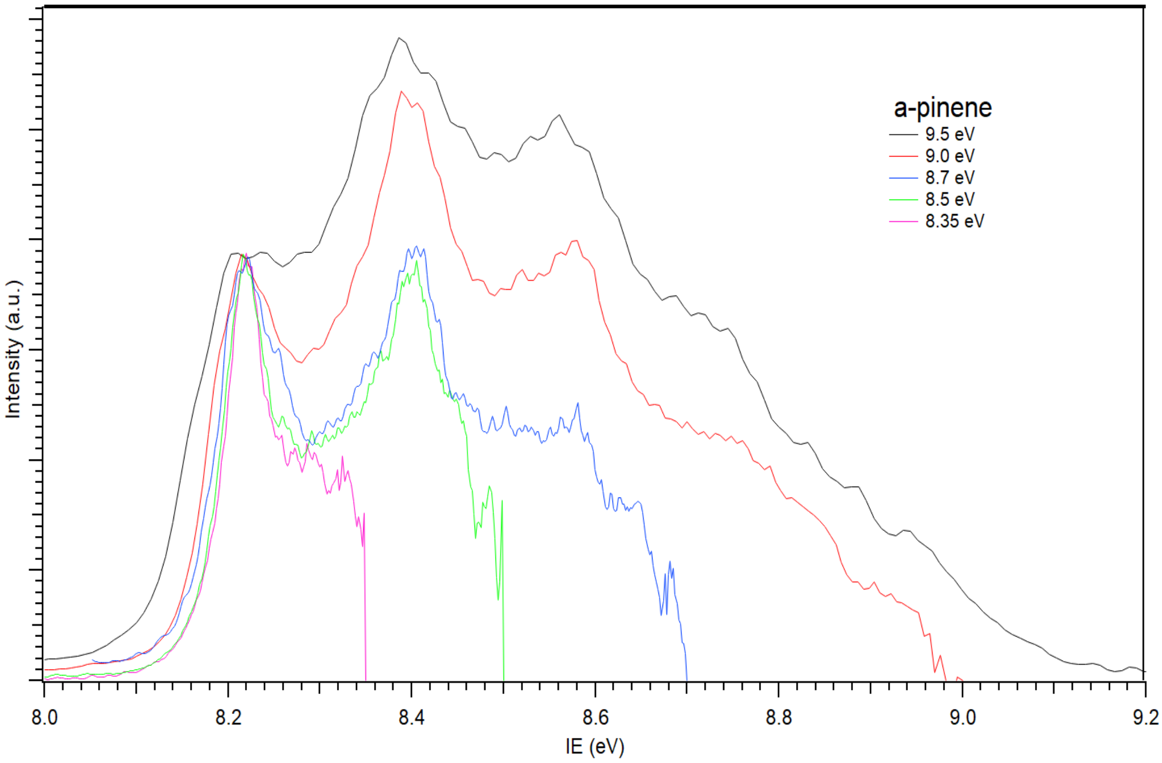

Fig. 118: PES of α-pinene at different photon energies. There are four major vibrational structures in the photoelectron spectrum of α-pinene over the X-band (see Sec. 3.1.1 also); here, it has been tried to choose the photon energies in a way that, going from hν=8.35 eV to hν=9.0 eV, in each step one more of those vibrational structures appear in the spectrum.

The next interesting thing would be a comparison of the PECD signals recorded at photon energies within our higher resolution class. If there is any vibrational dependency for α-pinene

PECD, it should be easier to see it at lower photon energies. Plotted in Fig. 119 is the PECD signals measured at lower photon energies as a function of IE. Some oscillations can be seen in the PECD curves with respect to the major vibrational structures in PES. However, opposite to 3-carene case, there is not a general king of oscillation pattern seen for all the photon energies tried here. For example, an obvious difference in the PECD curves when going from hν=9.5 eV to hν=9.0 eV and then to hν=8.7 eV is that they are looking like being shifted vertically. Although all of them are showing vibrational modulation, they do not take the same PECD values for a given IE. The rough guess as a reason for such a discrepancy is the dependency of PECD on electron kinetic energy. In Fig. 108, the PECD of α-pinene at two of these photon energies, hν=9.5 eV and hν=9.5 eV, are plotted as a function of eKE. It seems that the PECD signal is growing over the plotted energy range monotonically when eKE increases. This emphasises eKE as an important factor affecting the PECD in the case of the α-pinene molecule.

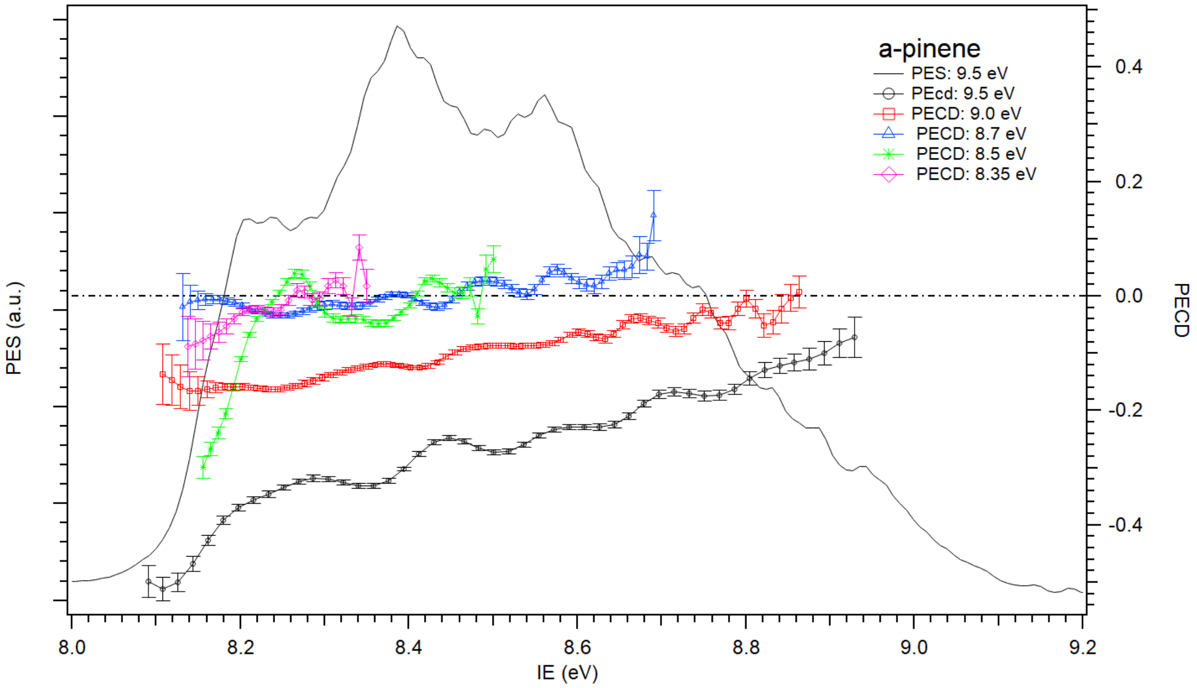

Fig. 119: Experimental PECD results of α-pinene at photon energies equal to and lower than 9.5 eV. The PES recorded at 9.5 eV is also plotted on top of the PECD curves to show the location of the vibration peaks. The PECD of hν=9.0 eV and hν=9.5 eV have been vertically flipped as they have been recorded with R-enantiomer.

To get this point better understood, we have plotted the PECD associating with the first vibrational peak centred at 8.22 eV as a function of eKE in Fig. 120. One can see that going from lower eKE to higher ones a bigger PECD signal is observed for the same peak in PES. This means that, in the case of α-pinene, PECD is intensively a function of eKE. By comparing Fig. 120 with Fig. 112 one can conclude that the PECD of different molecules is not depending on eKE in the same way. Such a comparison tells us that for 3-carene the dependency of PECD on eKE was not as much as it is the case for α-pinene. However, this conclusion is true only over the photoelectron kinetic energy range below 1.5 eV. We will return to this point at the end of this section when we present the results of CMS-Xα calculation for α-pinene PECD.

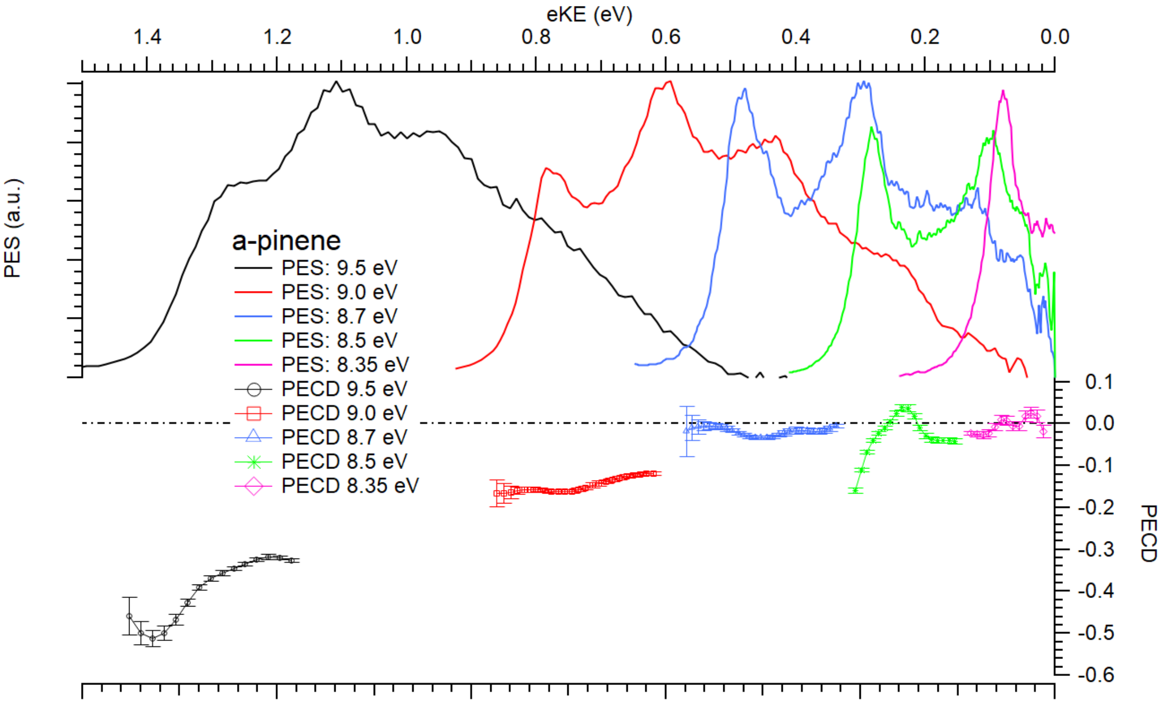

Fig. 120: PES and PECD of α-pinene recorded at different lower photon energies vs eKE, the axis on the top. The PES spectra are rescaled to make the plot clearer. For each photon energy, the PECD corresponding only to the first vibrational peak is plotted here.

Now, we can try to exclude the eKE effects on PECD just to see how the pure vibrational dependency of PECD is. Like 3-carene, we can consider some eKE windows where two peaks with different vibrational character, from the PESs recorded at two different photon energies, get aligned. The first example of such a window is shown in Fig. 121 where the first vibrational peak of hν=8.7 eV is aligned with the third vibrational peak of hν=9.0 eV. In Sec. 3.1.1 (see Fig. 53), it was shown that the third peak in the α-pinene PES has the same vibrational character of the first peak in addition to two quanta excitation of normal mode ν56, double bond stretching. So any difference in PECD of these two peaks can be considered as the effect of two quantum level excitation in normal mode ν56. One can see from Fig. 121 that exciting ν56 to its second quantum level is leading to a higher absolute PECD signal for α-pinene. This is the opposite of what we observed for 3-carene, where excitation in double bound stretching normal mode was resulting in a smaller absolute PECD signal, see Fig. 113 and Fig. 114.

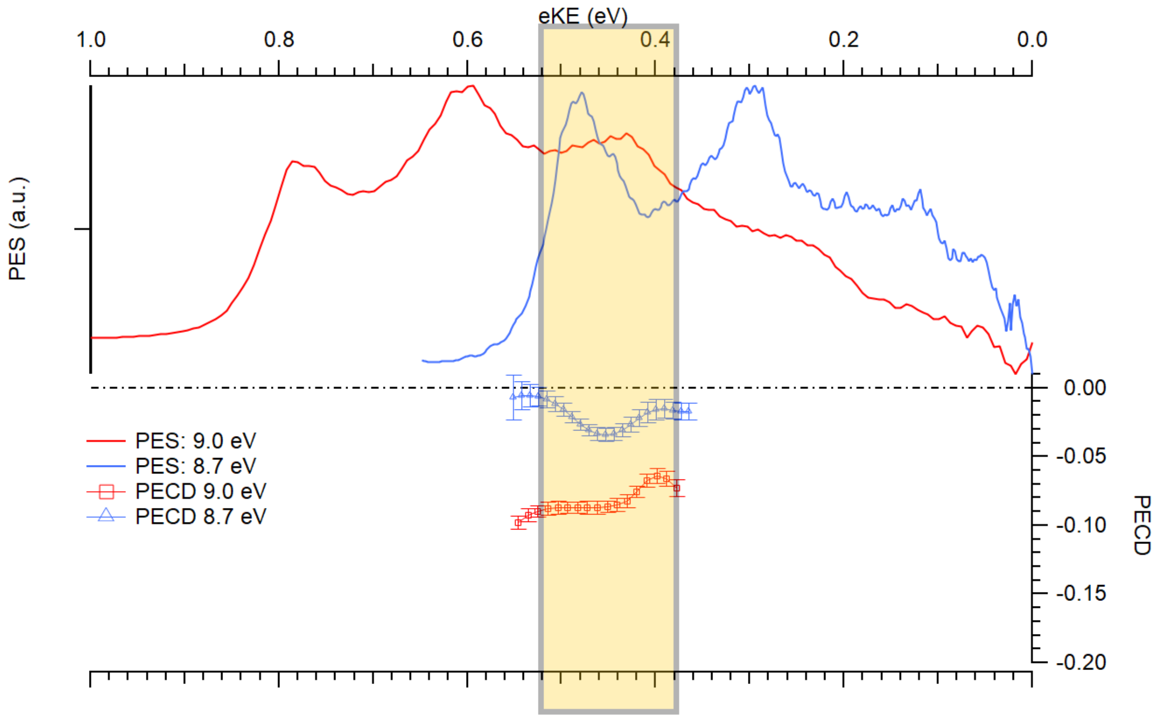

Fig. 121: PES and PECD of a-pinene recorded at two photon energies, hν=9.0 eV (red curves) and hν=8.7 eV (blue curves) as a function of eKE, the axis on the top. For each photon energy, the PECD in association with only the interesting vibrational peaks in the eKE window is plotted here, see the text.

One possible explanation to such different observations for our two molecules, 3-carene and α-pinene, could be that the PECD is still implicitly depending on eKE. In other words, in the case of α-pinene for example, if we had considered another eKE window, we might not conclude that higher vibrational excitation of normal mode ν56 can lead to higher absolute PECD values. To make this point more clear, another eKE window is considered in Fig. 122, where the second vibrational peak of hν=8.5 eV is aligned with the third vibrational peak of hν=8.7 eV. Referencing to Fig. 53, we can say that the difference between the second and the third peaks in α-pinene PES is one quanta excitation of ν56. However the changes when going from hν=8.5 eV (one quanta excitation of ν56) to hν=8.7 eV (two quanta excitation of ν56) in this eKE window is not simply an increase in absolute PECD signal; for instance, at eKE=1.3 eV, the PECD signal is reversed with having approximately the same amplitude. Therefore, the vibration dependency of PECD should always be discussed in conjugation with the eKE effects.

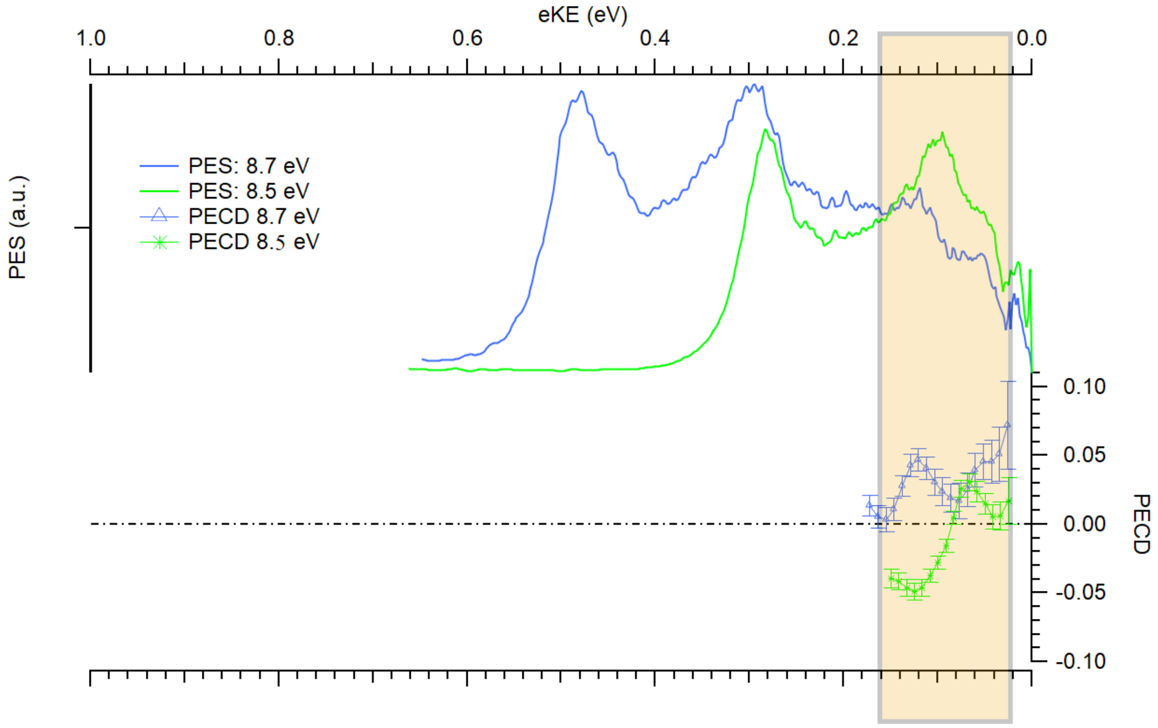

Fig. 122: PES and PECD of a-pinene recorded at two photon energies, hν=8.7 eV (blue curves) and hν=8.5 eV (green curves) as a function of eKE, the axis on the top. For each photon energy, the PECD in association with only the interesting vibrational peaks in the eKE window is plotted here, see the text.

At this point, we turn to the medium resolution class of our data. The PES and PECD results for the photon energies included in this class are plotted in Fig. 123. The resolution is not as high as it was the case for our lower photon energies but still some vibrational features can be seen in PESs. The PECD spectra are also showing some modulations but not as intense as they were at lower photon energies. The main point that we can realize from Fig. 123 is that, over the whole X-band region, the PECD signal is looking like being attenuated when going from hν=10.5 eV to hν=11.0 eV and then to hν=12.0 eV. This means that, over such an energy range, the PECD decreases by an increase in eKE. This trend is the opposite of what we saw for α-pinene over the eKE range below 1.5 eV, see Fig. 120 also.

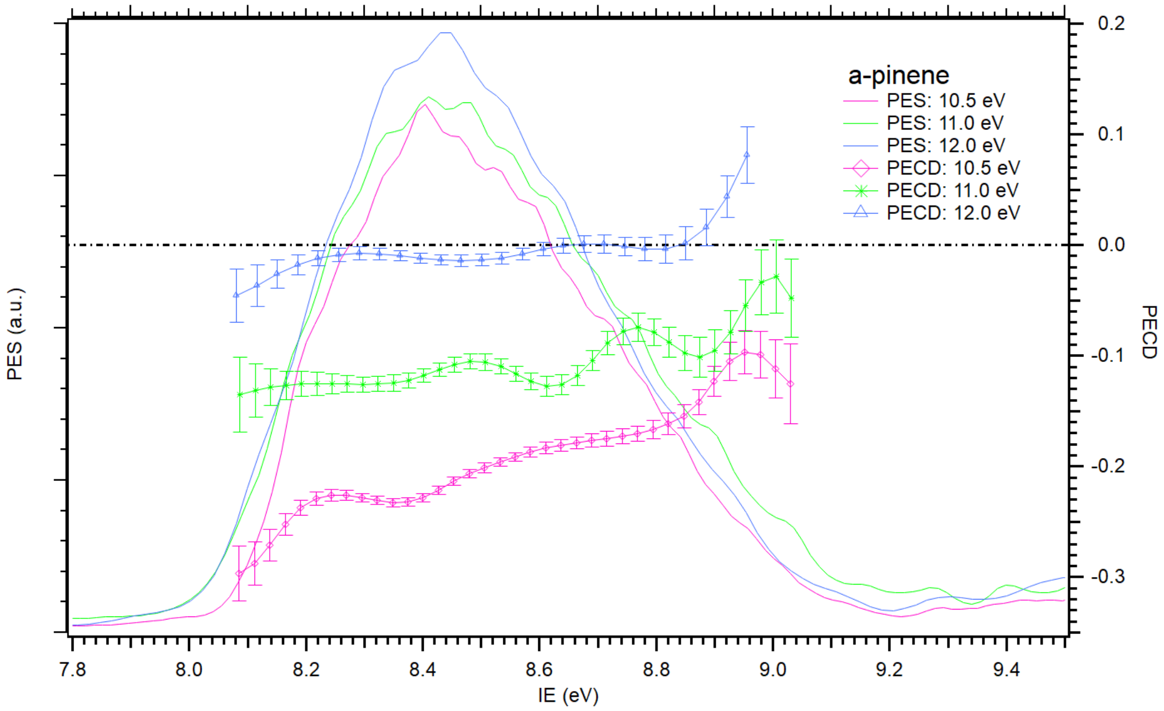

Fig. 123: PES and PECD of medium resolution data set (hν=10.5, 11.0, 12.0 eV) of α-pinene. The PESs are plotted with different scales just to make them comparable in the same frame as clear as possible. PECD of hν=10.5 eV and hν=10.5 eV have been vertically flipped here as they have been recorded with the R-enantiomer.

Going to higher photon energies hν=13.0, 15.0, 19.0 eV (higher eKE release), a PECD sign change is observed over the X-band region, as shown in Fig. 124. At hν=13.0 eV, the PECD signal is still negative over the whole X-band region while going to hν=15.0 eV results in approximately zero percent PECD on average. Going to hν=19.0 eV, the PECD changes sign to totally positive values. Here, we cannot attribute such a change in PECD sign to vibrational effects as the resolution is not high enough to have them well resolved. On the other hand, the change in the PECD sign is happening for the whole X-band range where several vibrational features are embedded in. So, over this range of eKE, the PECD is more dependent on eKE rather than vibrational levels.

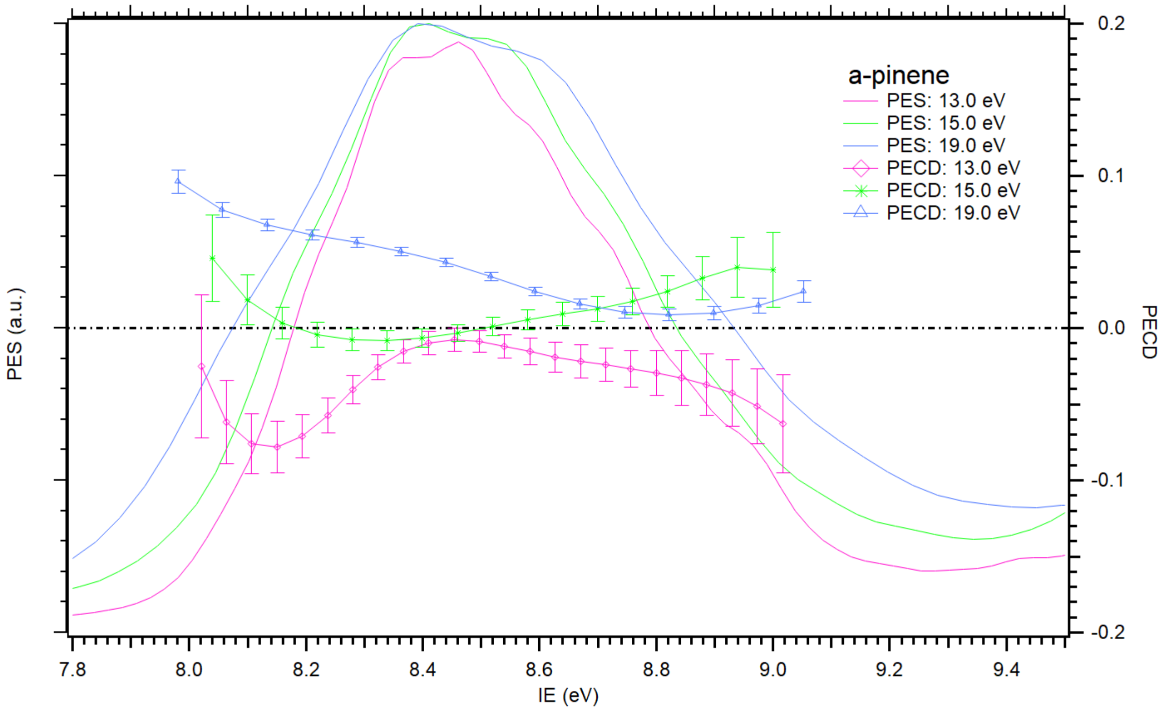

Fig. 124: PES and PECD of low resolution data set (hν=13.0, 15.0, 19.0 eV) of α-pinene. The PESs are plotted with different scales just to make them comparable in the same frame as clear as possible.

So far, we have seen different trends in the PECD signal over different photoelectron kinetic energies. Now, we can sum up with a broader look at the whole eKE ranges presented above, expanding from near zero kinetic energies up to 10 eV. A comparison between our experimental results and the PECD obtained from CMS-Xα method would also be worthwhile. In Fig. 125 we have presented the PECD results of our CMS-Xα calculation. As mentioned before, CMS-Xα is calculating PECD in a fixed geometry of molecule, equilibrium geometry of the ground state. So, to make the comparison between the theory and experiment reasonable, only the experimental PECD values at α-pinene IP, 8.20 eV, have been chosen to be plotted on top of the CMS-Xα results. To provide more reliable theoretical data as the output of the CMS-Xα method, it has been tried to solve the problem with various reduction factors and lmax values four of which are presented in Fig. 125. It can be seen that all the cases are converging to nearly the same results, giving us a feeling of confidence in our theoretical method.

The dependency of PECD on the eKE can be now obviously seen from experimental data points presented in Fig. 125; PECD goes from zero to 45% and returns back to zero again just by going from eKE=0.1 eV to eKE=4.1 eV. The agreement between the theory and experiment is not so bad here. Particularly for the eKE ranging from 1.0 eV to 8.0 eV, the general trend of the PECD is predicted very well by the CMS-Xα method. We should notice that there is a remarkable assumption in CMS-Xα which completely ignores the vibrational effects. This can explain the mismatch between the experiment and the theory at very low eKE (lower photon energies) where the resolution is higher and vibrations come to effect more significantly. One of the important points that can be realised in Fig. 125 is that the record-breaking PECD value we have observed for a-pinene at hν=9.5 eV, around 40% of asymmetry, is also predictable by theory. The experimental data point at eKE=1.3 eV is what we have measured for α-pinene at 9.5 eV; one can see from Fig. 125 that CMS-Xα method is also giving that amount of asymmetry for this molecule.

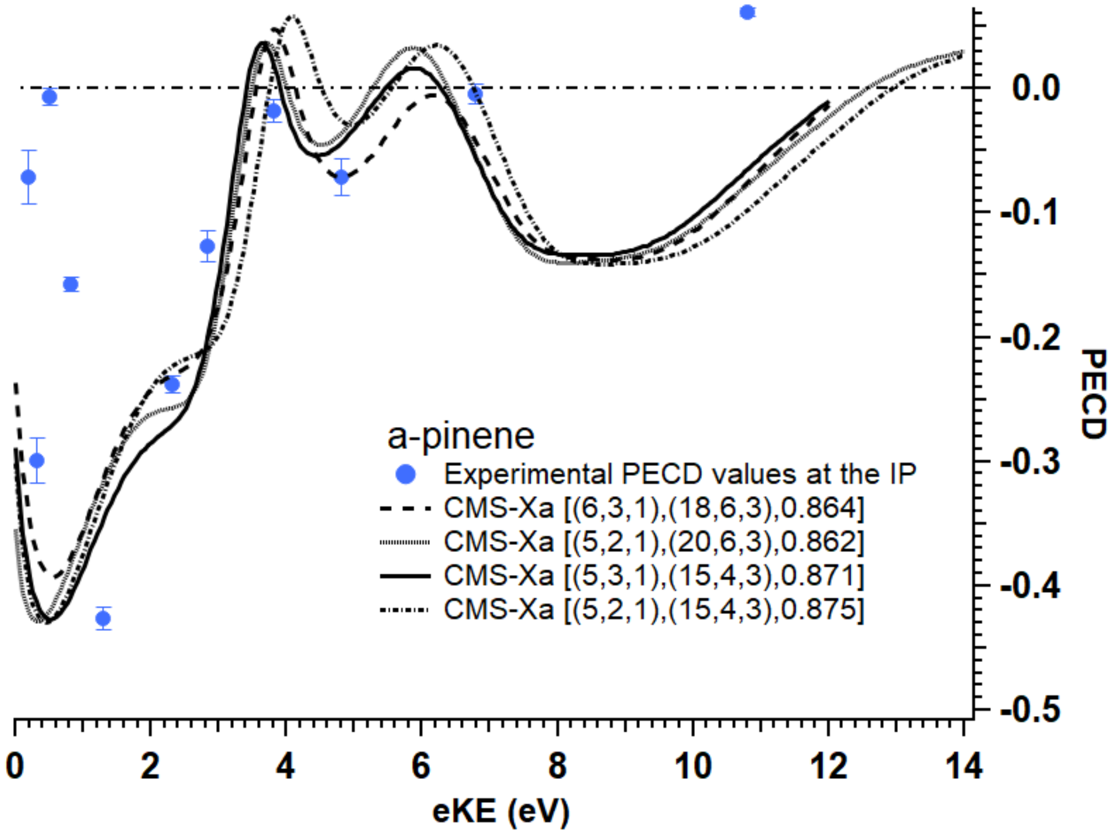

Fig. 125: PECD of α-pinene as a function of electron kinetic energy: solid black curves are the results of CMS-Xα calculation and each of the blue dots is the PECD value at α-pinene IP for one of the photon energies we tried experimentally. In the CMS-Xa method, we have tried various spherical atomic reduction factors as well as different lmax values to truncate the spherical harmonic angular basis in either the initial state or the final cation state in order to get a reliable set of results. These are mentioned in the legend as [(lmax for the outsphere in the initial state, lmax for C atoms in the initial state, lmax for H atoms in the initial state), (lmax for the outsphere in the final state, lmax for C atoms in the final state, lmax for H atoms in final state), Norman reduction factor].

6.2. Conclusion

PECD of α-pinene and 3-carene at eleven fixed photon energies ranging from near-threshold up to 19.0 eV were studied. Regarding the vibrational resolution of the X-band region, the measurements were divided into three classes: high-resolution, medium resolution, and low-resolution. The assignment of the vibrational structures, done in Chapter 3 was acting as a key here, which enabled us to interpret the results.

The photon energies in the high-resolution class were selected in a way that when their results are plotted as a function of eKE, some peaks with a different vibrational character from different photon energy measurements become aligned within a very narrow eKE window. Within such windows, the kinetic energy effects are negligible or at least affecting the vibrational transitions similarly. So, any change in the PECD signal was attributed to differences in the vibrational character of the peaks. For example, purely vibrational effects resulting from adding a single quanta to the normal modes ν56 and ν60 (endocyclic C=C double bond stretching and symmetric methyl group stretching attached to the main ring, respectively) were identified. On the other hand, trying different photon energies also provides us with the opportunity to compare the PECD of photoelectrons correlated to the same vibrational transitions but carrying different kinetic energies. For instance, in the case of 3-carene, the PECD signal correlated to the first vibrational structure in the X-band (lowest frequency normal modes ν1, ν2, and ν3) changed from -15% to -21% due to a variation of only 0.54 eV in eKE.

To study the eKE effects over a longer range of energies, we simulated the PECD of 3-carene using CMS-Xα and verified that by the experimental PECD values we obtained for the adiabatic IP of the molecules. The CMS-Xα method shows that the PECD of α-pinene and 3-carene changes sign several times as eKE increases, in excellent agreement with our experimental results. Particularly, both our theoretical and experimental methods are confirming 20% and 40% absolute PECD signal change for 3-carene and α-pinene, respectively, within an eKE range of 1.0 eV.

7. Resonance Enhanced Multiphoton Ionization- (REMPI-) PECD of α-pinene

So far, most of the PECD experimental studies have been done in the single photon ionization regime using VUV synchrotron radiation in order to establish the concept of the PECD itself. However, people are recently moving from synchrotron-based single-photon PECD experiments to laser-based REMPI-PECD experiments. REMPI with laser light provides scientists with the opportunity of studying the role of intermediate states on the PECD [56, 57]. Also, in delay pump-probe laser experiments people can study time-resolved PECD [62]. Nanosecond lasers REMPI experiment has also been used to study the CD in the ion yield [147].

The other interesting subject is studying the effect of the vibronic quantum states on PECD. Actually, it has already been proven that the vibrations can even induce inversion in the PECD signal [51]. Using synchrotron radiation, it is possible to study the effect of the vibronic states of the cation [97], while resonantly enhanced multiphoton ionization with laser light enables us to study the effect of vibrationally excited intermediate states [56]. Based on our previous single-photon VUV measurements, monoterpenes limonene, α-pinene, and 3-carene show some structures in their X-band, which are supposed to be different vibrational states [56, 97], see Chapter 3 also. Moreover, we have shown that there is an intense modulation between the PECD and those vibrational structures, as demonstrated in Chapter 5. In this chapter, the results of some REMPI-PECD measurements on α-pinene are presented revealing the dependency of the PECD on intermediate vibronic states.

If the intermediate state is a Rydberg state, the electron will be so far from the core that ionization will not affect the core geometry too much. Therefore, if the neutral is in a certain vibrational state, after ionization the cation core will remain at the same vibrational state. This is the so called *propensity* rule, which acts as a non-rigid selection rule. The propensity rule makes it possible to compare the vibrational progression of the cation with that of deffuse intermediate electronic states, such as Rydberg states. In the following sections, we will frequently use the propensity rule to interpret the PES and PECD spectra of α-pinene recorded in MPI at different wavelengths.

7.1. Laser system and experimental setup

The experiment was done in the Artemis beamline of Central Laser Facility (CLF). An amplified femtosecond laser system (Red Dragon, KM Labs) generates 30 fs pulses of 800 nm light, with a pulse energy of up to 10 mJ and at a repetition rate of 1 kHz. The output of this system can either be used to generate high harmonics or be fed to an optical parametric amplifier (OPA, TOPAS Light Conversion) to generate tunable pulses spanning the spectral range from 235 nm to 15 microns. Here, a 2-photon PECD measurement at 200 nm as well as a couple of 3-photon PECD measurements at 370 nm and 400 nm were done. The wavelengths 200 nm and 400 nm could be generated by frequency doubling (FD) and sum-frequency mixing (SFM) techniques while for the other wavelengths like 370 nm we used the TOPAS system. The wavelength 400 nm was simply generated as the second harmonic of the fundamental wavelength by a Frequency Doubling (FD) crystal. However, to generate the 200 nm wavelength, we mixed 400 nm with the fundamental using an SFM crystal to generate the third harmonic, 266 nm, and then mixed 400 nm and 266 nm using another SFM crystal. Fig. 126 shows the schematic of the beamline.

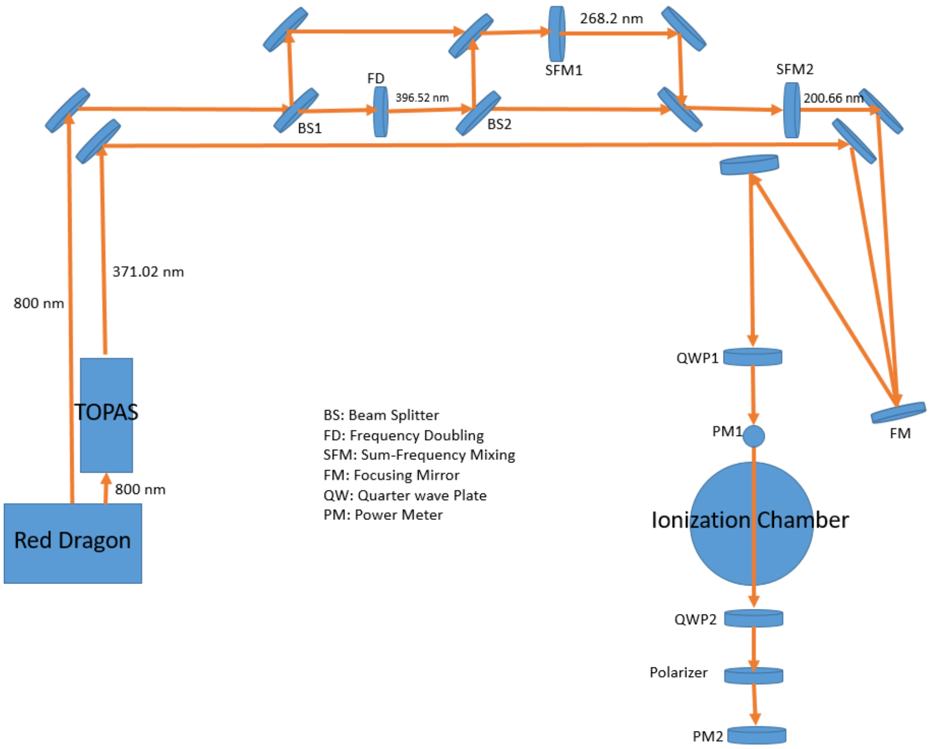

Fig. 126: Schematic of the beamline. Dependent on the wavelength that we need, the laser can either go through the TOPAS (to generate 370.02 nm) or be simply frequency-doubled (to generate 396.52 nm) or go through a combination of frequency doubling and sum-frequency mixing (to generate 200.66 nm). The beam eventually is focused on a zero degree focusing mirror. The laser power normally is measured using PM1, but for the polarimetry purposes, the power is monitored by PM2.

Looking at the spectrum of the source laser system, we found that the fundamental wavelength was not exactly 800 nm. This caused the second and fourth harmonics not to be exactly 400 nm and 200 nm. In Fig. 127 the spectra of the laser just before going into the ionization chamber are given for three wavelengths at which all the measurements of this chapter are done. As we can see, the peaks are centred at 200.66 nm, 371.02 nm, and 396.52 nm.

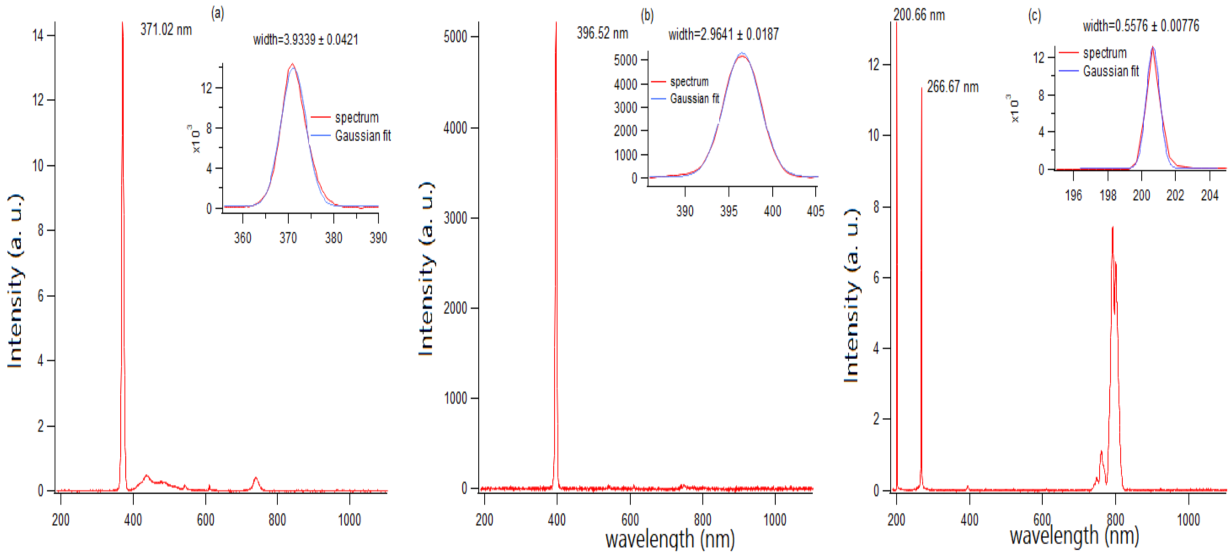

Fig. 127: Spectra of the laser just before going into the ionization chamber for three wavelengths: (a) 371.02 nm, (b) 396.52 nm and (c) 200.66 nm. Insets show the broadband of the laser around the main wavelength in each subset. The width of the spectra is calculated by fitting Gaussian curves to them.

Right/Left circularly polarized light could be simply generated by passing the linearly polarized light through a quarter wave plate whose axis makes an angle of +45/-45 degree with respect to the polarization axis of the incoming light; however, we used the rotating quarter-wave plate method explained in Ref. [148] (a practical application of which can be found in Ref. [30]) because we needed to do the polarimetry and estimate the degree of polarization of the circularly polarized light at the same time. The results of the polarimetry for PECD measurements at 396.52 nm with a laser power of 5.0 mW are given in Fig. 128 (a) (data points presented by markers). Based on Ref. [148], the Stokes parameter for left and right circularly polarized light can be calculated by fitting the following function to their corresponding data

$$I(\theta) = \frac{1}{2}(S_0 + S_1 cos^2 2(\theta + \theta_0) + S_2 cos2(\theta + \theta_0) sin2(\theta + \theta_0) + S_3 sin2(\theta + \theta_0)) \qquad \text{(Eq. 43)}$$

Such a fit is also shown in Fig. 128, giving S_3 for right/left circular polarization as 0.8570/-0.8871. We also repeated the polarimetry with a lower power, 4.4 mW, the next day and found a higher degree of polarization, S_3 for right/left circular polarization as 0.8973/-0.9770. The data points and the fitted curve for this polarimetry are also shown in Fig. 128 (b).

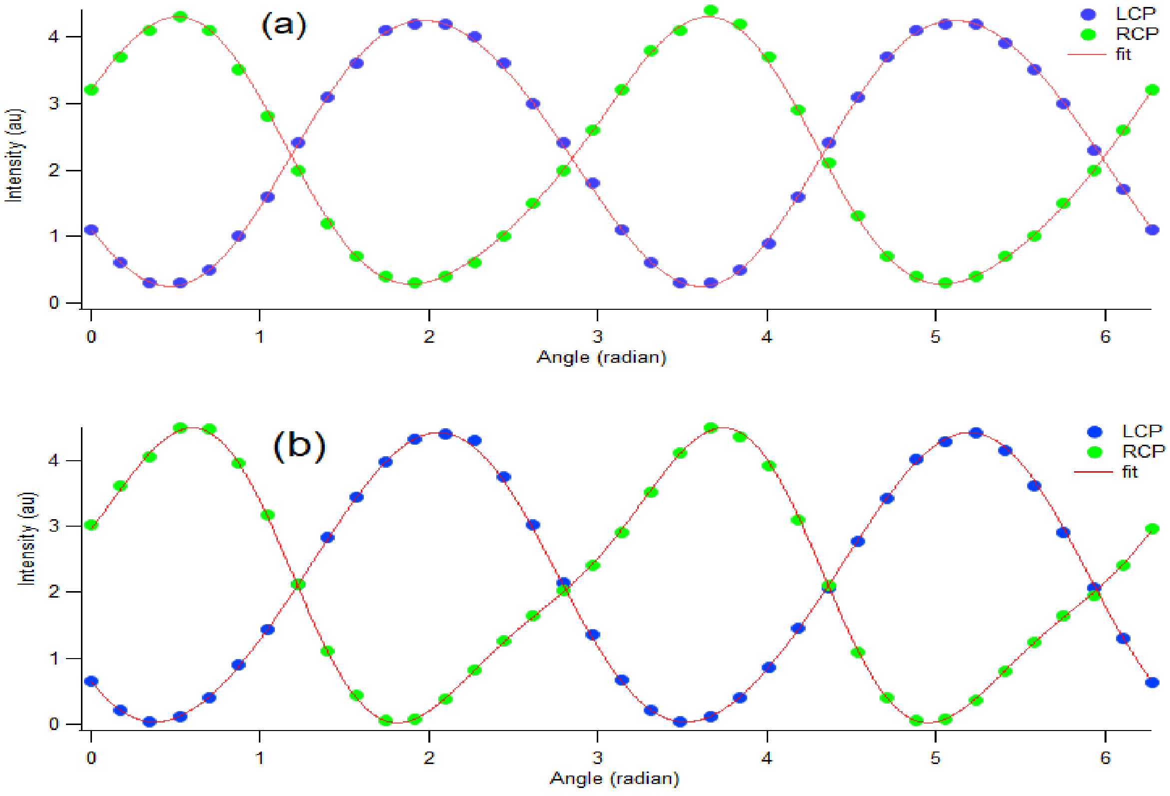

Fig. 128: Two polarimetry at 396.52 nm: (a) the first with the laser power set as 5.0 mW and (b) the second with a laser power of 4.4 mW.

The molecular beam is generated through the expansion of α-pinene, carried by He, through a 1 kHz pulsed nozzle with a 200 μm aperture. The resulting expansion passes through a 0.75 mm skimmer and enters the interaction region of the spectrometer through a hole in the centre of the repeller plate of the VMI. The typical pressures in the gas and ionization chamber were 1.36×10^{-5} mbar and 4.11×10^{-6} mbar, respectively, and the helium backing pressure was typically -0.3/-0.4 bar, relative to the atmospheric pressure. The detector consists of an 80 mm diameter microchannel plate (MCP) and a phosphor screen, which is imaged using an sCMOS camera.

7.2. Three-photon ionization PECD at 396.52 nm

Wavelength 396.52 nm was our first choice for α-pinene MPI-PECD; as mentioned in Sec. 7.1, this wavelength was generated as the second harmonic of the fundamental wavelength of a Ti-sapphire laser. The total energy of three photons of this wavelength was 9.38 eV which lies above the ionization potential of α-pinene; based on the VUV synchrotron experiments, the IP of α-pinene is roughly 8.2 ev (Fig. 49). Absorption of two photons provides an energy of 6.25 eV which excites the molecule to one of its Rydberg states, from which the ionization will happen by absorbing the third photon. Before doing the PECD measurement, we recorded a couple of images using horizontal and vertical linear polarization. The laser power was set at 12.0 mW and the acquisition time for each image was 30 minutes. The pressure in the gas and ionization chamber were 1.36×10^{-5} mbar and 4.11×10^{-6} mbar, respectively and the helium backing pressure was -0.3 bar, relative to atmospheric pressure. The valve operated at 1 kHz with an opening time of 25 μs.

The photoelectron images are presented in Fig. 129 showing an anisotropy for horizontal polarization as is expected (the direction of propagation of the laser light is from right to left in the images and the electric field of the laser for the horizontal polarization is along the top-bottom direction).

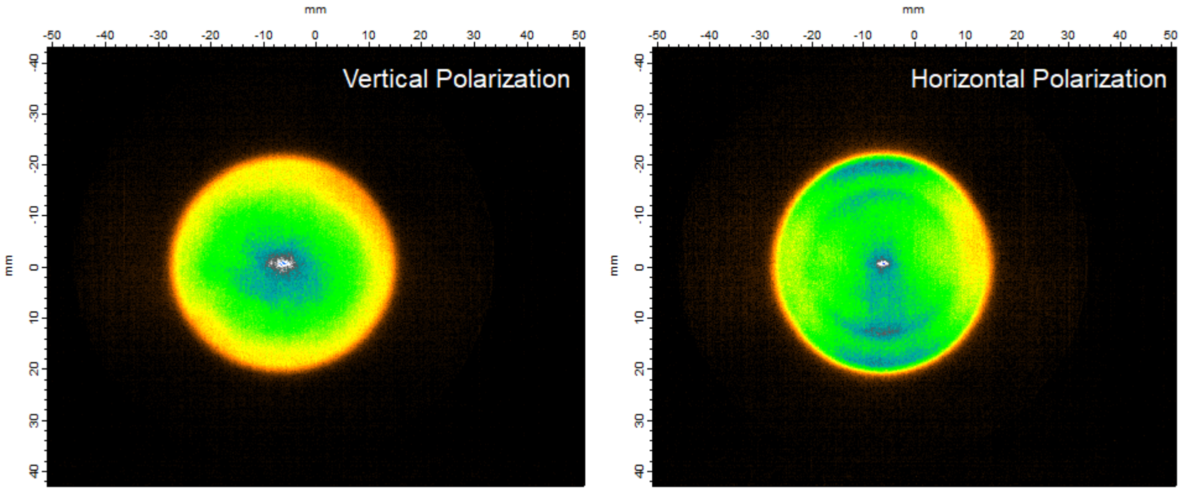

Fig. 129: VMI images recorded for 3-photon ionization of α-pinene at 396.52 nm using vertical (left) and horizontal (right) polarization. The laser beam is crossing from right to left *in the images. The polarization axis is along to south-north direction for horizontal polarization and is perpendicular to the image for vertical polarization.*

A pBASEX analysis of these images gives the PES spectra shown in Fig. 130. A small difference between the spectrum recorded with Horizontal polarization and that recorded with vertical polarization can be seen. This is because the pBASEX algorithm is working better for horizontal polarization in this case. Actually, the pBASEX algorithm is using the Abel inverse transformation whose assumption is the existence of an axis of symmetry lying in the image plane. Here, with the linearly polarized light, the symmetry axis is the direction of polarization which lies in the image plane for the horizontal polarization (south to north in Fig. 129, right hand side). For the vertical polarization, the direction of the polarization is perpendicular to the image plane, so there is no symmetry axis in the image plane to satisfy the requirement of the Abel inverse transformation.

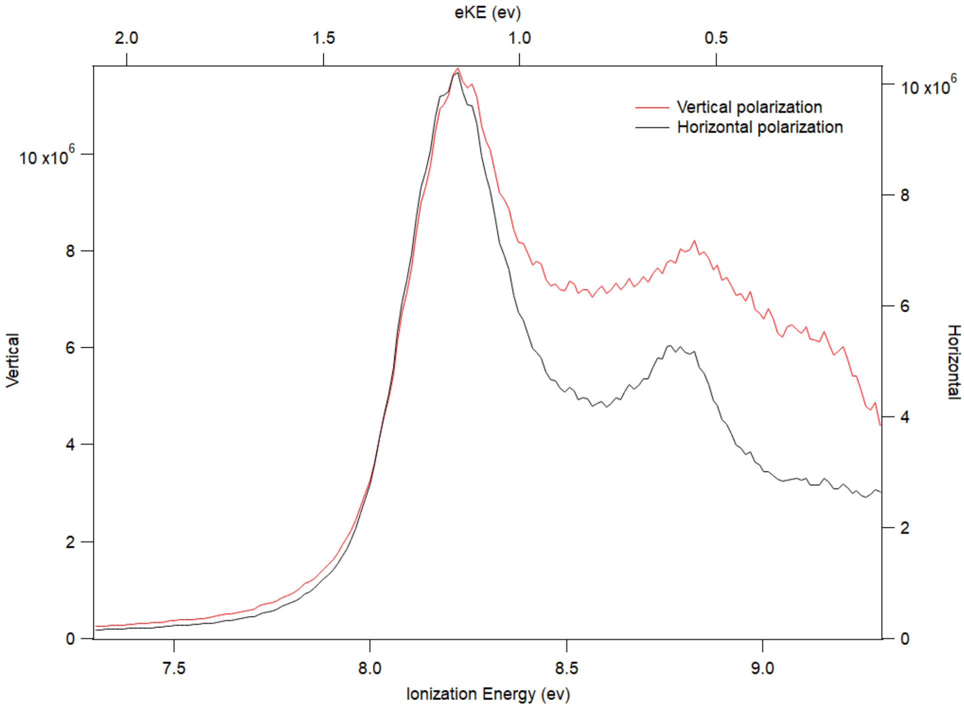

Fig. 130: PES spectrum obtained via pBASEX analysis for 3-photon ionization of α-pinene at 396.52 nm using horizontal (black) and vertical (red) linear polarization with a laser power of 12 mW.

Circularly polarized light for the PECD measurement was generated by passing the laser light through a quarter wave plate. The laser power in this case, just before going into the ionization chamber was 5 mW. We accumulated an image for any polarization, LCP for left polarization and RCP for right polarization, over one hour. The differential image (DI=LCP-RCP) and its Abel inverse transformation are shown in Fig. 131.

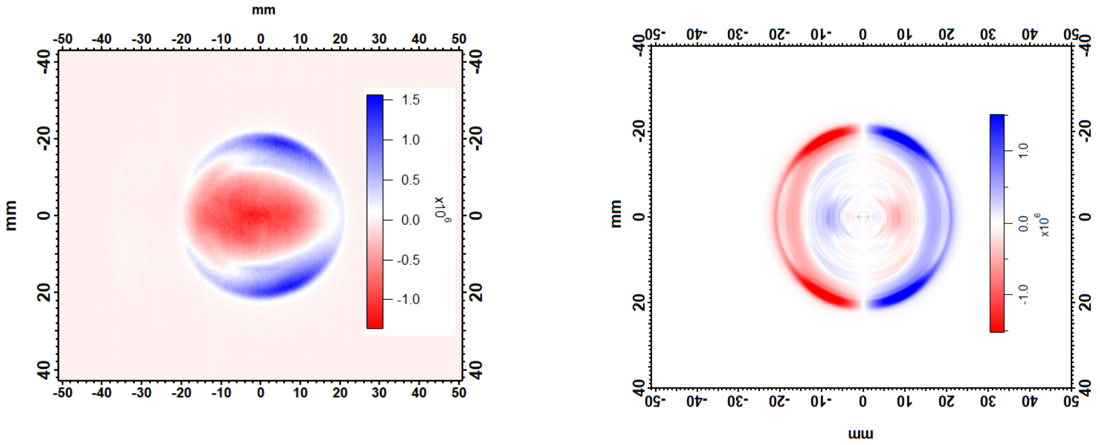

Fig. 131: Differential image, left, and its Abel inverse transformation, right, for 3-photon PECD of S-α-pinene at 396.52 nm with a laser power of 5 mW. Light is crossing from right to left in the images.

One point about Fig. 131 is that the differential image before the Abel inversion is not antisymmetric. Principally, if the degree of circular polarization in the LCP and RCP was 100%, the differential image should be antisymmetric about the vertical axis crossing the centre of the image, which is the intersection of the forward and backward hemispheres with respect to the light propagation direction. We can manually decouple the symmetric and antisymmetric components of the differential image, shown in Fig. 132, from which the symmetric part is believed to be due to any impurity in the circular polarization of the light. As discussed in Sec. 7.1, the circular light we generated was not perfect and there was always some degree of ellipticity in the polarization of light.

To separate the symmetric and antisymmetric parts we take the differential image, DIF, shown in Fig. 132 (a), and flip it around the vertical axis crossing the centre of the image. We name the flipped differential image as FDIF. Then, we define the symmetric and antisymmetric part of the differential image, SDIF and ADIF respectively, as:

$$SDIF = \frac{DIF + FDIF}{2} \qquad \text{(Eq. 44)}$$

$$ADIF = \frac{DIF - FDIF}{2} \qquad \text{(Eq. 45)}$$

From the above definition it is obvious that the DIF image is equal to the sum of its symmetric and antisymmetric part, $DIF = SDIF + ADIF$.

If we feed the antisymmetrised part of the differential image to our pBASEX algorithm, the Abel inverted image, and consequently, the PECD signal is obtained to be the same as when we feed the pBASEX algorithm with the whole differential image. This is showing the reliability of the Legendre polynomial fitting happening within our pBASEX algorithm.

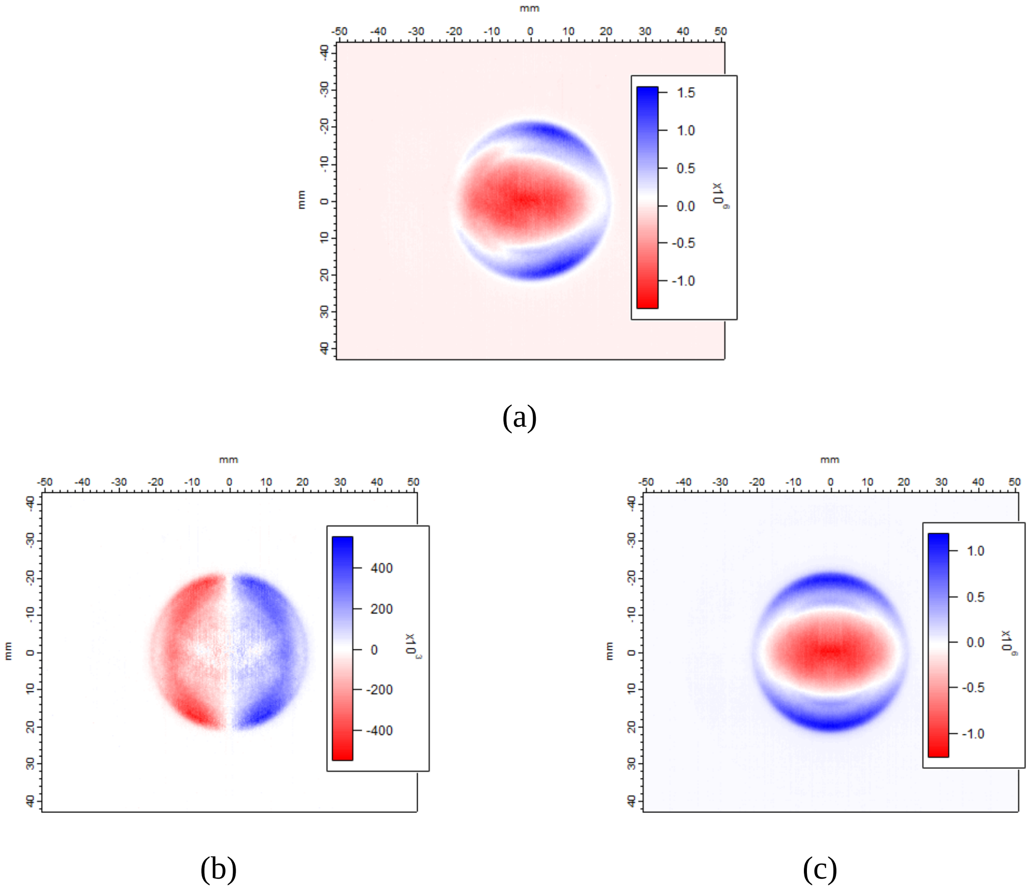

(a)

(b)

(c)

Fig. 132: Differential image (a), and its symmetric (c) and antisymmetric (b) compound for 3-photon PECD of S-α-pinene at 396.52 nm with a laser power of 5 mW. Light is crossing from right to left in the images.

PES and PECD signals for this measurement are also presented in Fig. 133. In the PES spectrum, we see two peaks at 8.22 eV and 8.79 eV which are expected to be corresponding to different vibrationally excited states of some Rydberg states. We can assign these two peaks with the help of Time-Dependent Density Functional Theory (TD-DFT) and FC simulation. What we need is to firstly apply TD-DFT calculation to find the position of the intermediate electronic states and then use FC simulation to find the vibrational progression of any of those electronic states.

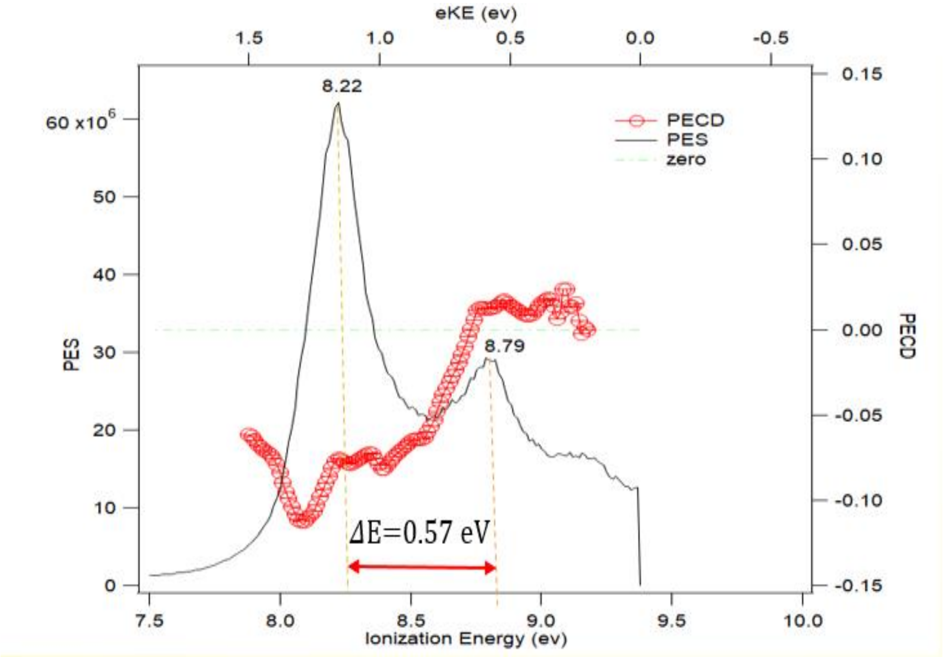

Fig. 133: PES and PECD of S-α-pinene using 3-photon ionization at 396.52 nm with a laser power of 5 mW. Error bars are small and cannot be seen in the graph.

Shown in Fig. 134 is the result of our TD-DFT done with the functional CAM-B3LYP using an augmented double zeta function, aug-DVZ, basis set. TD-DFT calculations overestimate the excitation transition energies [56]. For molecules of this kind, empirically, an offset of -0.1 eV is needed [60]. However, the results plotted in Fig. 134 are the outputs of our TD-DFT calculation without any shift in energy, as finally the energy difference between the excited states is important for us in this work.

The shape of the molecular orbital corresponding to the first five electronic states are also presented to show how they look like in appearance. As can be seen from Fig. 134, the first excited electronic state is an s-Rydberg state followed by three p-Rydberg states and then the d-Rydberg states.

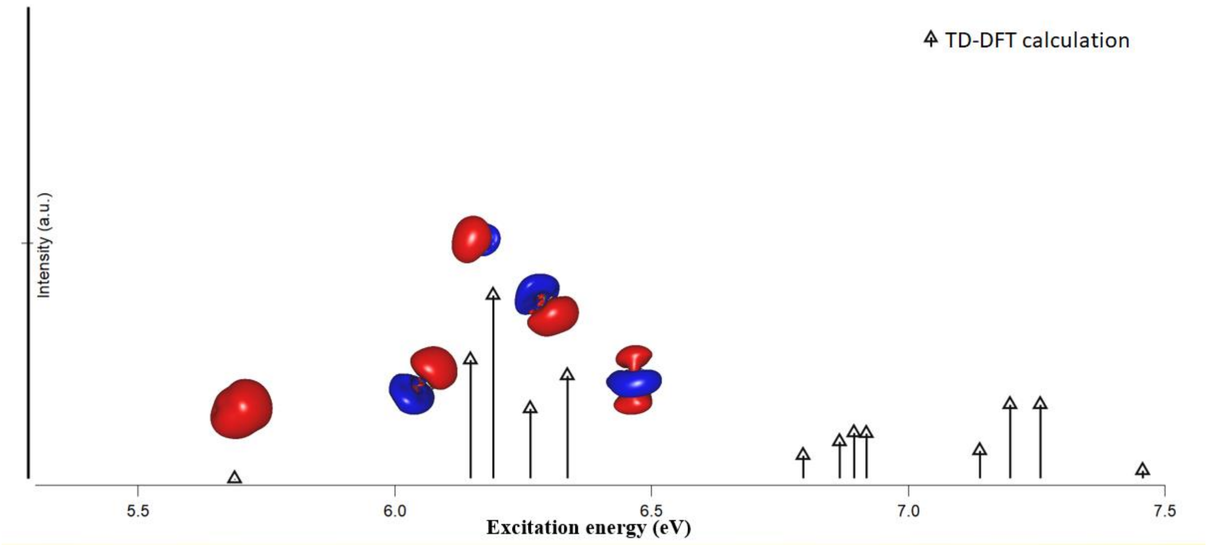

Fig. 134: TD-DFT calculation for α-pinene done with aug-cc-pVDZ basis set. The calculation was performed to obtain the energy transition for the first 20 electronic intermediate states; the plotted results are the direct outcomes of the TD-DFT simulations without any energy shift. Each arrow is representing one electronic intermediate state whose position and length show the excitation energy and the probability of the corresponding excitation, respectively. The molecular orbitals for the first five state are showing on top of the just to illustrate how they look like in appearance. For more details see the main text.

Any of the electronic states calculated through the TD-DFT simulation has its own vibrational progression. As the intermediate electronic states calculated for α-pinene are diffused Rydberg states, it is expected that the geometry of them is more and less the same as the geometry of the cation state. So, the result of our FC calculation for the cation state, presented in Sec. 3.1.1 can be considered for any of these intermediate electronic states as well. We just need to shift the FC spectrum in a way that the first peak to be aligned with the origin of any of the electronic states of interest.

In Fig. 135, the spectrum of the laser at two-photon energy level (as we are doing 2-photon absorption plus 1-photon ionisation) is plotted together with the results of our TD-DFT calculation as well as the FC simulation for two of the electronic states, $3s$ and $3p_z$. It can be seen that the first vibrational structure of the $3p_z$ state and the fourth vibrational structure of the $3s$ state are accessible by the photon energy we had. Therefore, two ionisation pathways are available for α-pinene in 3-photon ionisation at 396.52 nm, one with a resonance to a higher vibrational level of the 3s-Rydberg state and the other with a resonance to a lower vibrational level of $3p_z$-Rydberg state. A schematic view presented in Fig. 136 can help to understand the process better.

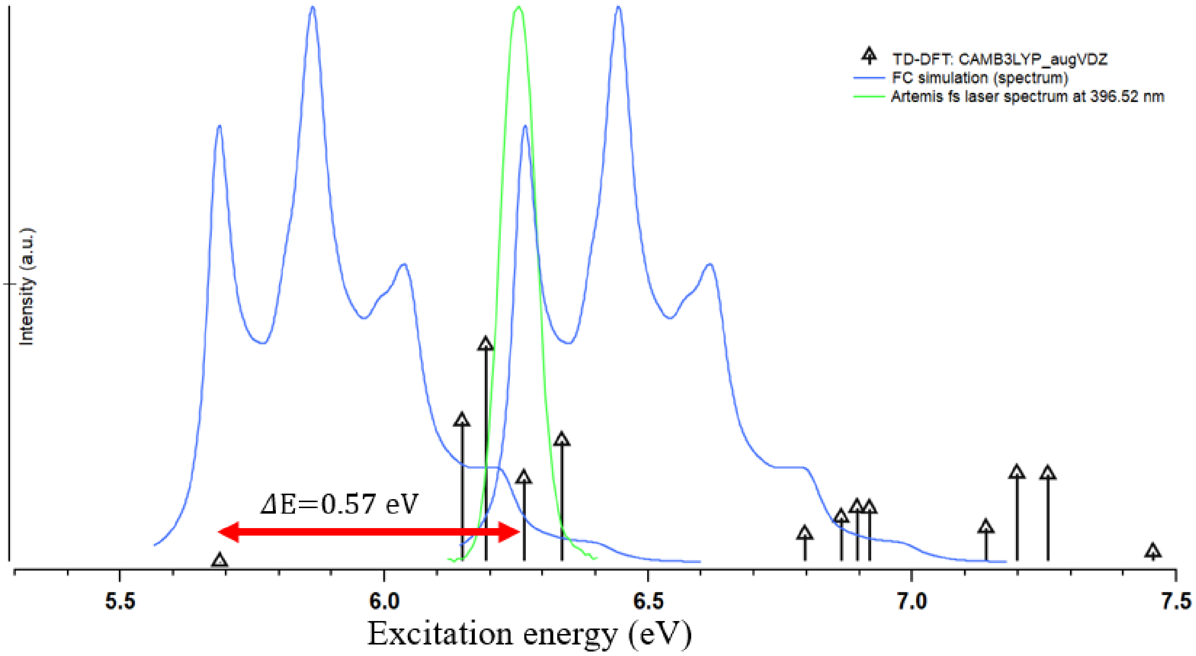

Fig. 135: TD-DFT calculation for α-pinene done using CAMb3LYP aug-cc-pVDZ basis set, the black arrows, plotted along with the laser band width at 396.52 nm at the two-photon energy level, the green curve. The FC simulation for the cation state, the blue curves, has been considered as the vibrational progression for each electronic Rydberg state and is plotted for 3s and $3p_z$. The FC spectrum has been shifted in a way its first peak gets aligned with the origin of the electronic states.

Additionally, the propensity rule now can help to reduce the complexity of the problem; it states that if we are hitting different vibrational levels of two different electronic states with the same wavelength, there must be two peaks in the cationic state whose energy difference is the same as the energy difference between the origins of those two intermediate states. This happens because the vibrational level for each of those two final cationic states should be the same as the vibrational level of the certain intermediate electronic states they are coming from. The eKE release for the ionisation pathway in which the resonance has been made with the 3s-Rydberg state must be lower because a higher energetic vibrational level has been accessed in this channel. Similarly, it can be argued that eKE for the ionisation channel in resonance with the $3p_z$-Rydberg state must be higher as the vibrational energy level is lower in this case.

The energy difference between the origins of the $3s$- and $3p_z$-Rydberg states, based on our calculation, is predicted to be ΔE=0.57 eV in excellent agreement with what we can see experimentally. Returning to Fig. 133, we can see that in the experiment we are observing two peaks in the cation PES of α-pinene at 396.52 nm which are different in eKE by exactly ΔE=0.57 eV. So, we assign the peak at IE=8.22 eV to a resonance ionisation via the first vibrational level of $3p_z$-Rydberg state while the peak at IE=8.79 eV is assigned to a resonance ionisation via the fourth vibrational level of $3s$-Rydberg state.

The assignment of the peaks in the PES, done above, is a great achievement which makes any further discussion on the PECD spectrum of the molecule possible. From Fig. 133, it can be seen that there is a very different PECD signal associated with the two peaks in the photoelectron spectrum; nearly -13% PECD for the peak at IE=8.22 eV but +0.02% PECD for the peak at IE=8.79 eV. The first thing that we can now say about this PECD signal inversion is that they are the PECD signals associating with two different intermediate electronic states, $3s$ and $3p_z$.

However, the electronic character of the intermediate states is not the only parameter affecting the PECD; based on Chapters 5 and 6, we know that there are two more factors affecting the PECD, the vibrational and the kinetic energy effects. Here, we just showed that not only the electronic character of the intermediate states associated with these two peaks in PES are different but also the vibrational character of them is different. Moreover, as can be seen from Fig. 133, the two peaks are different in eKE: one of them appears at eKE=1.16 eV and the other one appears at eKE=0.59 eV. So, we need to decouple these three effects, similarly to the analysis in Chapter 6, with the difference that we have three effects to decouple instead of two. To achieve such a goal, one can record several more 2+1 PECD measurements at different wavelengths, which could be the next step of research in this direction.

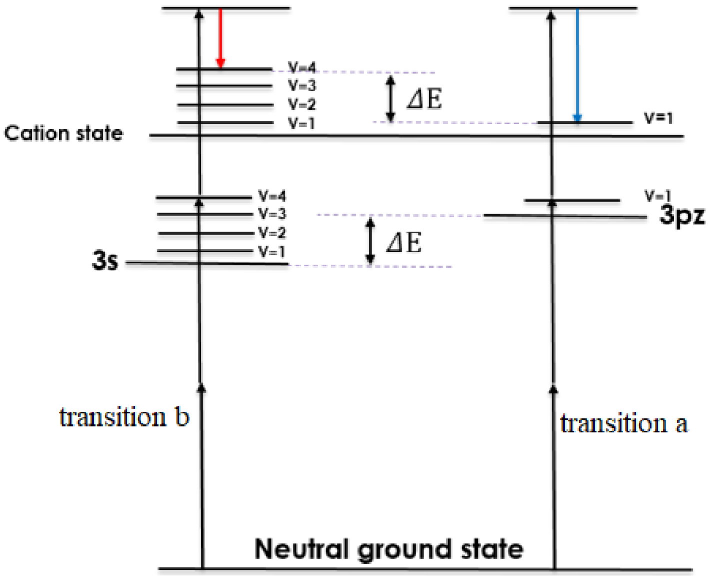

Fig. 136: Schematic of two different ionisation channels available at 396.52 nm. In 2+1 ionisation with this wavelength the ionisation can happen either via resonance with the fourth vibrational level of 3s or with the first vibrational level of $3p_z$.

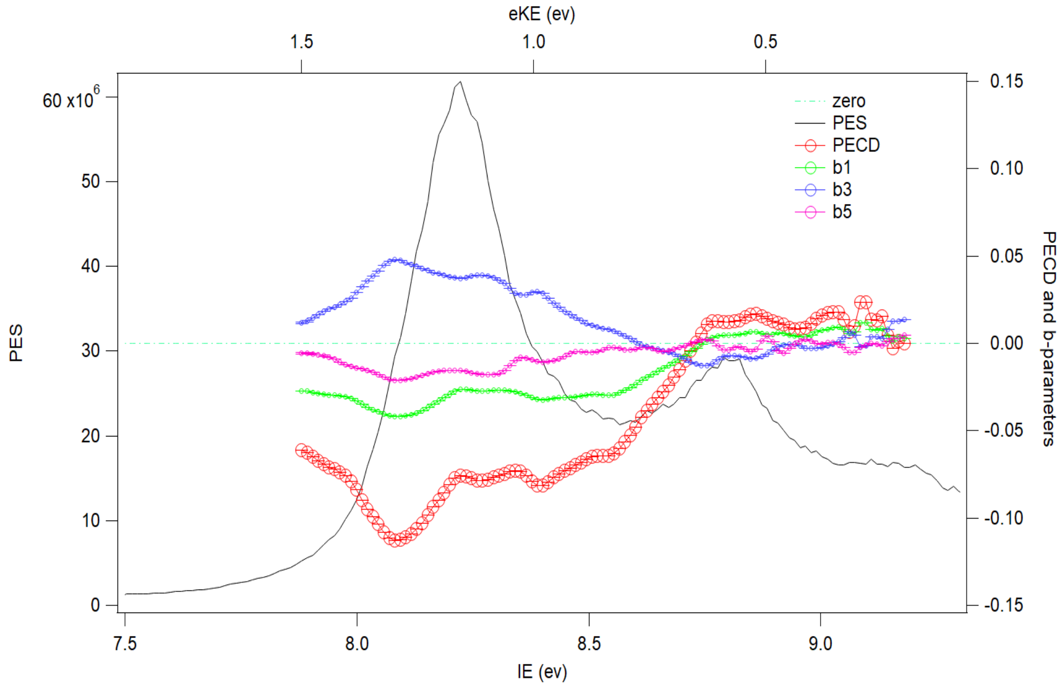

Fig. 137: Different odd beta parameters contributing to the PECD of S-α-pinene in 3-photon ionization at 396.52 nm with a laser power of 5 mW. Error bars are smaller than the marker size and cannot be seen in the figure.

The algorithm that we use to analyse the images applies (Eq. 6) to get the PECD signal. It would be worthwhile if we plot the individual asymmetry parameters contributing to the total PECD to have a sense of how big they are relative to each other; this is done in Fig. 137. For 3-photon ionization, the odd parameters up to the order five (b_1, b_3 and b_5) are contributing, so in Fig. 137 we have plotted only these parameters.

Our results presented in Fig. 137 show that not only b_3 is contributing to the PECD spectrum but also it is even larger than b_1. So, in contrast to single photon ionisation, in the multiphoton ionisation regime, it would be worth paying attention to the higher asymmetry parameters as well. Here, we should also consider that there might be two different origins for the odd beta parameters like b_3 and b_5. They might originate from the intrinsic chiral potential of the molecule, just like b_1. Or, they can be due to any *induced excitation alignment* [64, 149]. As in the resonantly enhanced multiphoton ionisation we have two steps, excitation and ionisation, it could be possible for the molecules with a big electric dipole moment to be selectively excited: in a randomly oriented ensemble of molecules, the probability of the excitation for those whose electric dipole moment is along the electric field of the laser is higher. So, the intermediate level would be mostly populated by the molecules aligned along the electric field of the laser. Therefore, the last ionisation step is happening from a partially oriented ensemble of the excited molecules. This alignment can be a potential reason for having higher odd beta parameters like b_3 [150]. Further work in this direction, in order to separate those parts from b_3 who are originating from the intrinsic chiral potential of the molecule from those parts which are due to the induced excitation alignment, could be interesting.

7.3. Three-photon ionization PECD at 371.02 nm

Another three-photon single colour PECD measurement that we made on α-pinene was at wavelength 371.02 nm; the wavelength, in this case, was tuned by the TOPAS system and the energy of three photons, in this case, was equal to 10.03 eV. Just like the 396.52 nm case, we did a couple of measurements, 30 minutes each, with horizontal and vertical polarization. The laser power, right before going into the ionization chamber was 17.0 mW. The PES spectra for these polarizations are shown in Fig. 138. We also have plotted the spectrum of 396.52 nm with horizontal polarization in this figure just to have a comparison between the PES at these two wavelengths. As we can see, like 396.52 nm, we have two major peaks here, at 8.2 eV and 8.68 eV which are better resolved for horizontal polarisation, where there is an axis of symmetry lying in the plane of the detector causing the pBASEX algorithm to work better.

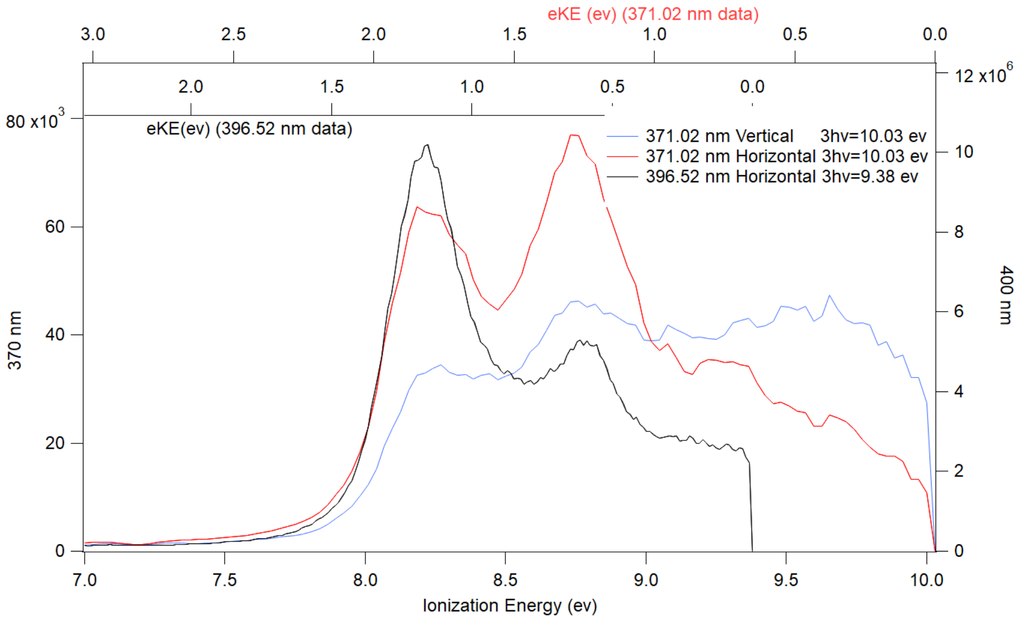

Fig. 138: PES spectrum for 3-photon ionization of α-pinene at 371.02 nm: horizontal (red) and vertical (blue) linear polarization.

For the PECD measurement, we recorded 10 pairs of left/right images, 5 minutes each, and at the end added all the files with the same polarization to create the LCP/RCP image. The laser power in this case, just before going into the ionization chamber was 17 mW. The differential image (DIF=LCP-RCP) after antisymmetrisation (Sec 7.2) and its Abel inverse transformation are shown in Fig. 139. The PES and PECD signal for this measurement are also plotted in Fig. 140.

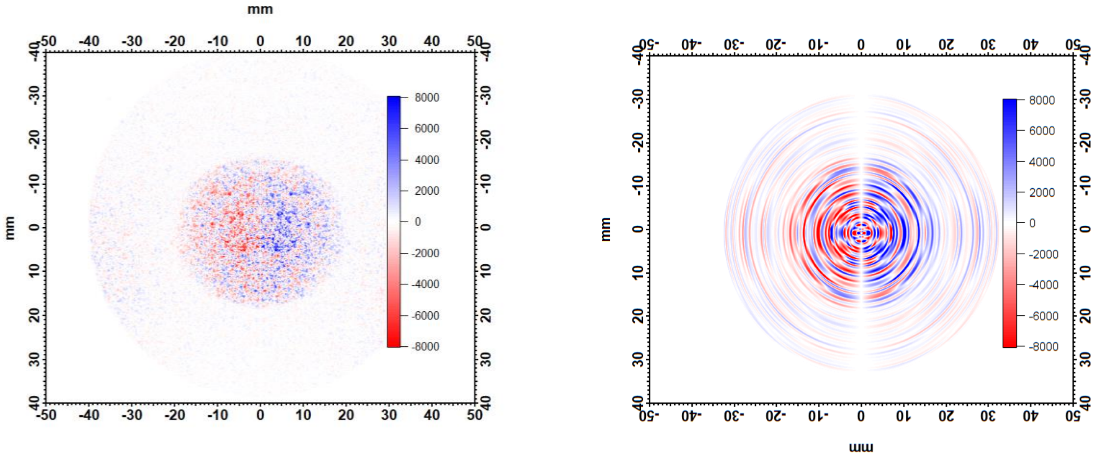

Fig. 139: Antisymmetrised differential image, left, and its Abel inverse transformation, right, for 3-photon PECD of S-α-pinene at 371.02 nm with a laser power of 17.0 mW. The laser beam is crossing from right to left in the images.

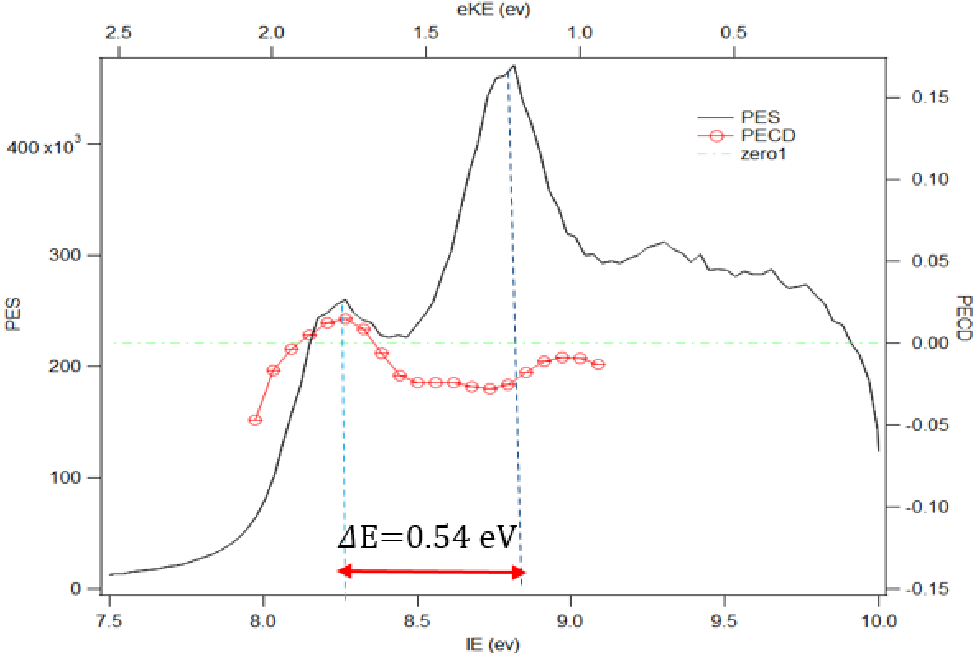

Fig. 140: PES and PECD of S-α-pinene using 3-photon ionization at 371.02 nm.

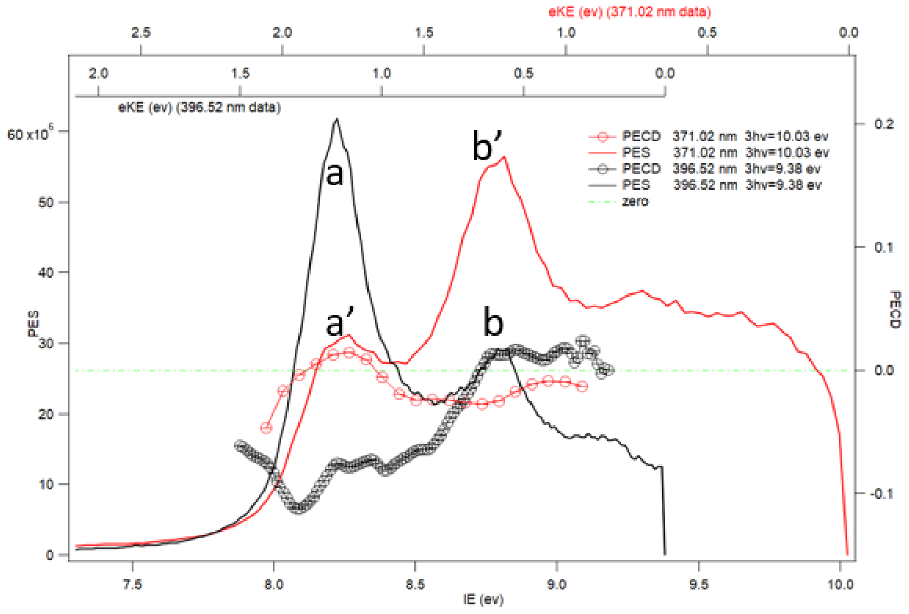

Fig. 141: Comparison between the PES and PECD of S-α-pinene using 3-photon ionization at two wavelengths: 371.02 nm (red) and 396.52 nm (black).

We have plotted the PES and PECD spectra at two different wavelengths, 396.52 nm, and 371.02 nm, on top of each other in Fig. 141 for comparison. The first point is that for both measurements we are observing two peaks (a and b for 396.52 nm measurement and a' and b' for 371.02 nm measurement) in the photoelectron spectra appearing roughly at the same ionisation energies. This fact might be just a coincidence inducing the confusion that the two peaks observed for the 371.02 nm could have the same vibronic character as the two peaks observed for 396.52 nm. To get the full insight about what is happening here, we definitely need to assign the two peaks that appeared in the PES of 371.02 nm as well.

To assign the peaks in the PES of 371.02 nm measurement, we follow the same procedure we used for the 396.52 nm one. Fig. 142 shows the TD-DFT calculation for the molecule along with the laser spectrum at 371.02 nm. Again, the FC simulation of the cation has been attributed to the electronic intermediate states. We can see that with the laser bandwidth of this wavelength, we can excite either the first vibrational level of $3d_2$-Rydberg state or the fourth vibrational level of the $3p_z$-Rydberg state at the two-photon energy level. Therefore, there will be two ionisation channels possible in resonance with these two intermediate vibronic states, whose schematic is shown in Fig. 143.

Based on the propensity rule, there should be two peaks in the cationic state after the ionisation from these intermediate states. The energy difference between the two peaks should also be roughly the same as the energy difference between the origins of the two intermediate electronic states, which is exactly what is happening here. The energy difference between the two electronic states is predicted to be ΔE=0.54 eV based on our TD-DFT calculation (Fig. 142), in good agreement with the eKE difference for the two peaks observed experimentally shown in Fig. 140. So, our assignment for the two peaks in the photoelectron spectrum at 371.02 nm is as: the peak appearing at IE=8.24 eV results from ionisation in resonance with the first vibrational level of the $3d_2$-Rydberg state and the second peak appearing at IE=8.78 eV results from ionisation in resonance with the fourth vibrational level of $3p_z$-Rydberg state.

However, we need to consider the fact that the propensity rule is not a very rigid rule and it is also possible for it not to be followed. So, our assignment of the peaks as mentioned above is subject to the propensity rule only, and other assignments may be possible if it is not governing the last step in the ionisation process.

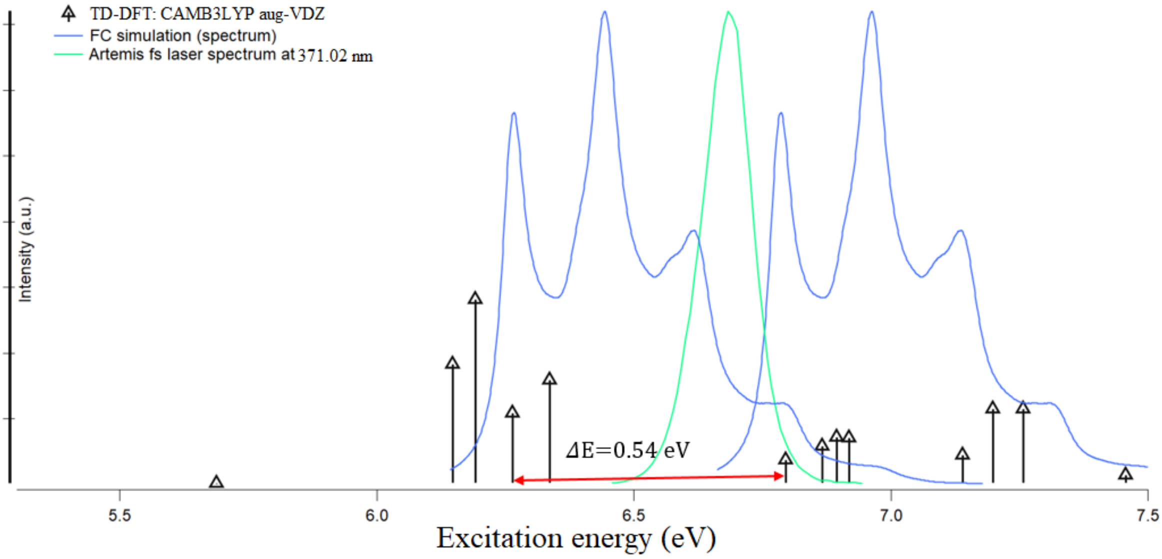

Fig. 142: TD-DFT calculation for α-pinene done using CAMb3LYP aug-VDZ basis set, the black arrows, plotted along with the laser band width at 371.02 nm at the two-photon energy level, the green curve. The FC simulation for the cation state, the blue curves, has been considered as the vibrational progression for each electronic Rydberg state and is plotted for $3p_z$ and $3d_2$. The FC spectrum has been shifted in a way that its first peak gets aligned with the origin of the electronic states.

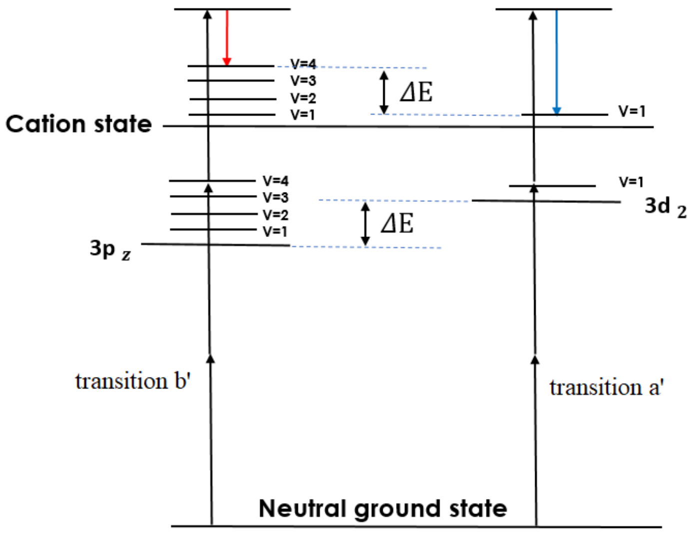

Fig. 143: Schematic of the two different ionisation channels available at 371.02 nm. In 2+1 ionisation with this wavelength the ionisation can happen either via resonance with the fourth vibrational level of $3p_z$ *or with the first vibrational level of* $3d_2$.

Having assigned the peaks, we can now talk more about the PECD signal and its variation. As mentioned above, for both measurements 396.52 nm and 371.02 nm, there are two peaks: a and b for 396.52 nm measurement and a' and b' for 371.02 nm measurement, see Fig. 141 . The first peaks, a and a', are appearing with an IE between 8.0 eV to 8.4 eV and the second ones, b and b', are appearing at IE between 8.6 eV to 9.0 eV. Focusing on the first peaks a and a', they are in resonance with the same vibrational level of two different electronic states, $3p_z$ and $3d_2$, for the 396.52 nm and 371.02 nm measurements, respectively. The different electronic character of the resonance intermediate states might be the reason for the inversion seen in the PECD signal over this region, from -12% for the 396.52 nm measurement to +2% for the 371.02 nm measurement. The inversion in the PECD signal is also happening over the region of the second peaks b and b' (which are in resonance with the same vibrational level of the two different electronic intermediate states 3s and $3p_z$) from positive values for the 396.52 nm measurement to negative values for the 371.02 nm measurement. However, we should be careful here as eKE is another parameter affecting the PECD and the inversion might be due to any difference in that. For example, peak a and a' possess eKE of 1.16 eV and 1.79 eV, respectively; we have shown in Chapter 6 that PECD changes dramatically even over such a short difference range in eKE.

Another conclusion we can make by comparing the PECD signals recorded at 396.52 nm and 371.02 nm is that we can decouple the photoelectron kinetic energy and the electronic state effects from the vibrational effects. In Fig. 141, peaks a and b' are respectively corresponding to the first and the fourth vibrational level of the same intermediate electronic state, $3p_z$-Rydberg. They also are roughly appearing at the same photoelectron kinetic energy. So, any difference in their PECD can be attributed to their different vibrational character. A PECD signal of about -12% corresponding to the peak a, the first vibrational level of $3p_z$-Rydberg state, is attenuated down to -4% corresponding to peak b', the fourth vibrational level of $3p_z$-Rydberg state. This is a great achievement in our research which was made possible thanks to the TD-DFT calculations used to assign the peaks. It can also be considered as a continuation of our previous works on the decoupling of the photoelectron kinetic energy effects from the vibrational effects, done in Chapter 6.

At the end of this section, we can look at the b-parameters contributing to the total PECD; this is shown in Fig. 144. Again, the main distribution in the total PECD is for higher b-parameters rather than b1.

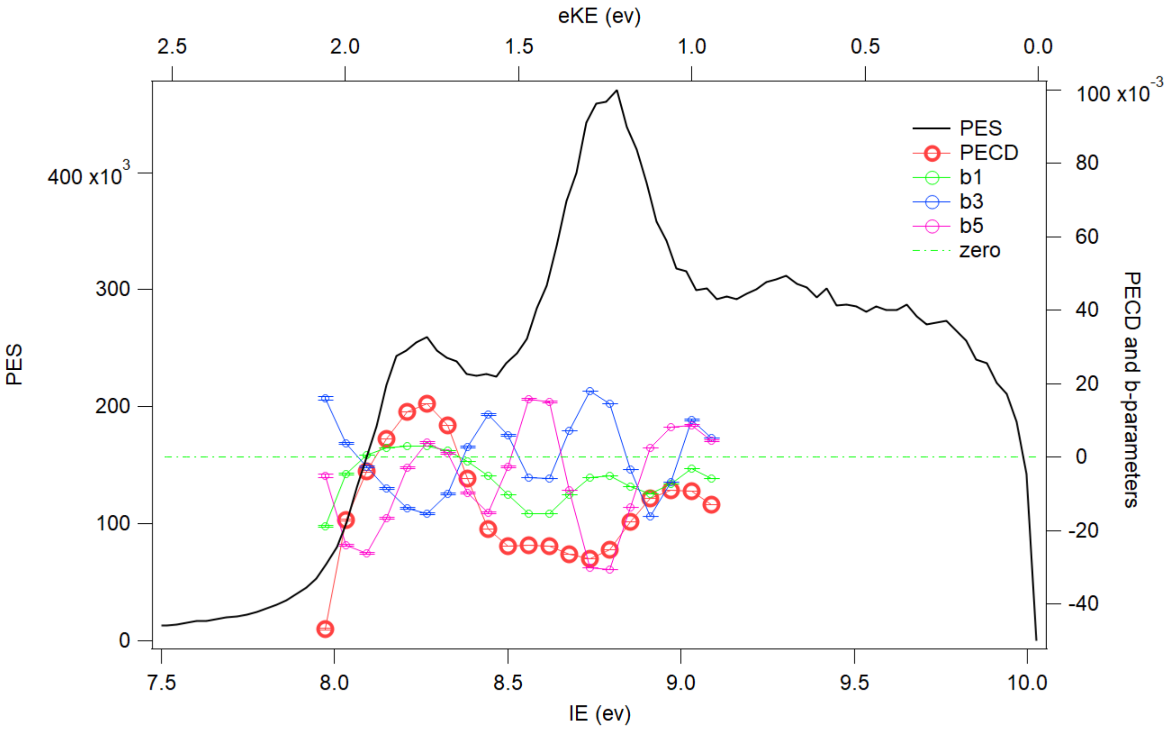

Fig. 144: Different odd beta parameters contributing in PECD of S-α-pinene in 3-photon ionization at 371.02 nm with a laser power of 17 mW.

7.4. Two-photon ionization PECD at 200.66 nm

Finally, in this section, we report the results of the 2-photon PECD that we did on α-pinene at the 200.66 nm wavelength. Looking back to Fig. 127 (c), we can see that in the beam, in addition to the fourth harmonic, 200.66 nm, we also have some residual from third harmonic

266 nm as well as from the fundamental 800 nm. Actually, we measured the total laser power as well as the power of any individual wavelength existing in the beam. The total laser power was 0.27 mW from which 0.02 mW was for 266 nm and 0.07 was for the fundamental wavelength, 800 nm, and the rest of that, 0.18 mW, was for 200.66 nm. The normal ionization pathway that we expect is a single colour 2-photon ionization (200.66+200.66); however, having 266 nm with an energy of 0.02 mW makes a two colour ionization (200.66+266 or 266+200.66) possible.

Here, the backing pressure was -0.4 bar, relative to the atmospheric pressure, and the pressure in the gas and ionization chamber was 1.11×10^{-5} mbar and 4.11×10^{-6} mbar, respectively. The valve was also working at 1 kHz with an opening time of 30 μs.

As at the other wavelengths, we did a couple of measurements using horizontal and vertical polarization, before doing the PECD. The photoelectron spectra for these two measurements are presented in Fig. 145. To have a comparison with 396.52 nm, we have also plotted the PES at this wavelength, the horizontal linear polarization one, in this figure. In the case of 200.66 nm, the total photon energy in the 1+1 regime is 12.36 eV.

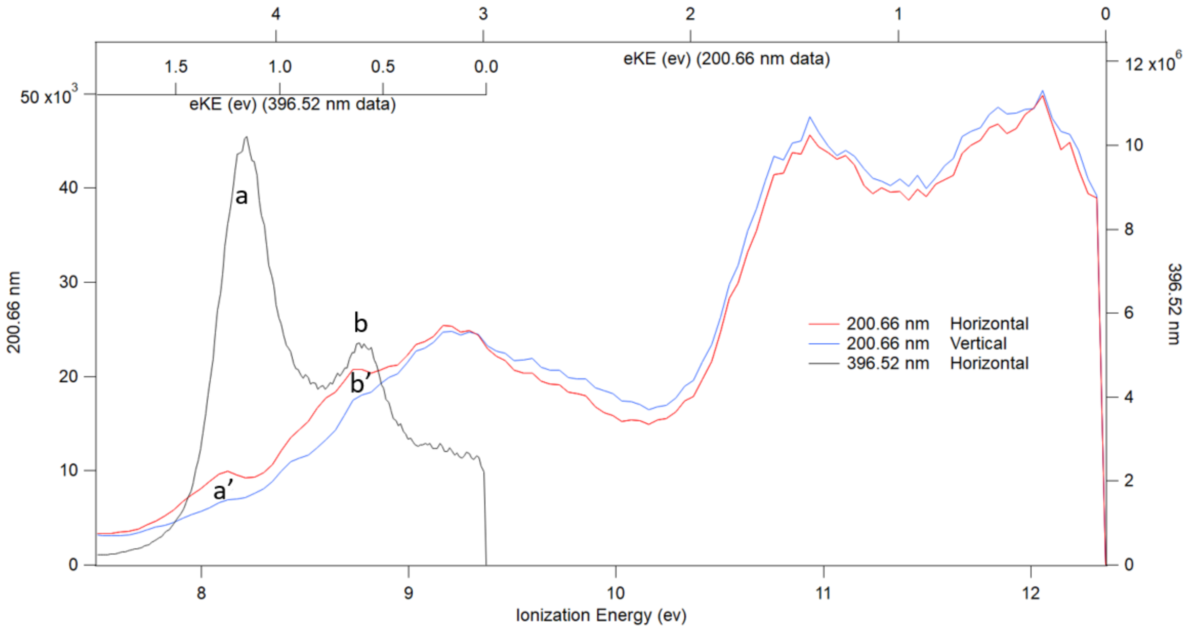

Fig. 145: PES of S-α-pinene at 200.66 nm with a laser power of 0.18 mW: horizontal (red) and vertical (blue) linear polarization. The black curve is the PES of S-α-pinene at 396.52 nm with horizontal polarization.

It can be seen that for 200.66 nm, in the ionization energy region between 8.0 eV to 9.0 eV, we still have two minor peaks, a' and b', corresponding to the peaks a and b in the PES recorded at 396.52 nm. These peaks are more resolved for horizontal polarization than for vertical polarization; this is what happened for the other wavelengths, 396.52 nm, and 371.02 nm, before. If we look at Fig. 130 and Fig. 138, we can see that these two peaks are well separated for horizontal polarization in those cases as well. As was mentioned before, it is because of the Abel inverse transformation working better for the horizontal polarization rather than vertical polarization.

For the PECD measurement, we recorded four pairs of left/right images, 15 minutes of acquisition time for each, and finally added all left/right images to each other to get the LCP/RCP image. The antisymmetrised differential image (DI=LCP-RCP) and its inversion are shown in Fig. 146.

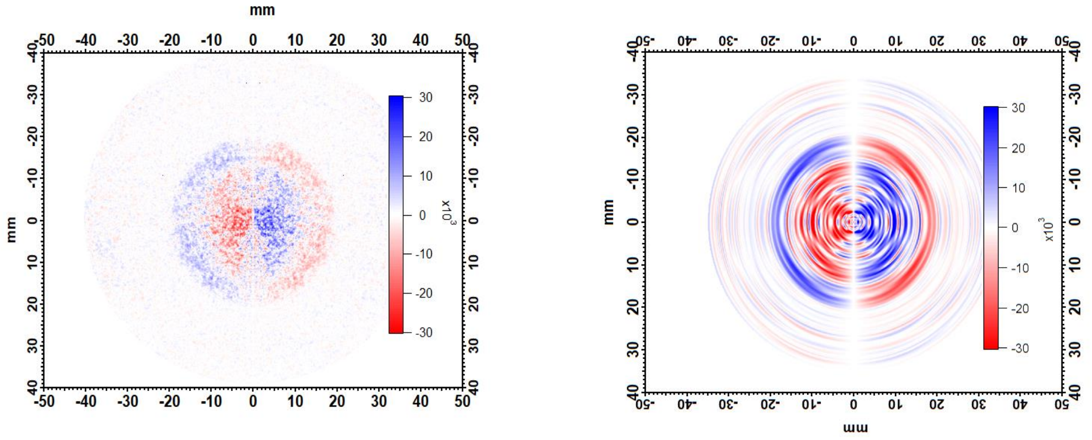

Fig. 146: Antisymmetrised differential image, left, and its Abel inverse transformation, right, for 2-photon PECD of S-α-pinene at 200.66 nm with a laser power of 0.18 mW. The laser beam is crossing from right to left in the images.

In this case, there are only two b-parameters contributing to the total PECD, b_1 and b_3. We have also plotted these individual asymmetry parameters in Fig. 147 to have a sense of their relative magnitude. In this case, b_1 has the major contribution to the total PECD.

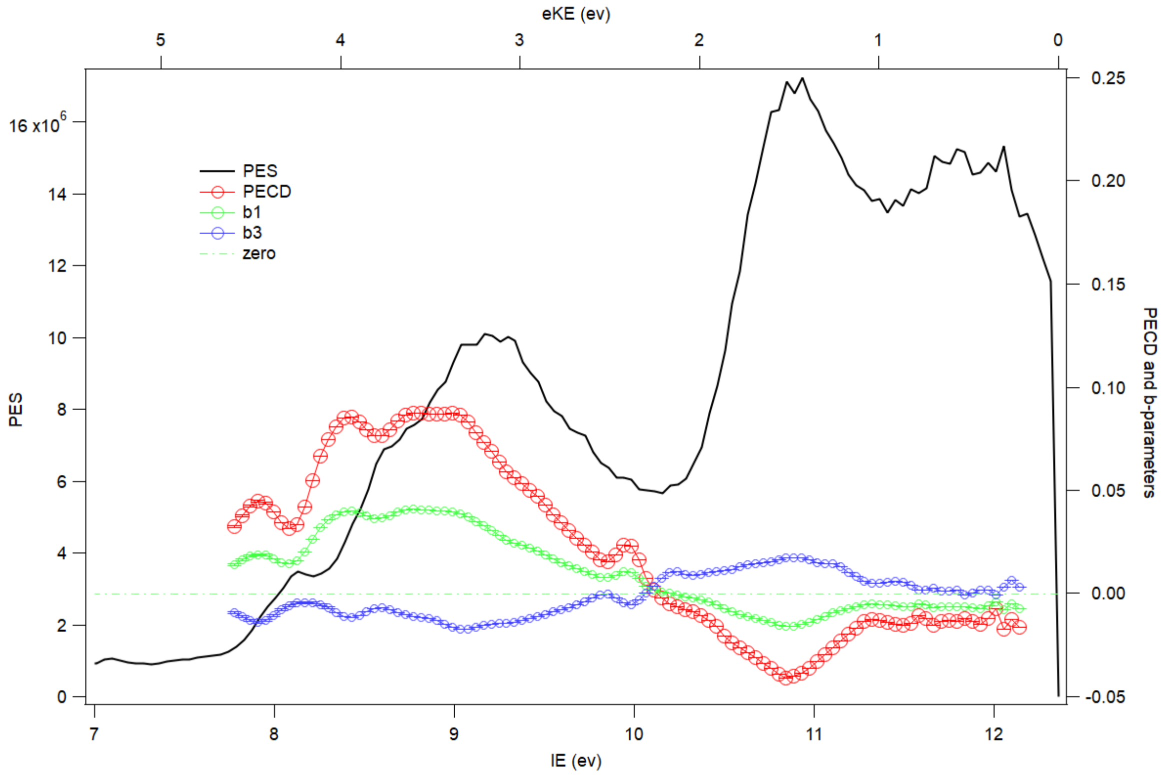

Fig. 147: PES and PECD -of S-α-pinene in 2-photon ionization at 200.66 nm with a laser power of 0.18 mW. The individual odd beta parameters are also plotted.

7.5. Conclusion

In this chapter, we presented the results of a laser experiment on α-pinene with the aim of investigating the dependency of the PECD on the intermediate vibronic states. In contrast to single-photon ionisation, in multiphoton ionisation, more than one photon is needed to eject the photoelectrons from the molecule. By one or more photons, the molecule is pumped to its electronic excited intermediate states and then one more photon ejects the electron. So, the question was: how the intermediate electronic or vibrational states can affect the PECD? We tried three different laser wavelengths to record the PECD of α-pinene. To complement these studies, we have done some TD-DFT calculations to interpret our experimental results, and particularly, to assign the peaks observed in the photoelectron spectrum. Assignment of the peaks, done by the author, helped us significantly in interpreting the results.

By comparing the PECD recorded at different wavelengths, we reached some conclusions on the vibrational dependency of the PECD at the intermediate level. For example, by comparing the results of λ=396.52 nm and λ=371.02 nm, we decoupled the photoelectron kinetic energy and the electronic state effects from the vibrational effects, which in turn allowed us to study the vibrational dependency of the PECD at the intermediate levels. A PECD signal of about -12% corresponding to the first vibrational level of $3p_z$-Rydberg state, was attenuated down to -4% corresponding to the fourth vibrational level of the same electronic state. This was a great achievement in our research being possible thanks to the TD-DFT calculation we did, which enabled us to assign the peaks observed in the photoelectron spectrum properly.

The other founding here was an inversion in the PECD signal due to a difference in the electronic character of the intermediate levels. We could find two peaks in the photoelectron spectra recorded at 396.52 nm and 371.02 nm, which matched with the same vibrational level of two different intermediate electronic states, $3p_z$ -Rydberg and $3d_2$-Rydberg. The PECD was inverting from -12% corresponding to the $3p_z$-Rydberg electronic state (396.52 nm excitation) to +2% corresponding to the $3d_2$-Rydberg electronic state (371.02 nm excitation).

We also observed that the asymmetry parameters of higher orders like b_3 and b_5 are contributing to the total PECD signal in multiphoton ionisation. In the case of three-photon ionisation at λ=396.52 nm and λ=371.02 nm, the magnitude of b_3 was obtained to be even bigger than b_1.

8. Conclusion

We had two main goals in this research. The first goal was to introduce and establish a new method for simultaneous chemical composition and enantiomer excess analysis in gas phase mixtures (essential oils in this work) using photoelectron spectroscopy and the second one was to investigate the dependency of PECD on some factors like vibrational quantum states and photoelectron kinetic energy.

In terms of essential oil analysis, we introduced the theoretical and experimental basis of our method in Chapter 4. The idea with the chemical composition analysis was that the photoelectron spectrum of a mixture must be a linear combination of the photoelectron spectra of its compounds, see (Eq. 23), with the coefficients of the linear combination to present the chemical composition (cc). Similarly, the PECD spectrum of the mixture can be presented as a linear combination of the weighted PECD spectra of the compounds, (Eq. 35), with the coefficients to be the enantiomer excess for each compound in this case. The mixtures selected for this study were black pepper oil and Mexican lime oil. Based on the literature a set of monoterpenes including α-pinene, β-pinene, limonene, 3-carene, sabinene, and γ-terpinene are supposed to constitute the majority of the volatile compounds in the two selected oils. So, we measured the high-resolution photoelectron spectrum of these two essential oils as well as that of their compounds using the SPES technique at the DESIRS beamline of the SOLEIL synchrotron in order to get the cc. We also measured the VMI-PES and VMI-PECD of the oils and their compounds at two fixed photon energies, $h\nu=9.0$ eV and $h\nu=9.5$ eV, from which the VMI-PES results were used to obtain the cc in a similar way to the SPES technique. The cc obtained using VMI-PES were in an excellent agreement with those obtained using the SPES technique, which itself verified the validity of our method. The VMI-PECD spectra weighted by the corresponding VMI-PES then were used to get the ee of each compound.

The results of SPES measurements on the basis set (the compounds) with full details were described in Chapter 3. As our experiments were done in coincidence mode, we could study the photoelectrons by tagging them with the masses present in the ToF-MS. This provided us with the chance of studying the fragmentation dynamics for the monoterpenes under study. To understand the photodissociation dynamics, we did some OVGF calculations, which leaded us to this conclusion that ionisation from the HOMO orbital of the monoterpenes reported in

Chapter 3 are non-dissociative while the ionisation from the HOMO-1 is remarkably dissociative in all the cases. To support interpret our experimental results, we also performed some FC simulations, which helped us to assign the vibrational structures observed in the SPES of the monoterpenes. The assignment of the vibrational structures was also crucial to investigate the vibrational dependency of the PECD, and was used in Chapters 5 and 6.

The results of our PECD measurements on the mentioned monoterpenes made in the purpose of ee analysis were presented in Chapter 5. In this chapter, we not only reported the VMI-PES and VMI-PECD results of individual monoterpenes but also we made some useful comparisons between the different measurements we had. For example, comparing two measurements made at two different photoion energies ($h\nu$=9.0 eV and $h\nu$=10.5 eV) but on the same monoterpene (α-pinene or 3-carene) led us to the conclusion that PECD is a more sensitive probe of the vibrational structures compared to PES. The resolution of a typical VMI decreases as the photoelectron energy increases; so, at a photon energy of 10.5 eV, we could hardly see the vibrational structures in the PES. However, the vibrational structures were yet well resolved in the PECD spectrum. This finding suggests the PECD is a more sensitive probe of the vibrational levels than PES.

In terms of investigating the dependency of PECD on factors like vibrational and electronic quantum states as well as photoelectron kinetic energy, we made several synchrotron- and laser-based experiments. In our synchrotron, single-photon experiments, we investigated the vibrational effects and the photoelectron kinetic energy effects, while in our multiphoton laser-based experiments, there was the chance for us to investigate the effect of intermediate electronic states on the PECD too. We selected a couple of the monoterpenes, α-pinene, and 3-carene, which had shown a reach vibrational structure in their SPES as well as a significant PECD signal and made more PECD measurements on them at several fixed photon energies ranging from near-threshold up to 19.0 eV. The first astonishing result was obtained when we made some CMS-Xα calculation to support our experimental data. PECD of α-pinene and 3-carene was changing sign and magnitude several times in an eKE range of 10.0 eV right above the ionisation threshold. This behaviour was verified as our experimental and theoretical results were in an excellent agreement. The second thing we observed in our results was an intensive vibrational modulation in the PECD of the two monoterpenes, which was very similar to the results we had previously reported for limonene [52]. The other significant results were obtained when we plotted several near threshold PECD measurements we made for each monoterpene as a function of eKE. In this way, we could get the vibrational and photoelectron kinetic energy effects decoupled. By selecting a proper set of photon energies, it was possible to look at the PECD of some structures with the same vibrational character but different photoelectron kinetic energy, and vice versa. It is the first time ever that such two effects on PECD have been decoupled which itself provides the opportunity to understand the PECD behaviour in a clearer way.

In this project, we also extended our experiments from single-photon ionisation to a multi-photon ionisation regime. We had a beamtime of three weeks in Artemis, one of the laser beamlines of the CLF, where we could try a few wavelengths to study the PECD of α-pinene in a pump-probe scheme. We could successfully record the PECD of α-pinene and break it down to its components, b_1, b_3, b_5 at each wavelength. To interpret the experimental results, we did a combination of the TD-DFT calculation and FC simulation. The former was needed to find the position of the electronic intermediate states (Rydberg states here) while the latter helped us to figure out how the vibrational progression of each of the electronic. Our calculations made it clear which vibronic states were being pumped by the laser; so, we could therefore assign the peaks observed in the PES to the possible ionization pathways. This helped us to study the dependency of the PECD on different vibrational and intermediate electronic states. In addition, by comparing the results obtained at different wavelengths, we could decouple the vibrational effects from those effects originating from a difference in eKE and intermediate electronic states.

In terms of future works, one can consider the potential applications of PECD in chemical structure determination as well as probing the electronic and vibrational dynamics of the molecules; particularly, for a family of larger chiral molecules such as biomolecules. For example, recently the electronic photodetachment circular dichroism has been used to assign the helical topology of the DNAs [151]. In addition, one could consider further development of our photoelectron spectroscopy method by studying the other citrus oils such as lemon oil and bergamot oil samples. These two samples are also composed of the same monoterpene family that we used as the basis set in Chapter 4 [109, 118]. Developing approaches using laser systems, could also be useful as they are available in a table-top setup, which makes the method more easily applicable for analytical purposes.

9. Bibliography

[1] L. Kelvin and W. Thomson, "The molecular tactics of a crystal," 1894.

[2] *https://en.oxforddictionaries.com/definition/chiral.* Available: https://en.oxforddictionaries.com/definition/chiral

[3] H. Park and R. N. Zare, "Molecular-orbital decomposition of the ionization continuum for a diatomic molecule by angle- and energy-resolved photoelectron spectroscopy .1. Formalism," *Journal of Chemical Physics,* vol. 104, no. 12, pp. 4554-4567, Mar 1996.

[4] R. A. Hegstrom and D. Kondepudi, "The Handedness of the Universe," *Sientific American,* pp. 108-115, 1990.

[5] A. Slosar *et al.*, "Galaxy Zoo: chiral correlation function of galaxy spins*," *Monthly Notices of the Royal Astronomical Society,* vol. 392, no. 3, pp. 1225-1232, 2009.

[6] L. Pasteur, "The Asymmetry of Naturally Occurring Organic Compounds, the foundations of esterochemistry," 1860.

[7] J. M. Hicks, "The Physical Chemistry of Chirality," *American Chemical Society,* vol. 810, 2002.

[8] J. S. Siegel, "Homochiral imperative of molecular evolution," *Chirality,* vol. 10, no. 1-2, pp. 24-27, 1998.

[9] Takahiro Asami, Robert H. Cowie, and Kako Ohbayashi, "Evolution of Mirror Images by Sexually Asymmetric Mating Behavior in Hermaphroditic Snails," *The American Naturalist,* vol. 152, no. 2, pp. 225-236, 1998.

[10] R. S. Chivukula, "Electroweak symmetry breaking," *Journal of Physics: Conference Series,* vol. 37, no. 1, p. 28, 2006.

[11] J. v. Klinken, "Tests of fundamental symmetries with beta decay," *Journal of Physics G: Nuclear and Particle Physics,* vol. 22, no. 9, p. 1239, 1996.

[12] O. Naviliat-Cuncic, T. A. Girard, J. Deutsch, and N. Severijns, "Left-right symmetry breaking sensitivity of beta -asymmetry measurements," *Journal of Physics G: Nuclear and Particle Physics,* vol. 17, no. 6, p. 919, 1991.

[13] L. Addadi and S. Weiner, "Biomineralization: Crystals, asymmetry and life," *Nature,* 10.1038/35081227 vol. 411, no. 6839, pp. 753-755, 06/14/print 2001.

[14] P. Cintas, "Chirality of Living Systems: A Helping Hand from Crystals and Oligopeptides," *Angewandte Chemie International Edition,* vol. 41, no. 7, pp. 1139-1145, 2002.

[15] M. Schilthuizen and A. Davison, "The convoluted evolution of snail chirality," *Naturwissenschaften,* journal article vol. 92, no. 11, pp. 504-515, 2005.

[16] K. Lord, *Baltimore Lectures on Molecular Dynamics and the Wave Theory of Light*. London: Clay and Sons 1884.

[17] J. Singh and T. J. Hagen, *Chirality and Biological Activity: Burger's Medicinal Chemistry and Drug Discovery*. John Wiley & Sons, 2010.

[18] K. Nakanishi, N. Berova, and R. W. Woody, *Circular Dichroism: Principles and Applications*. New York: VC H Publishers, 1994.

[19] A. M. Stalcup, *In Encyclopedia of Separation Technology: .* New York: John Wiley, 1997.

[20] E. Charney, *The Molecular Basis of Optical Activity*. Malabar: Robert E. Krieger Publishing Co., 1985.

[21] T. Baer, J. Booze, and K.-M. Weitzel, "Photoelectron Photoion Coincidence Studies of Ion Dissociation Dynamics," *World Scientific Pub Co,* pp. 259-296, 1991-02.

[22] M. H. Levi and J. S. Garth, "Chirality in Nonlinear Optics," *Annual Review of Physical Chemistry,* vol. 60, pp. 345-365, 2009.

[23] L. P. Prasad and K. C. Dilip, "Absolute Stereochemistry of Chiral Molecules from ab Initio: Theoretical and Experimental Molecular Optical Rotations,". *Am. Chem. Soc., 1998,* vol. 120, pp. 6160-6164, 1998.

[24] G. A. Garcia, B. K. C. de Miranda, M. Tia, S. Daly, and L. Nahon, "DELICIOUS III: A multipurpose double imaging particle coincidence spectrometer for gas phase vacuum ultraviolet photodynamics studies," *Review of Scientific Instruments,* vol. 84, no. 5, May 2013, Art. no. 053112.

[25] I. Powis, *Photoelectron Circular Dichroism in Chiral Molecules*. Hoboken, NJ, USA: John Wiley & Sons, 2008.

[26] A. Rodger and B. Nordén, *Circular dichroism and linear dichroism*. Oxford: Oxford University Press, 1997.

[27] W. Kuhn and E. Braun, "Measurement of circular dichroism in the ultra-violet," *Z. Physik. Chem.,* vol. 8, pp. 445–54, 1930.

[28] N. A. Cherepkov, *Chem. Phys. Lett.,* vol. 87, 1982.

[29] B. Ritchie, *Phys. Rev. A,* vol. 13, 1976.

[30] C. S. Lehmann, N. B. Ram, I. Powis, and M. H. M. Janssen, "Imaging photoelectron circular dichroism of chiral molecules by femtosecond multiphoton coincidence detection," *The Journal of Chemical Physics,* vol. 139, no. 23, p. 234307, 2013.

[31] B. Ritchie, "Theory of the angular distribution of photoelectrons ejected from optically active molecules and molecular negative ions," *Physical Review A,* vol. 13, no. 4, pp. 1411-1415, 04/01/ 1976.

[32] I. Powis, "Photoelectron Spectroscopy and Circular Dichroism in Chiral Biomolecules: l-Alanine," *The Journal of Physical Chemistry A,* vol. 104, no. 5, pp. 878-882, 2000.

[33] I. Powis, "Photoelectron circular dichroism of the randomly oriented chiral molecules glyceraldehyde and lactic acid," *The Journal of Chemical Physics,* vol. 112, no. 1, pp. 301-310, 2000.

[34] N. Böwering, T. Lischke, B. Schmidtke, N. Müller, T. Khalil, and U. Heinzmann, "Asymmetry in Photoelectron Emission from Chiral Molecules Induced by Circularly Polarized Light," *Physical Review Letters,* vol. 86, no. 7, pp. 1187-1190, 2001.

[35] G. A. Garcia, L. Nahon, M. Lebech, J.-C. Houver, D. Dowek, and I. Powis, "Circular dichroism in the photoelectron angular distribution from randomly oriented enantiomers of camphor," *The Journal of Chemical Physics,* vol. 119, no. 17, pp. 8781-8784, 2003.

[36] M. Stener, G. Fronzoni, D. D. Tommaso, and P. Decleva, "Density functional study on the circular dichroism of photoelectron angular distribution from chiral derivatives of oxirane," *The Journal of Chemical Physics,* vol. 120, no. 7, pp. 3284-3296, 2004.

[37] G. A. Garcia, H. Dossmann, L. Nahon, S. Daly, and I. Powis, "Photoelectron circular dichroism and spectroscopy of trifluoromethyl- and methyl-oxirane: a comparative study," *Physical Chemistry Chemical Physics,* vol. 16, no. 30, pp. 16214-16224, 2014.

[38] U. Hergenhahn *et al.*, "Photoelectron circular dichroism in core level ionization of randomly oriented pure enantiomers of the chiral molecule camphor," *The Journal of Chemical Physics,* vol. 120, no. 10, pp. 4553-4556, 2004.

[39] L. Nahon, G. A. Garcia, C. J. Harding, E. Mikajlo, and I. Powis, "Determination of chiral asymmetries in the valence photoionization of camphor enantiomers by photoelectron imaging using tunable circularly polarized light," *The Journal of Chemical Physics,* vol. 125, no. 11, p. 114309, 2006.

[40] L. Nahon *et al.*, "Determination of accurate electron chiral asymmetries in fenchone and camphor in the VUV range: sensitivity to isomerism and enantiomeric purity,"

Physical Chemistry Chemical Physics, 10.1039/C6CP01293K vol. 18, no. 18, pp. 12696-12706, 2016.

[41] V. Ulrich *et al.*, "Giant Chiral Asymmetry in the C 1s Core Level Photoemission from Randomly Oriented Fenchone Enantiomers," *The Journal of Physical Chemistry A,* vol. 112, no. 16, pp. 3544-3549, 2008.

[42] S. Turchini, "Conformational effects in photoelectron circular dichroism," *Journal of Physics: Condensed Matter,* vol. 29, no. 50, p. 503001, 2017.

[43] D. Di Tommaso, M. Stener, G. Fronzoni, and P. Decleva, "Conformational Effects on Circular Dichroism in the Photoelectron Angular Distribution," *ChemPhysChem,* vol. 7, no. 4, pp. 924-934, 2006.

[44] S. Stranges *et al.*, "Valence photoionization dynamics in circular dichroism of chiral free molecules: The methyl-oxirane," *The Journal of Chemical Physics,* vol. 122, no. 24, p. 244303, 2005.

[45] G. A. Garcia, H. Soldi-Lose, L. Nahon, and I. Powis, "Photoelectron Circular Dichroism Spectroscopy in an Orbitally Congested System: The Terpene Endoborneol," *The Journal of Physical Chemistry A,* vol. 114, no. 2, pp. 847-853, 2010.

[46] S. Turchini *et al.*, "Conformational Effects in Photoelectron Circular Dichroism of Alaninol," *ChemPhysChem,* vol. 10, no. 11, pp. 1839-1846, 2009.

[47] S. Turchini *et al.*, "Conformational Sensitivity in Photoelectron Circular Dichroism of 3-Methylcyclopentanone," *ChemPhysChem,* vol. 14, no. 8, pp. 1723-1732, 2013.

[48] L. Nahon, G. A. Garcia, H. Soldi-Lose, S. Daly, and I. Powis, "Effects of dimerization on the photoelectron angular distribution parameters from chiral camphor enantiomers obtained with circularly polarized vacuum-ultraviolet radiation," *Physical Review A,* vol. 82, no. 3, p. 032514, 2010.

[49] I. Powis, S. Daly, M. Tia, B. Cunha de Miranda, G. A. Garcia, and L. Nahon, "A photoionization investigation of small, homochiral clusters of glycidol using circularly polarized radiation and velocity map electron–ion coincidence imaging," *Physical Chemistry Chemical Physics,* vol. 16, no. 2, pp. 467-476, 2014.

[50] G. Contini *et al.*, "Vibrational state dependence of β and D asymmetry parameters: The case of the highest occupied molecular orbital photoelectron spectrum of methyl-oxirane," *The Journal of Chemical Physics,* vol. 127, no. 12, p. 124310, 2007.

[51] G. A. Garcia, L. Nahon, S. Daly, and I. Powis, "Vibrationally induced inversion of photoelectron forward-backward asymmetry in chiral molecule photoionization by circularly polarized light," *Nature Communications,* Article vol. 4, p. 2132, online 2013.

[52] M. M. Rafiee Fanood, H. Ganjitabar, G. A. Garcia, L. Nahon, S. Turchini, and I. Powis, "Intense Vibronic Modulation of the Chiral Photoelectron Angular Distribution Generated by Photoionization of Limonene Enantiomers with Circularly Polarized Synchrotron Radiation," *ChemPhysChem,* vol. 19, no. 8, pp. 921-933, 2018.

[53] C. Lux *et al.*, "Circular Dichroism in the Photoelectron Angular Distributions of Camphor and Fenchone from Multiphoton Ionization with Femtosecond Laser Pulses," *Angewandte Chemie International Edition,* vol. 51, no. 20, pp. 5001-5005, 2012.

[54] C. Lux, M. Wollenhaupt, C. Sarpe, and T. Baumert, "Photoelectron Circular Dichroism of Bicyclic Ketones from Multiphoton Ionization with Femtosecond Laser Pulses," *ChemPhysChem,* vol. 16, no. 1, pp. 115-137, 2015.

[55] L. Christian, S. Arne, S. Cristian, W. Matthias, and B. Thomas, "Photoelectron circular dichroism observed in the above-threshold ionization signal from chiral molecules with femtosecond laser pulses," *Journal of Physics B: Atomic, Molecular and Optical Physics,* vol. 49, no. 2, p. 02LT01, 2016.

[56] M. M. R. Fanood, M. H. M. Janssen, and I. Powis, "Wavelength dependent photoelectron circular dichroism of limonene studied by femtosecond multiphoton laser ionization and electron-ion coincidence imaging," *The Journal of Chemical Physics,* vol. 145, no. 12, p. 124320, 2016.

[57] A. Kastner *et al.*, "Intermediate state dependence of the photoelectron circular dichroism of fenchone observed via femtosecond resonance-enhanced multi-photon ionization," *The Journal of Chemical Physics,* vol. 147, no. 1, p. 013926, 2017.

[58] A. Kastner *et al.,* "Enantiomeric Excess Sensitivity to Below One Percent by Using Femtosecond Photoelectron Circular Dichroism," *ChemPhysChem,* vol. 17, no. 8, pp. 1119-1122, 2016.

[59] J. Miles *et al.,* "A new technique for probing chirality via photoelectron circular dichroism," *Analytica Chimica Acta*, vol. 984, pp. 134-139, 2017.

[60] M. M. Rafiee Fanood, M. H. M. Janssen, and I. Powis, "Enantioselective femtosecond laser photoionization spectrometry of limonene using photoelectron circular dichroism," *Physical Chemistry Chemical Physics,* vol. 17, no. 14, pp. 8614-8617, 2015.

[61] M. M. R. Fanood, N. B. Ram, C. S. Lehmann, I. Powis, and M. H. M. Janssen, "Enantiomer-specific analysis of multi-component mixtures by correlated electron imaging–ion mass spectrometry," *Nature Communications,* Article vol. 6, p. 7511, online 2015.

[62] A. Comby *et al.*, "Relaxation Dynamics in Photoexcited Chiral Molecules Studied by Time-Resolved Photoelectron Circular Dichroism: Toward Chiral Femtochemistry," *The Journal of Physical Chemistry Letters,* vol. 7, no. 22, pp. 4514-4519, 2016.

[63] S. Beaulieu *et al.*, "Multiphoton photoelectron circular dichroism of limonene with independent polarization state control of the bound-bound and bound-continuum transitions," *The Journal of Chemical Physics,* vol. 149, no. 13, p. 134301, 2018.

[64] S. Beaulieu *et al.*, "Probing ultrafast dynamics of chiral molecules using time-resolved photoelectron circular dichroism," *Faraday Discussions,* vol. 194, no. 0, pp. 325-348, 2016.

[65] S. Beaulieu *et al.*, "Universality of photoelectron circular dichroism in the photoionization of chiral molecules," *New Journal of Physics,* vol. 18, no. 10, p. 102002, 2016.

[66] A. Ferré *et al.*, "A table-top ultrashort light source in the extreme ultraviolet for circular dichroism experiments," *Nature Photonics,* vol. 9, p. 93, online 2014.

[67] A. T. J. B. Eppink and D. H. Parker, "Velocity map imaging of ions and electrons using electrostatic lenses: Application in photoelectron and photofragment ion imaging of molecular oxygen," *Review of Scientific Instruments,* vol. 68, 1997.

[68] S. Manzhos and H.-P. Loock, "Photofragment image analysis using the Onion-Peeling Algorithm," *Computer Physics Communications,* vol. 154, no. 1, pp. 76-87, 2003.

[69] G. M. Roberts, J. L. Nixon, J. Lecointre, E. Wrede, and J. R. R. Verlet, "Toward real-time charged-particle image reconstruction using polar onion-peeling," *Review of Scientific Instruments,* vol. 80, no. 5, p. 053104, 2009.

[70] P. Johnsson *et al.*, "Field-free molecular alignment probed by the free electron laser in Hamburg (FLASH)," *Journal of Physics B: Atomic, Molecular and Optical Physics,* vol. 42, no. 13, p. 134017, 2009.

[71] M. M. Wolff and W. E. Stephens, "A Pulsed Mass Spectrometer with Time Dispersion," *Review of Scientific Instruments,* vol. 24, no. 8, pp. 616-617, 1953.

[72] W. C. Wiley and I. H. McLaren, "Time-of-Flight Mass Spectrometer with Improved Resolution," *Review of Scientific Instruments,* vol. 26, no. 12, pp. 1150-1157, 1955.

[73] J. A. Browder, R. L. Miller, W. A. Thomas, and G. Sanzone, "High-resolution TOF mass spectrometry. II. Experimental confirmation of impulse-field focusing theory," *International Journal of Mass Spectrometry and Ion Physics,* vol. 37, no. 1, pp. 99-108, 1981.

[74] N. L. Marable and G. Sanzone, "High-resolution time-of-flight mass spectrometry," *International Journal of Mass Spectrometry and Ion Physics,* vol. 13, no. 3, pp. 185-194, 1974.

[75] B. A. Mamyrin, V. I. Karataev, D. V. Shmikk, and V. A. Zagulin, "

The mass-reflectron, a new nonmagnetic time-of-flight mass spectrometer with high resolution," *oviet Physics JETP,* vol. 37, p. 45, 1973.

[76] T. Bergmann, H. Goehlich, T. P. Martin, H. Schaber, and G. Malegiannakis, "High-resolution time of-flight mass spectrometers. Part II. Cross beam ion optics," *Review of Scientific Instruments,* vol. 61, no. 10, pp. 2585-2591, 1990.

[77] T. I. Wang, C. W. Chu, H. M. Hung, G. S. Kuo, and C. C. Han, "Design parameters of dual-stage ion reflectrons," *Review of Scientific Instruments,* vol. 65, no. 5, pp. 1585-1589, 1994.

[78] U. Boesl, "Time-of-flight mass spectrometry: Introduction to the basics," *Mass Spectrometry Reviews,* vol. 36, no. 1, pp. 86-109, 2017.

[79] B. Brehm and E. von Puttkamer, "Koinzidenzmessung von Photoionen und Photoelektronen bei Methan," *Zeitschrift für Naturforschung A,* vol. 22, no. 1, p. 8, 1967.

[80] H. M. M. Janssen and I. Powis, "Direct Enantiomer-Selective Mass Spectrometry of Chiral Mixtures by Mass-Selected Photoelectron Circular Dichroism," *Spectroscopy,* vol. 15, no. 2, pp. 16–23, 2017.

[81] J. H. D. Eland, "Predissociation of N2O+ and COS+ ions studied by photoelectron-photoion coincidence spectroscopy," *International Journal of Mass Spectrometry and Ion Physics,* vol. 12, no. 4, pp. 389-395, 1973.

[82] T. Baer and R. P. Tuckett, "Advances in threshold photoelectron spectroscopy (TPES) and threshold photoelectron photoion coincidence (TPEPICO)," *Physical Chemistry Chemical Physics,* 10.1039/C7CP00144D vol. 19, no. 15, pp. 9698-9723, 2017.

[83] S. Leach *et al.*, "Ionization photophysics and spectroscopy of dicyanoacetylene," *The Journal of Chemical Physics,* vol. 139, no. 18, p. 184304, 2013.

[84] J. C. Poully *et al.*, "Photoionization of 2-pyridone and 2-hydroxypyridine," *Physical Chemistry Chemical Physics,* vol. 12, no. 14, pp. 3566-3572, 2010.

[85] P. Downie and I. Powis, "The 5a1−1 photoionization of oriented CF3I molecules: Angular distributions of the ka1 and ke photoelectron continua," *The Journal of Chemical Physics,* vol. 111, no. 10, pp. 4535-4547, 1999.

[86] I. Powis, C. J. Harding, G. A. Garcia, and L. Nahon, "A Valence Photoelectron Imaging Investigation of Chiral Asymmetry in the Photoionization of Fenchone and Camphor," *ChemPhysChem,* vol. 9, no. 3, pp. 475-483, 2008.

[87] G. A. Garcia, H. Dossmann, L. Nahon, S. Daly, and I. Powis, "Identifying and Understanding Strong Vibronic Interaction Effects Observed in the Asymmetry of Chiral Molecule Photoelectron Angular Distributions," *ChemPhysChem,* vol. 18, no. 5, pp. 500-512, 2017.

[88] J. G. N. Jr., "SCF-X αSW calculations on PH3 using a nonempirical scheme for choosing overlapping-sphere radii," *The Journal of Chemical Physics,* vol. 61, no. 11, pp. 4630-4635, 1974.

[89] M. J. Frisch *et al.*, "Gaussian 16 Rev. C.01," ed. Wallingford, CT, 2016.

[90] I. Pugliesi and K. Müller-Dethlefs, "The Use of Multidimensional Franck−Condon Simulations to Assess Model Chemistries: A Case Study on Phenol," *The Journal of Physical Chemistry A*, vol. 110, no. 14, pp. 4657-4667, 2006.

[91] W. von Niessen, J. Schirmer, and L. S. Cederbaum, "Computational methods for the one-particle green's function," *Computer Physics Reports,* vol. 1, no. 2, pp. 57-125, 1984.

[92] H. Ganjitabar, R. Hadidi, G. A. Garcia, L. Nahon, and I. Powis, "Vibrationally-resolved photoelectron spectroscopy and photoelectron circular dichroism of bicyclic monoterpene enantiomers," *Journal of Molecular Spectroscopy,* vol. 353, pp. 11-19, 2018.

[93] P. Lahiri, K. B. Wiberg, and P. H. Vaccaro, "A Tale of Two Carenes: Intrinsic Optical Activity and Large-Amplitude Nuclear Displacement," *The Journal of Physical Chemistry A,* vol. 116, no. 38, pp. 9516-9533, 2012.

[94] E. M. Neeman, J. R. A. Moreno, and T. R. Huet, "The gas phase structure of α-pinene, a main biogenic volatile organic compound," *The Journal of Chemical Physics,* vol. 147, no. 21, p. 214305, 2017.

[95] I. Novak and B. Kovač, "Photoelectron spectroscopy of natural products: terpenes," *Spectrochimica Acta Part A: Molecular and Biomolecular Spectroscopy,* vol. 61, no. 1, pp. 277-280, 2005.

[96] M. A. Śmiałek *et al.*, "Limonene: electronic state spectroscopy by high-resolution vacuum ultraviolet photoabsorption, electron scattering, He(i) photoelectron spectroscopy and ab initio calculations," *Physical Chemistry Chemical Physics,* 10.1039/C2CP22847E vol. 14, no. 6, pp. 2056-2064, 2012.

[97] R. F. M. M., G. Hassan, G. G. A., N. Laurent, T. Stefano, and P. Ivan, "Intense Vibronic Modulation of the Chiral Photoelectron Angular Distribution Generated by Photoionization of Limonene Enantiomers with Circularly Polarized Synchrotron Radiation," *ChemPhysChem,* vol. 19, no. 8, pp. 921-933, 2018.

[98] T. Müller, K. B. Wiberg, and P. H. Vaccaro, "Cavity ring-down polarimetry (CRDP): A new scheme for probing circular birefringence and circular dichroism in the gas phase," *Journal of Physical Chemistry A,* Article vol. 104, no. 25, pp. 5959-5968, 2000.

[99] D. Kubala *et al.*, "Electron impact ionisation and UV absorption study of α- and β-pinene," *International Journal of Mass Spectrometry,* vol. 280, no. 1, pp. 169-173, 2009.

[100] M. Cao *et al.*, "Dissociative Photoionization of β-Pinene: An Experimental and Theoretical Study," *European Journal of Mass Spectrometry,* vol. 20, no. 6, pp. 419-428, 2014.

[101] J. R. Calo, P. G. Crandall, C. A. O'Bryan, and S. C. Ricke, "Essential oils as antimicrobials in food systems – A review," *Food Control,* vol. 54, pp. 111-119, 2015.

[102] L. M. Calvo-Irabien, "Native Mexican aromatic flora and essential oils: Current research status, gaps in knowledge and agro-industrial potential," *Industrial Crops and Products,* vol. 111, pp. 807-822, 2018.

[103] T. L. Collins, G. L. Jones, and N. J. Sadgrove, "Volatiles from the Rare Australian Desert Plant Prostanthera centralis B.J.Conn (Lamiaceae): Chemical Composition and Antimicrobial Activity," *Agriculture,* vol. 4, no. 4, pp. 308-316, 2014.

[104] T. K. T. Do, F. Hadji-Minaglou, S. Antoniotti, and X. Fernandez, "Authenticity of essential oils," *TrAC Trends in Analytical Chemistry,* vol. 66, pp. 146-157, 2015.

[105] S. A. Khayyat and L. S. Roselin, "Recent progress in photochemical reaction on main components of some essential oils," *Journal of Saudi Chemical Society,* vol. 22, no. 7, pp. 855-875, 2018.

[106] N. Sadgrove and G. Jones, "A Contemporary Introduction to Essential Oils: Chemistry, Bioactivity and Prospects for Australian Agriculture," *Agriculture,* vol. 5, no. 1, pp. 48-102, 2015.

[107] T. H. Tran *et al.*, "Optimization of Microwave-Assisted Extraction of Essential Oil from Vietnamese Basil (Ocimum basilicum L.) Using Response Surface Methodology," *Processes,* vol. 6, no. 11, p. 206, 2018.

[108] H. Zhai, H. Liu, S. Wang, J. Wu, and A.-M. Kluenter, "Potential of essential oils for poultry and pigs," *Animal Nutrition,* vol. 4, no. 2, pp. 179-186, 2018.

[109] G. Dugo and L. Mondello, *Citrus oils: composition, advanced analytical techniques, contaminants, and biological activity*. London: CRC Press Inc., 2010, p. 586 pp.

[110] P. N. Ravindran, *Black Pepper: Piper nigrum*, 1st ed. CRC Press, 2000, p. 526.

[111] D. Teneva *et al.*, "Chemical Composition and Antimicrobial Activity of Essential Oils from Black Pepper, Cumin, Coriander and Cardamom Against Some Pathogenic Microorganisms," (in English), vol. 20, no. 2, p. 39, 2016.

[112] N. Mahato, K. Sharma, R. Koteswararao, M. Sinha, E. Baral, and M. H. Cho, "Citrus essential oils: Extraction, authentication and application in food preservation," *Critical Reviews in Food Science and Nutrition,* vol. 59, no. 4, pp. 611-625, 2019.

[113] K. Fisher and C. Phillips, "Potential antimicrobial uses of essential oils in food: is citrus the answer?," *Trends in Food Science & Technology,* vol. 19, no. 3, pp. 156-164, 2008.

[114] A. D. G. Giovanni Dugo, *Citrus: The Genus Citrus*. CRC Press, 2002, p. 656.

[115] H. M. RICHARD and W. G. JENNINGS, "VOLATILE COMPOSITION OF BLACK PEPPER," *Journal of Food Science,* vol. 36, no. 4, pp. 584-589, 1971.

[116] K. A. BUCKLE, M. RATHNAWATHIE, and J. J. BROPHY, "Compositional differences of black, green and white pepper (Piper nigrum L.) oil from three cultivars," *International Journal of Food Science & Technology,* vol. 20, no. 5, pp. 599-613, 1985.

[117] N. Bousbia, M. A. Vian, M. A. Ferhat, B. Y. Meklati, and F. Chemat, "A new process for extraction of essential oil from Citrus peels: Microwave hydrodiffusion and gravity," *Journal of Food Engineering,* vol. 90, no. 3, pp. 409-413, 2009.

[118] *Handbook of Essential Oils* (Handbook of Essential Oils). CRC Press, 2015.

[119] R. C. Menary, *Authenticating essential oil flavours and fragrances : using Enantiomeric Composition Analysis : a report for the Rural Industries Research and Development Corporation / by RC Menary and SM Garland* (RIRDC publication ; no.99/125., no. Accessed from). Barton, A.C.T: Rural Industries Research & Development Corporation, 1999.

[120] P. Q. Tranchida, I. Bonaccorsi, P. Dugo, L. Mondello, and G. Dugo, "Analysis of Citrus essential oils: state of the art and future perspectives. A review," *Flavour and Fragrance Journal,* vol. 27, no. 2, pp. 98-123, 2012.

[121] W. Bertsch, "Two-Dimensional Gas Chromatography. Concepts, Instrumentation, and Applications – Part 1: Fundamentals, Conventional Two-Dimensional Gas Chromatography, Selected Applications," *Journal of High Resolution Chromatography,* vol. 22, no. 12, pp. 647-665, 1999.

[122] C. Bicchi, A. D'Amato, and P. Rubiolo, "Cyclodextrin derivatives as chiral selectors for direct gas chromatographic separation of enantiomers in the essential oil, aroma and flavour fields," *Journal of Chromatography A,* vol. 843, no. 1, pp. 99-121, 1999.

[123] G. Dugo *et al.*, "Characterization of Oils from the Fruits, Leaves and Flowers of the Bitter Orange Tree," *Journal of Essential Oil Research,* vol. 23, no. 2, pp. 45-59, 2011.

[124] D. Sciarrone *et al.*, "Thorough evaluation of the validity of conventional enantio-gas chromatography in the analysis of volatile chiral compounds in mandarin essential oil: A comparative investigation with multidimensional gas chromatography," *Journal of Chromatography A,* vol. 1217, no. 7, pp. 1101-1105, 2010.

[125] I. Bonaccorsi, D. Sciarrone, A. Cotroneo, L. Mondello, P. Dugo, and G. Dugo, "Enantiomeric distribution of key volatile components in Citrus essential oils," *Revista Brasileira de Farmacognosia,* vol. 21, pp. 841-849, 2011.

[126] D. J. Daferera, P. A. Tarantilis, and M. G. Polissiou, "Characterization of Essential Oils from Lamiaceae Species by Fourier Transform Raman Spectroscopy," *Journal of Agricultural and Food Chemistry,* vol. 50, no. 20, pp. 5503-5507, 2002.

[127] H. Schulz, B. Schrader, R. Quilitzsch, and B. Steuer, "Quantitative Analysis of Various Citrus Oils by ATR/FT-IR and NIR-FT Raman Spectroscopy," *Applied Spectroscopy,* vol. 56, no. 1, pp. 117-124, 2002.

[128] B. Steuer, H. Schulz, and E. Läger, "Classification and analysis of citrus oils by NIR spectroscopy," *Food Chemistry,* vol. 72, no. 1, pp. 113-117, 2001.

[129] M. Baranska *et al.*, "Vibrational spectroscopic studies to acquire a quality control method of Eucalyptus essential oils," *Biopolymers,* vol. 78, no. 5, pp. 237-248, 2005.

[130] R. B. Godinho, M. C. Santos, and R. J. Poppi, "Quality control of fragrances using Raman spectroscopy and multivariate analysis," *Journal of Raman Spectroscopy,* vol. 47, no. 5, pp. 579-584, 2016.

[131] M. Sandasi, G. P. P. Kamatou, M. Baranska, and A. M. Viljoen, "Application of vibrational spectroscopy in the quality assessment of Buchu oil obtained from two commercially important Agathosma species (Rutaceae)," *South African Journal of Botany,* vol. 76, no. 4, pp. 692-700, 2010.

[132] M. Sandasi, G. P. P. Kamatou, C. Gavaghan, M. Baranska, and A. M. Viljoen, "A quality control method for geranium oil based on vibrational spectroscopy and chemometric data analysis," *Vibrational Spectroscopy,* vol. 57, no. 2, pp. 242-247, 2011.

[133] K. R. Strehle, P. Rösch, D. Berg, H. Schulz, and J. Popp, "Quality Control of Commercially Available Essential Oils by Means of Raman Spectroscopy," *Journal of Agricultural and Food Chemistry,* vol. 54, no. 19, pp. 7020-7026, 2006.

[134] S. Y. Tankeu, I. Vermaak, G. P. P. Kamatou, and A. M. Viljoen, "Vibrational spectroscopy and chemometric modeling: An economical and robust quality control method for lavender oil," *Industrial Crops and Products,* vol. 59, pp. 234-240, 2014.

[135] *MATLAB R2016a*, 2016.

[136] S. J.S, P. Mishra, J. Thomas, A. Mukherjee, and N. Chandrasekaran, "Antimicrobial potency of high-energy emulsified black pepper oil nanoemulsion against aquaculture pathogen," *Aquaculture,* vol. 491, pp. 210-220, 2018.

[137] F. Zhu, R. Mojel, and G. Li, "Structure of black pepper (Piper nigrum) starch," *Food Hydrocolloids,* vol. 71, pp. 102-107, 2017.

[138] F. Zhu, R. Mojel, and G. Li, "Physicochemical properties of black pepper (Piper nigrum) starch," *Carbohydrate Polymers,* vol. 181, pp. 986-993, 2018.

[139] T. H. Tran *et al.*, "The Study on Extraction Process and Analysis of Components in Essential Oils of Black Pepper (Piper nigrum L.) Seeds Harvested in Gia Lai Province, Vietnam," *Processes,* vol. 7, no. 2, p. 56, 2019.

[140] H. Schulz, M. Baranska, R. Quilitzsch, W. Schütze, and G. Lösing, "Characterization of Peppercorn, Pepper Oil, and Pepper Oleoresin by Vibrational Spectroscopy Methods," *Journal of Agricultural and Food Chemistry,* vol. 53, no. 9, pp. 3358-3363, 2005.

[141] A. Orav, I. Stulova, T. Kailas, and M. Müürisepp, "Effect of Storage on the Essential Oil Composition of Piper nigrum L. Fruits of Different Ripening States," *Journal of Agricultural and Food Chemistry,* vol. 52, no. 9, pp. 2582-2586, 2004.

[142] D. Sruthi, J. Zachariah, L. Nk, and J. K, "Correlation between chemical profiles of black pepper (Piper nigrum L.) var. Panniyur-1 collected from different locations," *Journal of Medicinal Plants Research*, vol. 7, pp. 2349-2357, 2013.

[143] *Gli olii essenziali agrumari in Italia / a cura di Angelo Di Giacomo e Biagio Mincione*. Reggio Calabria: Laruffa, 1994.

[144] D. Materić *et al.*, "Selective reagent ion-time of flight-mass spectrometry study of six common monoterpenes," *International Journal of Mass Spectrometry,* vol. 421, pp. 40-50, 2017.

[145] P. K. Misztal, M. R. Heal, E. Nemitz, and J. N. Cape, "Development of PTR-MS selectivity for structural isomers: Monoterpenes as a case study," *International Journal of Mass Spectrometry,* vol. 310, pp. 10-19, 2012.

[146] V. Simon, M.-L. Riba, A. Waldhart, and L. Torres, "Breakthrough volume of monoterpenes on Tenax TA: influence of temperature and concentration for α-pinene," *Journal of Chromatography A,* vol. 704, no. 2, pp. 465-471, 1995.

[147] A. Bornschlegl, C. Logé, and U. Boesl, "Investigation of CD effects in the multi photon ionisation of R-(+)-3-methylcyclopentanone," *Chemical Physics Letters,* vol. 447, no. 4, pp. 187-191, 2007.

[148] B. Schaefer, E. Collett, R. Smyth, D. Barrett, and B. Fraher, "Measuring the Stokes polarization parameters," *American Journal of Physics,* vol. 75, no. 2, pp. 163-168, 2007.

[149] S. Beaulieu *et al.*, "Photoexcitation circular dichroism in chiral molecules," *Nature Physics,* vol. 14, no. 5, pp. 484-489, 2018.

[150] K. L. Reid, "PHOTOELECTRON ANGULAR DISTRIBUTIONS," *Annual Review of Physical Chemistry,* vol. 54, no. 1, pp. 397-424, 2003.

[151] S. Daly, F. Rosu, and V. Gabelica, "Mass-resolved electronic circular dichroism ion spectroscopy," *Science,* vol. 368, no. 6498, p. 1465, 2020.

[152] O. Hüter and F. Temps, "Note: Energy calibration of a femtosecond photoelectron imaging detector with correction for the ponderomotive shift of atomic ionization energies," *Review of Scientific Instruments,* vol. 88, no. 4, p. 046101, 2017.

10. Appendices

10.1. Appendix A: VMI calibration

In section 2.1 we explained the VMI technique in detail. However, in order to analyse and interpret the results obtained using this technique, we have to calibrate the system. As it was mentioned before, different rings in a given image recorded in a VMI setup correspond to different electron kinetic energies. The calibration is needed to enable the users to get the PES or PECD spectrum vs the right scales of electron kinetic energy (or equivalently vs the right scale of ionization energy). The equation which links the rings in the VMI images to the electron kinetic energies is

$$eKE = V_{rep}(\frac{R^2}{C^2} - \frac{R^3}{B^3}) \qquad \text{(Eq. 46)}$$

where eKE is the kinetic energy of the electrons, V_{rep} is the voltage applied to the repeller electrode, R is the radius of a given ring and C and B are some constants called calibration factors. The cubic term in (Eq. 46) is taken into account only when there is some additional electrode acting as the electrostatic lens. This may be the case when some more focusing or defocusing of the electrons is needed. In our current setup, no electrostatic lens was active and we used only the three conventional VMI plates: repeller, extractor and ground. So, the equation we use to convert the R to the eKE (or other way around) is

$$eKE = V_{rep}\frac{R^2}{C^2} \qquad \text{(Eq. 47)}$$

In this equation, C is the only calibration factor that we need to determine. The calibration factor depends generally on the geometry of the VMI setup and the size of the plates as well as the distance between them. So, every VMI system has its own calibration factor.

To obtain the calibration factor C in (Eq. 47), we should record images of some species having well separated and established ionization potentials (separated and narrow peaks in their PES), like Xe gas. To do this, in general, we can write the eKE term as

$$eKE = nh\nu + n'h\nu' - IE \qquad \text{(Eq. 48)}$$

where n and n' are the total number of photons involved in excitation and ionization steps, $h\nu$ and $h\nu'$ are their corresponding single-photon energies, respectively, and IE is the ionization energy. If we are doing a single colour MPI, $h\nu$ and $h\nu'$ will be identical and defining $N = n + n'$ leads to

$$eKE = Nh\nu - IE \qquad \text{(Eq. 49)}$$

Combining (Eq. 49) with (Eq. 47) gives us the following expression for the calibration factor

$$C = R\sqrt{\frac{V_{rep}}{Nh\nu - IE}} \qquad \text{(Eq. 50)}$$

If there is only one ring present in the VMI image of the calibration gas, we can simply use the above expression to get the calibration factor; however, if the laser intensity is high enough, we may also see some more rings in the image, corresponding to the ionization from deeper orbitals. In such a case, we can fit a curve to all data points, any of which is for one ring in the image. To do this, we can look at a useful, simple rearrangement of the above equations as

$$eKE = kR^2 \qquad \text{(Eq. 51)}$$

in which

$$k = \frac{V_{rep}}{C^2} \qquad \text{(Eq. 52)}$$

So, if we have a set of data points as (eKE, R), fitting a polynomial of the second degree to that will give us the k factor in (Eq. 51). Then, we can subsequently calculate C using (Eq. 52). A sample VMI calibration with Xe is reported in Ref. [152]; this paper is interesting because it also discusses the ponderomotive effect and how it can affect the calibration of a VMI setup. The idea is that if we are calibrating a VMI system at some certain laser intensity, the calculated calibration factor may not be necessarily valid for other laser intensities. In other words, the size of the same ring in the VMI image changes when it is measured at different laser intensities. The AC Stark effect causes an atom in a high-intensity field to experience an increase in IP leading to a decrease in the size of its corresponding ring in VMI image, look at (Eq. 49) and (Eq. 51). This can be theoretically expressed as

$$eKE_1 = eKE_0 - U_p \qquad \text{(Eq. 53)}$$

where eKE_0 and eKE_1 are the electron kinetic energy without considering the ponderomotive effect and electron effective kinetic energy that we measure, respectively, and U_p is the ponderomotive energy shift given by

$$U_p = \frac{e^2}{2m_e c\epsilon_0\omega^2} I \qquad \text{(Eq. 54)}$$

Here, I and ω are the intensity and the frequency of the laser, respectively. Assuming the laser frequency to be constant, combining (Eq. 54), (Eq. 53) and (Eq. 51) leads to

$$r_1^2 = r_0^2 - \alpha I \qquad \text{(Eq. 55)}$$

where $\alpha = \frac{e^2}{2m_e c\epsilon_0\omega^2 k}$ and $r_1$and r_0 are connected to eKE_1 and eKE_0 via (Eq. 51). The recent equation shows a linear correlation between r_1^2 and the laser intensity, I. Having a set of measurements done with the same calibration gas and looking at the same ring at different laser intensities, one can fit a line to the data points (r_1^2, I) and calculate r_0^2 which is supposed to be the squired of the radius of the same ring at the near-zero laser intensity. However, after getting the equation of the fitted line, it is possible to calculate the radius of the same ring at any other laser intensity and find the corrected calibration factor with respect to that, see (Eq. 50).

This procedure is useful when we are doing the calibration of our VMI system at a given laser intensity while the subsequent measurements with the VMI system are going to be done at another, different laser intensity. This happens quite often when the measurements are done at relatively long wavelengths, for which the ionizing of the calibration gas needs more photons to be absorbed. In such cases, we need to increase the laser intensity in order to improve the ionization cross-section. Now, if we are interested in some molecules with a relatively lower IP, the number of photons for ionization from such a molecule is less, requiring lower laser intensities. So, for this typical molecule, the laser intensity will not be as same as that used for the calibration. Anyway, the same situation may happen where the ionization potential of the calibration gas is quite higher than that of the other molecules under the study. In these cases, we need higher intensities for ionization from the calibration gas. Furthermore, the ionization for the calibration gas is often a direct MPI without any intermediate resonance while the ionization of the other molecules may be resonantly enhanced. This means that even if the ionization potential for the calibration gas and the molecules under the study are roughly the same, we still may need higher laser intensities for calibration.

Fig. 148, taken from Ref. [152], shows four measurements done for Xe at different laser intensities. The y-axis is presenting the squared of the radius of the same ring (an ionization from ${}^5P_{3/2}$at four-photon absorption) vs different laser intensities. The wavelength of the laser in all measurements is fixed at 402 nm. Based on the equation of the fitted line to the experimental measurements, the authors can correct the calibration factor for any given laser intensity. However, at such high intensities, the authors have also seen two more rings in the VMI images, corresponding to five-photon ionization channels. The same figures as Fig. 148 can be drown for any of those peaks as well. So, when the authors want to correct the calibration factor, they consider the corrections for all the three peaks. Actually, to get the corrected calibration factor at any given intensity, they calculate the expected radius for all three peaks at that intensity and then by considering (Eq. 51), they fit a second degree polynomial to the three data points. They calculate the correction to the calibration factor due to the ponderomotive effect to be %2.8, going from pulse energy of 50 $\mu J$to near zero.

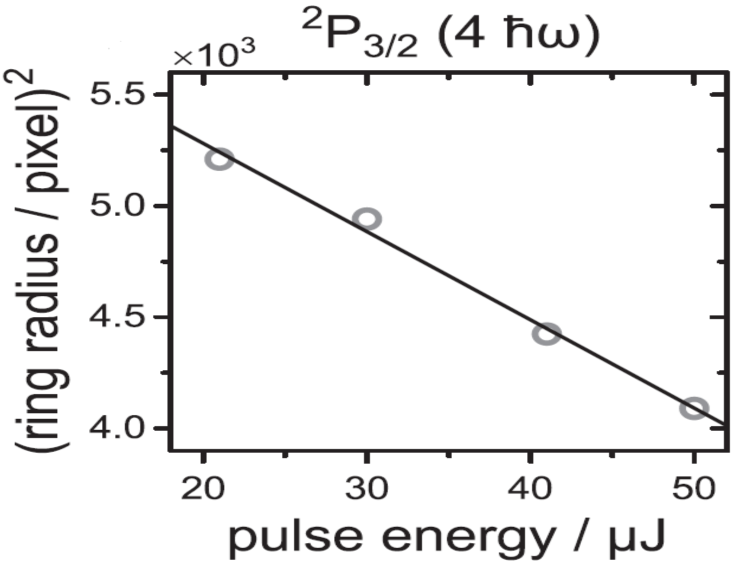

Fig. 148: fitting a line to the Xe calibration measurements (ionization from $^5P_{3/2}$ *via four-photon absorption) done with different pulse energies at 402 nm, Ref. [152].*

In our experiment, we used Xe and CS2 to calibrate the VMI system; several measurements with Xe were done at two wavelengths 396.52 nm and 200.66 nm, while the calibration with CS2 was done only at 200.66 nm. In the following sub-sections, the results are presented.

10.1.1. Xenon calibration at 396.52 nm

The repeller voltage principally should not affect the calibration factor, however, it controls the size of the VMI rings on the detector screen. The higher the repeller voltage, the smaller the size of the ring (at the same photon energy and for the same ionization pathway). This can be understood by looking at (Eq. 50) and keeping the calibration factor constant in mind. We used this idea to record images with different sizes, but originating from the same ionization pathway at the same photon energy, in order to have more data points to calculate the calibration factor with higher reliability. Actually, we recorded eight images applying different repeller voltages ranging from 200 V to 1600 V. The PES spectra resulted from pBASEX analysis for the images are given in Fig. 149, in which we consider the location of each peak as the radius of its corresponding image.

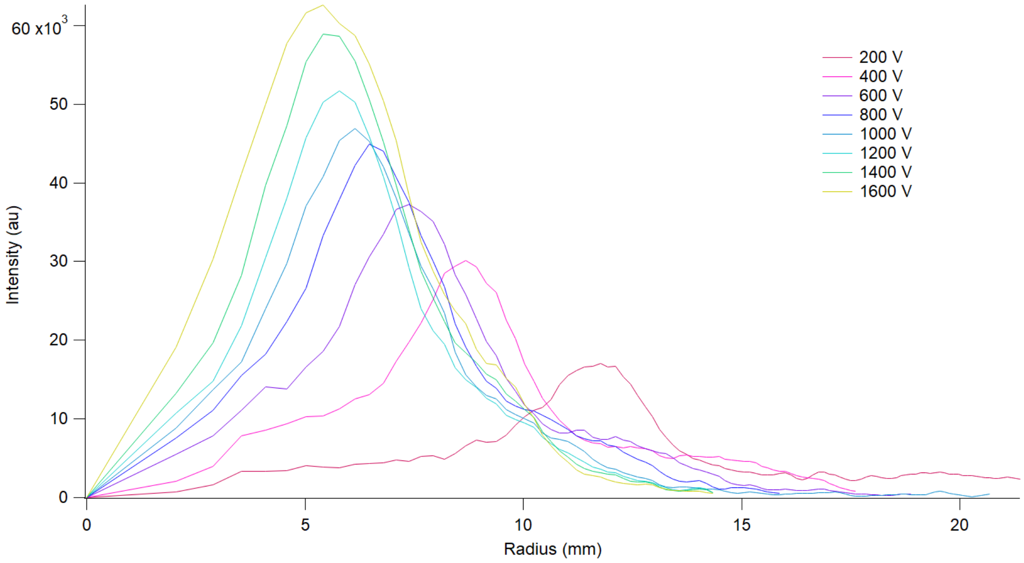

Fig. 149: different radii for PES spectrum peak of Xe calibration measurements (ionization from $^5P_{3/2}$ *via four-photon absorption) done with different* V_{rep} *but constant* $\eta = {}^{V_{ext}}/_{V_{rep}} = 0.71$.

Rearranging (Eq. 50) in the following way

$$R^2 = \frac{(Nh\nu - IE)C^2}{V_{rep}} \qquad \text{(Eq. 56)}$$

gives R^2 as a linear function of $^1/_{V_{rep}}$. So we can fit a line to data points $(R^2, {}^1/_{V_{rep}})$ to find the calibration factor. The results of such a fitting are shown in Fig. 150. Table 14 shows the individual calibration factors at any repeller voltage as well as the calibration factor obtained through the fitting. The ionization energy for Xe that we are putting into the (Eq. 56) is IE=12.13 for a four-photon ionization from $^5P_{3/2}$ state. It should also be noticed that all the measurements on Xe for calibration used in this section are done with a laser power of 20 mW.

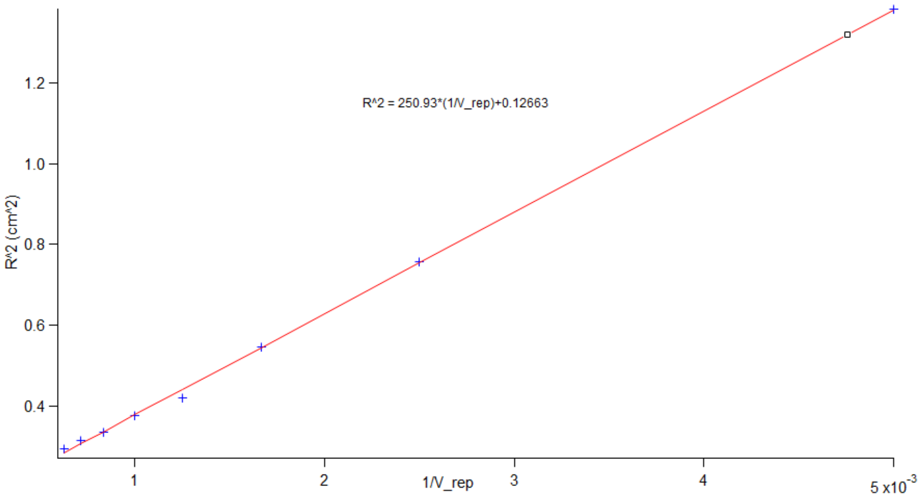

Fig. 150: fitting a line to data points $(R^2, {}^{1}/_{V_{rep}})$ *obtained in Xe calibration at 396.52 nm with a laser power of 20 mW.*

The individual calibration factors presented in Table 14 are not showing a normal fluctuation around some constant value, but instead of that, they are increasing as the repeller voltage increases. Also, the fit-line presented in Fig. 150 is showing an intercept, which was not expected in (Eq. 56). This is the case because there is another factor affecting the shape of the images which is the ratio of the voltages applied to the extractor and repeller electrodes, $\eta = {}^{V_{ext}}/_{V_{rep}}$. Setting this factor properly makes the VMI images perfectly circular; otherwise, the images may be elliptical or in some cases two-centred.

Table 14: Calibration factor obtained in Xe calibration at 396.52 nm with a laser power of 20 mW and different repeller voltages.

V_{rep}	R (mm)	Individual C factors	C factor obtained by fitting a linear curve to all data points
200	11.761	26.97697	25.69
400	8.6959	28.2084	
600	7.3816	29.32649	
800	6.4741	29.70013	
1000	6.1419	31.50189	
1200	5.7906	32.5348	
1400	5.6	33.9849	
1600	5.4166	35.14153	

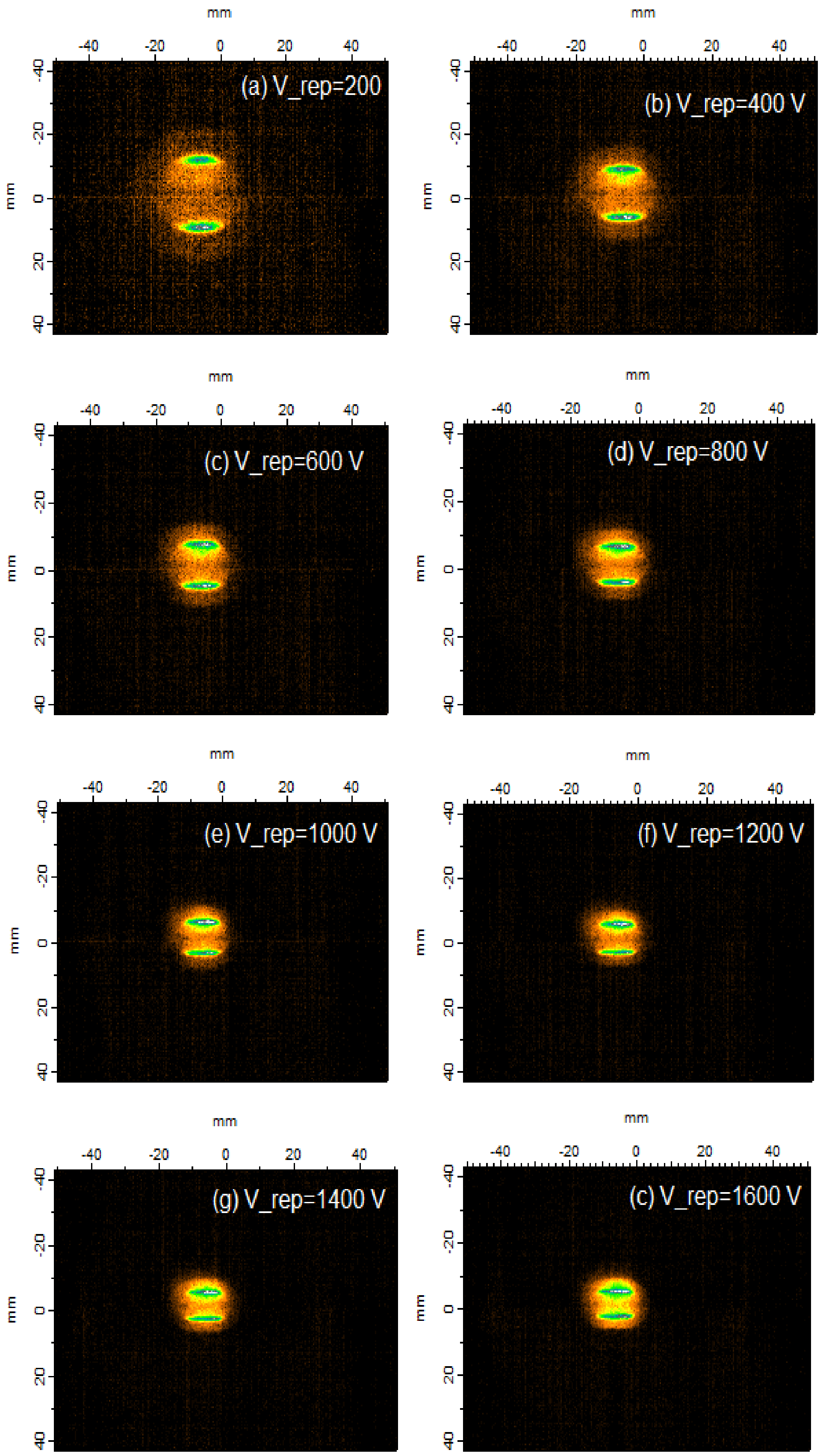

Fig. 151: VMI images for Xe calibration measurements done at $\eta = 0.71$, *but with different* V_{rep}, *using wavelength 396.52 nm with a laser power of 20 mW. Ionization is happening from* ${}^5P_{3/2}$ *state with ionization energy of 12.13 eV.*

The value of η for all of the data presented in Table 14 was 0.71. Actually, this value was not the proper one for this VMI system. This can be realized by looking at the VMI images corresponding to the data of Table 14, plotted in Fig. 151. It can be seen that the images for higher values of V_{rep} are elliptical; however, the degree of ellipticity for lower repeller voltages is less. For instance, the image recorded at $V_{rep} = 200\ V$ is looking like circular. So, for two reason we will trust only on the individual calibration value obtained at $V_{rep} = 200$ first of which is the circular shape of the image recorded with this voltage. The second reason is that the PECD measurement for α-pinene at 396.52 nm is done with $V_{rep} = 205$ V to which this is the closest one.

To find the best value of η for which the images are circular, we kept the V_{rep} constant at 396.52 V and changed the V_{ext} a little bit. Table 15 and Fig. 152 show the data and images for such measurements, respectively. Looking at the images presented in Fig. 152, the conclusions were that for this VMI system, the best value for η is 0.74. Actually, we used this ratio for all of our subsequent measurements, but the PECD measurements on α-pinene at 396.52 nm were done with $\eta = 0.71$, before we set η properly. Additionally, as we will see in sec 7.2, the VMI images for α-pinene recorded with $\eta = 0.71$ are not so far away from a perfectly circular shape because they have been recorded at a low repeller voltage, 205 V.

Table 15: Different values of η (extractor voltage) with the same repeller voltages, $V_{rep} = 400\ V$ in Xe calibration.

V_{rep} (V)	η	V_{ext} (V)
400	0.76	304
	0.75	300
	0.74	296
	0.73	292
	0.72	288
	0.71	284

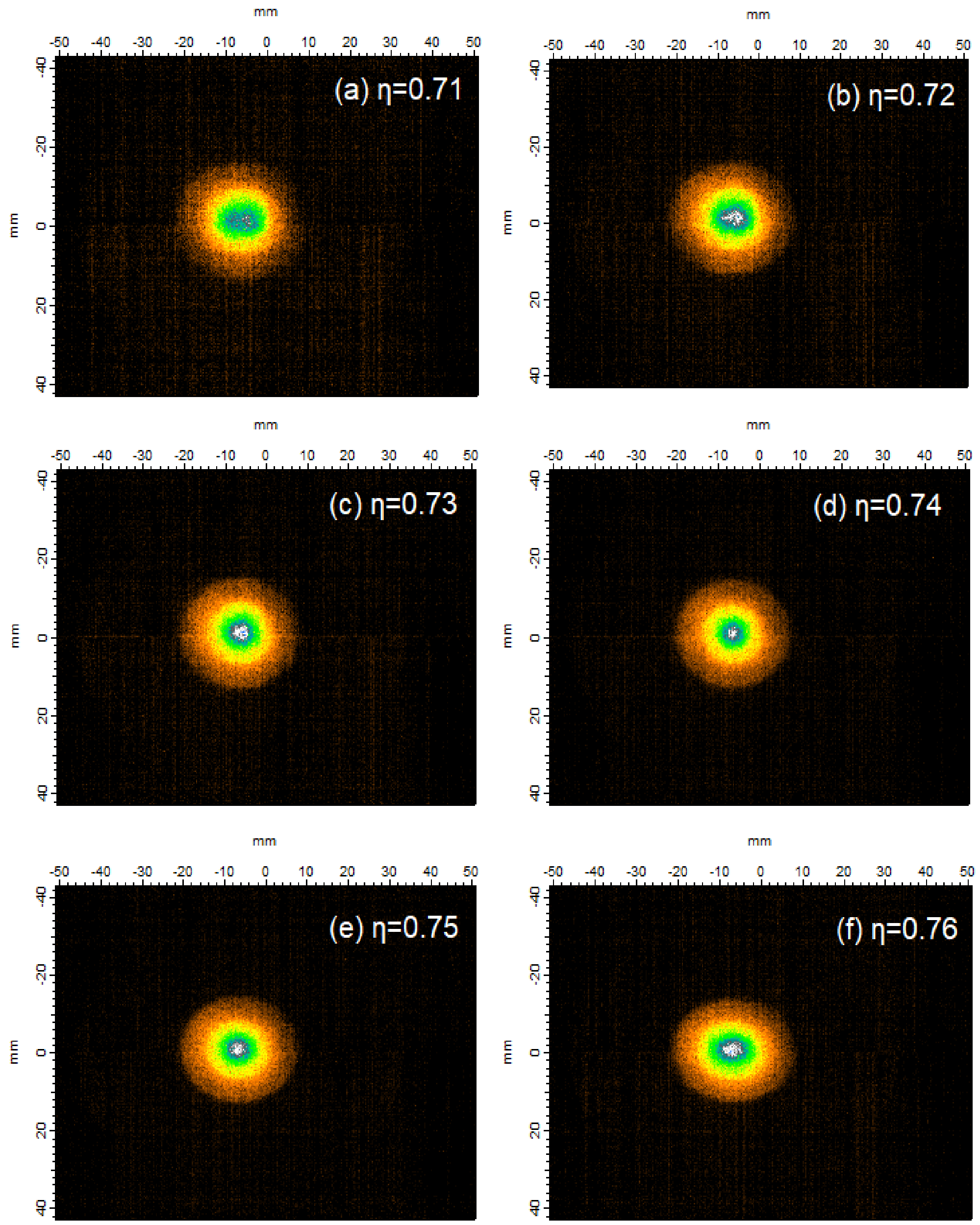

Fig. 152: VMI images for Xe calibration recorded at $V_{rep} = 400\ V$ *with different* η *values, using wavelength 396.52 nm with a laser power of 20 mW.*

Now, we can discuss more on what we mentioned previously about the ponderomotive effect. In fact, for α-pinene ionization at 396.52 nm, we need three photons while Xe requires at least four photons with the same wavelength to be ionized; furthermore, the ionization of Xe is not resonantly enhanced. So, we had to do the calibration at a relatively higher laser power. The question is that can we use the calibration factor obtained with a high laser power for treating the data that have been recorded with a low laser power? The answer depends on how big might the ponderomotive effect be and consequently how much it can affect the calibration factor.

We can get a sense of the amount of the calibration factor correction needed just by looking at the data presented in the Ref. [152]. Below, we briefly explain the instruction to estimate the correction to the calibration factor.

Suppose that we are doing the calibration at a given laser power and see three peaks, R_1, R_2 and R_3 in the Xe PES; we can fit a curve like $eKE = kR^2$ to the data points (eKE, R) to get the calibration factor. Then, for getting the calibration factor at any other laser intensity, we should calculate the radius of these three rings at that specific intensity (say R_1', R_2' and R_3') and fit the same curve $eKE = k'R'^2$to them. (Here, two laser powers that we are interested in are 20 mW and 5 mW; actually, in one part of our experiment, we are doing the Xe calibration using a laser power of 20 mW. Then, the result of calibration is used in the analysis of α-pinene PECD measurement done with a laser power of 5 mW. The laser repetition rate is 1 kHz which offers a power of 1 mW is equivalent to a pulse energy of 1 μJ) Fig. 153 (a) and Fig. 153 (b) show two curves fitted to the data points of pulse energies 20 μJ and 5 μJ (from Ref. [152]) , respectively. The calibration factor obtained from the fitting for pulse energy 5 μJ is 2296.33 which is %0.37 larger than that of 20 μJ ($C_{5\,\mu J} = 1.0037 \times C_{20\,\mu J}$; $C_{20\,\mu J} = 2287.91$).

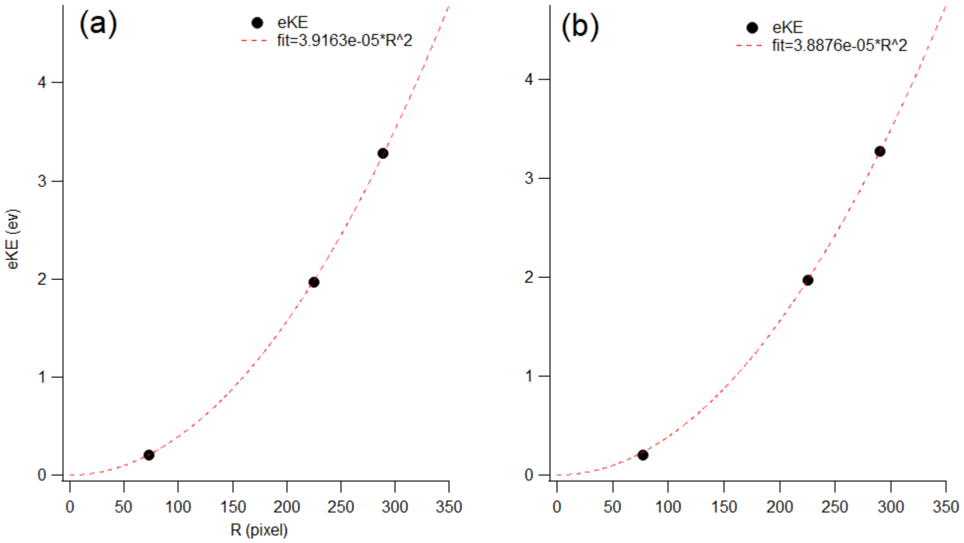

Fig. 153: (a) fitting $eKE = kR^2$ to data points (eKE, R) for pulse energy of 20 μJ (b) fitting $eKE = kR^2$ to data points (eKE, R) for pulse energy of 5 μJ.

This calculation offers the correction to the calibration factor, due to the ponderomotive effect, to be small. In our case, the calibration factor resulted from Xe measurements at 20.0 mW is 26.98 (see Table 14, $V_{rep} = 200$ V case), so we need to correct it like

$$C_{5\,\mathrm{mW}} = 1.0037 \times C_{20\,\mathrm{mW}} = 27.08 \qquad \text{(Eq. 57)}$$

We should notice that this correction is calculated based on the data provided in Ref. [152] just to get an estimation of the ponderomotive effect and we are not going to use it directly in our analysis; however, this helps us to be aware of some probable, small uncertainties that may appear in our PES and PECD spectra. When we are extracting PES and PECD spectra from an image, we should feed our software with a calibration factor. Any uncertainty in the calibration factor will be reflected in the horizontal axis (ionization energy or electron kinetic energy) in PES or PECD spectrum.

10.1.2. CS2 calibration at 200.66 nm

In this run of the experiment, we also were interested to do some MPI-PECD measurements of α-pinene at 200.66 nm. So, it was worthwhile to have some calibration at this wavelength too. The gas that we chose to do the calibration with, in this case, was CS2 having an ionization potential of 10.073. At 200.66 nm and with this ionization potential, only two photons are needed for ionizing CS2, which in turn requires lower laser powers, in comparison to the four-photon ionization of the Xe. Actually, the laser power for CS2 calibration was 0.18 mW, two orders of magnitude smaller than that for Xe. The calibration image was recorded with $\eta = 0.74$ at 200.66 nm shown in Fig. 154. The calibration factor obtained in this case was $C = 26.68$, which is verifying our Xe calibration at 396.52 nm very well (see Sec. 10.1.1). Here, we inserted the location of the peak in the PES spectrum (shown in right hand side of Fig. 154,) as R, into the (Eq. 50) to get the calibration factor. In this equation, we also considered the energy of two photons at 200.66 as 12.36 eV.

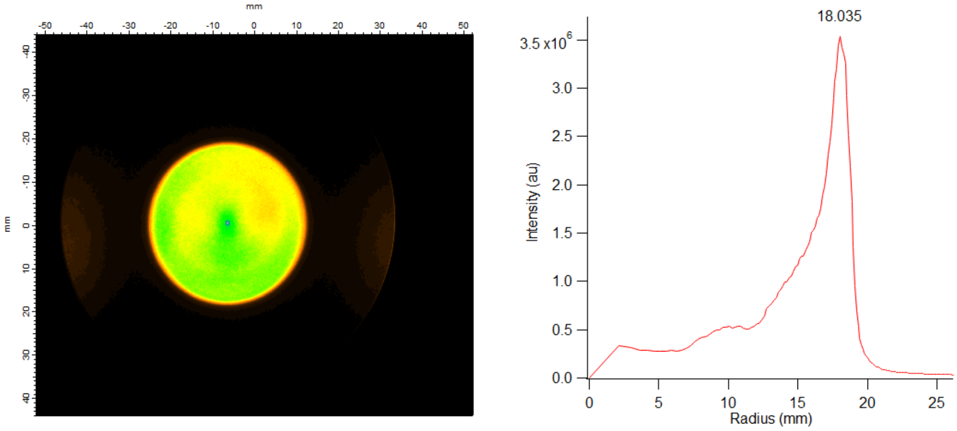

Fig. 154: VMI image, left, and the PES spectrum, right, for CS2 calibration with $\eta = 0.74$ ($V_{rep} = 500\ V$) at 200.66 nm. Laser power was 0.18 mW and the energy of two photons at this wavelength was 12.36 eV.